CNWRA 92-006

THEORETICAL AND EXPERIMENTAL INVESTIGATION OF THERMOHYDROLOGIC PROCESSES IN A PARTIALLY SATURATED, FRACTURED POROUS MEDIUM: A SUMMARY OF WORK THROUGH DECEMBER 1991

Prepared for

Nuclear Regulatory Commission
Contract NRC-02-88-005

Prepared by

Center for Nuclear Waste Regulatory Analyses
San Antonio, Texas

April 1992

Property of
CNWRA Library

THEORETICAL AND EXPERIMENTAL INVESTIGATION OF THERMOHYDROLOGIC PROCESSES IN A PARTIALLY SATURATED, FRACTURED POROUS MEDIUM: A SUMMARY OF WORK THROUGH DECEMBER 1991

Prepared for

Nuclear Regulatory Commission
Contract NRC-02-88-005

Prepared by

Ronald T. Green
Randall D. Manteufel
Franklin T. Dodge
Steven J. Svedeman

April 1992

ABSTRACT

The performance of a geologic repository for high-level nuclear waste will be influenced to a large degree by thermohydrologic phenomena created by the emplacement of heat-generating radioactive waste. The importance of these phenomena is manifest in that they can greatly affect the movement of moisture and the resulting transport of radionuclides from the repository. Thus, these phenomena must be well understood prior to a definitive assessment of a potential repository site. For this reason the Thermohydrology Research Project was initiated.

An investigation has been undertaken along three separate avenues of analysis to attain the objectives of the research project: (i) laboratory experiments, (ii) mathematical models, and (iii) similitude analysis. A summary of accomplishments to date is as follows.

- A comprehensive review of the literature on the theory of heat and mass transfer in partially-saturated porous medium was completed and documented.
- A detailed development of the governing conservation and constitutive equations was completed and documented.
- A detailed development of a dimensionless form of the governing equations has been completed and documented.
- A numerical study of the importance and sensitivity of flow to a set of dimensionless groups has been completed and documented.
- A survey and evaluation of experimental measurement techniques were performed and documented.
- A series of scoping experiments was performed to study the capabilities and limitations of experimental instruments.
- A series of separate-effect experiments was performed to study individual aspects of thermohydrologic processes of nonisothermal flow in a porous medium with a simulated fracture.
- A numerical study was performed and the results compared with the data from a separate-effect experiment.

TABLE OF CONTENTS

TABLE OF CONTENTS (continued)

TABLE OF CONTENTS (continued)

TABLE OF CONTENTS (continued)

TABLE OF CONTENTS (continued)

APPENDICES

TABLE OF CONTENTS (continued)

TABLE OF CONTENTS (continued)

LIST OF FIGURES

LIST OF FIGURES (continued)

LIST OF FIGURES (continued)

LIST OF FIGURES (continued)

APPENDICES

LIST OF TABLES

APPENDICES

NOMENCLATURE

Bo	=	Bond number, ratio of gravity to surface tension forces [dimensionless] $Bo = \frac{(\rho_l - \rho_{g,o}) g L \sqrt{k_{sat}/\phi}}{\sigma_o}$
c_a	=	specific heat of air [J/kg-C]
$c_{a,g}$	=	specific heat of air in the gaseous phase [J/kg-C]
$c_{p,a,g}$	=	specific heat at constant pressure for air in the gas phase [J/kg-C]
$c_{p,w,g}$	=	specific heat at constant pressure for water in the gas phase [J/kg-C]
$c_{w,g}$	=	specific heat of water (H_2O) in the gaseous phase [J/kg-C]
$c_{w,l}$	=	specific heat of water (H_2O) in the liquid phase [J/kg-C]
Ca	=	Capillary number, ratio of viscous to surface tension forces [dimensionless] $Ca \equiv \frac{(\mu_l)^2}{\rho_l \sigma_o \sqrt{k_{sat}/\phi}}$
d	=	mean pore diameter [m]
$D_{wa,g}$	=	binary diffusion coefficient of water and air in the gas phase [m^2/s]
$D_{wa,g,o}$	=	reference binary diffusion coefficient [m^2/s]
e_{slg}	=	volumetric-average energy density over the solid, liquid and gas phases [J/m^3]
f_g	=	volume fraction of gaseous phase, ($f_g = \phi S_g$) [dimensionless]
f_l	=	volume fraction of liquid phase, ($f_l = \phi S_l$) [dimensionless]
f_s	=	volume fraction of solid phase ($f_s = 1 - \phi + \phi S_s$) [dimensionless]
Fo	=	Fourier number [dimensionless]
g	=	magnitude of gravity body force ($g = 9.81\ m/s^2$).
g	=	gravity body force vector with magnitude g, in direction of decreasing elevation [$9.81\ m/s^2$]
Gr	=	Grashof number, ratio of bouyancy to viscous forces [dimensionless] $Gr \equiv \frac{g \beta_g \Delta T_{max} (k_{sat}/\phi) L}{(\nu_g)^2}$
h_{lg}	=	change in enthalpy for water, from liquid to gas phase ($h_{lg} \simeq 2400$ kJ/kg at approximately 40 C)
$h_{a,g}$	=	enthalpy of air in gas phase [J/kg]
$h_{w,g}$	=	enthalpy of water in the gaseous phase [J/kg]

NOMENCLATURE (continued)

$h_{w,l}$	=	enthalpy of liquid water [J/kg]
H	=	enthalpy number (sometimes called Jacob or Jakob number) [dimensionless] $H \equiv \frac{h_{lg}}{C_l \Delta T_{max}}$
j_d	=	mechanical dispersion flux vector [1/m^2-s]
j_e	=	diffusive flux of energy [W/m^2]
$j_{m,a}$	=	diffusive mass flux of air [kg/m^2-s]
$j_{m,w}$	=	diffusive mass flux of water [kg/m^2-s]
$j_{m,a,g}$	=	diffusive mass flux of air in the gas phase [kg/m^2-s]
$j_{m,w,g}$	=	diffusive mass flux of water in the gas phase [kg/m^2-s]
$J(S_l)$	=	J-Leverett function relating capillary pressure and liquid saturation [dimensionless]
k_{sat}	=	saturated hydraulic permeability [m^2]
K_{sat}	=	saturated hydraulic conductivity [m/s]
K_{rel}	=	relative hydraulic conductivity [dimensionless]
$k_{rel,g}$	=	relative permeability of the gaseous phase [dimensionless]
$k_{rel,l}$	=	relative permeability of the liquid phase [dimensionless]
k_t	=	porous medium thermal conductivity [W/m-C]
$\hat{k}$	=	unit vector in direction of increasing elevation [dimensionless]
Le_g	=	gas Lewis number, ratio of molecular to thermal diffusivities [dimensionless] $Le_g \equiv D_{wa,g}/\alpha_g$
M_a	=	molecular weight of air (M_a = 28.97 kg/kgmole)
$m_{a,g}$	=	mass fraction of air in the gas phase [dimensionless]
M_w	=	molecular weight of water (M_w = 18.02 kg/kgmole)
$m_{w,g}$	=	mass fraction of water in the gas phase [dimensionless]
$P_{a,g}$	=	partial pressure of air in the gaseous phase [N/m^2]
P_c	=	capillary pressure (assumed positive for unsaturated conditions) [N/m^2]
P_g	=	gas pressure [N/m^2]
P_l	=	liquid pressure [N/m^2]
P_o	=	reference pressure [N/m^2]
P_v	=	vapor pressure of water (planar air-water interface) [N/m^2]
$P_{v,o}$	=	reference vapor pressure ($P_{v,o}$ = 7.4 x 10^3 N/m^2 at $\simeq$ 40 C) [N/m^2]

NOMENCLATURE (continued)

$P_{w,g}$	=	partial pressure of water in the gaseous phase [N/m^2]
$\tilde{P}_g$	=	nonhydrostatic component of gas pressure [N/m^2]
$\hat{P}_g$	=	dimensionless nonhydrostatic component of gas pressure [dimensionless] ($=\tilde{P}_g/((\mu_g)^2/(\rho_{g,o}k_{sat}/\phi))$)
Pr_g	=	gas Prandtl number [dimensionless] $Pr_g = (\nu_g/\alpha_g)$
Pr_l	=	liquid Prandtl number [dimensionless] $Pr_l \equiv \nu_l/\alpha_l$
q_e	=	advective energy flux [J/m^2-s]
$q_{e,a,g}$	=	advective energy flux due to air in the gas phase [J/m^2-s]
$q_{e,g}$	=	advective energy flux in the gaseous phase [J/m^2-s]
$q_{e,l}$	=	advective energy flux in the liquid phase [J/m^2-s]
$q_{e,w,g}$	=	advective energy flux due to water in the gas phase [J/m^2-s]
$q_{e,w,l}$	=	advective energy flux due to water in the liquid phase [J/m^2-s]
$q_{m,a}$	=	advective mass flux of air [kg/m^2-s]
$q_{m,a,g}$	=	advective mass flux of air in the gaseous phase [kg/m^2-s]
$q_{m,a,l}$	=	advective mass flux of air in the liquid phase [kg/m^2-s]
$q_{m,w}$	=	advective mass flux of water [kg/m^2-s]
$q_{m,w,g}$	=	advective mass flux of water in the gaseous phase [kg/m^2-s]
$q_{m,w,l}$	=	advective mass flux of water in the liquid phase [kg/m^2-s]
$Q_{a,s}$	=	source/sink term for air [kg/m^3-s]
$Q_{w,s}$	=	source/sink term for water [kg/m^3-s]
Q_e	=	volumetric generation of energy [J/m^3-s]
$\hat{Q}_e$	=	heat source [dimensionless] $\hat{Q}_e \equiv \dfrac{Q_e}{\left(\dfrac{k_t \Delta T_{max}}{L^2}\right)}$
R	=	ideal gas law constant (R = 8314 J/kgmole-K)
Ra	=	Rayleigh number (Ra = Gr - Pr) [dimensionless]
Re	=	Reynold's number (Re = ud / ν) [dimensionless]
S_{bot}	=	liquid saturation at bottom of medium in Test 6 [dimensionless]
S_{eff}	=	effective saturation [dimensionless]
S_g	=	gas saturation (m^3 gas / m^3 void) [dimensionless]
S_l	=	liquid saturation (m^3 liquid / m^3 void) [dimensionless]
S_r	=	residual liquid saturation (m^3 liquid / m^3 void) [dimensionless]

NOMENCLATURE (continued)

S_s = solid saturation (m^3 solid non-rock / m^3 void) [dimensionless]
S_{top} = liquid saturation at top of medium in Test 6 [dimensionless]
Su = surface tension ratio (m^3 solid non-rock / m^3 void) [dimensionless]

$$Su \equiv \frac{\Delta T_{max}}{\sigma_o} \left.\frac{d\sigma}{dT}\right|_o$$

t = time [s]
t_{ss} = time to reach steady state (near-equilibrium) [s]
$\hat{t}$ = dimensionless time

$$\hat{t} \equiv \frac{t}{\left(\frac{L^2}{\alpha}\right)}$$

T = temperature [C]
T_o = reference temperature [C]
T_{ref} = reference temperature [C]
ΔT = temperature difference ($= T - T_{ref}$) [C]
ΔT_{max} = maximum temperature difference ($= T_{max} - T_{ref}$) [C]

$u_{a,g}$ = specific internal energy of air in the gaseous phase [J/kg]
u_g = specific internal energy of the gaseous phase [J/kg]
u_l = specific internal energy of the liquid phase [J/kg]
u_{lg} = change in specific internal energy for water, from liquid to gas phase [J/kg]
u_s = specific internal energy of the solid phase [J/kg]
$u_{w,g}$ = specific internal energy of water in the gaseous phase [J/kg]
U = internal energy number [dimensionless]

$$U = \frac{u_{lg}}{C_l \Delta T_{max}}$$

v_g = area-average (Darcy's) velocity of the gaseous phase [m/s]
v_l = area-average (Darcy's) velocity of the liquid phase [m/s]

$\hat{x}$ = dimensionless length scale ($= x/L$) [dimensionless]
X_a = liquid phase air mole fraction [dimensionless]

Y_a = gas phase air mole fraction [dimensionless]

z = elevation or height [m]
Z_o = reference elevation [m]

NOMENCLATURE (continued)

Greek

α	=	media thermal diffusivity [m^2/s] $\alpha \equiv \frac{k_{t,sat}}{\rho_{s,slg} c_s}$
β_g	=	gas thermal expansion coefficient [1/K]
β_l	=	liquid thermal expansion coefficient [1/K]
η	=	nonisothermal mass diffusion enhancement factor [dimensionless]
θ	=	dimensionless temperature ($=\Delta T/\Delta T_{max}$) [dimensionless]
μ_g	=	dynamic viscosity of gas [$N\text{-}s/m^2$]
μ_l	=	dynamic viscosity of liquid [$N\text{-}s/m^2$]
ν_g	=	kinematic viscosity of gas [m^2/s]
ν_l	=	kinematic viscosity of liquid [m^2/s]
$\rho_{a,g}$	=	density of air ($m_{N2,a} = 0.7556$, $m_{O2,a} = 0.2315$, $m_{Ar,a} = 0.01289$, etc...) in the gaseous phase [kg/m^3]
$\rho_{a,l}$	=	density of air in the liquid phase [kg/m^3]
$\rho_{a,s}$	=	density of air in the solid phase [kg/m^3]
$\rho_{a,slg}$	=	volumetric average air density over the porous medium which includes solid, liquid and gas phases [kg/m^3]
ρ_e	=	bulk resistivity [ohm-m]
ρ_g	=	gas density [kg/m^3]
$\rho_{g,o}$	=	reference gas density [kg/m^3]
$\hat{\rho}_g$	=	dimensionless gas density $\hat{\rho}_g \equiv (\rho_g)/(\rho_{g,o})$ [dimensionless]
ρ_l	=	density of liquid water [kg/m^3]
$\rho_{s,slg}$	=	volumetric average solid density over the porous media [kg/m^3]
$\rho_{w,g}$	=	density of water (H_2O) in the gaseous phase [kg/m^3]
$\rho_{w,l}$	=	density of water (H_2O) in liquid phase [kg/m^3]
$\rho_{w,s}$	=	density of water (H_2O) in solid phase [kg/m^3]
$\rho_{w,slg}$	=	volumetric-average water density over the porous medium which includes solid, liquid and gas phases [kg/m^3]
σ	=	surface tension [N/m]
σ_o	=	reference surface tension [N/m]
τ	=	tortuosity [dimensionless]

NOMENCLATURE (continued)

ϕ	=	porosity (m^3 void / m^3 medium) [dimensionless]
Ψ_g	=	gravitational water potential energy in soil per unit volume [N/m^2]
Ψ_o	=	osmotic water potential energy in soil per unit volume [N/m^2]
Ψ_p	=	pressure water potential energy in soil per unit volume [N/m^2]
Ψ_t	=	total water potential energy in soil per unit volume [N/m^2]
∇	=	gradient [1/m]
$\nabla\circ$	=	divergence [1/m]
$\hat{\nabla}$	=	dimensionless gradient ($=L\nabla$) [dimensionless]
$\hat{\nabla}\circ$	=	dimensionless divergence ($=L\nabla\circ$) [dimensionless]

ACKNOWLEDGEMENTS

The authors express their thanks to R. Ababou, R. Baca, B. Gureghian, W. Patrick, and B. Sagar for their careful review and helpful suggestions. It is no small task to review a document this large. We also thank D. Bump for her patience and quick turnaround in typing, assembling, and proofing this document. The authors appreciate the computer expertise provided by R. Martin, A. Johnson, and R. Janetzke. We also thank C. Gray and M. Gruhlke for their assistance in assembling figures and editing. The authors are indebted to them for their patience and efforts which helped produce a better document.

This report was prepared to document work performed by the Center for Nuclear Waste Regulatory Analyses (CNWRA) for the U.S. Nuclear Regulatory Commission under Contract No. NRC-02-88-005. The activities reported here were performed on behalf on the NRC Office of Nuclear Regulatory Research, Division of Regulatory Applications. The report is an independent product of the CNWRA and does not necessarily reflect the views or regulatory position of the NRC.

1 INTRODUCTION

1.1 INTRODUCTION

It is widely recognized that thermohydrologic phenomena will play a key role in the performance of a high-level waste (HLW) repository. The Nuclear Regulatory Commission (NRC) has specified in 10 CFR Part 60 the necessity of understanding thermohydrologic mechanisms as they affect the repository overall system performance (10 CFR 60.112) and the components to the multiple barrier system: waste package [10 CFR 60.113(a)(1)(ii)(A)]; controlled release [10 CFR 60.113(a)(1)(ii)(B)]; and the disturbed zone as part of the geologic setting [10 CFR 60.113(a)(2)]. Because of the current lack of a comprehensive experimental data base relevant to the proposed repository setting, questions have been raised regarding the adequacy of the present state of knowledge about these phenomena. There is a broad consensus that a detailed understanding of thermohydrologic phenomena is needed to assess the thermal effects of HLW on fluid flow and associated radionuclide transport through both the near-field and the far-field zones to guide the design of the proposed repository and performance assessment of the response of the geologic setting to the impact of the emplacement of heat-generating HLW.

In particular, the objectives of this project are designed to assess coupled interactions, identify a representative elementary volume for unsaturated fractured rock, assess the role of fractures with regard to impeding or augmenting groundwater flow, identify those parameters critical to understanding the heat and mass transfer in the geologic system, extrapolate laboratory and field data and model validation. This report summarizes the progress of the Thermohydrology Research Project from mid-1989 through December 1991 at the Center for Nuclear Waste Regulatory Analyses (CNWRA), located at Southwest Research Institute (SwRI), and sponsored by the NRC.

The knowledge base of thermohydrologic phenomena employed in this research is primarily derived from studies of geothermal systems (Cheng, 1978), soil physics (Bear, 1972; Hillel, 1980a,b), and from the drying of porous media (Whitaker, 1977). This knowledge, while valuable, is frequently not directly applicable to the proposed HLW repository which has the characteristic of being in a zone of highly fractured, low-permeability rock.

A detailed literature review was conducted to evaluate the current state of knowledge on thermohydrologic phenomena with the particular aim of identifying specific theories and approaches that are applicable to the physical mechanisms expected at the proposed repository setting. The review was also designed to identify areas where quantitative knowledge is lacking or incomplete. Information gained from this review has been used to design a series of laboratory experiments. To date, a series of laboratory-scale scoping and separate-effect experiments was conducted and a second series of experiments has been initiated to investigate coupled thermohydrologic mechanisms. The benefit of these laboratory-scale experiments has been to: (i) advance the state of knowledge of thermohydrologic mechanisms, (ii) provide data

against which to evaluate mathematical models, and (iii) gain insight to assess the performance of the proposed HLW repository associated with the thermal affect of HLW.

1.2 SCOPE

In broad terms, the objectives of the research project are pursued along three avenues of analysis: (i) laboratory experiments, (ii) mathematical models, and (iii) dimensional analysis. Each of these endeavors is discussed here.

1.2.1 Laboratory Experiments

The laboratory experiments have been and are anticipated to continue to be a primary objective of the project. The purpose of experimentation has been to test experimental techniques, explore coupled processes, and resolve specific technical issues. The experimental aspect of this project has been conducted at three levels: scoping, property measurement, and hypothesis testing.

Scoping experiments are typically described as being expedient and are used to identify the important phenomenological processes or the capabilities of instrumentation or laboratory methodologies. In this project, scoping experiments were performed to aid and advance the design of two-dimensional laboratory-scale experiments.

Measurement experiments are relatively simple experiments designed to measure a specified physical parameter. Typically, measurement experiments are based on a proposed or accepted mathematical model. The mathematical model may incorporate a set of identifiable physical properties or constants (density, relative permeability, thermal conductivity, particle diameter, etc.). Measurement experiments are then conducted to quantify these properties so that the mathematical model can be used for predictions. Measurement experiments are necessary and become most important after the physical processes are sufficiently understood and a mathematical model is identified.

Hypothesis testing experiments are used to substantiate or refute a clearly identified and proposed hypothesis. The experiment should be designed to test the hypothesis in such a way that the data are interpreted as clearly either supporting or refuting the hypothesis. The anticipated experimental results should be identified and the experimental design should concentrate on the hypothesis, and, hence, accentuate the processes which are critical to the hypothesis and diminish the influence of the other processes (which are hopefully understood and well characterized). As such, hypothesis experiments are the most complex types of experiments because they require: (i) a mathematical model to be tested, (ii) a clearly stated hypothesis to be tested, (iii) an experimental design which will test the hypothesis, (iv) pre-experiment prediction of the anticipated data assuming the hypothesis is true, (v) pre-experimental prediction of the anticipated data assuming the hypothesis is false, (vi) identification of key experimental data to be gathered, (vii) experimental instrumentation to obtain the data, and (viii) final comparison of predictions and data to either confirm or refute the hypothesis. The experimental

aspect of this project is evolving from scoping experiments and towards hypothesis testing experiments, as the project matures.

1.2.2 Mathematical Models

Ultimately, quantitative predictions will be required to determine the adequacy of the proposed HLW repository to meet performance objectives. It is a part of this project to extensively review the technical literature concerning the development of mathematical models for nonisothermal flow through partially saturated, fractured porous medium. Through mathematical models, predictions can be made to gauge the relative importance and magnitudes of heat and mass transfer mechanisms. A review of the literature has indicated a consensus on portions of a mathematical model with some identified areas of uncertainty. Hopefully, many uncertainties will be resolved through extensive background research. If a consensus does not exist, then an area will be identified for further theoretical and experimental investigation.

1.2.3 Dimensional Analysis

Dimensional analysis has been pursued in this project as a way to extend the range of applicability of laboratory experiments so that mathematical models can be used to predict the flow of heat and mass in other systems, such as (i) laboratory experiments conducted with varying shapes, sizes and conditions, (ii) field experiments, and (iii) the proposed HLW repository. Dimensional analysis is based on a mathematical model which is valid for both the experiment and the extended applications (where predictions are based on laboratory results). If the mathematical models are different, then dimensional analysis may not be applicable (depending on the differences). At this time, the proposed mathematical model is cast in dimensionless form in order to determine the necessary dimensionless terms which need to be matched. A preliminary assessment has been performed to identify which dimensionless terms significantly affect the thermohydrologic flow field.

1.3 TECHNICAL OBJECTIVES

Through a review of the literature, experimentation and direct analysis, the research effort to date has emphasized the identification of technical issues and development of plans to resolve issues relevant to nonisothermal flow through fractured porous media. For ease of comparison, a list of the important technical issues within the scope of the Thermohydrology Research Project has been compiled (Table 1-1). Future experiments are planned to evaluate not only the broad technical questions but also to address specific issues. Because of limited resources, however, many of the questions in Table 1-1 will not be directly evaluated experimentally, but instead will be answered through a review of the literature.

The specific objectives of this research project may be summarized as follows.

- Perform a critical assessment of the state-of-knowledge of thermohydrology in unsaturated fractured media, in the context of present HLW-NRC program activities.

Table 1-1. IMPORTANT QUESTIONS WITHIN THE SCOPE OF THE THERMOHYDROLOGY RESEARCH PROJECT

- What is the dominant heat transfer mechanism?
- What is the dominant mass transfer mechanism?
- What is the extent of the thermally-disturbed zone?
- What is the thermal-fluid environment for the waste canisters?
- At what time is the maximum repository temperature reached?
- At what time is the maximum temperature reached for a given location above or below the repository?
- At what temperature will water vapor condense in the porous medium?
- At what time will the repository around the canisters begin to resaturate?
- How quickly will the repository around the canisters resaturate?
- At what time will water vapor condense around the canisters?
- Can moisture be driven from hotter canisters to cooler canisters, and thereafter condense on the cooler canister?
- Will liquid water vaporization lead to pressure driven gas phase advection?
- What is the maximum extent of the anticipated dry-zone?
- Will a vapor-liquid counterflow (heat pipe) be established?
- What is the influence of a vapor-liquid counterflow on heat transfer?
- What is the magnitude and flow pattern of buoyancy driven gas phase advection (natural convection) on the repository scale? Liquid phase?
- Under what conditions is an effective continuum model of a fracture network acceptable? Not acceptable?
- Under what conditions will fractures and matrix be in thermohydrologic equilibrium?
- What are the available experimental techniques to measure a physical property? What are their relative strengths and weaknesses? What are their ranges of applicability?
- Given a specific mathematical model, what are the important physical or phenomologic properties that need to be experimentally measured?
- What are the anticipated weaknesses and limitations of the mathematical models that the DOE is expected to use to predict the temperature, liquid saturation, gas pressure, liquid phase velocity, and gas phase velocity for the proposed repository?

This assessment will require an in-depth review of existing literature and on-going programs. The assessment will focus on flow processes, heat transfer mechanisms, and the state of experimental methods in porous and fractured media.

- Perform a detailed dynamic similarity or similitude analysis on the complete set of governing equations relevant to partially saturated flow and to determine the set of dimensionless parameters required to conduct appropriate laboratory simulations. In this analysis of modeling parameters, the range of parameter applicability and limitation on the magnitude of these parameters, as constrained by the principles of dynamic similarity, will be determined.

- Identify potential problems associated with the design and performance of laboratory simulations with scaled geometry, fluid, media, and other relevant properties subject to modeling distortion.

- Perform a series of separate-effect experiments in order to identify and understand the role of each effect in the overall, coupled processes involved in thermohydrologic phenomena.

- Design and perform comprehensive experiments whose results will continue to identify key dependent and independent parameters and their relationships in the context of thermohydrologic issues.

- Develop the laboratory facilities, experimental methods, measurement techniques, and associated analytic skills to evaluate and validate other program results and to provide a high quality of technical assistance and research in support of NRC's licensing of an HLW repository.

- Examine and correlate laboratory results with field data, to aid in the design of future field experiments.

- Perform numerical simulations of two-phase flow through partially saturated, fractured porous media under nonisothermal conditions as part of the dynamic similitude analysis and to evaluate the capability to numerically simulate thermohydrologic processes.

1.4 STRUCTURE OF REPORT

The structure of the report is as follows:

- Chapter 2 - Review of Mathematical Models
- Chapter 3 - Review of Experimental Techniques
- Chapter 4 - Design of Laboratory Experiments
- Chapter 5 - Summary of Data from the Laboratory Experiments

- Chapter 6 - Analysis of Moisture Content Measurement Data
- Chapter 7 - Analysis of Water Redistribution Mechanisms
- Chapter 8 - Numerical Analysis of Test 6
- Chapter 9 - Numerical Analysis Based on Dimensional Analysis
- Chapter 10 - Summary and Conclusions.

2 THEORETICAL CONSIDERATIONS OF THERMOHYDROLOGICAL PHENOMENA IN FRACTURED POROUS MEDIA

Fluid flow and heat transfer through partially saturated, fractured porous media involve several different physical processes such as: (i) gas and liquid convection, interaction, and counter flow; (ii) matrix/fracture interactions; and (iii) liquid infiltration and distribution. Many of these processes are complex, especially when coupled with each other. Therefore, in the study of thermohydrological phenomena, either theoretically or in the laboratory, the approach taken in this research project has been to first investigate the individual processes separately that contribute to the phenomenon of interest, then after sufficient understanding has been attained, investigate the processes when coupled. Chapter 2 and Chapter 3 contain discussions of, respectively, the theoretical and experimental aspects of nonisothermal flow through fractured, porous media as investigated during the research project.

The theoretical development of the relationships governing thermohydrological phenomena in fractured porous media is investigated by initially examining isothermal flow in saturated media, then introducing nonisothermal conditions. Partially saturated conditions are next considered, first for isothermal conditions then under nonisothermal conditions, the most complex situation of those discussed. A discussion of the physical mechanisms associated with two-phase flow through fractured porous media is given in Section 2.1. It is followed by development of the governing equations for flow of heat and mass through partially saturated, fractured porous media (Section 2.2). Physical mechanisms introduced in Section 2.1, if important in nonisothermal flow through partially saturated media, are discussed in greater detail in Section 2.2.

2.1 CONCEPTUALIZATION OF PHYSICAL MECHANISMS OF TWO-PHASE FLOW THROUGH FRACTURED POROUS MEDIA

2.1.1 Flow in Saturated Media

Conceptual models of the isothermal flow of a fluid in a saturated, permeable porous medium are based on well understood and plausible physical mechanisms. The fluid is conceived to flow in a multitude of interconnected channels of varying length and diameter, under the combined action of pressure difference, gravity, and viscous friction (Batchelor, 1967 Bear, 1972: Freeze and Cherry, 1979; Domenico and Schwartz, 1990).

The medium is characterized geometrically by its porosity ϕ, which is the percentage of void space per unit volume, and its average pore diameter d. At any cross-section perpendicular to the flow, the area-average velocity v is defined as the flow rate divided by the total cross-sectional area and is commonly referred to as the Darcy velocity. This velocity is contrasted to the interstitial or seepage velocity, which is defined as the flow rate divided by the

area actually open to the flow. Theoretically, the interstitial velocity is the more important since it determines the fluid stresses, nature of flow (laminar or turbulent), and the velocity with which pollutants or solutes are transported from one location to another. Practically, the area-average velocity is more useful because it is more readily measured. Fluid mobility is assumed to be proportional to area-average velocity and inversely proportional to fluid viscosity. The assumed linear relation between velocity and driving force, or pressure gradient $\Delta P/\Delta x$, is Darcy's law:

$$v = \frac{-k}{\mu}\left(\frac{\Delta P}{\Delta x} - \rho g \Delta z\right) \qquad (2\text{-}1)$$

The proportionality constant k is the permeability of the medium; k depends on ϕ, d, and the connectivity of the pores, all of which are geometric properties of the medium. The permeability can be computed from first principles only for simple geometries such as a medium composed of spheres or of capillary bundles (Burdine, 1953; Wylie and Gardner, 1958; Bear and Bachmat, 1991); these computations show that k is proportional to the square of the linear dimensions of the interstices (and the "dimensions" of k are in fact length squared). In general, k must be inferred from measurements of flow rate as a function of pressure difference for a given medium. If the medium has geometric properties that are widely different in different directions, k depends upon the flow direction and should be considered as a tensor quantity rather than a scalar. Cross-coupling effects can occur in anisotropic media; that is, a pressure gradient in one direction can cause a flow in another direction.

When a saturated porous medium is heated to temperatures below the boiling point of the liquid, buoyancy forces can induce a natural convection flow. Although the mathematical description of these buoyancy-driven flows is complicated in detail, experiments have shown that overall the flow is similar to that of fluid confined in a volume of the same geometric shape which contains no solid material, porous or otherwise (Kulacki and Emara, 1975, 1976). Small-scale experiments of such natural convection flows can be interpreted in terms of larger-scale behavior by consideration of the dimensionless Rayleigh (or Grashof), Prandtl, and Reynolds numbers (Keyhani et al., 1981). This is discussed in greater detail in Chapter 9.

2.1.2 Flow in Partially Saturated Media

Compared to a saturated medium, flow in a permeable porous medium that is not saturated presents a difficult challenge to model conceptually (Narasimhan, 1982; Wang and Narasimhan, 1986; Evans and Nicholson, 1987; Rasmussen and Evans, 1989). The difficulties arise primarily because of (i) the strong influence of surface forces at the interfaces between the liquid and gas phases, and (ii) the possibility that the phases may not be distributed as continuous bodies in the medium.

As an example of these conceptual difficulties, consider a situation in which a porous medium is saturated with water and a pressure difference is applied to produce an

infiltration of air into the medium. Initially, only water will flow out of the downstream boundary, at the same flow rate as the air entering the upstream face. During this period, the medium becomes partially saturated (i.e., contains a mixture of air and water) but, since the air is not yet distributed throughout the medium, the outflow does not contain air. Eventually, however, the air "breaks through" and appears at the downstream face. There follows a period when both air and liquid are caused to flow out the downstream face by the imposed pressure gradient. Finally, when the saturation level has decreased sufficiently, the outflow of water ceases (except for that which is evaporated into the air). The saturation level of the medium at this point is variable depending upon the porosity and pore size distribution. Even though the medium still contains water, the water no longer exists as a continuous body across the test volume; instead it occurs as individual droplets or discontinuous segments of water adhering to the solid pores and surrounded by air. Darcy's equation, modified for partially saturated flow by expressing permeability as a function of suction pressure, is commonly used to describe the movement of water under these conditions.

At even lower levels of liquid saturation, only molecular layers of "liquid" water adhering to the surface of the matrix of the medium remains. This residual water is essentially "immobile." The immobile water is not governed by Darcy's law (unless the liquid-phase permeability is considered to be zero for these saturation levels). More generally, two or more co-existing phases will be mobile when the fluid in each phase forms a continuous body; that is, when any point in a given phase is reachable from any other point in that phase by a path that lies entirely within the phase or when the potential energy of a particular segment of liquid is sufficiently large for that isolated body of liquid to overcome adsorption forces and move in response to body forces. The various phases are then clearly intertwined. This fact implies that flow in partially saturated porous media is inherently three dimensional, since two or more phases cannot each be continuously connected in a two-dimensional granular or porous medium unless they exist essentially as one dimensional.

Suction pressures of tens or even hundreds of atmospheres are possible for moderate saturation levels (i.e., greater than 70 percent) in tight matrices such as are present in Yucca mountain tuff (Eaton et al., 1985; Wang and Narasimhan, 1985). Since the surface tension of pure water in air is about 70 dyne/sq.cm., a suction pressure of, say, 10^3 kPa if attributed entirely to surface tension forces would require a capillary diameter of approximately 3 angstroms, which is about the diameter of a water molecule. Obviously, these high suction pressures must be due to adhesion of the water to the solid, or some other effect, rather than to capillarity. Consequently, conceptual modeling is made even more difficult because of the lack of an easily measured physical property that can be used to characterize suction pressures for moderate or low saturations.

When a liquid is mobile in a partially saturated medium, the permeability is less than the saturated permeability. This can be imagined as a consequence of the flow channels not being completely full of fluid, thus increasing the wetted area per unit cross-sectional area. The actual permeability is usually cited as a fraction of the saturated permeability, called the relative permeability. Relative permeability, like suction pressure, depends on the saturation

level of the medium. For media with a pore-size distribution comparable to the matrix material at Yucca Mountain, the relative permeability decreases rapidly as the saturation level is reduced only marginally from 100 percent (Wang and Narasimhan, 1985; Martinez, 1988). Relative permeability and the other quantities of interest cannot usually be predicted directly as a function of saturation level without additional assumptions, so flow computations must employ measured "characteristic" curves of suction pressure and permeability against saturation for the medium in question (e.g., van Genuchten, 1978, 1980).

As a result of the dependence of permeability on saturation, the flow of liquid in a medium whose saturation level changes as the result of the flow can exhibit various kinds of instabilities. For example, consider the infiltration of water at a boundary of a partially saturated medium. The flow rate at a point in the medium depends in part on the permeability at that point, which depends on the saturation level at the point, which in turn depends on the amount of infiltration that has already occurred at the point. Although the flow might be thought to fill the entire infiltration cross section uniformly, typically, a kind of "fingering" occurs in which the infiltrating liquid travels in one or more distinct flow channels formed by an initial instability and then promoted by the lower flow resistance of the channels (Miller and Miller, 1956; Miller and Gardner, 1962; Glass et al., 1989a,b).

When the fluids in a partially saturated porous medium are heated, the internal distribution of the fluids can change by several mechanisms, and two-phase internal circulations may occur. Infiltration at a boundary adds an additional complexity. For reasons discussed below, it is difficult to form a completely satisfactory conceptual physical model of nonisothermal flow in a partially saturated, fractured porous media, or to conceive of laboratory experiments or instrumentation that would permit the various postulated mechanisms to be thoroughly isolated and measured. Consequently, there still exists some degree of speculation in the mathematical models of nonisothermal or two-phase flow in a partially saturated porous medium.

As one example of the conceptual difficulties, local heating in a saturated medium can cause a natural convection-like flow because of instabilities due to buoyancy forces created by the differential fluid densities (Kulacki and Emara, 1975). But it is difficult to conceive how a similar natural convection of liquid can occur in a partially saturated medium. Even though the liquid may exist as a continuous body so that "lighter" liquid is under "heavier" liquid (thus making the liquid susceptible to instability), the pressure in the liquid is controlled by capillary forces at nearby liquid-gas interfaces, independently of the overall pressure gradient caused by the weight of the liquid. Thus, it would seem that liquid buoyancy can be active as an instability mechanism only over the largest volume of saturated media. If so, natural convection cells can be no larger on average than the size of the saturated portion of the medium. In a partially saturated medium, the volumes of fully saturated medium are expected to be small, hence, the convection cells would be small. Conversely, if the gas is distributed as a continuous body, buoyancy can lead to natural convection in the gas phase since the gas is also subject to the gravity pressure gradient.

Three other phenomena that must be considered in a conceptual model of nonisothermal flow in a partially saturated, fractured porous medium are discussed below.

Surface Tension Gradients. Since surface tension is a function of liquid temperature, local heating that results in a nonuniform temperature distribution produces a surface tension variation in the medium liquid and thereby a suction pressure variation. During the transient period required for the temperature distribution to reach a new steady state, the time-varying suction pressures will lead to a redistribution of the liquid (i.e. a liquid flow) until a new steady-state liquid distribution is obtained at a time when the suction pressure is uniform throughout the medium (or in balance with the gravity body forces).

Two-Phase Effects and "Heat Pipes." Vapor generated by local heating of liquid in a porous medium can flow to distant, cooler parts of the medium where it may condense. This kind of two-phase flow is thus an additional mechanism by which liquid can be redistributed in the medium. If both the liquid and the gas phases are mobile, the liquid can be drawn back to the hotter part of the medium (because of the difference in suction pressure) where it will evaporate, thereby setting up a kind of "heat pipe" flow (Pruess et al., 1985). Such a heat pipe can be effective in transporting a large amount of heat away from the local heating source. If so, the temperature near the heating source will not significantly exceed the vaporization temperature of the liquid; but when the heat pipe effect is small, the temperature of the medium near the heat source will increase until other mechanisms, such as conduction, can transfer the heat (Pruess et al., 1984). Apparently, heat pipes are more efficient when the vapor can be transported in fractures and the liquid return by way of the matrix or the fracture; however, heat-pipe flow can occur in a nonfractured medium so long as both the liquid and vapor are mobile (Buschek and Nitao, 1988).

Fracture and Matrix Interaction. The importance of fractures was mentioned above for isothermal flow. Fractures and the amount of liquid bound or adsorbed on the fracture walls may be even more important for two-phase, nonisothermal flows. For example, computer modeling (Pruess et al., 1985) indicates that a small amount of mobile liquid in the fractures (e.g., saturation level as small as 0.0122 percent for the examples given) leads to a large heat-pipe effect, because the condensed liquid can travel back to the heat source in the fractures. On the other hand, if the liquid in the fractures is not mobile, the liquid must return through the matrix, which has a considerably lower permeability and correspondingly larger flow resistance, and the heat-pipe effect is not large. It would appear to be difficult to verify or disprove experimentally these predicted large effects of almost vanishingly small saturations of mobile liquid in fractures.

The above discussion indicates that modeling nonisothermal flow in a partially saturated porous medium, even if it is not fractured, is a much more difficult conceptual problem than the modeling of nonisothermal flow in a saturated medium. Development of the governing equations which represents this type of flow regime is presented in Appendix A and summarized in Section 2.2.

2.2 CONSERVATION AND CONSTITUTIVE EQUATIONS

In this section, we summarize a mathematical model for heat and mass transfer in a partially saturated porous medium. The mathematical model is developed and discussed in Appendices A, B, and C. The highlights are summarized here.

Conservation equations and constitutive equations are used to present the mathematical model. The conservation equations will be presented first, and the constitutive equations second. Within the catagory of constitutive equations, material properties and basic definitions (or closure relations) are identified.

2.2.1 Conservation Equations

Heat transfer and fluid flow can be summarized in three conservation equations. The first conservation equation is for water in both the liquid and gas phase:

$$\frac{\partial}{\partial t}\left(\rho_{w,l} S_l \phi + \rho_{w,g} S_g \phi\right) = -\nabla \cdot \left(\rho_{w,l} \mathbf{v}_l + \rho_{w,g} \mathbf{v}_g\right) - \nabla \cdot \left(\mathbf{j}_{m,w,g}\right) \tag{2-2}$$

where

$\rho_{w,l}$	=	density of water (H_2O) in liquid phase [kg/m^3],
S_l	=	liquid saturation (m^3 liquid / m^3 void) [dimensionless],
ϕ	=	porosity (m^3 void / m^3 medium) [dimensionless],
$\rho_{w,g}$	=	density of water (H_2O) in the gaseous phase [kg/m^3],
S_g	=	gas saturation (m^3 gas / m^3 void) [dimensionless],
$\mathbf{v}_l$	=	area-average (Darcy's) velocity of the liquid phase [m/s],
$\mathbf{v}_g$	=	area-average (Darcy's) velocity of the gaseous phase [m/s], and
$\mathbf{j}_{m,w,g}$	=	diffusive mass flux of water in the gaseous phase [kg/m^2- s].

The conservation equation for air is:

$$\frac{\partial}{\partial t}\left(\rho_{a,g} S_g \phi\right) = -\nabla \cdot \left(\rho_{a,g} \mathbf{v}_g\right) - \nabla \cdot \left(\mathbf{j}_{m,a,g}\right) \tag{2-3}$$

where

$\rho_{a,g}$	=	density of air in the gaseous phase [kg/m^3], and
$\mathbf{j}_{m,a,g}$	=	diffusive mass flux of air in the gaseous phase [kg/m^2-s].

The conservation equation for thermal energy is:

$$\frac{\partial}{\partial t}\left(\phi \rho_{s,slg} u_s + \phi S_l \rho_l u_l + \phi S_g \rho_g \left(m_{w,g} u_{w,g} + m_{a,g} u_{a,g}\right)\right) = -\nabla \cdot \left(h_l \rho_l v_l + h_g \rho_g v_g \right) - \nabla \cdot \left(j_{e,cond} \right) + Q_e \quad (2\text{-}4)$$

where

$\rho_{s,slg}$, ρ_l, ρ_g	=	densities [kg/m^3],
u_s, u_l, $u_{w,g}$, $u_{a,g}$	=	internal energies [J/kg],
h_l, h_g	=	enthalpies [J/kg],
$j_{e,cond}$	=	conductive heat flux [W/m^2], and
Q_e	=	heat source/sink [W/m^3].

In many cases, the conservation equations can be reduced in complexity as additional assumptions and approximations are applied. As presented here, Eqns. (2-2), (2-3) and (2-4) represent a general form of the equations.

2.2.2 Constitutive Equations

In this work, constitutive equations are summarized in three catagories: (i) flux laws (i.e., Darcy's, Fick's and Fourier's Law), (ii) material properties, and (iii) basic definitions or closure relations.

Darcy's Law relates the porous medium velocities as:

$$v_l = -\frac{k_{sat}\, k_{rel,l}}{\mu_l}\left(\nabla P_l + \rho_l g \hat{k} \right) \quad (2\text{-}5)$$

$$v_g = -\frac{k_{sat}\, k_{rel,g}}{\mu_g}\left(\nabla P_g + \rho_g g \hat{k} \right) \quad (2\text{-}6)$$

where

k_{sat}	=	saturated permeability [m^2],
$k_{rel,l}$, $k_{rel,g}$	=	relative permeabilities [dimensionless],
μ_l, μ_g	=	dynamic viscosities [kg/m-s],
P_l, P_g	=	liquid and gas pressure [N/m^2], and
g	=	gravitational constant [9.81 m/s^2].
$\hat{k}$	=	unit vector in direction of increasing elevation [dimensionless]

Fick's Law relates the molecular diffusive mass fluxes:

$$j_{m,w,g} = -\tau \phi S_g \rho_g D_{wa,g} \nabla m_{w,g} \quad (2\text{-}7)$$

$$j_{m,a,g} = -\tau \phi S_g \rho_g D_{wa,g} \nabla m_{a,g} \quad (2\text{-}8)$$

where

τ	=	tortuosity (m straight line path / m average fluid streamline path) [dimensionless],
$D_{wa,g}$	=	molecular diffusion coefficient of water in air [m^2/s], and
$m_{w,g}$, $m_{a,g}$	=	mass fractions [dimensionless].

Fourier's Law relates the conduction heat flux:

$$j_{e,cond} = -k_t \nabla T \quad (2\text{-}9)$$

where

k_t	=	thermal conductivity [W/m-K], and
T	=	temperature [K].

The mathematical models for material properties are the next group of constitutive equations. The densities of water or air in the gas phase can be calculated using the ideal gas law:

$$\rho_{w,g} = \frac{M_w P_{w,g}}{R T} \quad (2\text{-}10)$$

$$\rho_{a,g} = \frac{M_a P_{a,g}}{R T} \quad (2\text{-}11)$$

where

$P_{w,g}$, $P_{a,g}$	=	partial pressures [N/m^2],
M_w, M_a	=	molecular weights [kg/kgmole], and
R	=	ideal gas constant [8314 J/kgmole-K].

Kelvin's equation is used to express the partial pressure of water in the gas phase as a function of both vapor pressure and capillary pressure:

$$P_{w,g} = P_v \exp\left(\frac{-M_w P_c}{\rho_l R T}\right) \quad (2\text{-}12)$$

where

P_v = vapor pressure [N/m^2], and
P_c = capillary pressure [N/m^2].

The Claperyon-Clausius (also known as Clausius-Claperyon or Claperyon) equation is used to estimate the vapor pressure as a function of temperature:

$$P_v = P_{v,o} \exp\left(\frac{h_{lg} M_w}{R}\left(\frac{1}{T_o} - \frac{1}{T}\right)\right) \quad (2\text{-}13)$$

where

$P_{v,o}$, T_o = reference values, and
h_{lg} = heat of vaporization [J/kg].

The molecular diffusion coefficient for water through air (or air through water) in the gas phase can be a function of temperature and pressure:

$$D_{wa,g} = D_{wa,g,o}\left[\frac{P_o}{P_g}\right]\left[\frac{T}{T_o}\right]^{3/2} \quad (2\text{-}14)$$

where

$D_{wa,g,o}$, P_o, T_o = reference values.

The internal energies of the solid and fluid materials are summarized as:

$$u_s = c_s (T - T_{ref}) + u_{ref,s} \quad (2\text{-}15)$$

$$u_l = c_l (T - T_{ref}) + u_{ref,l} \quad (2\text{-}16)$$

$$u_g = m_{w,g} u_{w,g} + m_{a,g} u_{a,g} \quad (2\text{-}17)$$

$$u_{w,g} = c_{w,g} (T - T_{ref}) + u_{ref,w,g} \quad (2\text{-}18)$$

$$u_{a,g} = c_{a,g}\left(T - T_{ref}\right) + u_{ref,a,g} \tag{2-19}$$

where

u_s, u_l, u_g, $u_{w,g}$, $u_{a,g}$	=	internal energies [J/kg],
c_s, c_l, $c_{w,g}$, $c_{a,g}$	=	specific heats [J/kg-K], and
$u_{ref,s}$, $u_{ref,l}$, $u_{ref,w,g}$, $u_{ref,a,g}$	=	reference values.

The effective thermal conductivity is noted to potentially be a function of liquid saturation, for example:

$$k_t = k_t(S_l=0) + \sqrt{S_l}\left[k_t(S_l=1) - k_t(S_l=0)\right] \tag{2-20}$$

The capillary pressure is a function of liquid saturation, for example the van Genuchten (1978) model yields:

$$P_c = \frac{\rho_l g}{\alpha}\left(S_{eff}^{\beta/(1-\beta)} - 1\right)^{1/\beta} \tag{2-21}$$

where

P_c	=	capillary pressure [N/m^2],
ρ_l	=	liquid density [kg/m^3],
α	=	parameter in van Genuchten model [1/m],
β	=	parameter in van Genuchten model [dimensionless],
S_{eff}	=	effective saturation, $S_{eff} = (S-S_r)/(1-S_r)$ [dimensionless],
S_r	=	residual saturation [dimensionless], and
g	=	gravitational constant [9.81 m/s^2].

The liquid phase relative permeability is a function of saturation, for example the Burdine (1953) model using the van Genuchten model is:

$$k_{rel,l} = \left(S_{eff}\right)^2\left[1 - \left(1 - S_{eff}^{\beta/(\beta-1)}\right)^{(\beta-1)/\beta}\right] \tag{2-22}$$

The gas phase relative permeability is a function of gas saturation, for example:

$$k_{rel,g} = \left(S_g\right)^3 \tag{2-23}$$

Other thermophysical properties of gases and liquids are left unspecified at this point, where models can be found in the literature.

The basic defintions or closure relations are simply stated:

$$P_c = P_g - P_l \tag{2-24}$$

$$P_g = P_{w,g} + P_{a,g} \tag{2-25}$$

$$\rho_g = \rho_{w,g} + \rho_{a,g} \tag{2-26}$$

$$m_{w,g} = \left(\frac{\rho_{w,g}}{\rho_g}\right) \tag{2-27}$$

$$m_{a,g} = \left(\frac{\rho_{a,g}}{\rho_g}\right) \tag{2-28}$$

$$S_l + S_g = 1 \tag{2-29}$$

$$m_{w,g} + m_{a,g} = 1 \tag{2-30}$$

2.3 SIMILITUDE ANALYSIS

In this section, the results of the similitude analysis which is developed in Appendix D are summarized. The details of the similitude analysis have been included in the appendix because of the length.

The dimensionless conservation of air equation has been developed to yield:

$$\left(\frac{\alpha}{\alpha_g}\right) \frac{\partial}{\partial \hat{t}}\left(m_{a,g}\ \hat{\rho}_g\ S_g\right) = \mathrm{Pr}_g\ \hat{\nabla}\cdot\left(m_{a,g}\ \hat{\rho}_g\ k_{rel,g}\left(\hat{\nabla}\hat{P}_g - \mathrm{Gr}\ \theta\ \hat{k}\right)\right) + \tau\ \mathrm{Le}_g\ \hat{\nabla}\cdot\left(\hat{\rho}_g\ S_g\ \hat{\nabla} m_{a,g}\right) \tag{2-31}$$

where

$\hat{\rho}_g$ = dimensionless gas density ($= \rho_g / \rho_{g,o}$),
$\rho_{g,o}$ = reference gas density [kg/m^3],
Pr_g = gas Prandtl number ($= \nu_g / \alpha_g$),

$\hat{P}_g$	=	dimensionless nonhydrostatic gas pressure,
Gr	=	porous medium Grashof number,
θ	=	dimensionless temperature,
$\hat{k}$	=	unit vector in direction of increasing elevation,
τ	=	tortuosity, and
Le_g	=	gas Lewis number ($= D_{wa,g} / \alpha_g$).

The dimensionless conservation of water equation is:

$$\left(\frac{\alpha}{\alpha_l}\right) \frac{\partial}{\partial \hat{t}}\left(S_l + \left(\frac{\rho_{g,o}}{\rho_l}\right) m_{w,g}\, \hat{\rho}_g\, S_g\right) =$$

$$Pr_l\, \hat{\nabla}\cdot\left(\left(\frac{1}{Ca}\right) k_{rel,l}\left(- J\, Su\, \hat{\nabla}\theta - \frac{dJ}{dS_l}\, \hat{\nabla}S_l + Bo\, \hat{k}\right)\right)$$

$$+ Pr_g \left(\frac{\alpha_g}{\alpha_l}\right)\left(\frac{\rho_{g,o}}{\rho_l}\right) \hat{\nabla}\cdot\left(m_{w,g}\, \hat{\rho}_g\, k_{rel,g}\left(\hat{\nabla}\hat{P}_g - Gr\, \theta\, \hat{k}\right)\right) \qquad (2\text{-}32)$$

$$+ \tau\, Le_g \left(\frac{\alpha_g}{\alpha_l}\right)\left(\frac{\rho_{g,o}}{\rho_l}\right) \hat{\nabla}\cdot\left(\hat{\rho}_g\, S_g\, \hat{\nabla}m_{w,g}\right)$$

where

Pr_l	=	liquid Prandtl number,
Ca	=	Capillary number,
Su	=	surface tension number, and
Bo	=	Bond number.

The dimensionless conservation of energy equation is:

$$\frac{\partial}{\partial \hat{t}}\Bigg(\theta + \phi\, S_l \left(\frac{\rho_l}{\rho_{s,slg}}\right)\left(\frac{c_l}{c_s}\right)\theta + \phi\, S_g\, m_{w,g}\, \hat{\rho}_g \left(\frac{\rho_{g,o}}{\rho_{s,slg}}\right)\left(\frac{c_l}{c_s}\right)\left(\left(\frac{c_{v,w,g}}{c_l}\right)\theta + U\right) + \phi\, S_g\, m_{a,g}\, \hat{\rho}_g \left(\frac{\rho_{g,o}}{\rho_{s,slg}}\right)\left(\frac{c_{v,a,g}}{c_s}\right)\theta\Bigg) =$$

$$\phi\, Pr_l \left(\frac{\alpha_l}{\alpha}\right)\left(\frac{\rho_l}{\rho_{s,slg}}\right)\left(\frac{c_l}{c_s}\right)\hat{\nabla}\cdot\Bigg\{\theta\left(\frac{1}{Ca}\right)k_{rel,l}\left(-JSu\,\hat{\nabla}\theta - \frac{dJ}{dS_l}\hat{\nabla}S_l + Bo\hat{k}\right) + \left(\left(\left(\frac{c_{p,w,g}}{c_l}\right)\theta + H\right)m_{w,g} + \left(\frac{c_{p,a,g}}{c_l}\right)\theta m_{a,g}\right)\left(\frac{\mu_g}{\mu_l}\right)\hat{\rho}_g k_{rel,g}\left(\hat{\nabla}\hat{P}_g - Gr\,\theta\hat{k}\right)\Bigg\}$$

$$+\phi Le_g \tau\left(\frac{\alpha_g}{\alpha}\right)\left(\frac{\rho_{g,o}}{\rho_{s,slg}}\right)\left(\frac{c_l}{c_s}\right)\hat{\nabla}\cdot\left(\left(\left(\frac{c_{p,w,g}}{c_l}\right) - \left(\frac{c_{p,a,g}}{c_l}\right)\right)\theta + H\right)S_g\,\hat{\rho}_g\,\hat{\nabla}m_{w,g} \qquad (2\text{-}33)$$

where

U	=	internal energy number, and
H	=	enthalpy number.

The reader's attention is directed to Appendix D for a development and discussion of the dimensionless equations.

3 EVALUATION OF INSTRUMENTATION USED IN THE INVESTIGATION OF THERMOHYDROLOGICAL PHENOMENA IN FRACTURED POROUS MEDIA

Experimental testing has the potential to provide insight into the mechanisms controlling heat and mass transfer in partially saturated, porous media and has been included as an integral aspect of this project. By comparing the results of both laboratory and field tests with predictive models, a better understanding of basic phenomena can be obtained and the validity of the predictive models tested. Presently, instrumentation available for measuring the spatially variable coefficients in constitutitive relations of interest lags behind the ability to perform numerical predictions of heat and mass transfer in a partially saturated porous media. For this reason, there is significant uncertainty in the validity of present predictive models. This uncertainty will be reduced as additional data from well-posed experiments become available to properly assist in validation of the predictive models.

A literature review was performed to provide an information base on the nature of instrumentation available for heat and mass transfer studies in partially saturated, fractured porous media. Any experimental study typically requires a variety of instrumentation to provide measurements of the parameters of interest. The independent variables of interest to the laboratory portion of the Thermohydrology Research Project include temperature, moisture content, and suction pressures throughout the spatial domain of the experiments. Accordingly, this literature survey focused essentially on instrumentation unique to measurements in partially saturated, fractured, porous media. For this reason, instrumentation commonly used in experimental programs directed toward the saturated zone is not applicable to this study. In addition, this study has primarily focused on instrumentation applicable to laboratory-scale testing. Instrumentation that is mostly useful for borehole logging or other large-scale field testing was not assessed in the study.

In order to test predictive models, a broad range of experimental data is required. Types of these data include measurements of the spatial distribution of local moisture content, suction pressure, liquid flow rate and direction, and vapor flow rate and direction in addition to measurements of local temperatures, heat fluxes, and boundary conditions. Instrumentation to measure the relationships of pressure to moisture content was also evaluated. Direct measurement of hydraulic conductivity as a function of moisture content was not evaluated at this time. This section contains a discussion of the types of instrumentation evaluated as part of this project. Tables 3-1 through 3-4 summarize the results of the instrumentation survey.

The instrumentation summary tables are delineated according to the parameter measured by the instrument. Table 3-1 summarizes the measurement methods for obtaining the moisture content of partially saturated porous media. Table 3-2 summarizes the measurement methods for obtaining matric potential or suction pressure. For a given porous medium and liquid, the matric potential and moisture content are related. Because of hysteresis in the wetting-drying

Table 3-1. SUMMARY OF INSTRUMENTATION FOR MOISTURE CONTENT MEASUREMENT

Instrument	Measured Parameter	Thermo-hydrological Parameter	Comments
Electrical resistivity or conductivity probes (Morrison, 1983; Keller and Frischknecht, 1966; Rasmussen and Evans, 1987)	Electrical potential between electrodes in media	Moisture content	Simple construction and measurement. Sensitive to packing, boundary conditions, water quality, and temperature. Calibration for matrix required. Measurement volume is not clearly defined.
Neutron detector (Prazák et al., 1990; Rasmussen and Evans, 1987)	Return count rate of slow neutrons (a function of hydrogen atom content)	Moisture content	Fast neutron penetration limited to about 15 cm. Measurement volume increases with decreasing moisture content.
Gamma beam densitometer (point measurement) *	Gamma-rays transmitted (attenuated) through or scattered in medium	Moisture content	Equipment alignment is critical. Sufficiently long sample times required to provide stable counts.
Light attenuation	Intensity of light scattered or transmitted through media	Moisture content	Method is only useful in translucent materials (e.g., glass beads). Sample must be in transparent container.
Thermal conductivity sensor (Thamir and McBride, 1985; Fredlund and Wong, 1989)	Thermal dissipation rate of medium	Moisture content	Requires heating of sample. Requires good contact with medium. Calibration required. Interpretation of thermal response signal required.
Capacitance Sensors (Morrison, 1983)	Capacitance between electrodes in media	Moisture content	Calibration in medium required. Method is sensitive to water quality and temperature.

* See Verma et al., 1983, 1985; Verma and Pruess, 1986; Nicholls and Heaviside, 1988; Stillwater and Klute, 1988; Persoff et al., 1989; Russo and Reda, 1989.

Table 3-1. SUMMARY OF INSTRUMENTATION FOR MOISTURE CONTENT MEASUREMENT (Continued)

Instrument	Measured Parameter	Thermo-hydrological Parameter	Comments
Nuclear Magnetic Resonance (NMR) (Morrison, 1983)	Radio frequency from hydrogen nucleus in oscillating magnetic field	Moisture content	Typically used for small specimen. Large systems are very expensive. Hydrogen in media or liquid will affect readings.
Time Domain Reflectometry (TDR) (Zegelin et al., 1989; Topp et al., 1980)	Time delay in voltage reflected from probe	Moisture content	Common field technique. Interpretation of signal required. Readings affected by installation, media type, and frequency.
Electromagnetic sensors (Daily and Ramirez, 1989)	Electromagnetic wave transmitted through media (magnitude or phase change)	Moisture content	Requires relatively complex electronic instrumentation. Commonly used in oil well logs. Affected by water quality (resistivity).
X-ray	X-rays transmitted through the media	Moisture content	Can be used to record moisture distribution. Limitations in contrast detection make this method more applicable for tracking water front movement than for recording small changes in saturation levels.
Soil Moisture Block (Morrison, 1983; Rasmussen and Evans, 1987)	Electrical resistance of sample block material between two electrodes	Moisture content	Must be calibrated. Affected by water quality. Slow response. Sensitive to temperature. Hysteresis.

Table 3-2. SUMMARY OF INSTRUMENTATION FOR SUCTION PRESSURE MEASUREMENT

Instrument	Measured Parameter	Thermo-hydrological Parameter	Comments
Thermocouple Psychrometer *	Relative humidity	Matric suction	1 to greater than 100 bar range. Susceptible to corrosion. Transient signal interpretation required. Must be calibrated.
Tensiometer (Chuang, et al., 1990; Rasmussen and Evans, 1987)	Suction pressure	Matric suction	Directly measures matric suction. Limited to 1 bar. Good matric-sensor contact required.
Filter Paper Contact (Rasmussen and Evans, 1987)	Mass of water pulled into paper by capillary action	Matric suction	Very simple method. Filter paper must be calibrated for matrix suction.
Soil Moisture Block (Morrison, 1983; Rasmussen and Evans, 1987)	Electrical resistance of sample block material between two electrodes	Matric suction	Must be calibrated. Affected by water quality. Slow response. Sensitive to temperature. Hysteresis.
Microwave resonators (Latorre and Glenn, 1991)	Water vapor partial pressure	Matric suction	Not yet extensively tested. Can be used at high temperatures (350 C).
Capacitance hygrometer (Morrison, 1983)	Relative humidity	Matric suction	Poor performance at humidities between 98-100%.
Osmotic tensiometer (Rasmussen and Evans, 1987)	Osmotic pressure	Matric suction	Method not sufficiently developed.

* Thamir and McBride, 1985; Rasmussen and Evans, 1987; Rousseau et al., 1989; Daniel et al., 1981; Briscoe, 1984; Wiebe et al., 1977.

Table 3-3. SUMMARY OF INSTRUMENTATION FOR LIQUID FLOW RATE AND DIRECTION MEASUREMENT

Instrument or Technique	Measured Parameter	Thermo-hydrological Parameter	Comments
Thermochromatic Liquid Crystals (TLC)	Color change with temperature change	Liquid and heat movement	Not effective in partially saturated media.
Dye tracer injection (Freeze and Cherry, 1979)	Tracer location	Liquid movement and velocity	Simple technique for 2-D experiments. Requires clear walled container.
Fiber optic dye tracing (Perkins and Jones, 1989; Yow et al., 1989)	Concentration of dye at sensor location	Liquid movement or diffusion	Method has been demonstrated in porous media for saturated, but not unsaturated conditions.
Solution Tracer (Chuang et al., 1989)	Presence or concentration of tracer	Liquid movement and direction	Diffusion of solute limits time a sample can be traced.
Dual energy gamma source (Stillwater and Klute, 1988)	Difference in the absorption of two different energy level gamma rays by the tracer element	Tracer concentration and movement	Requires accurate measurement of count rates to determine tracer concentration.
X-ray	X-rays transmitted through the medium	Liquid movement	Detection not sensitive to small changes in moisture content.

Table 3-4. SUMMARY OF INSTRUMENTATION FOR VAPOR FLOW RATE AND DIRECTION MEASUREMENT

Instrument	Measured Parameter	Thermo-hydrological Parameter	Comments
Solute deposition	Concentration of solute in liquid due to evaporation of liquid	Vaporization site	Does not actually track vapor flow. Usually requires disruptive sampling techniques. Changes in deposition can occur.
Pressure sensors	Pressure drop due to vapor flow through media	Vapor flow direction (towards lower pressure region) and rate	Difficult to measure extremely low pressure drops if vapor flows are low. To determine flow velocity, the media flow-pressure drop relationship must be known (function of saturation).

curves, measurements of both matric potential and moisture content in an experimental test are desirable. Measurement of the matric potential distribution (and the gravity potential) provides a means to determine the driving potential of the liquid. From this distribution and a knowledge of the thermohydrologic properties of the medium, the flow of liquid can be predicted.

Identification of the liquid flow paths in partially saturated porous media is necessary for determining the transport of soluble chemicals and for the convective transport of heat. It is also some of the most difficult experimental information to observe and quantify. The reasons for the difficulties are the liquid is "hidden" inside the medium, the liquid is distributed throughout the medium and mixed with vapor, movements are generally very slow (at partially saturated conditions), and instrumentation inserted in the medium can easily disrupt the direction of the flow. Methods using tracers can be used to measure liquid flow velocity and direction. The methods used to track fluid movement are summarized in Table 3-3. None of these methods provide a detailed distribution of all liquid movement, since they only provide information on the movement of the "tagged" liquid (tagged implies the tracer).

The movement of the vapor phase can be an important consideration under nonisothermal conditions (from 0 to 120 C). Vapor movement can transport significant amounts of mass in addition to large amounts of heat. Table 3-4 summarizes experimental methods for tracking vapor movement. Techniques for vapor phase tracking are even more limited than those available for tracking the liquid phase.

In addition to a condensable vapor phase, an incondensable gas phase (typically air) is usually present. There are presently no adequate methods of measuring the movement of the incondensable gas phase. Its movement is generally considered to be similar to that of water vapor by assuming that the volume not occupied by water is filled with the vapor phase. This is a reasonable approach since the majority of heat and mass transport is accomplished by the water and condensable vapor migration, but the incondensable gas phase has been shown to have significant effects on limiting heat transport within heat pipes by limiting circulation of water vapor.

Additional summaries of instrumentation for measurements in partially saturated porous media are given by Morrison (1983) and Rasmussen and Evans (1987) and for measurements at Yucca Mountain by Osiensky and Davis (1988). Details of experimental use of many of the different instrumentation summarized in Tables 3-1 through 3-4 are discussed in the following section.

3.1 LOCAL TEMPERATURE MEASUREMENT TECHNIQUES

The local temperature within the test media and at the heated (or cooled) boundaries of laboratory experiments must be determined accurately. Probes for temperature measurement are needed to verify the temperature at the boundaries and locally within the porous media. Several common temperature probes are available to perform this function. Thermocouples, resistance temperature detectors (RTD), and thermistors are all capable of providing the detailed data

necessary for local temperature measurements. Heat flux meters are also available for flush mounting on the boundary heat exchangers.

Some important temperature sensor selection criteria are listed below:

- Small sensor size to provide minimal influence on local porosity;
- Functional in submersed environments for extended periods;
- Long-term stability;
- Minimal thermal influence due to self-heating;
- Reasonable cost due to the quantity required;
- Response time on the order of a few seconds;
- Corrosion resistance;
- Temperature range 0-120 C; and
- Resolution better than 0.1 C.

All the devices listed above satisfactorily comply with these criteria. Depending upon the type of measurement to be made (surface or immersed), more than one sensor type may be utilized. For example, temperature measurements performed in the evaluation of an electrical resistivity probe (Section 3.2.1) and flow visualization (Section 3.4) utilized both thermocouples and RTDs. However, thermistors have been used to measure temperature in the separate effects experiment and in Test 7 of Task 3 (Chapter 4).

3.2 MOISTURE CONTENT MEASUREMENT

The volume of water contained globally in the test apparatus during a given experiment can be controlled; however, the local distribution within the media must be measured. As thermal gradients are applied to the media, the local changes in moisture content must be determined. It is anticipated that moisture content sensors must function over a wide range of saturation, from nearly dry to saturated. The sensor should have a response time on the order of minutes and provide measurements from a small sample volume.

A wide variety of moisture content measuring techniques and sensors was considered and evaluated. Many of these are described in the literature with sufficient detail to allow cursory evaluation. Other techniques were tested directly for applicability in the laboratory-scale experiments of the research project. Techniques considered for measurement of moisture content in the laboratory-scale experiments were:

- Electrical Resistivity
- Thermal Conductivity
- Gamma Ray Attenuation
- Light Transmission/Scatter
- Dielectric Constant
- Neutron Count
- Acoustic Wave Velocity

- X-ray Radiography
- Nuclear Magnetic Resonance
- Microwave Resonance
- Moisture Block

The microwave resonance technique has been eliminated for measurement of moisture content in this project at this time because of the limited development of this technique. The neutron count method is not applicable to the currently envisioned laboratory-scale thermohydrology experiments, but could be useful in field-scale experiments and possibly in other larger laboratory-scale experiments. Measurement of water content using moisture blocks was dismissed because of the intrusive nature of the blocks and their sensitivity to temperature.

Acoustic wave velocity measurements in porous media have been used to show that the wave velocity is a direct function of the saturation level (Allen et al., 1980). However, the range over which approximately 85 percent of the change in wave velocity occurs is between 99.5 and 100 percent saturation. This fact severely limits the applicability of the acoustic wave velocity technique in our experiments. Efforts on this sensor development are continuing and this technique may be needed where high temperatures eliminate other types of sensors.

Nuclear magnetic resonance (NMR), as with other tomographic methods, have potential, but are rather complex and would require time and resources not available at this time. Tomography is a general term which refers to an imaging technique used with a variety of measurements (x-ray, acoustic waves, magnetic resonance, and electrical conductivity). It provides a cross-sectional view of the parameter field intensity by inverting a matrix of spatial measurements. The NMR technique employs an intense magnetic field which forces media at different saturations to resonate at different frequency levels. The frequency data generated by NMR can be related to specific saturation levels. Evaluation of these techniques and instruments was conducted using documentation from the technical literature.

The laboratory investigation of techniques and instruments to measure moisture content was focused on the following: electrical resistivity, real-time X-ray radiography, thermal conductivity, light transmission or scatter, gamma ray attenuation, dielectric constant, and tensiometer. Each of these methods has the potential to provide the required moisture measurements without the need for extensive development or cost. These methods are discussed in the following sections.

3.2.1 Electrical Resistivity Probe

Electrical resistivity of media has been demonstrated to be a quantifiable function of the moisture content (Keller and Frischknecht, 1966; Morrison, 1983; Rasmussen and Evans, 1987). Electrical resistivity or conductivity can be measured with probes consisting of two electrical conductors, a transmitter and a receiver, separated by a resistance distance. They have been used in well logging activities. For water-bearing media, most of the electrical conduction will occur through the water and not the solid, which can be considered an insulator. For

partially saturated media, the resistivity can be expressed as an empirical function of saturation by Archie's formula (Archie, 1942; Telford et al., 1976)

$$\rho_e = a\phi^{-m} S^{-n} \rho_w \tag{3-1}$$

where

ρ_e	=	bulk resistivity of the sample [ohm-m],
ρ_w	=	resistivity of the fluid [ohm-m],
S	=	fraction of the total pore volume filled with water [dimensionless],
n	=	experimentally determined (typically a value of 2) [dimensionless], and
a, m	=	constants ($0.5 \leq a \leq 2.5$; $1.3 \leq m \leq 2.5$) [dimensionless].

Archie's formula is modified for applications to partially water-saturated media (Archie, 1942; Telford et al., 1976)

$$S = (\rho_o / \rho_t)^{-1/n} \tag{3-2}$$

where

ρ_o	=	bulk water-wet resistivity of the rock sample [ohm-m],
ρ_t	=	true resistivity of the rock [ohm-m], and
n	=	saturation exponent ($1.5 \leq n \leq 3$), usually assumed to be 2 where there is no evidence to the contrary.

Resistance, R, is related to resistivity by the expression (Telford et al., 1976)

$$\rho = RA/L \tag{3-3}$$

where

R	=	resistance [ohm],
A	=	cross-sectional area of conductor [m^2], and
L	=	length of conductor [m].

A resistivity sensor may be adequate to determine local saturation in the media based upon the empirical relationships between resistivity and saturation level and a correction factor for the change in resistivity with temperature. Preliminary electrical resistivity tests were performed on porous media made of 160 mm glass microbeads at saturation levels between 0 and 100 percent. A resistivity probe consisting of two 0.3 cm diameter cylinders spaced 1.9 cm apart was fabricated and tested. The probe was inserted into the microbead test material. A 1.4 VAC, 500Hz potential was established across the resistivity probe. The corresponding electric current induced through the sample by this potential was measured and the corresponding resistance calculated using Ohm's Law. The results displayed in Figure 3-1 illustrate the measured response. Based on the positive results of this test, a prototype resistivity probe was constructed and tested. The prototype probe was a 7.6 cm long by 0.64 cm diameter cylinder

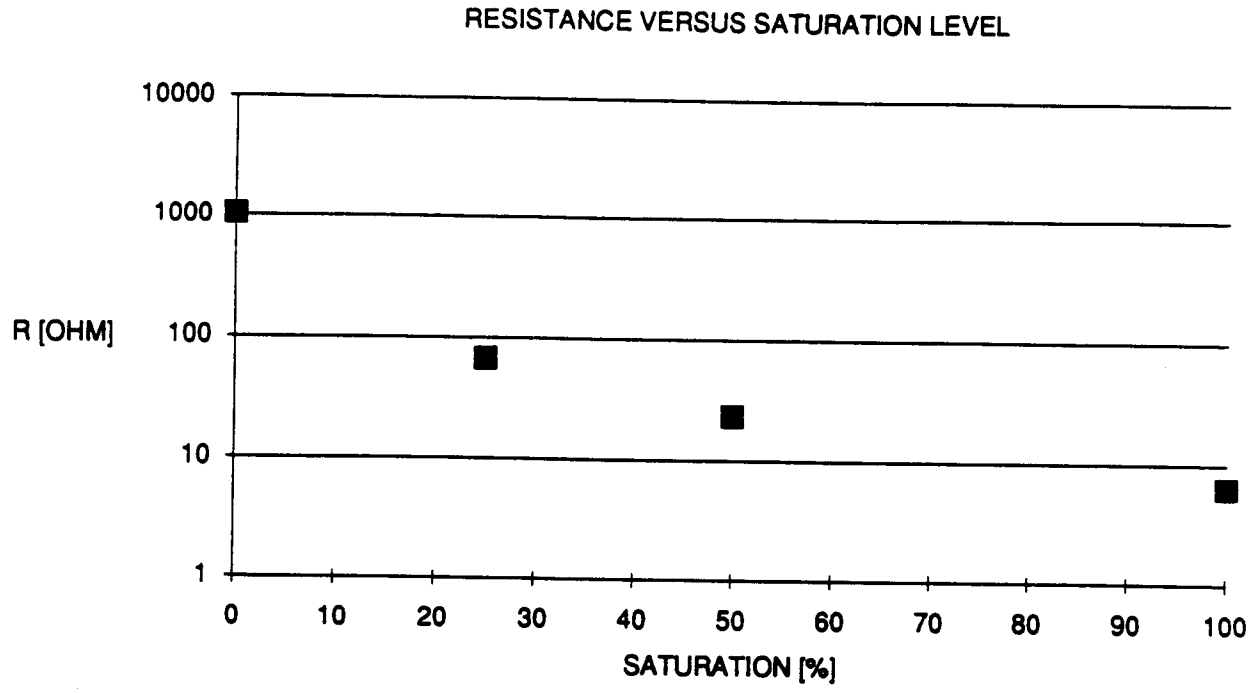

Figure 3-1. Initial test of resistivity probe response for various saturation levels of water in glass microbeads

with two conductors (stainless steel bands 0.64 cm OD by 0.5 cm long) separated by 1.3 cm of acrylic insulating material. Initial electrical resistivity test results determined with this probe had the same trends as shown in Figure 3-1.

Since the packing of the glass beads around the probe and proximity to the test container walls can affect the measurements, a test with greater control was designed. The sensor was placed in a 7.6 cm diameter jar filled to a depth of approximately 10 cm with 160 μm diameter glass beads and saturated with water. The test jar was capped and placed in an insulated box to minimize temperature variations. A voltage was established across the probe conductors. The current, voltage, and temperature were monitored for a day, at which time the measured potential appeared stable. The saturation level in the medium was then decreased to 92 percent by removing water through a porous cylinder buried in the bottom of the container. The sample was returned to the insulated box and temperature and the electric current across the probe conductor were monitored for six days. The resistance decreased during the entire 7-day test period of monitoring after the water was removed from the jar (Figure 3-2). The increase in resistivity at approximately 20 hours into the test corresponded to the removal of water from the sample. With less conductive fluid present, the resistivity initially increased as predicted by Archie's formula [Eqn. (3-1)], but then decreased steadily.

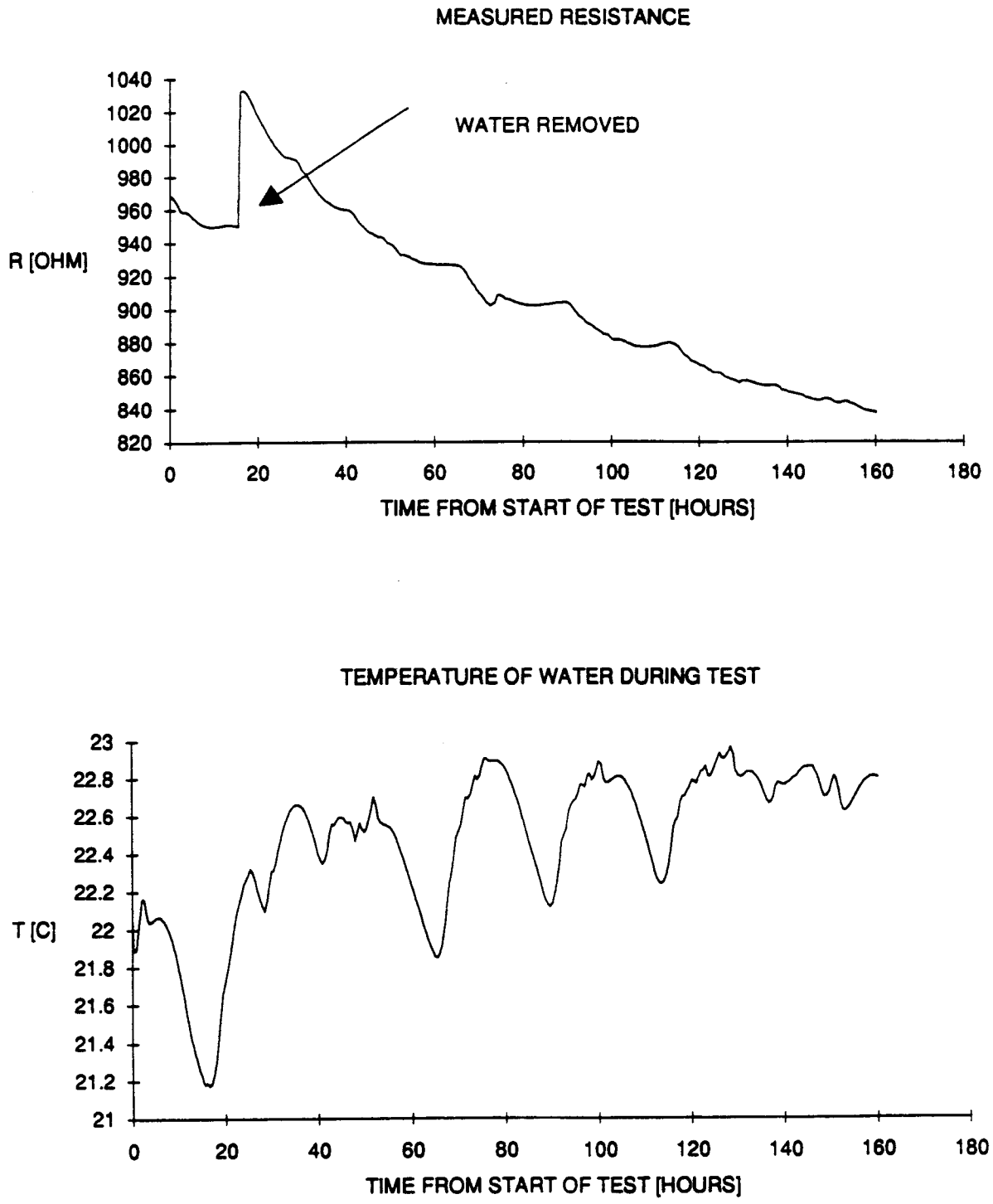

Figure 3-2. Resistance measurements recorded in glass microbeads over a 7-day period. The initial saturation level of 100 percent was reduced to 92 percent after approximately 20 hours.

The temperature of the sample measured during the test varied by less than 2 C. Therefore, temperature does not appear to be the cause of the decreasing resistance. It is interpreted that the calculated resistance was well below the resistance for saturated media when the experiment was terminated. In general, partially saturated media should have greater resistivity than saturated media, in contrast to these results.

Several reasons can be postulated for the unexpected results. The method used to measure resistance was also checked for a 7-day period to ensure the probe and instrumentation were stable for a medium of only water (Figure 3-3). As illustrated in this graph, resistance fluctuations correlate directly with temperature fluctuations. The resistance variations correspond to temperature variations of approximately 2.5 percent per 1 C. This result is interpreted to demonstrate that the instrumentation was stable and was not the cause of the continued decrease in resistivity encountered in the microbead and water media.

Another possible cause for changing resistance is interpreted to be a change in the ionic content of the water. Highly purified deionized water of 18 mega-ohm resistance was initially used to saturate the microbeads. If any material or coating on the beads, glass jar, resistivity probe, or stainless steel porous cylinder dissolved into the water, the resistance would also decrease over time. The resistivity of the water would change with temperature, since solubility is a function of temperature.

Other possible causes of the temporal decline in resistance include bacteria growth in the medium, change in amount of air dissolved in the water, water selectively moving into the void space around the probe (and trapped voids present during the saturated readings), change in the fluid resistivity caused by silica dissolution, or probe electrical insulation failures.

Based on the results of the tests conducted, it was observed that several parameters which affect resistivity would have to be closely monitored. Correction factors would need to be applied to the measurements from resistivity probes in the test medium during experimentation to account for the amount of soluble material in the water. Compensation for temperature-induced variations in electric current would also be required. Careful packing of resistivity probes would be critical to ensure repeatability of results. The method of insertion of the probe into the media would also influence fluid movement and thermal transport, thus affecting electric current and hence, resistivity values. Consequently, reliable application of an electric conductivity probe to measurements of saturation would therefore require an inordinate level of ancillary monitoring and related correction.

3.2.2 X-Ray Radiography

The x-ray radiography method was assessed for monitoring moisture distribution. This type of measurement is nonintrusive since no sensor is inserted in the media. Although the primary reason for evaluating this technique was to assess the ability of a real-time x-ray radiography system to monitor motion of fluid fronts (for flow visualization) through the media,

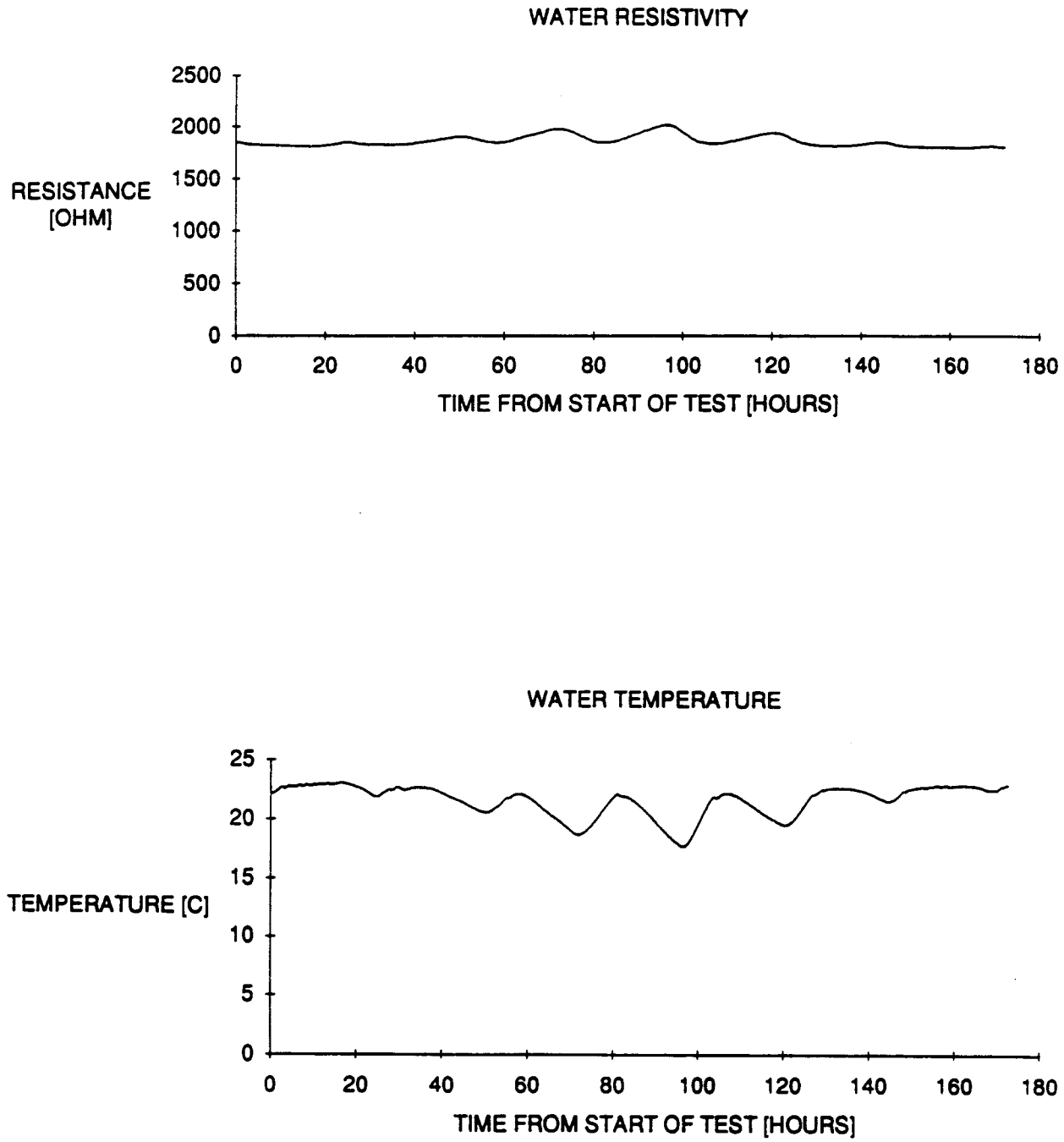

Figure 3-3. Test of the resistance probe stability in water. The resistance of the sample is stable and only varies with temperature changes of the water.

the technique may also be applicable to the measurement of moisture distribution if sufficient contrast exists.

X-ray radiography is a technique which uses an x-ray source and detector to determine the attenuation of x-rays passing through a medium. The attenuation is a function of the sample thickness and the sample density. For a mixture of glass microbeads and water, the difference in density between dry glass microbeads (bulk specific gravity of 1.5) and fully saturated microbeads (mixture specific gravity of 1.85) is small. This suggests that the differential attenuation of the x-rays at the two water-content levels would also be small. For this reason, a test was performed to determine the amount of resolution using x-rays to distinguish between saturated and partially saturated regions.

The tests were performed using a Philips M6161 constant potential x-ray source and a Precise Optics P1600A cesium iodide image intensifier. The glass microbeads (160 μm average diameter) were contained in a rectangular cross-section (22.9 cm by 15.2 cm) acrylic box that was 1.9 cm thick in the sampling direction. Dry glass microbeads were packed into the container and the container was positioned in front of the x-ray source. While viewing the "live" x-ray image, water was slowly introduced by infiltration into the container filled with glass beads. The water "front" was monitored.

It was extremely difficult to distinguish the relative saturation of the microbeads in these initial tests. By simply looking at the acrylic container, the outline of the saturated zone was clearly visible, however, to the image intensifier, the variation in density was too slight to distinguish between partially saturated zones. The detected contrast between the wet and dry zones displayed by the x-ray system could not be improved by changing source power levels, various source, sample, and detector separation distances; or shielding of the detector. Using this method, it would be difficult to quantify local moisture content for two reasons. First, the "gray scale" between fully saturated media and dry media is extremely narrow for this type of detector and absorption media. The second reason is the difficulty in quantifying the local moisture level or moisture distribution from a video display. While this method might possibly work with additional refinement, it would require significant development effort and time to achieve this goal.

3.2.3 Thermal Conductivity Probe

Changes in the thermal conductivity of a porous medium as a function of changes in moisture content have been documented by many researchers (Shaw and Baver, 1939a,b; de Vries, 1963; Phene et al., 1971a,b; Keller and Frischknecht, 1966; Wong et al., 1987; Fredlund et al., 1989). This relationship has generally been applied in agriculture. In theory, changes in thermal conductivity have been associated with soil suction pressure, primarily because suction pressure is the parameter of interest to agronomists. However, the thermal conductivity is more directly related to the moisture content of the porous medium (Shaw and Baver, 1939a,b; Thamir and McBride, 1985; Fredlund and Wong, 1989).

A thermal conductivity probe operates on the principle of transient heat flow. A heat source is used to provide thermal energy and a temperature detector (such as a thermistor) is used to determine the transient temperature at a fixed distance. The transient temperature response is a function of the moisture content. The relationships between thermal conductivity and moisture content (or soil suction) have been shown to be media specific (Fredlund and Wong, 1989), therefore, a probe would require laboratory calibration in the desired medium.

Commercially available sensors from Agwatronics of Merced, California, contain a heating element and a thermistor mounted in a ceramic block. These sensors are generally calibrated in the lab using a modified pressure plate and a reference soil mixture. The thermal conductivity of the ceramic is measured as a function of the moisture content during calibration. Therefore, when the ceramic block is placed in soil, and comes to equilibrium with the soil, measurement of thermal conductivity provides a determination of moisture content. The large size of the ceramic block, however, precludes the application of thermal conductivity probes to the laboratory-scale experiments of this project.

3.2.4 Light Transmission/Scatter

The light transmission property is one of the unique features of using glass microbeads in experimentation. Each individual glass microbead acts as a refraction surface that will scatter an incoming light beam. For this reason, a beam will not penetrate far into dry glass microbeads before it is diffused by refractive scattering. When water is added to the beads, the water-filled pores act as a "light pipe" between beads and allow an incident beam to penetrate farther into the medium.

The light-pipe property of the microbead and water medium could be used to measure local moisture content of the mixture. The use of very fine optical fibers in the laboratory experiments would inflict minimal impact on the fluid movement due to their small size. Additionally, this technique is independent of the electrical properties (of the water or microbeads), temperature, or pressure. The fiber optic probe could be used to monitor the movement of dye tracers through the medium.

In order to evaluate this method, several glass jars filled with 160 μm diameter beads at varying saturation levels were prepared. The glass jars were sufficiently small (1.65 cm OD) to allow a detectable amount of light to penetrate through the test medium. Each of these test containers was placed in the path of an argon ion laser (wavelength 488 nm, although any light source should work) to provide an initial indication of the usefulness of this technique. The transmitted light was detected with a Spectra Physics 404 light meter.

The results of the light transmission tests are illustrated in Figure 3-4, plotted as saturation relative to output voltage from the light meter. No attempt was made to quantify the light intensity in terms of power density. The plots show a definite increase in output voltage with increasing saturation level. The 100 percent saturated reading shows a significantly

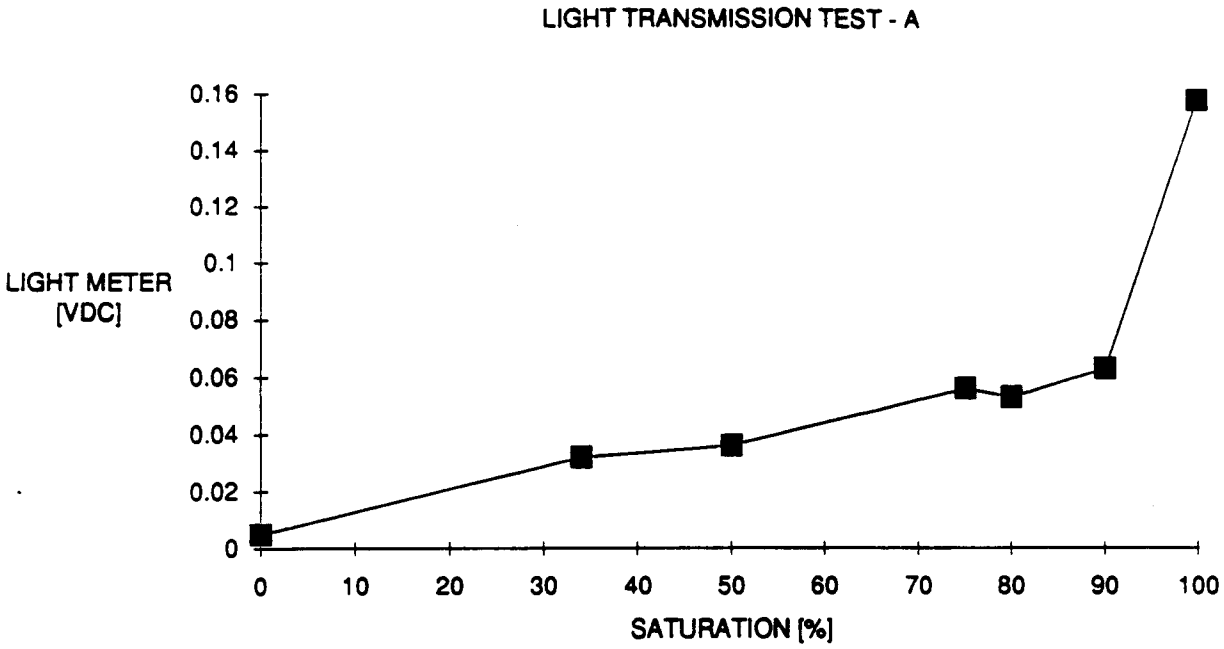

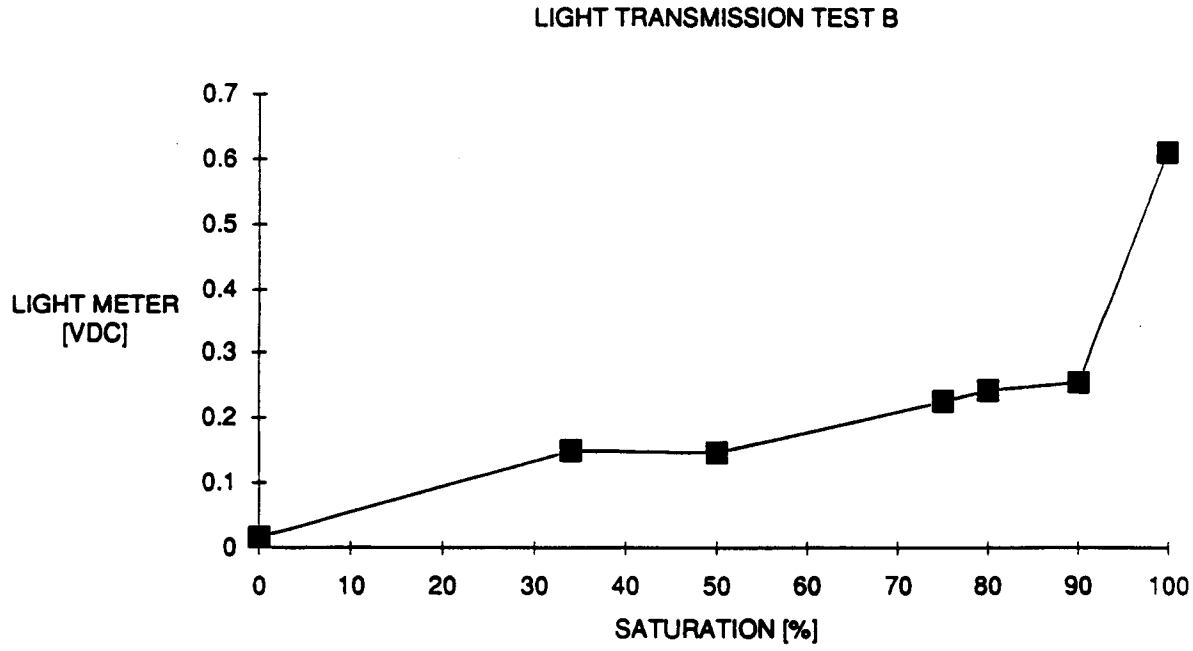

Figure 3-4. Light transmission through glass microbeads as a function of saturation level with water

increased output voltage and is attributed to the effects of the small container. When the test medium was fully saturated, the void space between the microbeads and the container wall was filled with water. The extra water is thought to have eliminated much of the scatter which the other less saturated samples experienced. An additional cause of the apparent increase in light transmission may be attributed to the pore water next to the glass walls present under fully saturated conditions. This water could provide a more uniform and direct path for light to reach the detector.

The results of these initial tests are encouraging, but more detailed testing is required to confirm this approach. Based on preliminary observations, it appears the detector (light meter) could be configured to detect either light transmission or light scattered back toward the source. With a fiber optic based sensor, the latter method could be more easily applied. This technique is obviously limited to translucent media and liquids.

3.2.5 Gamma-Ray Attenuation

The gamma-ray attenuation technique is routinely used to measure density variations (Nicholls and Heaviside, 1988). In this method, a gamma-ray source is placed on one side of the medium to be tested and gamma-rays are directed through the medium to a detector on the opposite side. The source and detector assembly are referred to as a densitometer. The ability of gamma rays to penetrate through a sample to a detector is proportional to the sample thickness and density. As material thickness or density increases (for example, due to increasing water content), the amount of radiation able to penetrate the sample decreases. The use of gamma-ray attenuation has been used by various researchers to measure local moisture content (Eaton et al., 1985; Verma et al., 1985; Rasmussen and Evans, 1987). This technique has been evaluated in the laboratory for application in the laboratory experiments of this project.

A test was performed to verify the gamma-ray attenuation method with the glass microbead and water media. Several test media comprised of 160 μm diameter glass beads in glass jars 7.6 cm OD by 8.9 cm tall were prepared at various saturation levels. A Texas Nuclear 9700D, EZCal Density System was used for the tests. The sample containers were placed inside a 10.2 cm diameter pipe and positioned between the source and detector to facilitate the measurement technique. The densitometer measured changes in the density of the media due to changing saturation levels. The densitometer reading was calibrated to 100 percent saturation. The densitometer response illustrated in Figure 3-5, between 20 percent and 100 percent saturation levels, appears to be nearly linear.

The densitometer reading of dry beads (0 percent saturation) deviated slightly from linearity and is attributed to the testing technique. During testing, as the test sample jars were inserted into the 10.2 cm diameter pipe, the samples were placed on their side which allowed the partially saturated beads to shift to the void region at the top of the container. Because of the limited sample size and large detector cross-sectional area, part of the gamma beam may not have been intercepted by beads in the sample. Therefore, this data point is

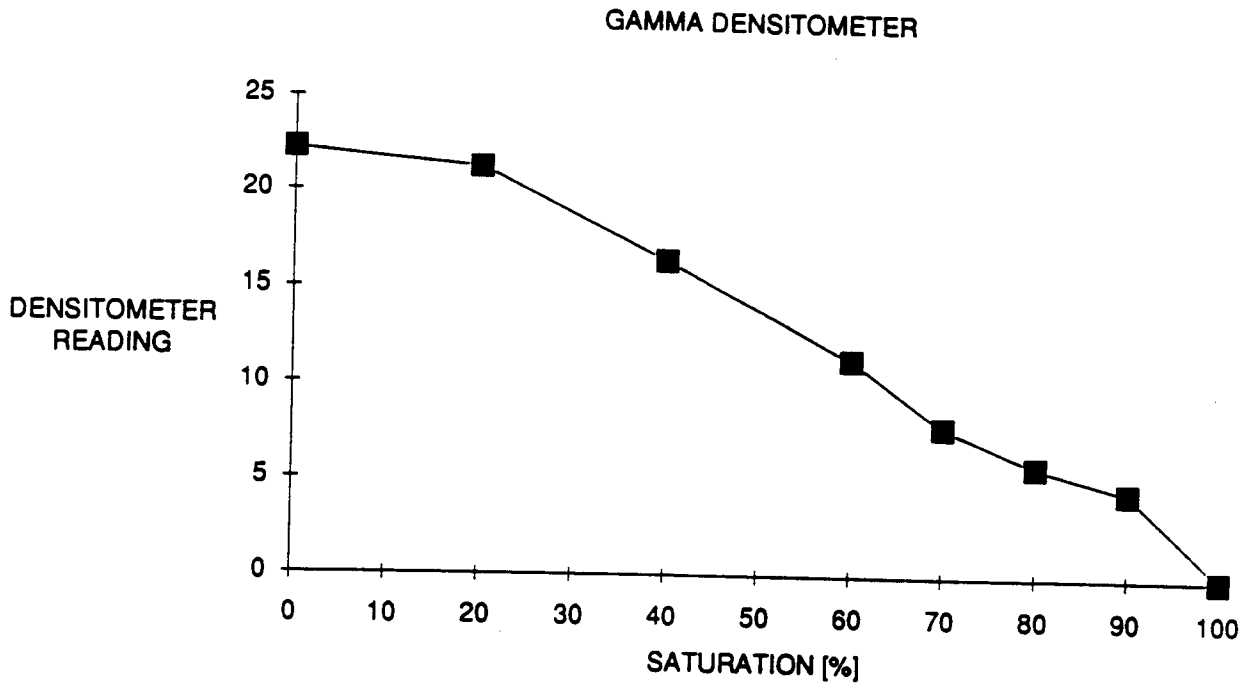

Figure 3-5. Gamma beam densitometer readings of various saturation levels of microbeads in water

believed to be a product of the experimental technique and not indicative of an improper or nonlinear measurement reading at low saturation.

The other data point that deviated slightly from the linear response was the measurement reading at 90 percent saturation. In a repeat test, the densitometer closely duplicated the measurements plotted in Figure 3-5, including the position of the 90 percent point. It is interpreted that this sample had slightly less water than 90 percent saturation (due to uncertainty in sample preparation or possible drying of the sample).

Based upon these scoping tests, the gamma-ray densitometer technique appeared to be useful for determination of moisture content in glass bead media. A drawback to the method is that the source is composed of radioactive material. A major advantage of this method, however, is that the method is not intrusive since a probe is not inserted into the sample that would disturb fluid movement, heat transfer, or microbead packing. Another advantage of this method is the ability to provide detailed rapid moisture measurement of the test sample.

3.2.6 Time Domain Reflectometry

Time Domain Reflectometry (TDR) is a technique used to determine the electromagnetic wave propagation velocity in the media, from which the apparent dielectric constant is determined (Davis and Chudobiak, 1975; Topp et al., 1980, 1983; Zegelin et al., 1989). The dielectric constant of a porous media is strongly dependent upon the moisture content and more weakly dependent upon medium type and density. When two electrical conductors are separated by a dielectric (the medium), the electromagnetic wave velocity transmitted through the dielectric can be related to the real portion of the complex dielectric constant. Unlike electrical resistivity methods, the effects of water chemistry and temperature on the dielectric constant are negligible (Topp et al., 1980). The effects of media type and density on the dielectric constant can be estimated a priori for the specific media, thus permitting estimation of the moisture content of the media.

To employ this technique, a probe consisting of an embedded transmitter and receiver is inserted into the test medium. The TDR technique requires measurement of the electromagnetic pulse times on the order of nanoseconds. This technique appears to be promising for application in the larger-scale experiments in porous media, but has not been evaluated for use in the laboratory experiments of the project or for application to consolidated media, in general.

3.2.7 Capacitance Sensors

Capacitance sensors are used to measure the combined capacitance of the media and the liquid within the media (Morrison, 1983). Since the dielectric constant of most media is almost two orders of magnitude lower than that of water, the combined capacitance can be essentially attributed to the liquid and the measured capacitance can be correlated to water content. Capacitance measurements are usually made with a oscillator circuit connected to the sensor. The sensor measurement region can be controlled by selection of the sensor geometry. Factors that affect the measurement accuracy include: electrical contact between the sensor and the media, temperature variations, water quality, and sampling frequency. As with most other indirect moisture measurement methods, capacitance sensors must be calibrated for specific media to correlate capacitance readings to moisture content. While some probe development effort would be required to utilize this methodology in laboratory experiments, the primary drawback to the use of capacitance sensors is that they are intrusive to the media and, therefore, disrupt the flow of fluid and heat within the media.

3.3 SUCTION PRESSURE MEASUREMENTS

Suction pressure measurements in fluid flow experiments are essential to investigating the driving forces present in media under less than fully-saturated conditions. Several suction pressure measurement techniques — thermocouple psychrometers, capacitance hygrometers, tensiometers, osmotic tensiometers and a microwave technique — were evaluated for use in this project.

Osmotic tensiometers were eliminated from consideration because of the limited development of the technique (Rasmussen and Evans, 1987). The filter paper absorber method and the soil moisture block were determined to be inappropriate for the laboratory-scale experiments. A microwave coaxial resonator system was developed by Lawrence Livermore National Laboratories (LLNL) for use in heater experiments to measure the partial pressure of water vapor in air in a borehole (Latorre, 1989). A notable advantage of microwave resonators is that they can operate at temperatures up to 350 C, considerably higher than thermocouple psychrometers which are limited to temperatures less than 150 C. Microwave resonators were not considered for use because they are still in the developmental stage. However, they may be used in the future pending additional development.

3.3.1 Thermocouple Psychrometers

Thermocouple psychrometers have been used for a number of years to measure water potential in partially saturated soil and rock (Wiebe et al., 1977; Daniel et al., 1981; Briscoe, 1984; Thamir and McBride, 1985; Rasmussen and Evans, 1987; Rosseau et al., 1989). Psychrometers measure the relative humidity of air in the pores of the media and relate this to water potential by the Kelvin equation. Their reported range of application is 2 to 80 atmospheres of suction pressure, which corresponds to saturations of 5 percent to 50 percent in sandy soils (Rasmussen and Evans, 1987; Mao and Wang, 1991). This would limit their application in the thermohydrology experiments, which typically have saturations in the range of 60 to 80 percent. Psychrometers are inexpensive, but require a precision microvoltmeter to obtain measurements. The psychrometer response time is approximately one hour, and the best isothermal calibration reproducibility of moisture content in salt solutions is ± 5 percent. Thermocouple psychrometers also require calibration for temperature compensation. However, their greatest limitation is the thermal gradient effect (Wiebe et al., 1977). If thermal gradients exist within the media, the temperature of the dry bulb thermocouple junction will not be in equilibrium with the temperature measured at the wet bulb thermocouple junction. This may lead to significant errors in the relative humidity measurement and, thus, errors in water potential.

3.3.2 Capacitance Hygrometer

A capacitance hygrometer determines water potential in porous media by the measurement of relative humidity in pore air, a method similar to that of the thermocouple psychrometer. However, performance of the hygrometer is poor at relative humidity levels above 98 percent, which correspondingly limits the range of saturation in which they yield reliable data. According to the Kelvin equation, the relative humidity of air in the pores of the test media exceeds 98 percent at moisture contents well below saturation.

3.3.3 Tensiometer

The tensiometer is a device used to measure suction pressure in partially-saturated media (Richards and Gardner, 1936; Evans, 1983; Rasmussen and Evans, 1987). The

tensiometer is constructed of a rigid thin-walled tube, connected at one end to a pressure transducer, and at the other end to a porous cup. The porous cup is inserted in the test media and allowed to come to hydrostatic equilibrium. The rigid tube is filled with purified water which transmits the tension force from the porous cup to the pressure transducer. When water is pulled out of the porous cup into the media, the water exerts a negative differential pressure on the attached transducer. The application of the tensiometer is generally limited to a range between 0 and 1 atmosphere (Morrison, 1983). In the glass microbead media used in the laboratory-scale experiments of this project, this range should not be a limitation, however, other methods may be required to measure suction pressure in welded tuff where greater suction pressures may be encountered.

Unfortunately, tensiometers physically intrude into the media. However, all techniques currently investigated for measuring water potential have this limitation. A strength of tensiometers is that they provide direct pressure measurements and are considered adequate over the anticipated pressure range of the experiments.

A similar tensiometer device has been used to measure local vapor pressure (Verma et al., 1985). For this device, a miniature heating element was incorporated within an air dry version of the tensiometer to prevent internal condensation. This vapor pressure technique was not evaluated for use in this series of experiments at this time.

3.4 FLOW VISUALIZATION

Flow visualization is a qualitative and possibly quantitative method to help understand the direction of flow and, hence, the transport mechanisms of partially saturated flow in porous and fractured media. If the direction of flow of fluid within a medium can be visualized, the observer is provided with an insight into the mechanics of the processes active in the medium. The use of fiber optics to detect the presence of a tracer was determined to be applicable to only saturated media (Perkins and Jones, 1989; Yow et al., 1989). Several methods which could provide flow visualization in partially saturated, fractured, porous media were investigated. Two of these methods, thermochromatic liquid crystals and dye injection tracers, take advantage of light transmission ability in the glass bead medium. The third method evaluated employs real-time x-ray radiography. A discussion of the assessment of these techniques is presented in the following section. Solution tracing (Chuang et al., 1989) does not currently appear to be a viable option. However, if used in combination with a dual energy gamma source, useful data could be provided (Stillwater and Klute, 1988).

3.4.1 Thermochromatic Liquid Crystals

Thermochromatic liquid crystal (TLC) microbeads consist of chiral nematic mixtures of cholesterol which are encapsulated in a polymer. The TLC microbeads react to changes in temperature by changing colors. The specific cholesteric mixture controls the temperature range over which the microbeads change color. The activation of the color play at the lower bound of the temperature range is termed the "red start." The TLC beads change

colors through the spectrum with an increase in temperature until the upper bound of the color play, the "blue stop," is reached. The range of colors has a linear correlation with temperature. TLCs used in the visualization experiments were purchased from Hallcrest Products of Glenview, Illinois.

Experiments were performed for both saturated and partially saturated conditions using glass beads with TLCs of two different color plays and two different sizes. Initially, glass beads of 80-micron diameter were used as the medium in the visualization studies, but it was found that a larger bead diameter would enhance the visibility of the TLC mixture within the media. Therefore, 160-micron diameter glass beads were chosen as the medium for visualization experiments.

Tests were also conducted with TLC mixtures of 15-micron diameter bead size and 100-micron diameter bead size to visualize water and thermal movement within the medium. The 15-micron TLC beads were conceivably small enough to move with the liquid through the pore spaces but with less color resolution. However, in initial tests with the 15-micron TLCs, movement of the beads with the liquid was not observed, possibly attributable to the reduced color resolution. The 100-micron TLCs offered the best color display. Additionally, two different color plays, a 4 C and a 15 C bandwidth of color between "red start" and "blue start," were tested.

Tests were conducted under both saturated and partially saturated conditions. In the initial tests, a saturated, glass-bead medium containing approximately 10 percent solution (in the liquid) of the 15-micron diameter TLCs was placed in an acrylic test apparatus having two vertically-oriented controlled-temperature opposing boundaries. The heat-exchanger boundaries were heated by constant temperature circulating baths and provided a constant temperature difference between boundaries. The colors displayed in the saturated tests were both bright and distinct.

In the partially saturated tests conducted using a medium with a water saturation of 88 percent, the light reflective properties of the TLC beads were sufficient to allow color display. The solution used in this test had 10 percent of 15-micron diameter TLC beads. The partially saturated tests were performed with horizontal temperature boundaries which provided a vertical temperature gradient. After the heat exchangers were turned on, the color bands moved uniformly toward the lower temperature surface as the interior region was heated.

In another test, a vertical heating boundary configuration was used in a similar acrylic test apparatus to assess the effect of variable saturation on the performance of TLC contained in the glass beads. The vertical plates were maintained at differing constant temperatures to provide a constant thermal gradient across the sample. In the saturated tests, light transmission through the sample was much better than the partially saturated tests and produced better color display. The partially saturated test was conducted with 40 percent degree of saturation. The color display was very faint but still visible for a water saturation of 40

percent. The results of this test indicate the resolution of color with TLC mixtures decreases with decreasing saturation.

The lighting used to illuminate the color in the TLCs greatly affects their visibility. A trial and error approach was used to visualize the best color displays. Light from different angles and geometries and polarized light were tried in different combinations. The best results were realized when the illuminating light was located in the test container.

TLC beads have been demonstrated to be potentially useful in visualization of the local temperature field within the media and can be used for approximate temperature measurements, although direct temperature measurements are more accurate. TLC mixtures were used to indicate uniformity of the temperature field and to visualize the presence of thermal gradients within the media.

3.4.2 Dye Tracer Injection

Several experiments were conducted to evaluate tracer methods that could be utilized for tracking liquid motion. The tests were performed using liquid dyes because they are easy to apply and track but other tracer methods (such as radioactive tracer materials, photosensitive dyes, or chemical tracers) could be used and should have the similar results.

The first tracer tests were conducted to verify that fluid motion in 160-micron diameter glass microbeads, at saturated conditions, could be monitored. The tests were performed in an acrylic container. The vertically-oriented, heat-exchanger plates of the container were heated by constant temperature baths to provide constant temperature surfaces at two boundaries of the container.

The initial test was conducted on a medium of fully-saturated 160-micron diameter beads. This experiment indicated that liquid dye injected near the hot heat-exchanger plate flowed up the plate until it reached the top surface and it then circulated towards the cold heat-exchanger plate. The dye flowed downward along the cold heat-exchanger surface and recirculated to the hot plate. Some diffusion of the dye occurred but it remained traceable in this general pattern for several hours. This flow pattern is similar to that observed in the classic heated side wall problem of fluid mechanics. Here, a thermal boundary layer developed at the hot plate, and because of density gradients in the fluid, buoyant forces created fluid motions.

Two tests were performed with 160-micron diameter glass beads under partially saturated conditions. In the first test, dry beads were packed into the acrylic container and water was injected at three locations (for an average saturation of 70 percent). This caused three areas of local full saturation separated by initially fully unsaturated areas. After the water was introduced, the mixture was allowed to sit for 24 hours prior to setting the temperature of the heating plates on the vertical ends of the acrylic container at 60 C and 28 C.

Dye was initially injected near the hot heat-exchanger plate set at 60 C (6.6 cm above the bottom and 1.3 cm to the right of the heat-exchanger). The photograph in Figure 3-6 illustrates the three dark zones of initially, fully saturated beads and the location of the dye after it had moved up and to the right from the injection position. Dye was later injected near the heat-exchanger plate, set at 28 C (14.2 cm above the bottom and 1.0 cm to the left of the cold plate). Figures 3-7 through 3-9 show the dye movement over the next 22 hours. Dye movement was confined to movement in the initially saturated zones in a clockwise circulation pattern (from heated boundary to cool boundary) as expected for the buoyancy driven flow. This test clearly shows the dye tracer method is suitable for tracking fluid movement, and by providing several dye injection locations, a detailed map of fluid flow can be obtained.

3.4.3 X-Ray Radiography

As discussed in Section 3.2.2, the use of x-ray radiography for visualization of fluid movement was investigated. The tests performed in a "real time" x-ray system indicated it was difficult to discern a clear distinction between dry and fully-saturated beads using x-ray radiography. This low level of detection is attributed to the small increase in the attenuation of x-rays due to changes of water content in the pores. These results were interpreted to indicate that the sensitivity of the detector (in this case a sodium iodide image intensifier) was not sufficient to distinguish between the small differences in x-ray attenuation present.

3.5 VAPOR TRANSPORT

Measuring or monitoring vapor transport within a porous medium is very difficult and few techniques are available. One method of detecting vapor movement within a porous media is to measure the vapor pressure gradient between two points and calculate the flow rate based on the media properties. Because the pressure drop experienced by vapor flowing in a media is a function of the saturation level, this method is difficult to use for quantitative flow measurements, unless a "flow through" experiment is performed and the gas is metered. One other method of determining the movement of vapor, reported by Matthews (1986) and Davies (1987) used a tracer that became concentrated in the region where the vapor flashed from the liquid phase. By monitoring the increase in concentration of the tracer, a qualitative measure of the vapor flow can be obtained. These two techniques do not provide detailed vapor flow measurements, so vapor movement is generally inferred from data on liquid flow and heat transfer.

3.6 MOISTURE CONTENT AND MATRIC PRESSURE RELATIONSHIP MEASUREMENTS

Instrumentation to measure moisture content as a function of suction pressure is fundamentally useful to several aspects of experimental investigation of partially saturated media. Knowledge of the moisture-content/suction-pressure relationship (commonly referred to as a moisture characteristic curve) allows calculation of the moisture content when only suction pressure is known or calculation of suction pressure when only moisture content is known.

Figure 3-6. Visualization of flow of nonuniformly distributed liquid in partially saturated glass beads. 10-18-89, 3:51 p.m.

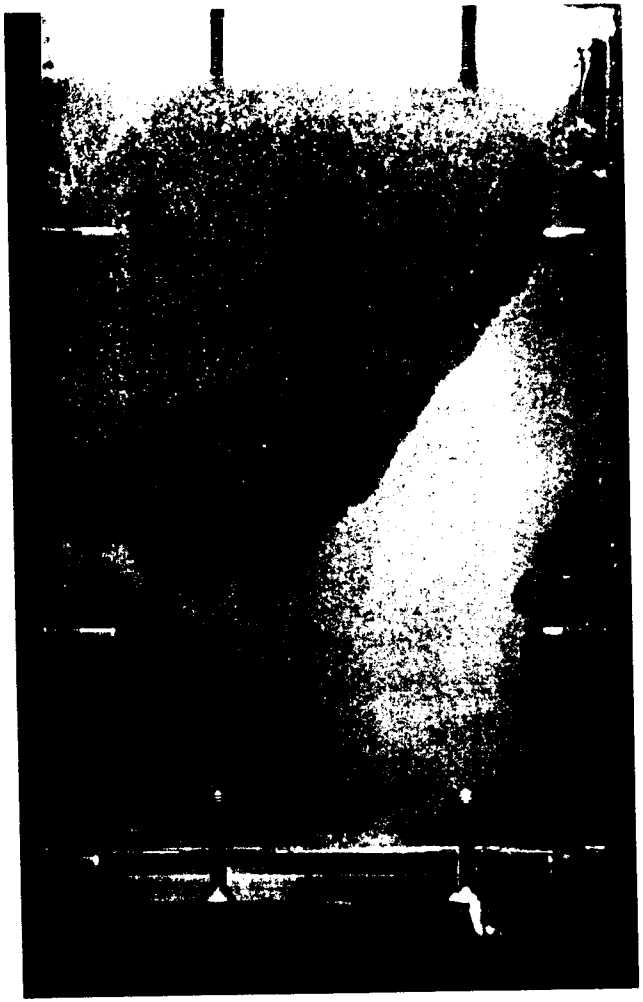

Figure 3-7. Visualization of flow of nonuniformly distributed liquid in partially saturated glass beads. 10-18-89, 5:32 p.m.

Figure 3-8. Visualization of flow of nonuniformly distributed liquid in partially saturated glass beads. 10-19-89, 8:12 a.m.

Figure 3-9. Visualization of flow of nonuniformly distributed liquid in partially saturated glass beads. 10-19-89, 1:54 p.m.

Thus, if the moisture-content/suction-pressure relationship for the test medium can be established independently of an experiment, measurement of either suction pressure or moisture content will permit calculation of the remaining unmeasured parameter or a confirmatory check if the parameter is measured. This is of use in experiments where either suction pressure or moisture content measurements, but not both, are collected at a particular location in an experiment. Measurement of only one of these parameters with knowledge of the independently determined moisture characteristic curve permits calculation of the remaining unmeasured parameter.

Measurement of the suction-pressure/moisture-content relationship allows calculation of the partially saturated hydraulic conductivity when a functional model defining conductivity in terms of this relationship has been assumed without having to make actual partially saturated hydraulic conductivity measurements. Additionally, if a functional model for partially saturated hydraulic conductivity and the suction-pressure/moisture-content relationship are known *a priori*, then measurement of either moisture content or suction pressure can provide the information necessary for determination of the remaining two hydraulic parameters, partially saturated hydraulic conductivity and either moisture content or suction pressure.

Techniques and instrumentation used to measure the suction-pressure/moisture-content relationship include the pressure plate (Osiensky and Davis, 1988; Chuang et al., 1990) psychrometer and mercury-intrusion measurements (Peters et al., 1984; Klavetter and Peters, 1987), gravimetric (Daily and Lin, 1989), and the submersible pressure outflow cell (SPOC) (Flint and Flint, 1991). The SPOC method is a variation of the gravimetric technique.

Commonly, these techniques are performed on a sample of the material independent of the primary experiment. The relationship measured on the sample material should be essentially the same relationship as the material in the primary experiment, providing the material tested with the pressure plate is representative of the material used in the primary experiment. This condition is usually considered to be valid for porous media, but may be erroneous for media with fractures. Measurement of the suction-pressure/moisture-content relationship for fractures is difficult and there is no currently acceptable technique for fracture hydraulic characteristics.

3.7 INSTRUMENT SELECTIONS

Based upon a technical literature review and laboratory investigations conducted to date, preliminary selections of measurement techniques and instruments applicable to monitoring thermohydrological phenomena were made.

The electrical resistivity method to measure moisture content is straightforward in principle, but the measurements using the resistivity technique are less desirable than other techniques due to the difficulty of accurately measuring additional physical variables such as the water chemistry, and correcting observed resistivity measurements for the effects of these variables. The apparent dielectric constant is reported to be independent of temperature and water chemistry and TDR should therefore be investigated for application in moisture content measurement in welded tuff. Additional necessary instrumentation, however, precludes the use

of this technique at this time. X-ray radiography was investigated for application to quantitative moisture content and moisture distribution determinations. However, the results of tests indicate insufficient resolution can be obtained using this technique.

Methods for measuring moisture content including thermal conductivity, light transmission/scatter, and gamma-ray attenuation have been evaluated in the laboratory. The thermal conductivity technique has been precluded from consideration due to the large size of the sensor. The resolution of the light transmission/scatter technique is not sufficient to be of use in this project. The gamma-ray attenuation technique appears to be most appropriate for moisture content measurements in laboratory-scale investigations. One major advantage of the gamma-ray technique is its nonintrusive measurement procedure. A planar motion table is required to position the gamma source and detector, but with this apparatus measurements of moisture content can be acquired virtually anywhere in the experimental test container. Additional methodologies, however, will be required to measure moisture content in larger, three-dimensional configurations.

Tensiometers are the most direct, effective method for obtaining suction pressure measurements within the medium over the range of pressures that was evaluated. However, corrections for nonisothermal conditions may be necessary to account for the temperature dependance of surface tension in the liquid. A variation of the tensiometer may be used to measure vapor pressure in the experiments based upon further laboratory investigation and evaluation.

Thermistors have been chosen for use in the measurement of temperature in the laboratory-scale experiments. Similarly, dyes will be used to trace liquid-flow movement in these experiments. A pressure plate referred to as a Tempe cell has been acquired to measure the moisture characteristic curve of the test medium. The Tempe cell will also provide a means to independently calibrate selected "probe-type" instruments used to measure suction pressure or moisture content within the test container.

4 LABORATORY-SCALE THERMOHYDROLOGY EXPERIMENTS

Investigation of thermohydrological phenomena at the repository scale is impractical because of temporal and spatial restrictions, namely, observation of the thermohydrological phenomena in a geologic repository setting would have to be made at longer distances and over long times that would obviate the possibility of providing the licensing process meaningful information in a timely manner. The conduct of laboratory-scale thermohydrological phenomenological experiments has been included as an integral part of this research project to provide information that can be used in the absence of meaningful, quantifiable information over the times and at distances of interest. Additionally, application of the precepts of similitude are used to scale laboratory results to processes that are expected at a geologic repository.

A progression of laboratory-scale experimentation has been performed in the pursuit of the objectives of the Thermohydrology Research Project. Initially, a series of "scoping" laboratory experiments were conducted to help identify instrumentation capable of providing meaningful information and to help in the design of separate-effect experiments. The results of these scoping experiments were used to improve subsequent experimentation.

Next, a series of six two-dimensional, separate-effect experiments (Tests 1 through 6) was designed and performed to identify the key thermohydrological phenomena and gauge their relative importances for (i) similarity studies, (ii) validation of numerical and analytical models, and (iii) design of future experiments. Subsequent to completion of the separate-effect experiments, a series of two-dimensional thermohydrology experiments was initiated. The objectives of these experiments are similar to the separate-effect experiments, except that this category of experiments is directed at the investigation of coupled thermohydrological processes. The first set of these experiments has been designed and initiated. The experimental design and conduct of the separate-effect and thermohydrological experiments are discussed in this section.

4.1 DESIGN AND EXECUTION OF PRELIMINARY SEPARATE-EFFECT EXPERIMENTS

Separate-effect tests were designed and performed to individually identify the key thermohydrological phenomena and to determine the magnitude of their influence for use in similarity studies, mathematical models, and future experimental design. In order to individually identify the key thermohydrological phenomena, the experiments were designed to investigate the following processes:

- Liquid infiltration and distribution;
- Local heating of pore liquid;
- Gas and liquid convection;
- Matrix/fracture interaction; and
- Transient heating.

To investigate these phenomena, experiments were designed to measure temperature, suction pressure, and moisture content using thermistors, tensiometers, and a gamma-ray densitometer, respectively, within a test container. The flow of liquid water was monitored using colored dyes injected into the test container. The location of the dyes was recorded periodically with photographs.

The complexity of the early experiments was minimized as much as possible but was increased as our understanding of the phenomena and experimental techniques improved. The first three experiments (Tests 1, 2, and 3) were conducted under isothermal conditions (more precisely, at the fluctuating ambient-temperature conditions) to investigate the processes affecting liquid infiltration and distribution. The latter tests (Tests 4, 5, and 6) were nonisothermal with a temperature gradient imposed across the test containers for investigation of the thermal effect on liquid and gas flow. The media contained in the test containers were comprised of uniform beads (Tests 1 and 2); uniform, bimodally-sized beads (Tests 3 and 4); and uniform, bimodally-sized beads with a superimposed fracture simulated with larger, uniformly-sized beads (Tests 5 and 6).

Similarly, subsequent tests were more focused in scope as the instrumentation and knowledge base improved. For example, nonisothermal boundaries were incorporated into Tests 4, 5, and 6 to provide laboratory-scale data on local heating of pore fluid and gas and liquid convection. A simulated fracture was incorporated into Tests 5 and 6 to help provide information on the effect of matrix/fracture interactions.

4.1.1 Separate-Effect Experimental Apparatus

Experiments were performed using two basic sizes of test containers. Tests 1 through 4 were performed using a 60.5 x 66.0 x 7.6-cm test container (Figure 4-1). A test container of this comparatively large size was initially selected to provide an opportunity to inspect the processes of interest in detail (for example, flow patterns and drying fronts), but its size resulted in several technical difficulties. The large side walls exhibited significant levels of heat loss and temperature fluctuations, and the large interior volume caused difficulties in fabricating a uniform medium, and resulted in prohibitively long times for the processes under investigation to approach steady state.

To alleviate these difficulties, separate-effect Tests 5 and 6 were performed using a smaller test container. The container for Test 5 measured 14.6 x 20.7 x 1.8 cm. Test 6 was conducted in a similarly sized container (15.2 x 20.3 x 5.3 cm); however, the thickness was increased to permit installation of monitoring instruments into the interior of the container and to provide a greater range of the densitometer readings from which to determine moisture content.

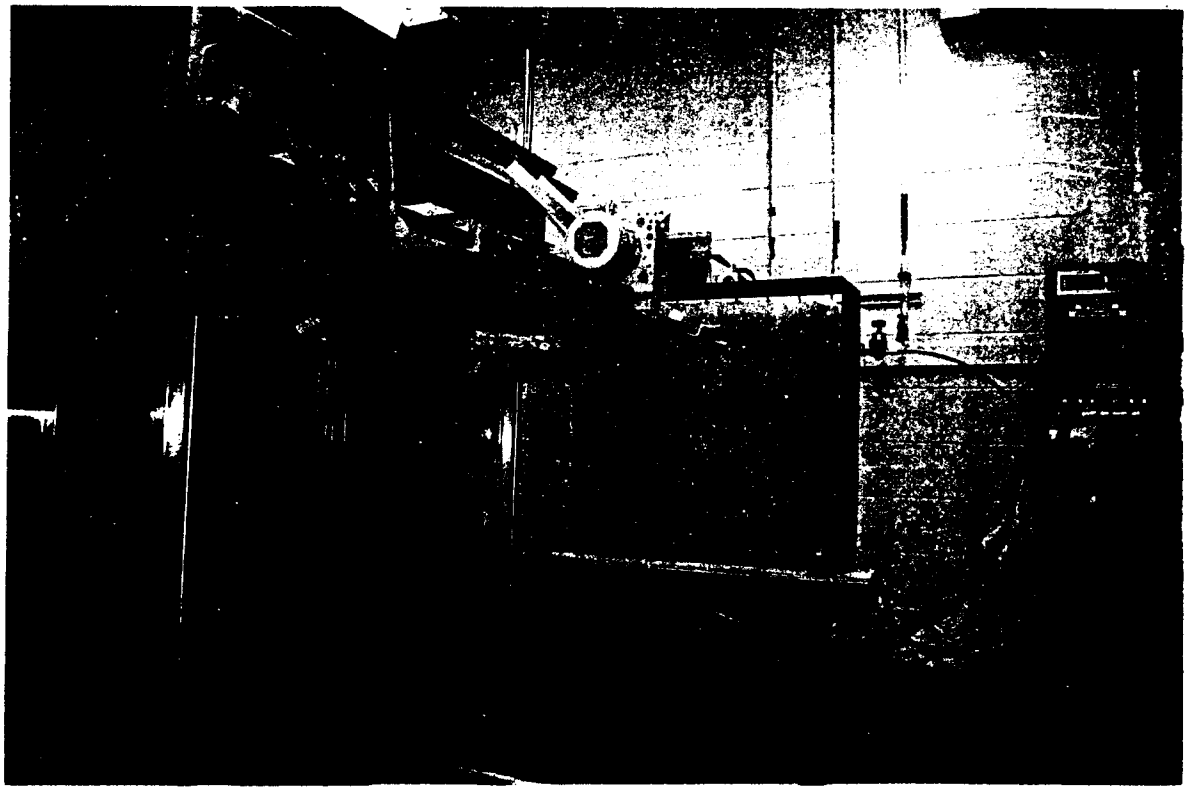

Figure 4-1. Test container used in Tests 1, 2, 3, and 4 - front view

4.1.1.1 Large Test - Container Construction

The two side walls of the large container used in Tests 1 through 4 were constructed of 1.9-cm thick clear acrylic plastic sheets. The four ends were constructed of anodized aluminum. The completed test container was sealed (with the exception of a small vent at the top of a side wall of the chamber to maintain atmospheric pressure) to prevent the loss of water or water vapor during the experiments. The small vent was presumed to not affect the balance of mass in light of the relatively short duration of these experiments.

The two vertical sides of the test container contained heat exchangers for maintaining those boundaries at constant temperatures. Although the first three experiments were conducted under approximately isothermal conditions, the heat exchangers permitted Test 4 to be performed under controlled, nonisothermal conditions.

A series of five tensiometers and seven thermistors was installed into the side of the larger test container for monitoring the suction pressure and temperature, respectively, during the experiment. The configuration of the sensor array is illustrated in Figure 4-2.

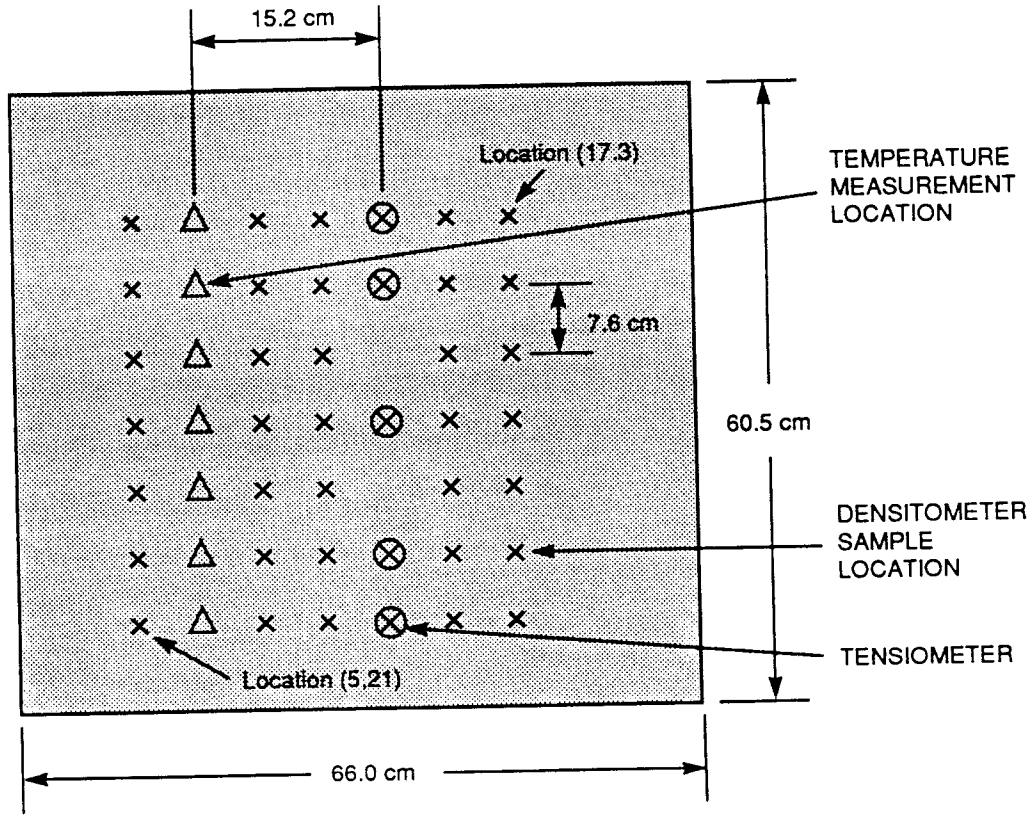

Figure 4-2. Configuration of sensors in the test container used in Tests 1, 2, 3, and 4

4.1.1.2 Small Test - Container Construction

Tests 5 and 6 were performed using smaller test containers. The two side walls were constructed of 1.3-cm thick acrylic plastic for Test 5 and 1.9-cm acrylic plastic for Test 6. A 1.9-cm thick sheet of styrofoam insulation was applied to each side wall of the test container to reduce heat loss and inhibit thermal fluctuations. As in the larger test container, this smaller size test container was also fitted with heat exchangers but in the two vertical sides only. Schematics in Figure 4-3 and 4-4 illustrate the design details of the smaller containers.

Because of the smaller size of the test container used in Test 5, neither temperature probes nor tensiometers were installed through the side walls into the medium. However, a temperature probe was installed into each of the two heat exchangers. The greater thickness of Test 6 permitted the installation of two tensiometers into the interior of the container.

Two ports (one on the left and one on the right, both approximately 2.5 cm from the side heat exchangers at one-third height) were installed in the side walls of the smaller test containers to permit injection of colored dyes into the medium. The outer ends of

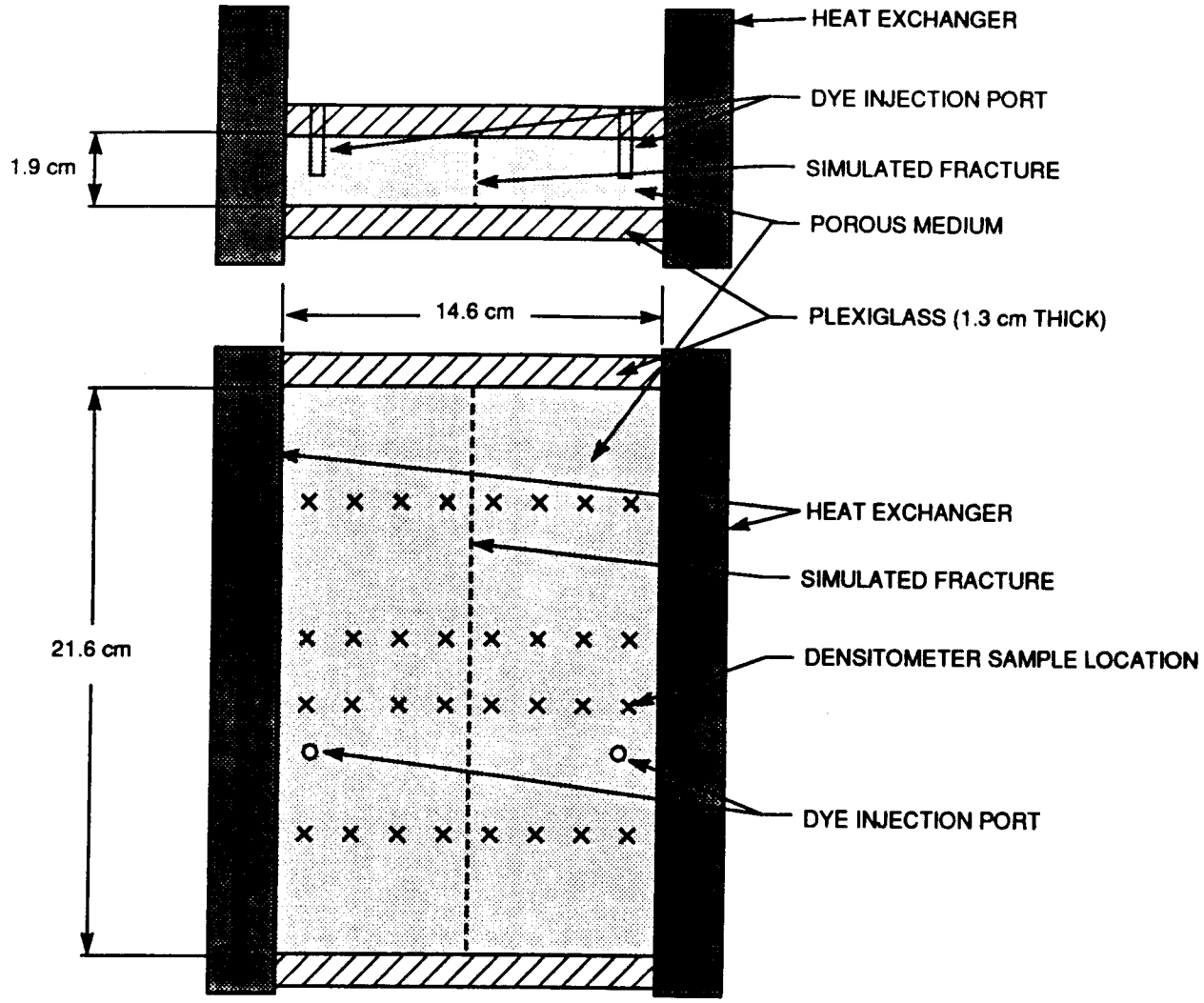

Figure 4-3. Design details with densitometer measurement locations of the test container used in Test 5

the ports were sealed with duct tape after injection to prevent water from moving into or out of the chamber. Additional access ports were installed into the top and bottom ends of the Test 6 container to allow full desaturation and saturation of the media in the container. This permitted baseline saturation measurements of the container with the densitometer after the termination of the experiment.

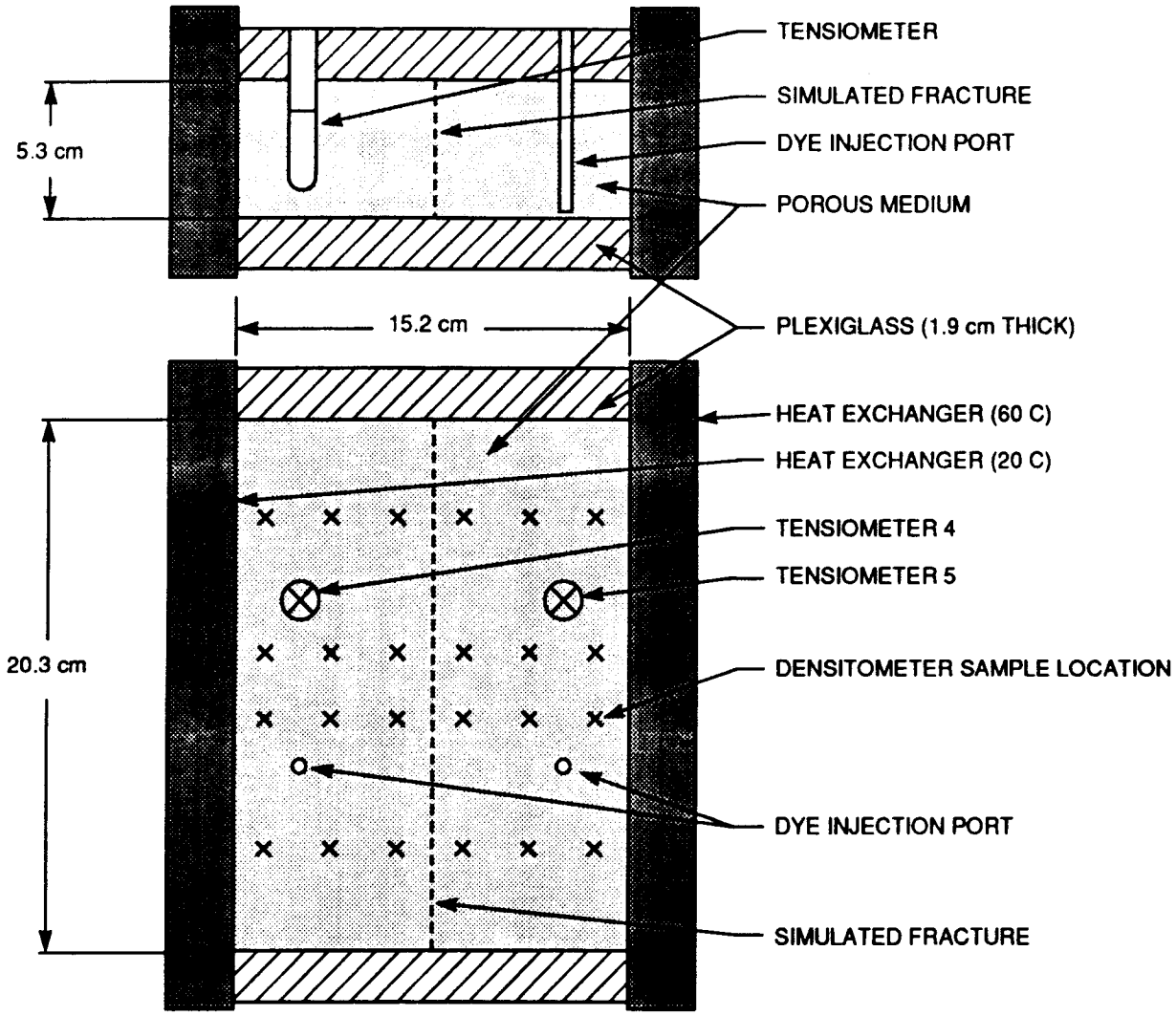

Figure 4-4. Design details with tensiometer and densitometer measurement locations of the test container used in Test 6

4.1.2 Support Equipment

4.1.2.1 Selection and Description

Selection of instrumentation used in the separate-effect experiments was based upon applicability and usefulness of instruments required for specific experiments. Suction pressure was measured during Tests 1 through 4 and 6 using tensiometers. The tensiometers were constructed of 0.95-cm diameter ceramic porous cups connected to pressure sensors (designed for negative gauge pressures of 0 to 3.5 meters of water) using 0.95-cm outer diameter (OD) polyvinyl chloride (PVC) tubing (Figure 4-5). The 140PC Series pressure

sensors, manufactured by Micro Switch, were equipped with an amplifier. The ceramic porous cups, manufactured by Soil Moisture Equipment Corporation, were one-bar high-flow cups. The ceramic porous cups are documented to have a pore size of 2.5 microns and a saturated hydraulic conductivity of 8.6×10^{-6} cm/sec.

The ambient temperature and the temperature within the test containers were measured during the experiments using thermistors. The thermistors are from the 46000 Series manufactured by Yellow Spring Instruments and are specified to be accurate to within 0.51 C over the range of interest (0 to 100 C).

A gamma-ray densitometer was used to measure density contrasts which were then used to calculate the moisture content in the separate-effect experiments. In Tests 1 through 4, a gamma-ray densitometer (Texas Nuclear, Model 9700D) was used with an ionization tube detector and a gamma-ray source of 500 millicuries of ^{137}Cs. In Tests 5 and 6, an ^{241}Am stabilized NaI scintillation detector (Ludlum Measurement Model 44-14) equipped with a stabilized gamma counter/scaler single-channel analyzer (Model 2200-1) was used with the same gamma source for the densitometer measurements. Styrofoam insulation was added to the detector during Test 6 to help reduce densitometer measurement fluctuations due to temperature variations. The gamma-ray densitometers in all tests were attached to a planar traversing table for scanning of the entire test chamber, thus leaving the test container stationary during the experiment. The traversing system had a location precision error of less than 0.4 mm in both the X and Z directions. The densitometer began and terminated each scanning sequence by recording the number of gamma-ray counts that penetrated through stationary aluminum blocks located at the edge of the chamber. The detection counts recorded prior to and subsequent to each scanning sequence were used to quantify instrument drift that may have occurred during the course of the experiment. The locations of the gamma-ray attenuation measurements collected during Tests 5 (32 locations) and 6 (24 locations) are illustrated in Figure 4-3 and 4-4, respectively.

The data produced by the experiment were collected using a data acquisition system (DAS) which included a multiplexer (HP3458A), a multimeter (HP3488A) and a traversing system controller (VELMEX 28351). The operation of the DAS was controlled by an IBM PS 2/80. Operational tasks conducted by the DAS included automatic data sampling, conversion of raw data to engineering units, control of the densitometer traversing system, data logging, data display and data plotting.

4.1.2.2 Instrumentation Modifications

Several components of the densitometer were modified or altered through the course of the experiments. The densitometer was originally designed for pipeline applications. Accordingly, the 500 millicurie source of ^{137}Cs had an incident source beam spread of 14 degrees from the principal direction. The incident gamma rays were collimated using 2.8-cm thick lead shielding with a 3.3 by 3.8-cm square aperture in the facing of the detector.

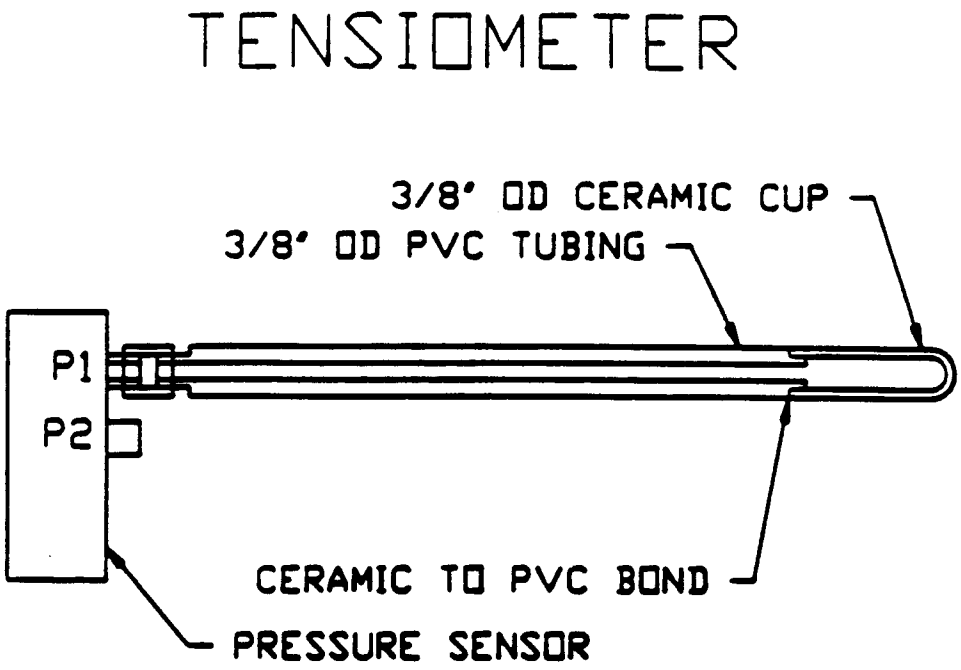

Figure 4-5. Schematic of the tensiometer

Incident gamma radiation from a ^{137}Cs source is attenuated through a medium according to the following approximation:

$$I/I_o = e^{-0.08\rho x} \qquad (4\text{-}1)$$

where I_o is the incident radiation and I is the attenuated radiation. The coefficient, 0.08, is peculiar to ^{137}Cs, which emits gamma radiation with an energy of 0.661 MeV and is approximately valid for both lead and water. The symbol ρ denotes the bulk density, and x is the thickness of the medium through which the gamma rays are attenuated. Therefore, the 2.8-cm thick sheet of lead shielding with density of 11.34 gm/cc absorbed approximately 93 percent of the incident gamma radiation everywhere except at the aperture. Therefore, only those gamma rays which travelled in a straight line from the source, through the porous medium, through the aperture and then struck the detector were measured by the densitometer.

Tests 1 through 4 were conducted using a test container with a width of 7.6 cm. Some portion of the difference in densitometer count rates recorded during these tests at various saturations may be attributed to the change in density of water resulting from temperature variations. The density of water is 0.9982 gm/cc at 20 C and 0.9832 at 60 C for a difference of 1.5 percent (CRC Handbook of Physics and Chemistry, 1982). The associated

change in gamma-ray attenuation for water-density-induced changes in the 7.6-cm thick medium is calculated using Eqn. (4-1) to be 0.3 percent. Changes in gamma-ray attenuation attributed to thermally induced changes in water density are thereby not considered significant. Based on this analysis, semi-qualitative use of the densitometer responses recorded during Tests 1 through 4 is possible.

The original densitometer detector was replaced with a NaI scintillation detector prior to Test 5 to permit greater accuracy in gamma radiation measurements and to provide increased flexibility and ease in operation. Gamma radiation was recorded in terms of the more conventional counts per minute method with the new detector and not according to the arbitrary scaling scheme used in Tests 1 through 4. In order to limit the count of the scattered gamma rays measured by the original detector, a 5.1-cm thick lead shielding with a 0.6 by 0.6-cm square aperture was attached to the facing of the detector. The smaller detector aperture permitted density measurements averaged over a smaller cross-sectional area (0.6 by 0.6 cm) compared to the cross-sectional area of the previously larger sized aperture (3.3 by 3.8 cm). Additionally, the thicker lead shielding at the face of the detector absorbed over 99 percent of the gamma radiation directed at the detector but not at the aperture.

The operation of the densitometer was further enhanced with the installation of a digital interface counter at day 89 of Test 6. The counter was installed in an effort to reduce fluctuations in the recorded densitometer measurements attributable to variations in temperature.

4.1.3 Separate-Effect Experiments

The six experiments conducted as part of Task 2 of the Thermohydrology Research Project are referred to as Tests 1 through 6 and described in this section and summarized in Table 4-1. In Tests 1 and 2, the container was filled with single-sized glass beads. Test 1 was conducted using No. 812 size glass beads, and Test 2 used No. 2740 size beads. The medium in Test 3 and 4 was comprised of a mixture of equal weights of Nos. 1420 and 2740 size glass beads. These bead size numbers are industrial designations to indicate bead size. The smaller the classification number, the larger the bead. Bead size 812 is reported to be sieved between 125 and 177 microns. In similar fashion, bead size 1420 was sieved between 79 and 105 microns and bead size 2740 was sieved between 28 and 53 microns. Results of tests conducted to measure the size of the beads are included in Section 5.1.1.

A medium with a simulated fracture was used in both Tests 5 and 6. The "matrix" medium was comprised of a mixture of equal parts of Nos. 1420 and 2740 size glass beads with a simulated "fracture" comprised of No. 812 size beads. The matrix mixture was premixed with a predetermined amount of water to provide a medium with an approximately uniform saturation of 60 percent. The partially-saturated bead mixture was placed in the upright container through the left side wall that had been removed. The moist mixture was periodically pressed into position during filling. After approximately half of the container was filled with the bead mixture, 2 ml of No. 812 size glass beads (with a factory-reported diameter of

Table 4-1. SUMMARY TO THE SEPARATE-EFFECT EXPERIMENTS

Test	Chamber Size (cm)	Thermal Boundary Conditions	Measurements		Saturation Measurements (Densitometer Measurements)	Mediums
			Temperature Sensors	Pressure Sensors		
1	60.5 x 66.0 x 7.6	isothermal	7 internal 1 ambient	5 internal 1 ambient	7 rows of 5	uniform beads No. 812
2	60.5 x 66.0 x 7.6	isothermal	7 internal 1 ambient	5 internal 1 ambient	7 rows of 5	uniform beads No. 2740
3	60.5 x 66.0 x 7.6	isothermal	7 internal 1 ambient	5 internal 1 ambient	7 rows of 5	Nos. 1420 and 2740 bead mix
4	60.5 x 66.0 x 7.6	right & left - adiabatic a) lower @ 20 C, upper @ 60 C b) lower @ 80,95,105 C upper @ 20 C	7 internal 1 ambient	5 internal 1 ambient	7 rows of 5	Nos. 1420 and 2790 bead mix
5	14.6 x 20.7 x 1.8	upper & lower - adiabatic a) rt @ 20 C, lf @ 60 C b) rt @ 60 C, lf @ 20 C	2 in heat exchanger 1 ambient	1 ambient	4 rows of 8	Nos. 1420 and 2790 bead mix w/ No. 812 fracture
6	15.2 x 20.3 x 5.3	upper & lower - adiabatic a) rt @ 20 C, lf @ 60 C	2 in heat exchanger 3 on side wall 1 ambient	2 internal 1 ambient	4 rows of 6	Nos. 1420 and 2790 bead mix w/ No. 812 fracture

approximately 160 microns) were evenly sprinkled over the exposed medium face. Since the area of the simulated fracture is 39.3 cm^2, the average calculated thickness of the fracture was approximately 500 microns, or an average thickness of approximately three glass beads. The remainder of the chamber was then filled and compacted with the moist glass-bead mixture. After the final end plate of the container was secured in place, the chamber was rotated to its upright position so that the simulated fracture was vertically oriented and the heat exchangers were located on the right and left sides of the container.

4.1.3.1 Test 1

Test 1 was performed during an 11-day period to observe water movement through the No. 812 size glass beads under near-isothermal conditions. A total of 3875 ml of deionized water was injected to fill 37 percent of the void space of the medium. After 8 days an additional 7600 ml of deionized water was added to the test chamber to bring the saturation to 100 percent. A vacuum pump was then used to remove 3065 ml of water. Measured during this experiment were the ambient temperature and barometric pressure, temperature recorded by seven sensors within the test chamber, suction pressures measured relative to the barometric pressure using five tensiometers and moisture content measured with the densitometer (expressed in terms of relative counts).

4.1.3.2 Test 2

Test 2 was performed over a 13-day period to observe water movement through No. 2740 size glass beads under near-isothermal conditions. A total of 1100 ml of deionized water was initially injected to fill 11 percent of the void space of the medium. After 3 days, a total of 5870 ml of water was added to increase the average level of saturation to 68 percent. After 5.5 more days, deionized water was added to bring the level of saturation to 100 percent. A total of 220 ml of water was removed under a vacuum of 2.1 meters of water. The same parameters measured during Test 1 were measured throughout Test 2.

4.1.3.3 Test 3

Test 3 was performed over a 12-day period to observe water movement through a mixture of Nos. 1420 and 2740 beads under isothermal conditions. A total of 2000 ml of deionized water was injected to fill 21 percent of the void space. An additional 7610 ml of water were injected under a hydraulic head of 61 to 91 cm to saturate the medium. A total of 1021 ml of water was extracted from the medium. The same parameters measured during Tests 1 and 2 were measured throughout Test 3.

4.1.3.4 Test 4

Test 4 was performed over a 23-day period to monitor water movement in a partially-saturated medium under nonisothermal conditions. The intact test

container and medium remaining after the termination of Test 3 was used in Test 4. At commencement of the test, the temperature of the top heat exchanger was set at 60 C. The temperature of the lower heat exchanger was maintained at approximately 20 C imposing a temperature gradient of 0.66 C/cm for 3 days after which the direction of the imposed vertical temperature gradient was reversed for the remainder of the experiment. At days 6, 8, and 9 of the experiment, the temperature of the lower heat exchanger was increased to 80 C, 95 C, and 105 C, respectively, while the top heat exchanger was maintained at 20 C. The temperature gradients for these three settings were 1.0 C/cm, 1.2 C/cm, and 1.4 C/cm, respectively. At day 9 and prior to setting the temperature to 105 C, approximately 20 ml of red dye was injected to help visualize the movement of water. At day 15, the constant temperature water bath was turned off but circulation of the fluid continued during the cool-down period. In addition to the parameters measured during Tests 1, 2, and 3, the movement of liquid was monitored during Test 4 using photographs of the injected dye movement.

4.1.3.5 Test 5

Test 5 was performed over a 40-day period to monitor water movement under nonisothermal conditions in a partially-saturated medium with a simulated fracture. The fracture was simulated by emplacing a thin layer (approximately 500 micron thick) of coarse beads (approximately 160 micron diameter) midway in the container. The heat exchangers on the right and left were initially held at 20 C and 60 C, respectively, thus imposing a temperature gradient of 2.7 C/cm. Approximately 2 ml of red dye and 2 ml of blue dye were injected with a syringe into the medium through the right and left ports, respectively, at essentially the same time. After 13 days, the temperatures of the right and left heat exchangers were reversed. As in the previous experiments, ambient temperature and barometric pressure, temperatures at the inlets of the two heat exchangers, and densitometer readings were measured throughout the experiment. Because no tensiometers were installed in the medium during Test 5, suction pressures were not measured.

4.1.3.6 Test 6

Test 6 consisted of a vertically-oriented, two-dimensionally configured test container filled with a uniform mix of glass beads. Similar to Test 5, a vertically-oriented artificial fracture was simulated in the medium by emplacing midway in the container a thin layer of glass beads that were coarser than the bead mix (see Table 5-1, Section 5.1.1). The thickness of this layer was estimated to be about 200 to 400 microns. The temperature of the right vertical boundary was held at 60 C, and the left vertical boundary was set at 20 C. The front and back vertical walls were constructed of clear plexiglass to permit visual inspection of the medium for the duration of the experiment. Tensiometers were installed at two locations in the container. Two ports permitted the introduction of dye as a tracer of liquid water flow. Thermistors were attached to the two vertical-boundary heat exchangers and to the test container at three locations. The test medium was initially saturated at an average of 65 percent. The moisture was redistributed by gravity drainage under isothermal conditions for approximately six days after the container was turned upright prior to initiation of the heating segment of the

test. The duration of the test was 120 days of which 99 days were the heating phase and 15 days were a cool-down phase.

Variables measured during Test 6 were temperature, barometric pressure, suction pressure, and moisture content (indirectly measured using a gamma-ray densitometer). Barometric pressure was measured at ambient conditions. Temperature was measured for the ambient condition, at the two heat exchangers and at three locations located equidistant along the lower back of the plexiglass side wall. Suction pressures were measured at two locations in the test container using tensiometers. Gamma-ray measurements were made at 24 locations (four rows of six measurements) in the test container to provide input for moisture content calculations and at 2 locations in aluminum blocks for baseline measurements. Additionally, dye was injected into the container at two points to indicate the direction of liquid water flow. A schematic of the test container dimensions and locations of the measurements is illustrated in Figure 4-4.

4.2 THERMOHYDROLOGICAL EXPERIMENTS

The first test in the next phase of experimentation, coupled-process thermohydrological experiments, has been started. This test, designated as Test 7, is a continuation of the series of two-dimensional experiments that were conducted as part of the scoping portion of the research project and as part of the separate-effect experiments.

The complexity of the experiments, starting with the initial scoping experiments and progressing through the separate-effect experiments and presently with the thermohydrological experiments, has been systematically increased. The complexity has increased to the point that the coupled effects of flow through partially-saturated, fractured porous media under nonisothermal conditions are being investigated for various geometries. Earlier experiments attempted to isolate individual processes or phenomena for evaluation.

Experiments that are two dimensional in scope have proven to be amenable to observation using instrumentation and measurement techniques currently available. In the two-dimensional experiment performed as part of this research project, gamma-ray densitometry has been a useful technique to measure density differences and infer changes in moisture content from these measurable differences. The series of two-dimensional experiments has continued because useful and insightful information has been provided and also because similarly useful data are not reasonably obtainable from experiments conducted at three dimensions using the currently available technology.

The design of Test 7 is similar to Test 6 and earlier tests. In essence, Test 7 consists of a vertically-oriented, two-dimensionally configured test container filled with a uniform mix of alumina powder. The alumina powder was sieved between 100 and 325 mesh (150 to 45 microns) to provide a controlled uniform medium. The size of the Test 7 container is 15.2 by 15.2 by 6.6 cm, which is shorter (5.1 cm) and slightly thicker (1.3 cm) than the Test 6

container. A schematic of the test-container dimensions and locations of the measurements is illustrated in Figure 4-6.

Alumina powder was used to avoid difficulties resulting from the dissolution of silica and bead degradation associated with the glass beads used in previous experiments. As was demonstrated in earlier tests, the prolonged duration of the thermohydrological tests, especially under nonisothermal conditions, can result in degradation of the medium, thus introducing additional unknowns into the experiment. Hopefully, use of alumina beads will eliminate degradation of the medium.

Although the entire medium in this experiment is uniform, future experiments, including Test 8, are being designed to contain a simulated or actual fracture. A fracture has not been incorporated into the design of Test 7 purposely to permit an examination of fluid movement not affected by a simulated or actual fracture. Results from Test 8, which will incorporate a fracture, will be evaluated against Test 7 results to assess the effect of the fracture.

The temperature of both the left and right vertical boundaries of the container in Test 7 has been held constant at 20 C. A point heat source held constant at 60 C has been placed in the mid-level right portion of the test container. The heat source actually spans the entire short dimension of the container. Therefore, even though it is a finite-length line source in the container, it is designed as a point source in the two-dimensional configuration. The temperature of the heat source may be raised during later stages of the experiment.

The front and back vertical walls of the container were constructed of clear plexiglass to permit visual inspection of the medium for the duration of the experiment. Tensiometers were installed at six locations in the container. Unfortunately, one of the tensiometers in the Test 7 container was damaged during start-up and does not appear to be functional for this experiment. Five ports permit the introduction of dye as a tracer of liquid water flow. Thermistors were attached to the two vertical-boundary heat exchangers and to each of the six tensiometers, thereby providing temperature measurement at a total of eight locations in the test container.

The gamma-ray densitometer will again be used to measure changes in density of the test container. The moisture content of the medium will be calculated from the density measurements in a procedure similar to that used in the evaluation of data collected during Test 6. Gamma-ray densitometer measurements will be recorded at a total of 96 locations during Test 7. This increase in measurement locations will provide greater resolution in moisture-content values than was available in earlier tests. Gamma-ray measurements will also be made of a stationary aluminum block prior to and subsequent to each set of gamma-ray measurements to permit removal of instrument drift during the course of the experiment. Instrument drift resulting from thermal and barometric fluctuations has been detected during previous experiments.

Variables measured during Test 7 are temperature, barometric pressure, suction pressure, and moisture content (indirectly measured using a gamma-ray densitometer). Barometric

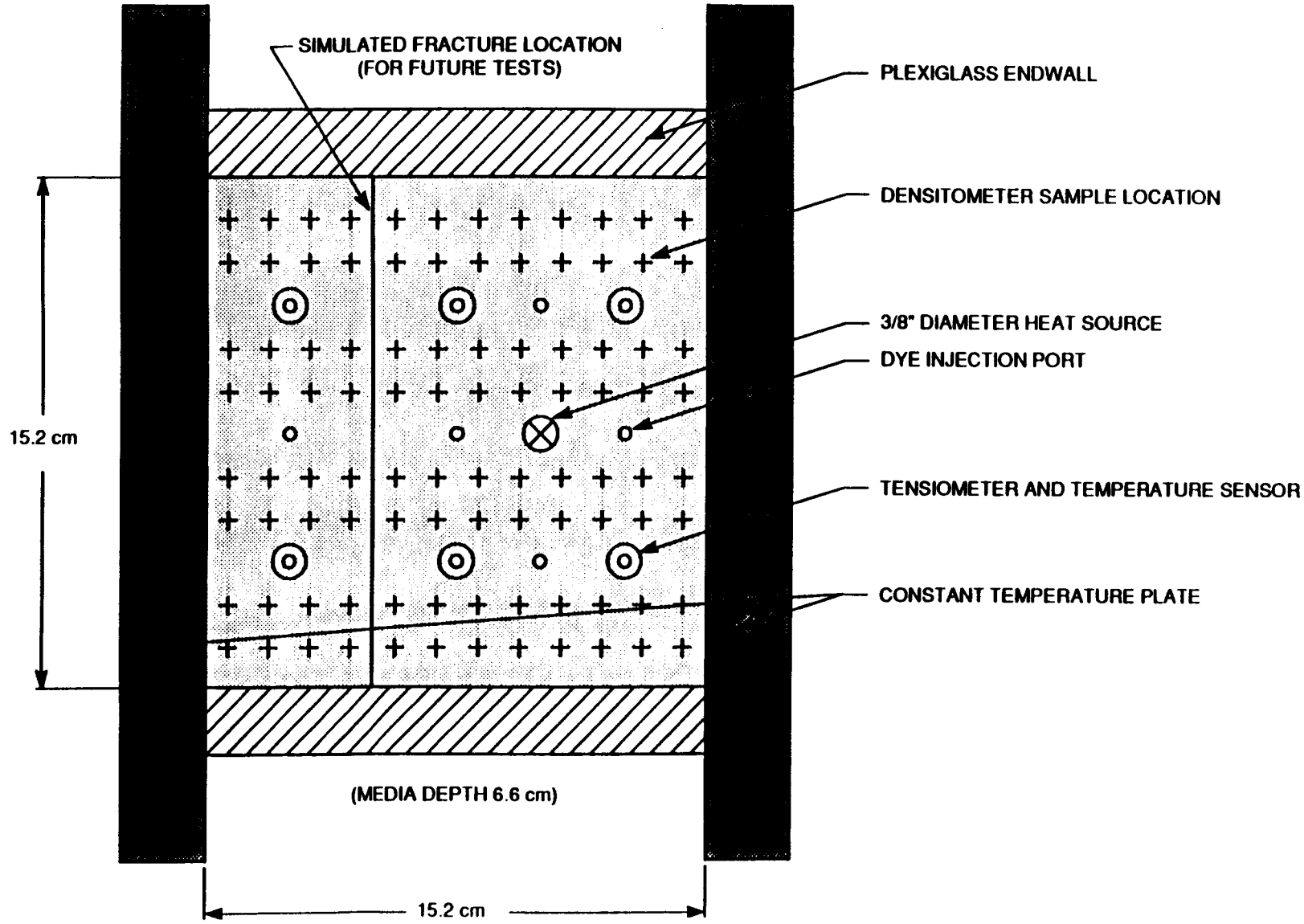

Figure 4-6. Schematic of Test 7

pressure and temperature are measured at ambient conditions. All measurements will be collected using an automated data acquisition system. Additionally, dye is being injected into the container at six points to indicate the direction of liquid water flow. Photographs of the dye are periodically taken through the clear plexiglass side walls to help ascertain and document liquid water movement.

The test medium was initially saturated at 75 percent. The total duration of Test 7 is not precisely known at this time but is anticipated to be similar to Test 6, which ran for about 120 days.

5 THERMOHYDROLOGICAL EXPERIMENTAL RESULTS

The results of the laboratory-scale experiments conducted as part of this research project are presented in this section. Section 5.1 contains the results of experiments that were designed to measure the experimental media characteristics (e.g., bead size, porosity, and hydraulic conductivity). The results of the separate-effect experiments are summarized in Section 5.2.

5.1 EXPERIMENTAL MEDIA CHARACTERISTICS

Industrial-grade, silica-glass beads were selected for use as the test media in the preliminary separate-effect experiments to avoid heterogeneity inherent to natural media and to have control over material properties. The values of media characteristics were either measured, when possible, or estimated. The bead media were characterized according to diameter, porosity, and hydraulic properties, as described in this section. Calculations and measurements of the characteristics evaluated during the execution of the six separate-effect experiments are included in these descriptions.

5.1.1 Bead Size Calculations

Three different bead sizes, factory designated as Nos. 812, 1420, and 2740, were used in Tests 1 through 6. The No. 812 size beads were factory-sieved between 125 and 177 microns; the No. 1420 size beads were factory-sieved between 74 and 105 microns, and the No. 2740 size beads were factory-sieved between 28 and 53 microns. Population and volume grain-size distribution statistics were measured at SwRI using a Colter counter for the three different bead sizes. Population statistics are calculated per bead and volume statistics are calculated per volume. The grain-size distribution characteristics for the beads are summarized in Table 5-1.

5.1.2 Porosity Measurements

Total porosity was measured for the various-sized, glass-bead media used in this investigation. The porosities of the bead media were primarily calculated from the volume and weight of the water content. Porosity was also checked during measurement of the media characteristics and during the execution of the separate-effect experiments.

The No. 812 size beads had a volumetric porosity of 37.2 percent and a porosity by weight of 37.1 percent. The No. 1470 beads had a porosity by volume of 38.1 percent and a porosity by weight of 37.7 percent. The smallest sized beads, No. 2740 size, had a volumetric porosity of 37.6 percent and a porosity by weight of 37.8 percent.

The porosity by volume of the No. 812 size beads was calculated during the moisture characteristic curve experiments to be 36.1 percent. Similarly, the porosity measurement was 34.8 percent for the No. 2740 size beads, and 31.4 percent for a 50 percent by weight mixture of the Nos. 1420 and 2740 bead sizes. The porosity by volume

Table 5-1. GLASS-BEAD DIAMETER STATISTICS

		Population Statistics				Volume Statistics			
Bead-Class No.	Sample #	Mean (μm)	Standard Deviation Log_{10} (μm)	Median (μm)	Coef. Variation %	Mean (μm)	Standard Deviation Log_{10} (μm)	Median (μm)	Coef. Variation %
812	160-1	130.27	1.46	140.09	1.12	159.54	1.40	162.61	0.88
812	160-2	134.95	1.46	143.51	1.08	171.25	1.42	175.79	0.83
1420	80-1	82.24	1.46	88.19	1.77	106.59	1.41	108.60	1.33
1420	80-2	89.42	1.46	96.31	1.64	114.64	1.40	116.90	1.22
2740	40-1	58.84	1.43	62.81	2.44	78.90	1.51	78.45	1.91
2740	40-2	58.97	1.44	63.00	2.43	79.49	1.52	78.91	1.91

measurements made during the separate-effect Test 3 was 31.7 percent for the Nos. 1420 and 2740 bead mix. The porosity measurements are summarized in Table 5-2.

5.1.3 Hydraulic Conductivity Calculations

A moisture characteristic curve was determined for the bead mix used in Tests 3 through 6 using the porous plate technique specified in ASTM D 2325 ("Capillary-Moisture Relationships for Coarse- and Medium-Textured Soils by Porous-Plate Apparatus," ASTM, 1977). A positive-pressure, porous-plate apparatus, referred to as a Tempe cell, was used to incrementally increase gas pressure on the medium and calculate the amount of water retained in the pores of the medium at those pressures. Consequently, only drying curves were determined using this procedure.

TABLE 5-2. BEAD POROSITY MEASUREMENTS

Bead Class	Porosity Type	Porosity (percent)	Calculation Method*
812	volumetric	37.2	1
812	weight	37.1	1
812	volumetric	36.1	2
1470	volumetric	38.1	1
1470	weight	37.7	1
2740	volumetric	37.6	1
2740	weight	37.8	1
2740	weight	34.8	2
1470/2740	volumetric	31.7	3
1470/2740	volumetric	31.4	2

* 1 denotes measurement was made during bead size calculations;
2 denotes measurement was made during moisture characteristic curve experiment;
3 denotes measurement was made during a separate-effect experiment

The capillary-moisture relationship for the Nos. 1420 and 2740 size bead mixture is illustrated as a water-retention curve in Figure 5-1. Measurement of pressures greater than 41 kPa were attempted but were not successful because a pressure seal failed at the higher pressure. Also illustrated in this figure is a nonlinear regression line that approximates the observed data. After the data for the capillary-moisture relationships were measured, the van Genuchten parameters were calculated by regressing a curve to the collected data and determining the parameters using the regressed line (van Genuchten, 1978). The van Genuchten parameters calculated from the regression line are a value of 0.759 for α, a value of 7.38 for β, and a residual water content value of $S_r = 0.03$.

The unsaturated hydraulic conductivity was calculated using the closed-form solution of van Genuchten (1980) [Eqn. (A-59)] and the above mentioned values for α, β and the residual water content. These values are plotted versus negative pressure head in Figure 5-2. The Mualem-based restriction of $\lambda = 1 - 1/\beta$ was assumed in these calculations.

5.2 SEPARATE-EFFECT EXPERIMENTS RESULTS

The tests were conducted, in part, to examine separate effects of thermohydrological processes and also to develop viable experimental procedures to meet the objectives of the experimental portion of the project. Accordingly, information gained during the conduct of the earlier tests was used to advance the development of subsequent tests. As a consequence, the more recent tests provide a more comprehensive level of information than do the earlier tests. Accordingly, results from earlier tests will be discussed in cursory fashion while an in-depth analysis is conducted on the results from Tests 5 and 6, the most recently conducted experiments.

The separate-effect experiments were conducted in laboratories that did not have a controlled environment, consequently the ambient temperature and barometric pressure fluctuated throughout the duration of the tests. A total ambient temperature fluctuation of 8 C and barometric pressure fluctuation of about 0.2 meters of water were recorded. The fluctuations in the ambient temperature were directly reflected in the temperatures recorded in the test container, although the temperatures recorded in the container relative to the ambient temperatures demonstrated slightly smaller fluctuations (approximately 5 C) during Tests 1, 2, and 3 and even less during the nonisothermal tests (Tests 4, 5, and 6).

5.2.1 Test 1

During the initial water injection event, the injected water spread vertically in a circular pattern away from the point of injection until it reached a diameter of about 15 cm. The water then flowed downward until it reached the bottom of the test chamber where it started to spread laterally toward the edges of the test container. The water in the initial 15 cm diameter region visually appeared to become redistributed slightly over the next few days by migrating toward the bottom of the test container. These observations correlated positively with

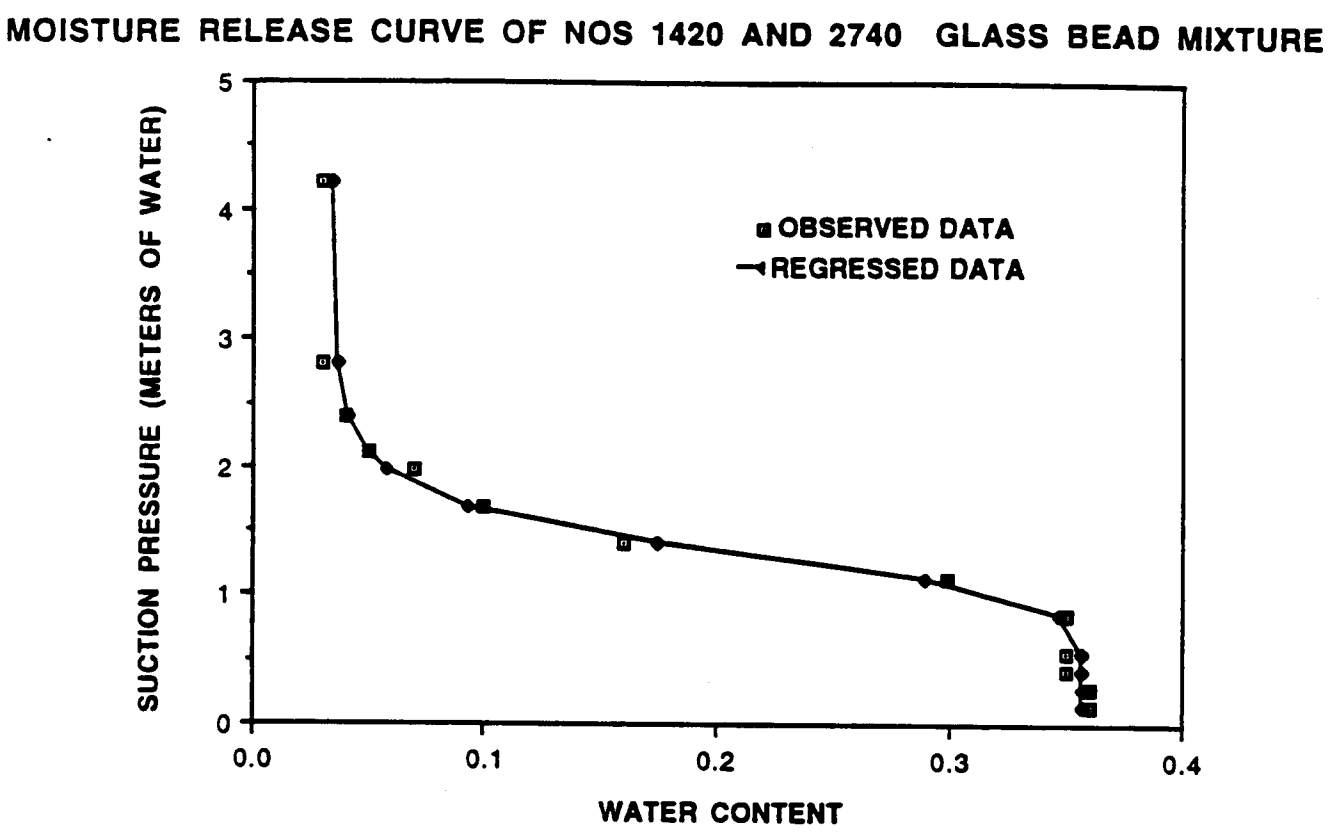

Figure 5-1. Moisture-release curve for Nos. 1420 and 2740 glass-bead mixture

the measurements recorded with the densitometer which measured lower densities in regions with lower saturation.

During desaturation at day 10 in the test, the free surface of the water was observed to drop as the water was removed. Measurements made with the densitometer indicated that in regions above the observed free surface, the pore space in the medium was nearly unsaturated and the pores below the free surface were close to full saturation.

Tensiometers 4 and 5 dried out during the eighth day of the test and had to be refilled with water. Tensiometers 1, 2, and 3 were located in the saturated portion of the media and recorded suction pressures of about -0.35 meters of water. Tensiometers 4 and 5 were initially in the dry region, and suction pressures of -3.5 meters of water were recorded at both

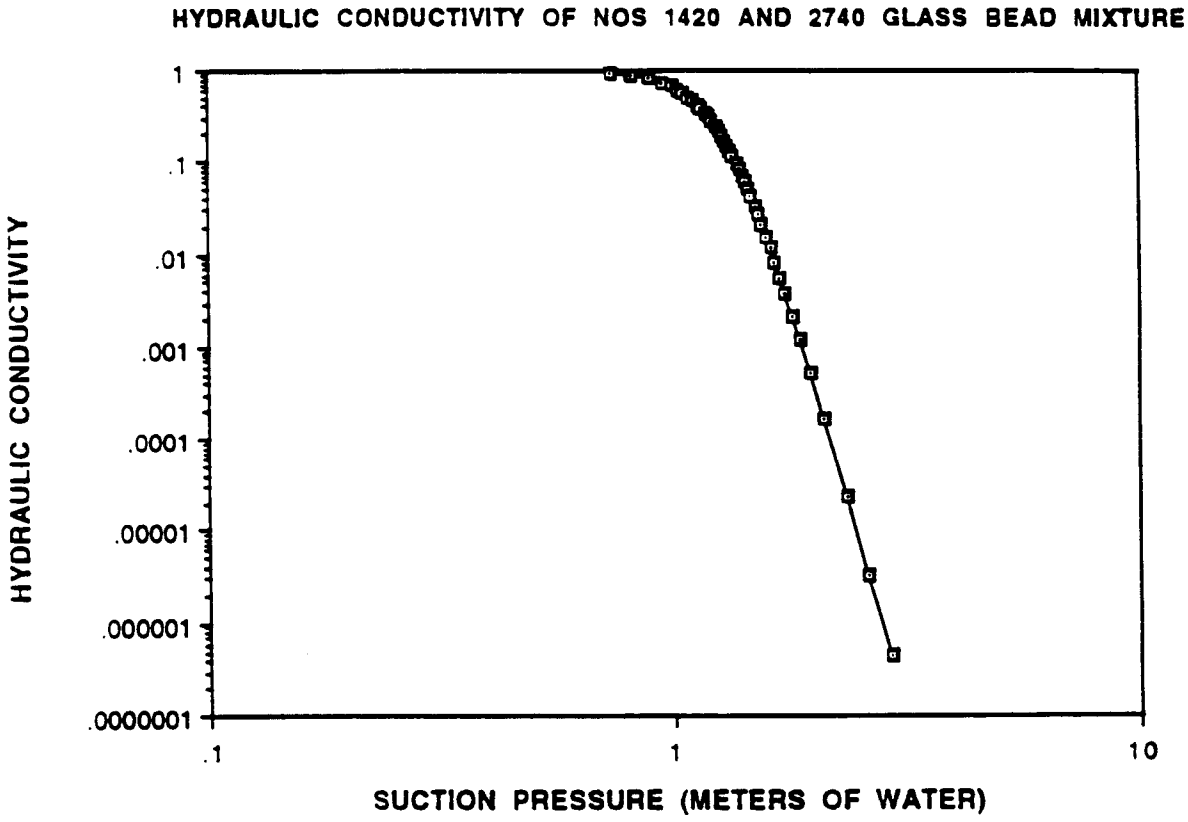

Figure 5-2. Calculated hydraulic conductivity curve for Nos. 1420 and 2740 glass-bead mixture

locations. Full scale for the sensors is -3.5 meters of water; therefore, negative pressures greater than -3.5 meters of water may have been present but were not detected by these sensors.

The tensiometer readings reflected the vertical difference in their positions with an approximate 0.07 meters of water difference for each 7.6-cm change in elevation. Measurements from tensiometers 4 and 5 did not indicate that the pores in the upper portion of the test chamber became desaturated during the removal of water in day 10 of the experiment.

5.2.2 Test 2

The initial injection of water was not readily accepted by the medium even though there was a positive head of 91 cm of water in the infiltration water column. This slow acceptance of water is attributed to the high air-entry pressure of the medium or to a possible impediment in the flow path at the point of injection. The initial water injection uniformly infiltrated the medium in a radial pattern relative to the point of injection.

The second injection of water was more readily accepted by the medium. A downward component in water movement became apparent as the moisture content of the medium was increased. A slight settling of the medium, noticed during the second injection, was manifested with a vertically-oriented, fault-like offset approximately 10 cm from the side of the chamber. The offset occurred in a region that had not yet been wetted by the infiltrating water. During infiltration, the offset acted as a barrier to water flow. Water did not infiltrate into media on the dry side of the offset until the water had advanced to the lower plate, moved laterally past the offset and then moved upward into the dry portion.

The tensiometers were initially filled with water when water was injected into the medium. The tensiometers that were located in the dry portions of the test container (tensiometers 4 and 5) remained at -3.5 meters of water (the full-scale negative output of the sensor) until the upper portion of the chamber became saturated, at which time the pressure increased to -1.4 meters of water. The response of tensiometer 1 at the base of the container was initially -3.5 meters of water, but gradually increased to -2.1 meters of water as water infiltrated into this region. Tensiometers 2, 3, and 4 were initially located in a wet region with suction pressures of about -1.4 meters of water. After the medium was fully saturated on day 10, the suction pressure decreased at these three locations to a point that positive pressures were recorded for a brief period. A slow leak in a thermistor connection allowed some water to escape with the result that pressure in the container decreased over the course of the day.

5.2.3 Test 3

The movement of moisture responded to gravity during this isothermal experiment. The decrease in water content at the upper portion of the visible water pattern concurred with decreased densitometer readings; however, the densitometer measurements were not quantitatively significant.

5.2.4 Test 4

Temperature and moisture content measurements collected during Test 4 concurred, in general, with the imposed boundary conditions. Temperature measurements were used to indicate that internal temperature fluctuations and thermal losses through the side walls were excessive. The densitometer measurements indicated the trend of moisture contents; but the actual measurements, as in the earlier tests, were not quantitatively significant. However, the general trend of the densitometer readings was sufficiently pronounced to indicate a change in moisture content in response to the changed temperatures at the boundaries.

5.2.5 Test 5

The movement of the colored dyes proved to be the most useful information collected during Test 5. Although general moisture-content trends can be made using the densitometer measurements, the resolution of the densitometer measurements was not sufficient to provide quantitatively significant data for evaluation purposes.

Shortcomings of the densitometer method used in Test 5 were the narrow depth of the test chamber, the effect of thermal and barometric fluctuations on the densitometer detector, and minor density differences in water attributable to temperature. The most significant of these shortcomings was the narrow depth (1.9 cm) of the test chamber. Since the porosity of the Nos. 1420 and 2740 glass-bead mix used in Test 5 was about 34.8 percent; at full saturation of the medium, water would only constitute about 0.6 cm of actual thickness. Therefore, the densitometer would be required to resolve minor quantities of total water for the water-content measurements to be significant. This proved to be beyond the capabilities of the densitometer used in this experiment.

The movement of water vapor was not monitored in this experiment. Movement of the colored dyes visually displayed liquid-moisture movement within the medium. As observed with the dye, the fabricated fracture had a pronounced effect upon the flow paths of water in the medium. In particular, liquid water had little movement across the fracture as evidenced by the dyes. Two flow cells were created whose boundaries were comprised of three sides of the test chamber and the fabricated fracture. Upon commencement of the experiment, the direction of the water flow was downward along the face of the heat exchanger until arriving at the lower end of the test chamber, then toward the interior of the chamber. This movement may have been due in part to gravity forces acting upon the localized higher moisture content at the point of injection.

Movement of water across the induced fracture was not noted until late in the test when the half of the medium near the higher temperature heat exchanger visibly began to dry and the medium on the other side appeared to be wetter. Some movement of the red dye (and presumably some water) was observed crossing the fracture when the moisture content of the cooler half of the medium became high enough to wet the pores of the larger pored fracture. The movement of the dye is illustrated in photographs taken at 7, 14, and 23 days into the test (Figures 5-3 through 5-5).

5.2.6 Test 6

Plots of ambient barometric pressure and temperature, suction pressures, heat exchanger plate temperatures and temperatures recorded along the back outside surface of the plexiglass side wall are given in Figures 5-6 through 5-9. As illustrated in Figure 5-6, the ambient temperature varied by almost 10 C, and the barometric pressure varied by approximately 0.34 kPa. Variations in temperature and barometric pressure had an effect upon the detector portion of the gamma-ray densitometer. The effect of the variation in temperature was mitigated by encapsulating the detector first in insulation and later in a constant temperature thermal jacket. However, the effect of variations in ambient pressure on the densitometer detector, were not as easily remedied.

The graph of tensiometer measurements illustrates changes in the suction pressures versus time (Figure 5-7). Tensiometer 4, located near the cooler boundary, recorded essentially constant suction pressures until the time the right boundary heat exchanger was

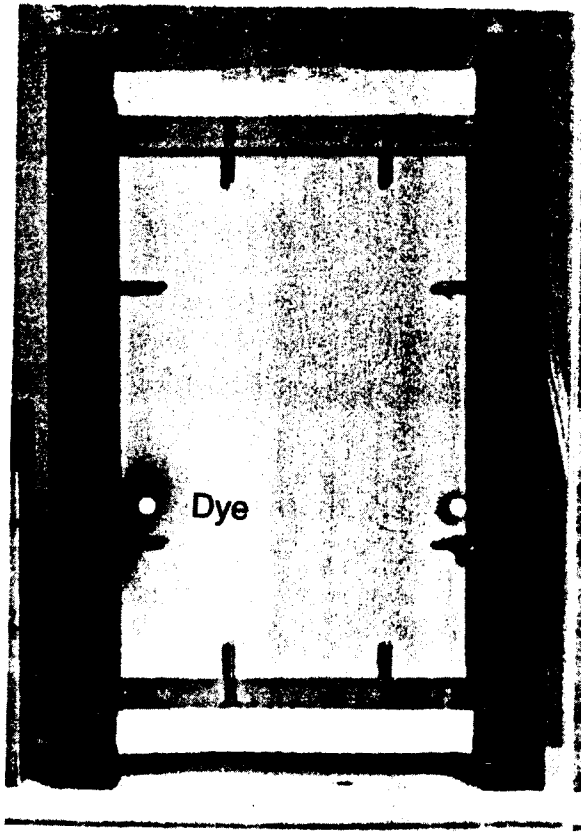

Figure 5-3. Photograph of test chamber at day 7 of Test 5

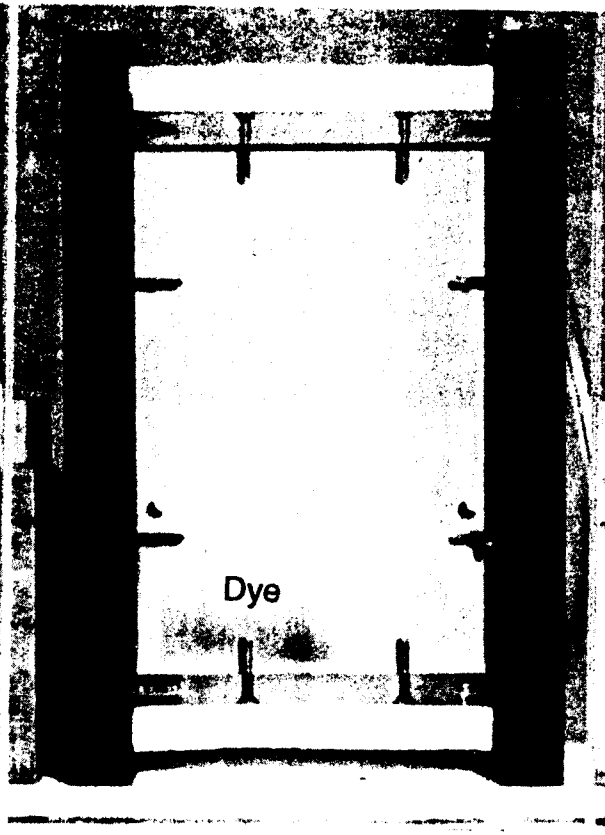

Figure 5-4. Photograph of test chamber at day 14 of Test 5

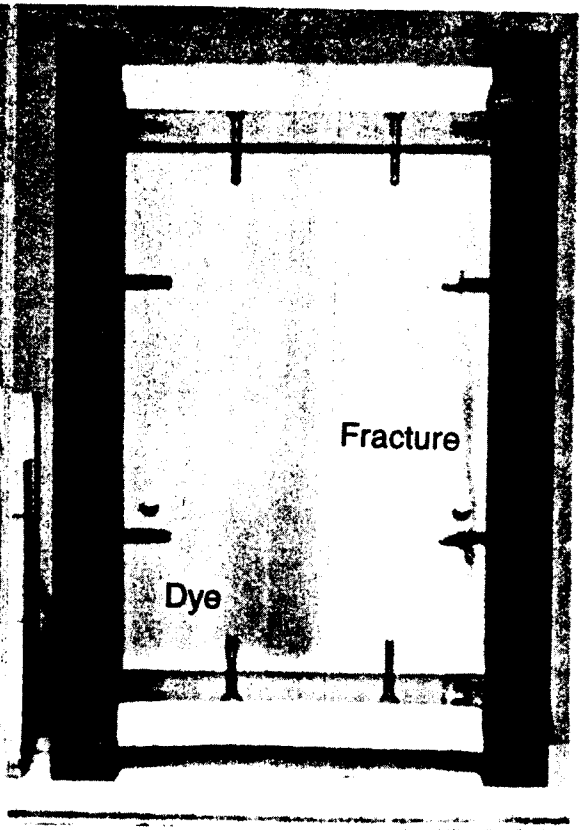

Figure 5-5. Photograph of test chamber at day 23 of Test 5

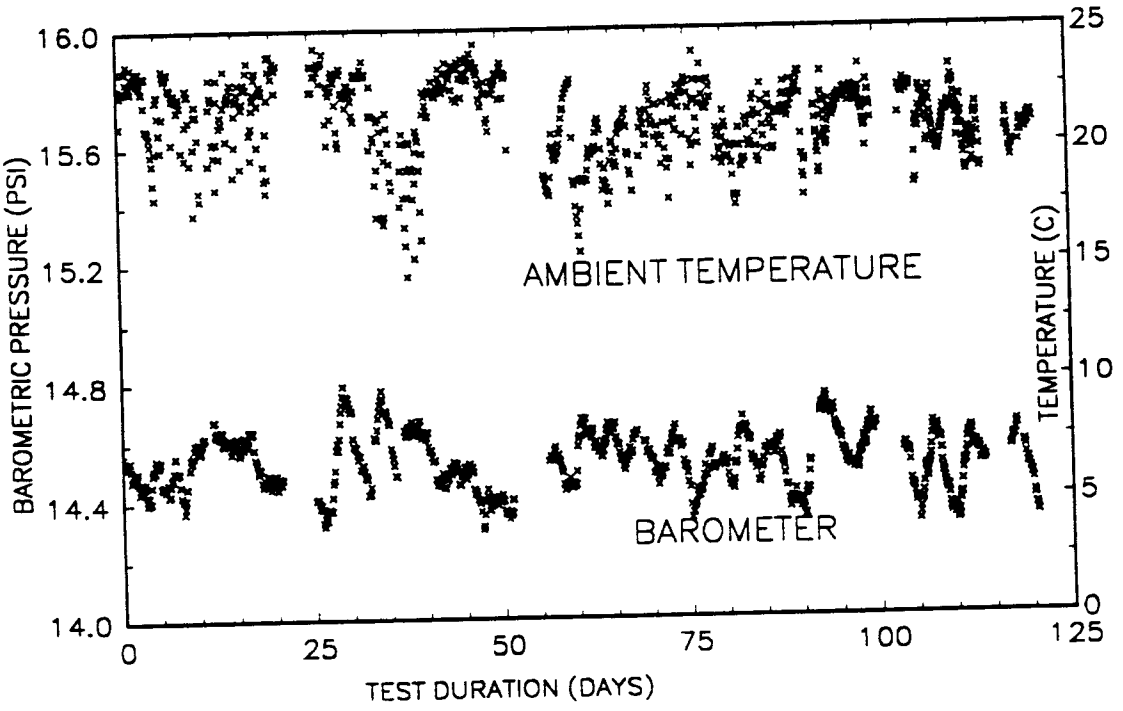

Figure 5-6. Plot of ambient barometric pressure and temperature during Test 6

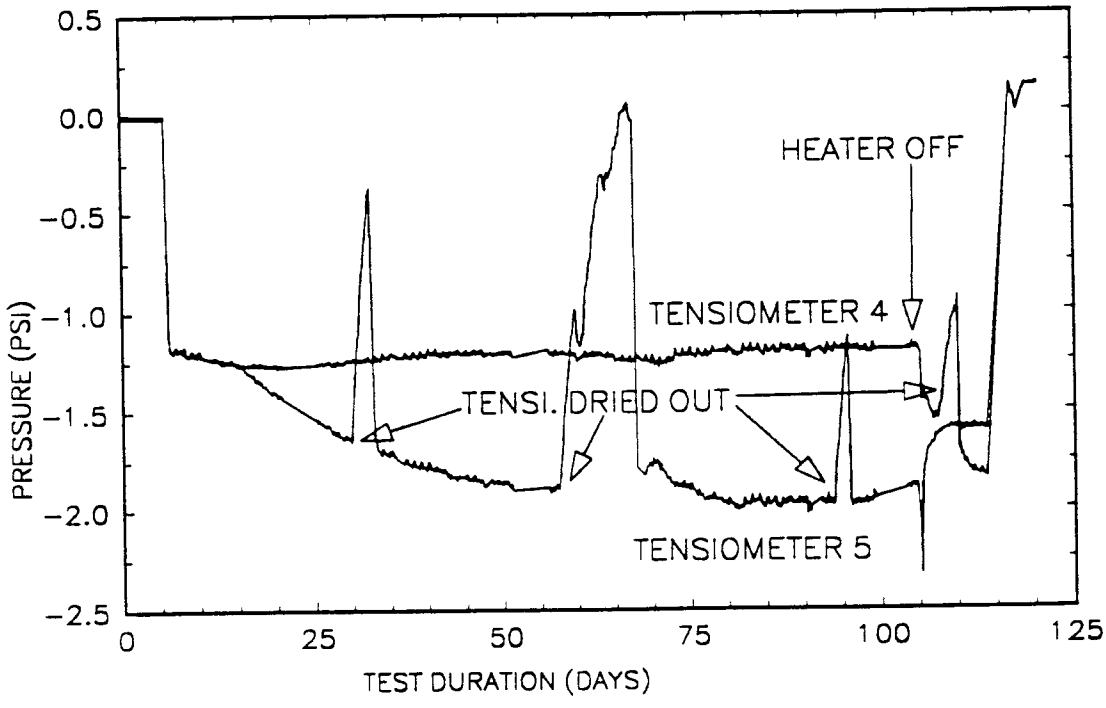

Figure 5-7. Plot of suction pressure during Test 6

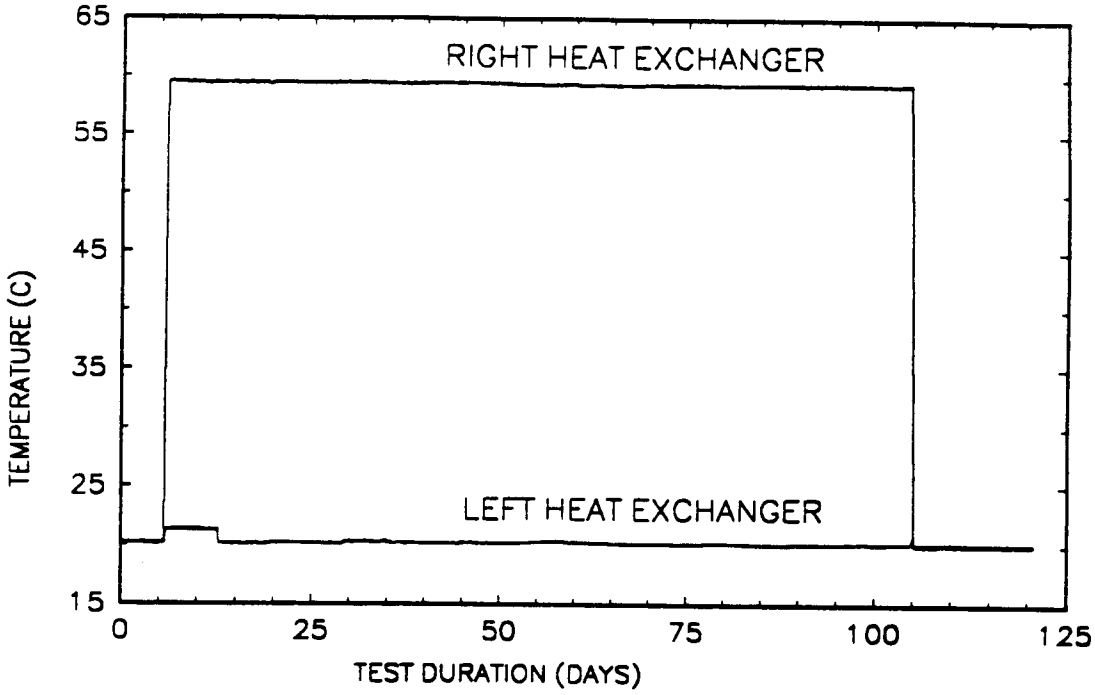

Figure 5-8. Plot of heat exchanger plate temperatures during Test 6

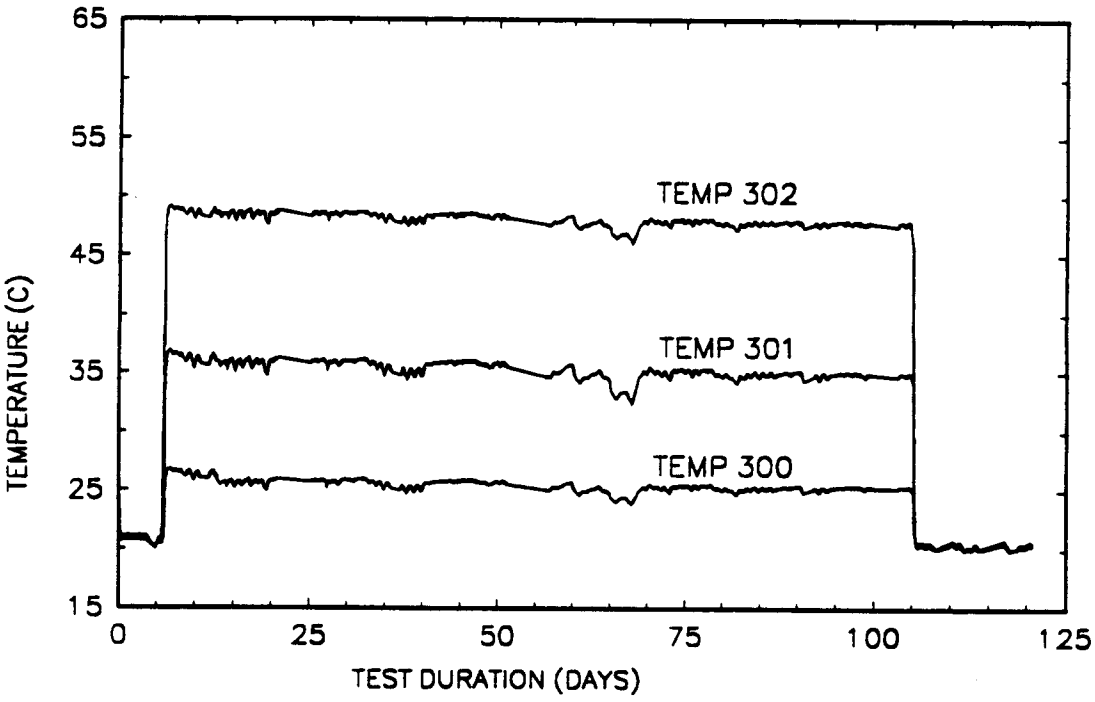

Figure 5-9. Plot of temperatures recorded during Test 6 along the back outside surface of the plexiglass side wall but inside the insulation

allowed to return to the ambient temperature. Tensiometer 4 dried out once late in the experiment and had to be refilled with water. Tensiometer 5 was located near the higher temperature heat exchanger. Tensiometer 5 dried out three times during the course of the experiment and had to be refilled with water. These events are labeled on Figure 5-7.

Tensiometer 5, located near the heated boundary, measured an increase in suction (negative pressure) shortly after the test started. This observation concurred with the presumption that the saturation content of the heated portion of the container medium became drier as water vaporized and moved toward the cooler portion of the medium where it recondensed. The suction at tensiometer 5 continued to increase (except for periods when the tensiometer dried out) through about day 80 of the test. A slight decrease in suction is detectable from about day 95 through day 105, indicating that (i) the test had not yet attained steady state even after over 100 days of activity and (ii) the decrease in suction means an increase in saturation content. This increase in saturation was not expected, and an explanation is being sought through modeling.

The trends of measurements of both tensiometers behaved in similar fashion at the time the heater was turned off. At that time the suction at each of the two tensiometers rapidly increased (within several hours at tensiometer 5 and within about a day at tensiometer 4) by about 0.35 kPa of water, then rapidly decreased. Tensiometer 5 decreased by about 0.5 kPa of water and then asymptotically approached a suction of about 1.0 kPa of water. Tensiometer 4, however, continued to increase suction (except for a period when the tensiometer dried out) until the time when the container medium was saturated at the end of the test. Tensiometer 4 eventually (near the 115th day of the test) increased suction to a level (about 1.25 kPa of water) that was greater than that recorded with tensiometer 5 (about 1.0 kPa of water), and it appeared that the recorded suction at this point would increase slightly more before stabilizing. It is not obvious what could cause the suction on the cooler side to increase to a higher value than the heated side.

6 THERMOHYDROLOGY EXPERIMENT MOISTURE CONTENT MEASUREMENTS

6.1 TEST 5

The sensitivity of the densitometer to changes in moisture content in the Test 5 test container medium has been evaluated. The thickness of the medium in Test 5 was 1.9 cm. Therefore, for a total porosity of 35 percent, the average cumulative thickness of pore space through the container would be 0.66 cm. The container was scanned with the medium at zero saturation with a response of approximately 130,000 counts per minute (cpm). At full (100 percent) saturation, the response was approximately 122,400 cpm for a difference of about 7,600 cpm between readings at zero and 100 percent saturation, which represents a total change of 5.8 percent.

A portion of the difference in count rates measured during Test 5 is attributed to the change in density of water resulting from temperature variations as in Tests 1 through 4. The change in gamma-ray attenuation resulting from thermally-induced density differences was calculated to be 0.1 percent. Therefore, changes in gamma-ray attenuation for Test 5 attributed to thermally-induced changes in water density are not considered significant.

Variations in the recorded responses at fixed saturation levels were observed to be approximately 2,000 cpm. This variation is attributed to thermal drift in the densitometer, gamma-count probabilistic uncertainty, and other unidentified causes. Therefore, even though the variation in measurements is only 1.5 percent of the total count rate, the magnitude of the variation is roughly one-fourth of the response attributed to changes in saturation from fully dry to fully saturated. It was concluded that, due to the small thickness of the test medium in the experiment, gamma-ray measurement noise was too great to justify the quantitative use of the unrefined densitometer responses recorded during Test 5. The semi-quantitative analysis of densitometer measurements, however, does provide useful insight of Test 5.

6.2 TEST 6

All densitometer measurements were normalized relative to measurements which were taken of an aluminum block (standard 1 - a 3.8-cm thick block) prior to the densitometer measurements taken of the test container. Direct densitometer measurements of the aluminum block and an example of the resulting normalized measurements are given in Figures 6-1 and 6-2, respectively. Figure 6-1 illustrates the densitometer measurements taken through the 5.08-cm thick aluminum block (standard 2). Figure 6-2 illustrates the densitometer measurements taken through the 5.08-cm thick aluminum block after they were normalized by dividing each measurement by the measurement from the 3.8-cm thick aluminum standard. Additionally, there appears to be a slight reduction in gamma count fluctuations after installation of the digital interface counter at day 88.9 that was added in an effort to reduce fluctuations attributable to variations in temperature. As indicated in the figure, erroneous data resulted when aluminum standard 2 was inadvertantly moved at day 105.

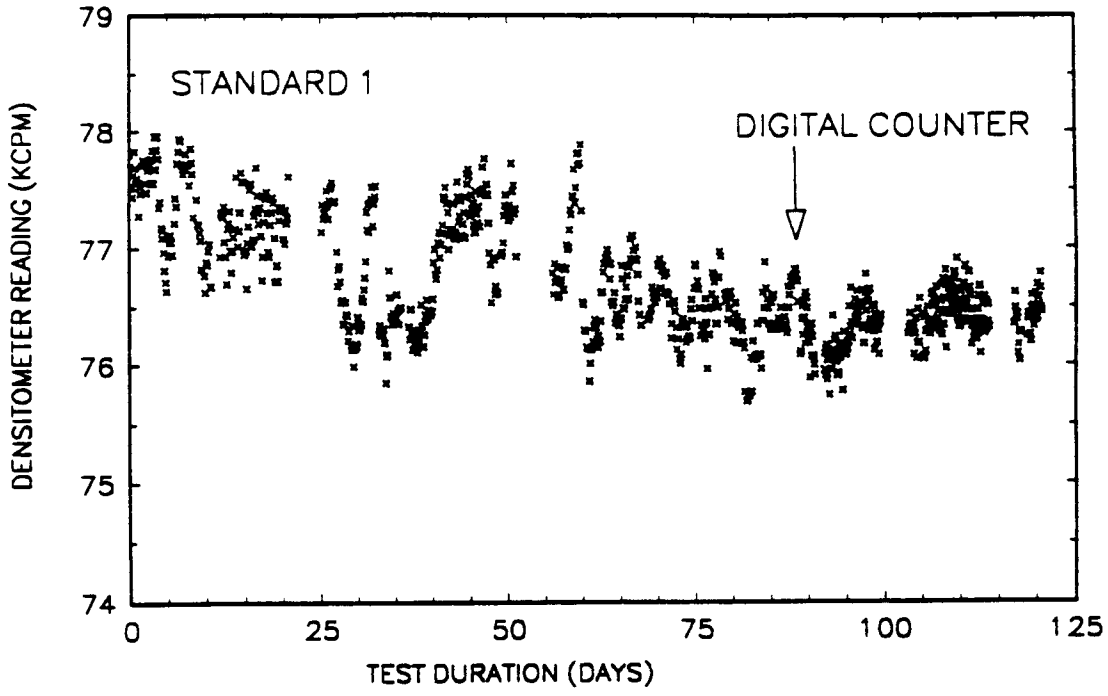

Figure 6-1. Densitometer measurements of 5.08 cm aluminum block

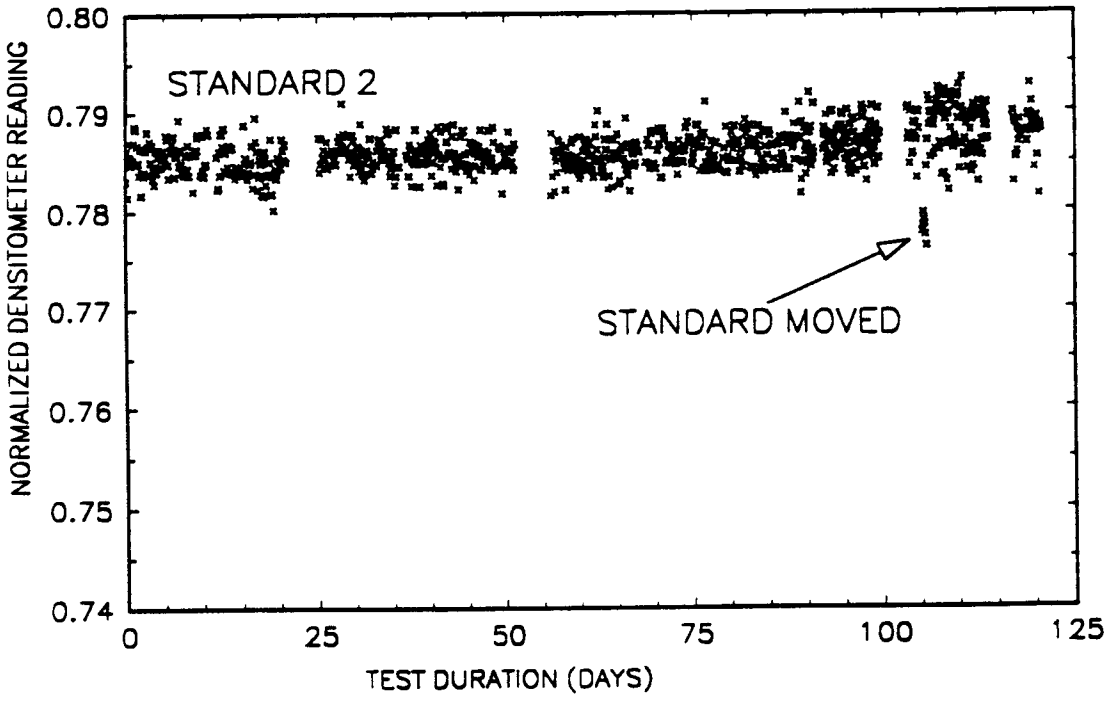

Figure 6-2. Normalized densitometer measurements of 5.08 cm aluminum block

Figures 6-3 and 6-4 illustrate normalized densitometer measurements for two positions in the container located at 5.5 inches from the left side and 6.5 or 4.5 inches from the top, respectively. The positions of measurement are denoted as (5.5,6.5) and (5.5,4.5) respectively and were very close (1.27 cm) from the right (60 C) heat-exchanger plate. The normalized values can be considered as relative counts with a decrease in the normalized count indicating an increase in moisture content. Little change in the moisture content calculated at the point (5.5,4.5) was detected from the time the container was placed in an upright position at day 0, to the time the heater was turned on at day 6, and through the first 50 days of the test. A change was detected after day 50 as the local moisture content increased through day 90 and then dried out. At day 105 the heater was turned off, and the local moisture level increased.

The normalized densitometer measurement at (5.5,6.5) (Figure 6-3) exhibited the same trend as the measurements at point (5.5,4.5). However, the maximum in moisture content at point (5.5,6.5) occurred more quickly, at day 65, than the maximum at point (5.5,4.5), which was observed to occur at day 90. Based on the densitometer data and visual evidence from the front of the container, the lower right corner of the test medium appeared to became noticeably drier. Associated with this drier area was an adjacent area of higher moisture content. The wetter area was located on the cool side of the demarcation line at the leading edge of the noticeably drier area. After the demarcation line, or front, progressed and the beads started to dry out, the measured water content decreased as indicated by the densitometer measurements. Water returned to the dried region only after the heater was turned off.

In an attempt to quantify the moisture distribution in the medium during the test, the normalized densitometer measurements were used to calculate moisture content at each measurement location. Plots were generated by averaging all the normalized densitometer measurements collected over a 1-day period (typically between 7 and 13 measurements per day). These averages were then converted into a saturation value by the following method.

(1) The initial normalized densitometer measurements were assigned a saturation value of 65 percent (day 1 average measurements). Recall that the medium was initially uniformly saturated at 65 percent. However, assigning all day 1 measurements a saturation of 65 percent was based on the assumption that no significant draining occurred during the first day after the container was placed in an upright position.

(2) The densitometer measurements at day 119 (after the medium was saturated) were assigned a saturation value of 100 percent, I_w.

(3) The dry (0-percent saturation) densitometer count, I_d, and the saturations of interest were calculated using the Beer-Lambert relation (Moore, 1963):

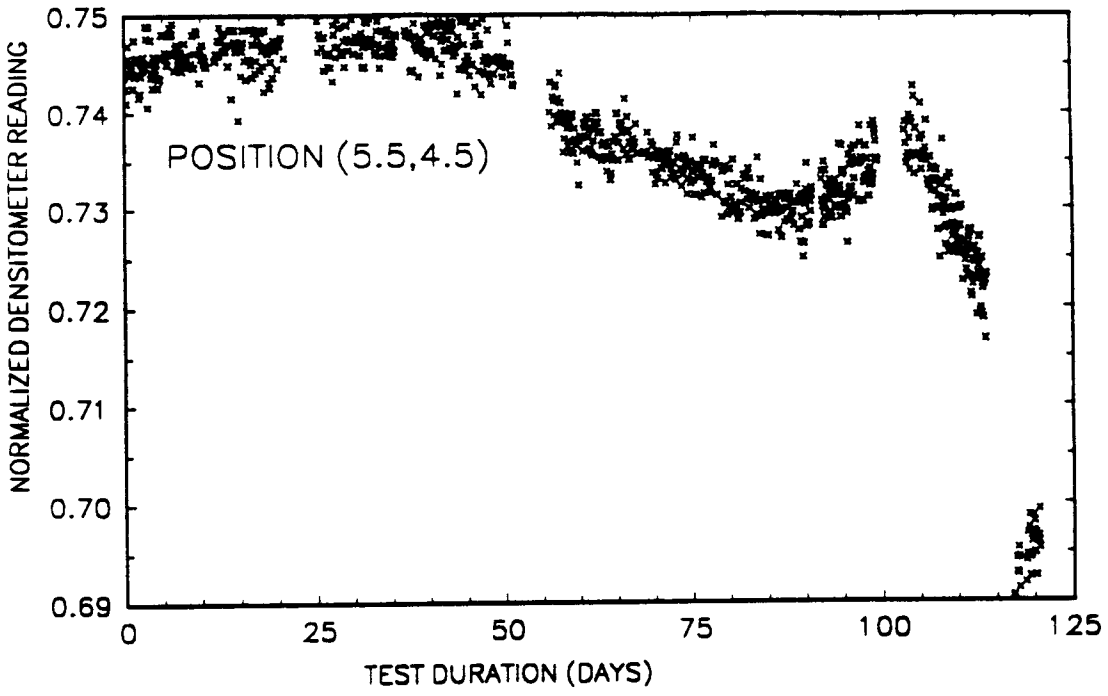

Figure 6-3. Normalized densitometer measurements at location (5.5,4.5)

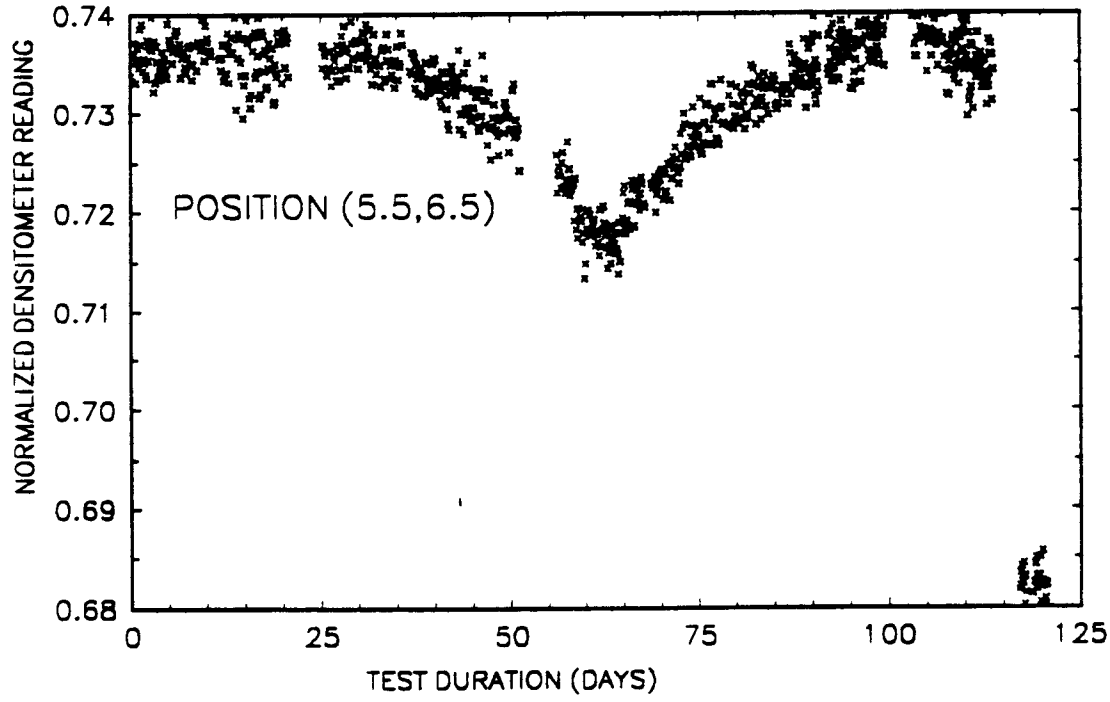

Figure 6-4. Normalized densitometer measurements at location (5.5,6.5)

$$\text{Saturation} = \frac{\ln (I_d / I)}{\ln (I_d / I_w)}$$

where I is the densitometer count of the point where saturation is to be calculated.

A second method was used to check the calculated saturation levels because the measured counts at some of the densitometer sampling locations near the top of the container did not indicate the expected change when the medium was saturated. It is possible that these locations were not fully resaturated when measured. The second method was as follows.

(1) The initial normalized densitometer measurements were assigned a saturation value of 65 percent (day 1 measurements). (Same assumption as first method.)

(2) The medium thickness (w) was assumed to be 5.3 cm; and the bead void fraction was assumed to be 0.35, resulting in an equivalent "thickness" of water in the medium of 65-percent saturation of 1.2 cm.

(3) Saturation was approximated using the following exponential attenuation formula (Gray, 1972):

$$\text{Saturation} = \frac{\frac{1}{(\frac{\mu_0}{\rho})\rho}\ln(\frac{I}{I_{65}}) + X_{65}}{w\phi}$$

where

μ_o	=	linear attenuation coefficient [1/m],
(μ_o/ρ)	=	mass attenuation coefficient [m^2/kg],
w	=	media thickness [m],
X_{65}	=	equivalent water thickness at 65-percent saturation ($X_{65} = w\ \phi\ S_l$) [m],
I	=	densitometer count for specified time [gamma-rays], and
I_{65}	=	densitometer count for specified time with initial 65-percent liquid saturation and no heating [number of gamma-rays detected].

The results of the second method were in close agreement (within 0.5-percent saturation) to the first method over the range of interest (approximately 58 to 82 percent) indicating the methods are consistent but not necessarily accurate, in an absolute sense.

As stated, results from these calculations were contingent upon the initial saturation value calculations assigned to the densitometer measurements taken during day 1 of Test 6. Densitometer measurements used in the day 1 saturation calculations were averages of all

measurements taken during the first day of the test. Although the average of measurements taken during the first day were uniformly assigned a saturation of 65 percent, subsequent analysis suggests significant redistribution of water occurred by the time the later measurements were taken. However, this day-long averaging technique was necessary to provide gamma-ray densitometer measurements with less fluctuation. Use of densitometer measurements from only one sampling had unacceptably high levels of fluctuation to be used in saturation calculations. Assignment of saturation levels which incorporate liquid redistribution due to gravity drainage is currently being evaluated.

Contour plots of liquid saturation calculated using the densitometer measurements at three separate days during the test (days 25, 75, and 113) are presented in Figures 6-5 through 6-7. These saturation values are estimates based upon the above mentioned methodology. The plots were obtained by spline fitting the saturation estimates and plotting equi-saturation contours using the resulting spline fits. The spline fit procedure smoothed the data, so care must be taken when interpreting the plots. Because of the smoothing routine, the precision suggested in the contour intervals is beyond the precision of the gamma-ray densitometer.

A significant saturation gradient appears to have formed between the heated wall and the fracture at later times with saturation greatest near the wall then decreasing toward the fracture. This saturation gradient is most severe close to the heated wall, but also relatively large in the area near the heated side of the fracture. The local minimum between the heated plate and the fracture is greatest at day 75 as compared to days 25 and 113.

The moisture gradients are considerably more apparent by day 75, as seen in Figure 6-6. The saturation values seen on the contour plot range from approximately 55 to 72 percent. A distinct saturation gradient is detected along the fracture. Because the data presented in these plots are from a sparse data set (24 points per set) smoothed with a cubic-spline, the gradual gradient between the sampling points on either side of the fracture could potentially be more closely approximated by a step function.

The drying front in the lower right-hand corner became apparent in the saturation plots by 113 days (Figure 6-7). It appeared that a surplus of water accumulated in front (to the left) of the drying front. Although this phenomenon is not entirely understood at this time, it appears that the moisture content is greatest ahead of the drying front, as the front advances away from the heated boundary. Furthermore, the majority of the saturation gradient was on the right side of the fracture. Another interesting feature was the decreased saturation level on the left side of the fracture by day 113 as compared to day 75. The saturation in the lower left corner decreased from 74 percent on day 75 to about 59 percent on day 113. These phenomena are not consistent with the physical theory presented in Section 2.2.

The initial trend in moisture content change appeared to be an accumulation of water on the left (cooler) side of the fracture after heating started. The trend reversed, however, as the test progressed; the left (cooler) side of the fracture subsequently became depleted in moisture. The dye-tracer data confirmed this, as the dye injected near the cooler heat exchanger initially

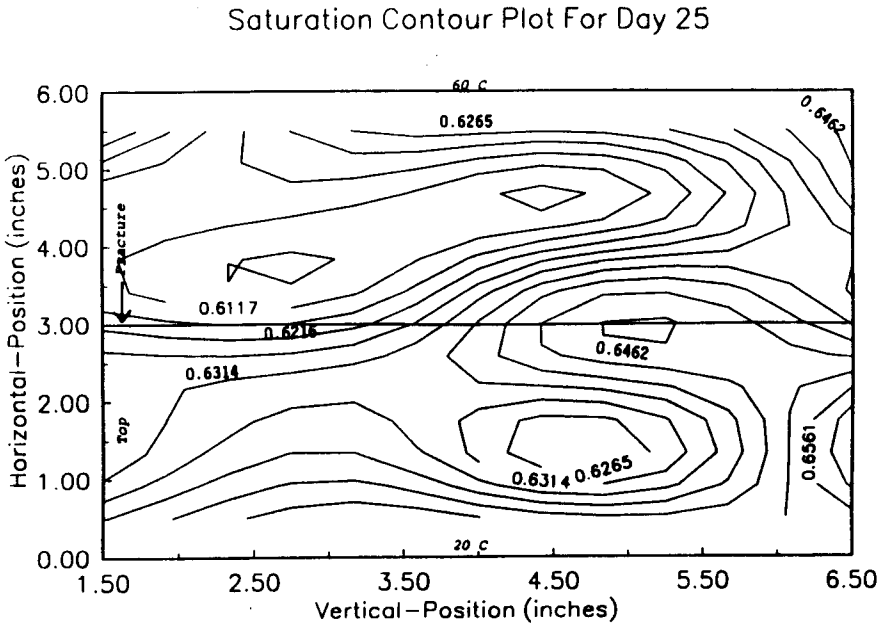

Figure 6-5. Saturation contour plot at day 25 of Test 6

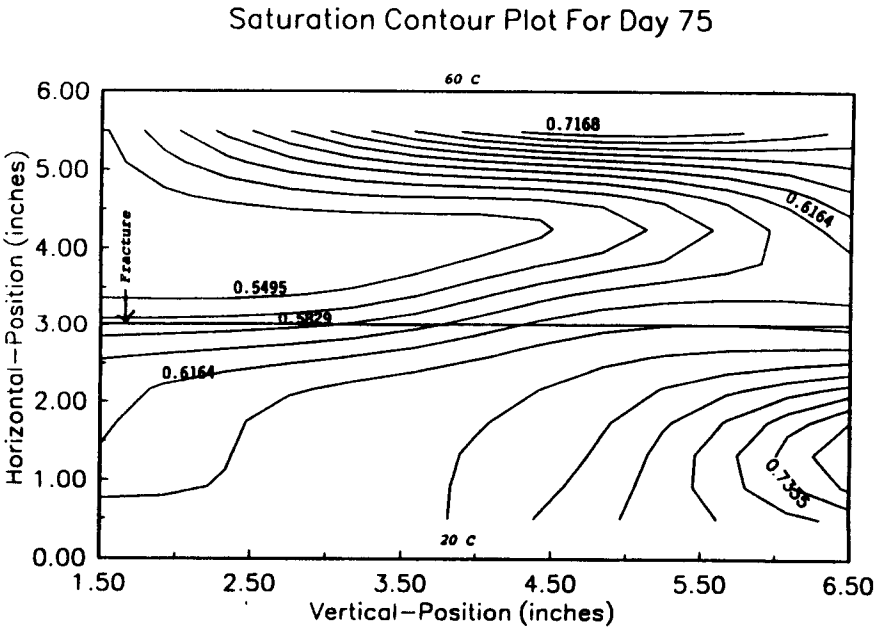

Figure 6-6. Saturation contour plot at day 75 of Test 6

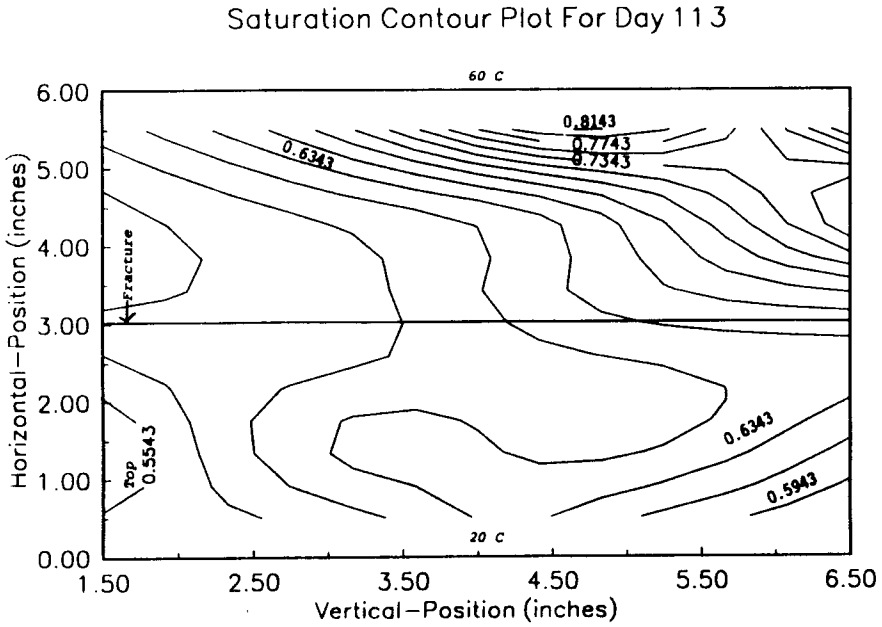

Figure 6-7. Saturation contour plot at day 113 of Test 6

moved upward. By day 75 the upward movement stopped, and the dye began to move downward toward the fracture along the bottom of the container.

Vector plots of suction pressures were prepared from moisture-saturation measurements collected on days 25, 75, and 113 of Test 6 to gain additional insight of fluid movement. To determine suction pressures from moisture content or saturation values, van Genuchten's equation (van Genuchten, 1978),

$$S=(1-S_r)\left[\frac{1}{1+|\alpha\psi|^{\beta}}\right]^{1-\frac{1}{\beta}}+S_r\ , \qquad (6\text{-}1)$$

was solved for suction pressure as follows:

$$\psi = \frac{1}{\alpha}\left[\left(\frac{S}{1-S_r}\right)^{\frac{\beta}{1-\beta}} - 1\right]^{\frac{1}{\beta}} \qquad (6\text{-}2)$$

where ψ is suction pressure, α and β are the van Genuchten parameters, and S is the degree of saturation. The subscript r denotes residual. Note that isothermal conditions are assumed in this expression.

The van Genuchten parameters were determined in the laboratory using a positive-pressure experiment conducted with a Tempe cell (Section 5.1.3). Since the medium tested using the Tempe cell was the same as that in the Test 6 container, the measured van Genuchten parameters for calculating the suction pressures from saturation should be appropriate.

Two sets of vector plots have been prepared from the results of Test 6. Figures 6-8 through 6-10 illustrate vector plots of the suction pressure gradient at 25, 75, and 113 days, respectively. Figures 6-11 through 6-13 illustrate the gradient of the total of pressure and pressure resulting from the changes in elevation, at the same time intervals (up is toward 1-5 on the vertical scale).

Interesting pressure regimes are illustrated in these vector plots. As presented in both vector plots at 25 days (Figures 6-8 and 6-11), there was no obvious effect by the heated boundary upon water potential at this time in the experiment. The effect of gravity, however, appeared to dominate the potential of liquid water. Based on this illustration and inherent in the stated assumption, significant time (greater than 25 days) was required for the moisture in the container to attain equilibrium with respect to gravity. This observation will be evaluated in greater detail in Chapter 7.

The effect of gravity is still apparent at 75 and 113 days, but the effect of the heated vertical boundary is also manifested. Even at the end of the experiment (day 113), the effect of the heated boundary upon suction pressure is apparent only within about 3 to 5 cm from the heated boundary, except along the lower boundary where thermal effects upon suction pressure approach the midpoint of the container (about 6 to 7 cm) (Figure 6-13).

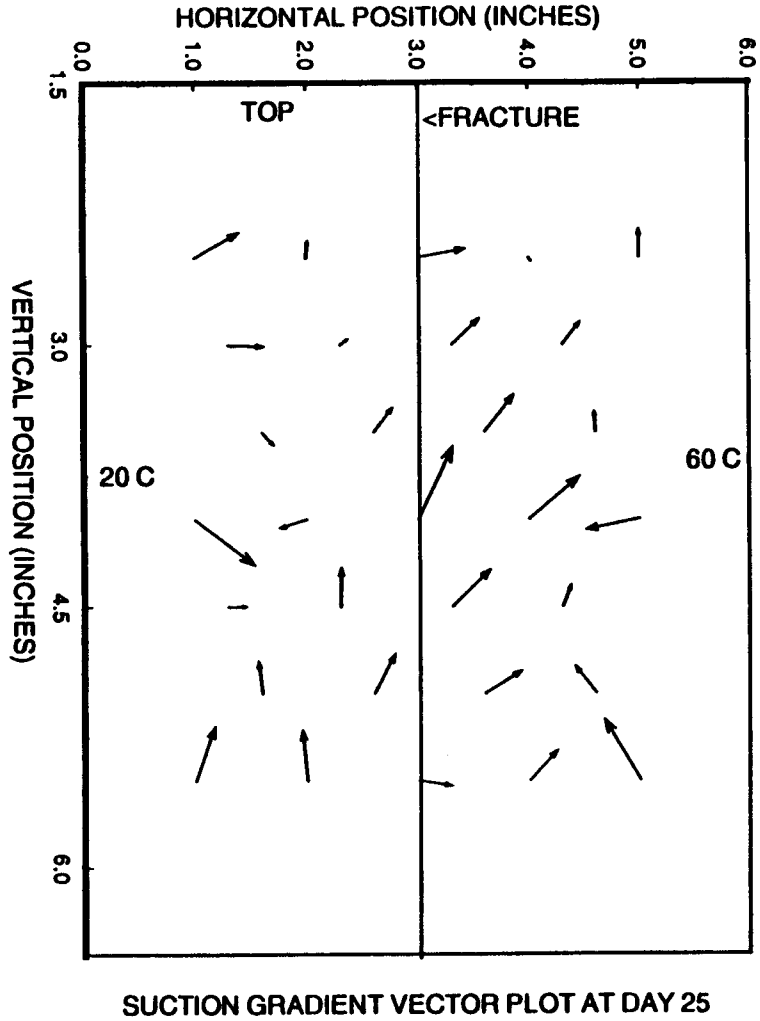

Figure 6-8. Suction gradient vector plot after 25 days during Test 6

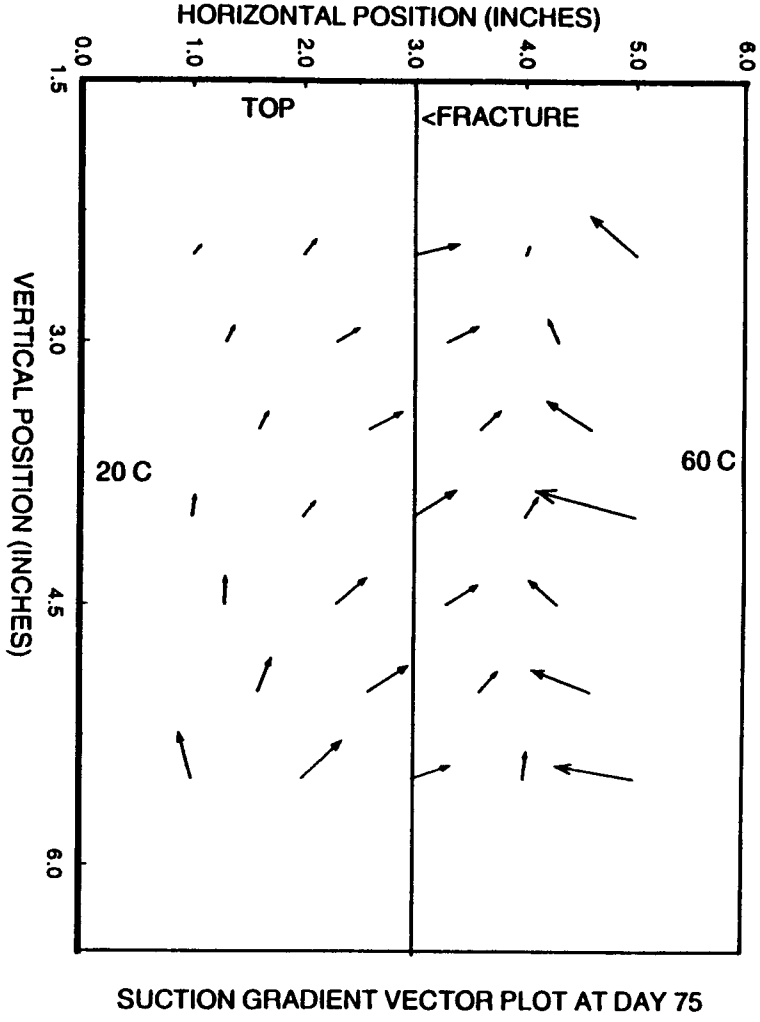

Figure 6-9. Suction gradient vector plot after 75 days during Test 6

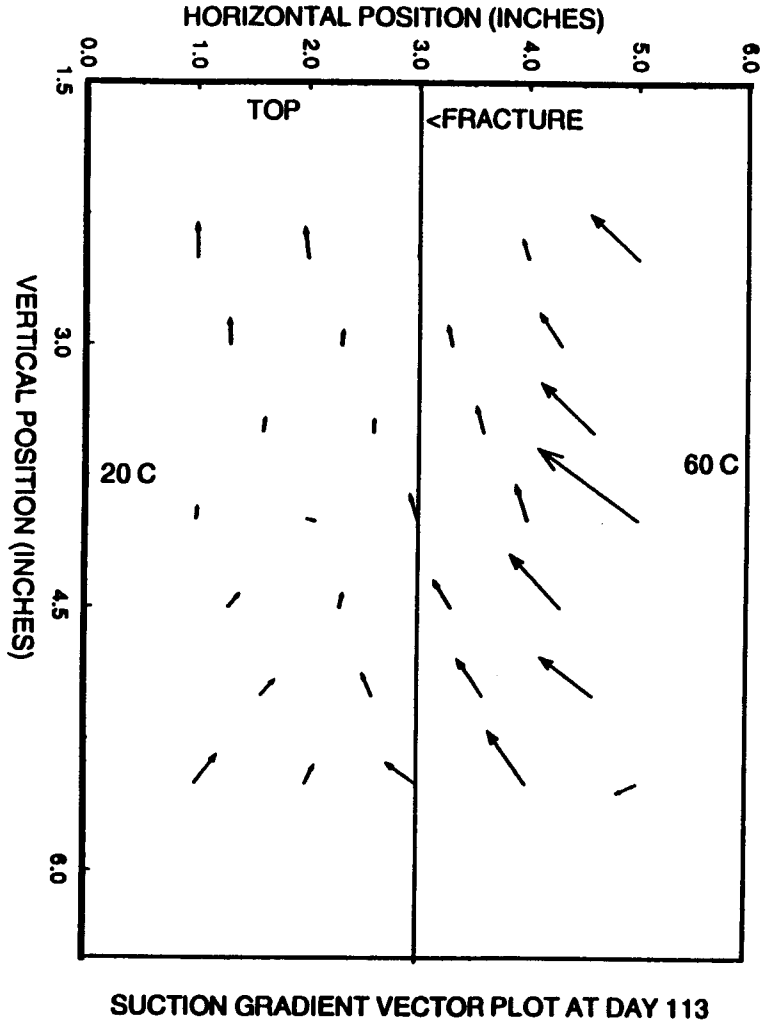

Figure 6-10. Suction gradient vector plot after 113 days during Test 6

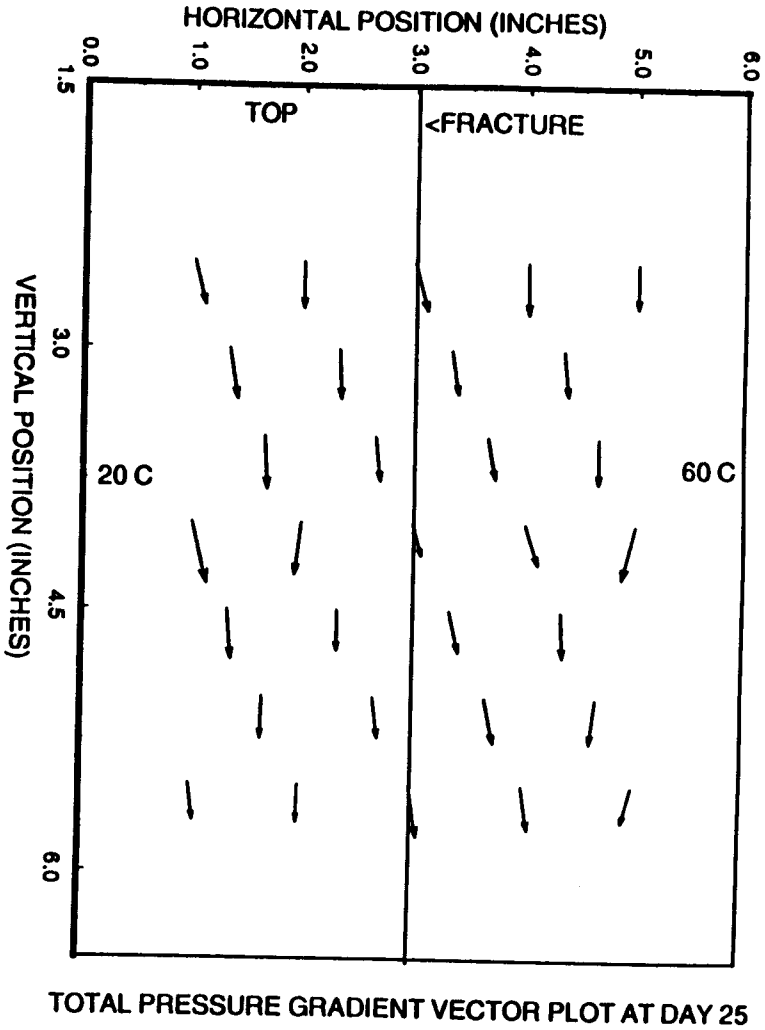

Figure 6-11. Total pressure gradient vector plot after 25 days during Test 6

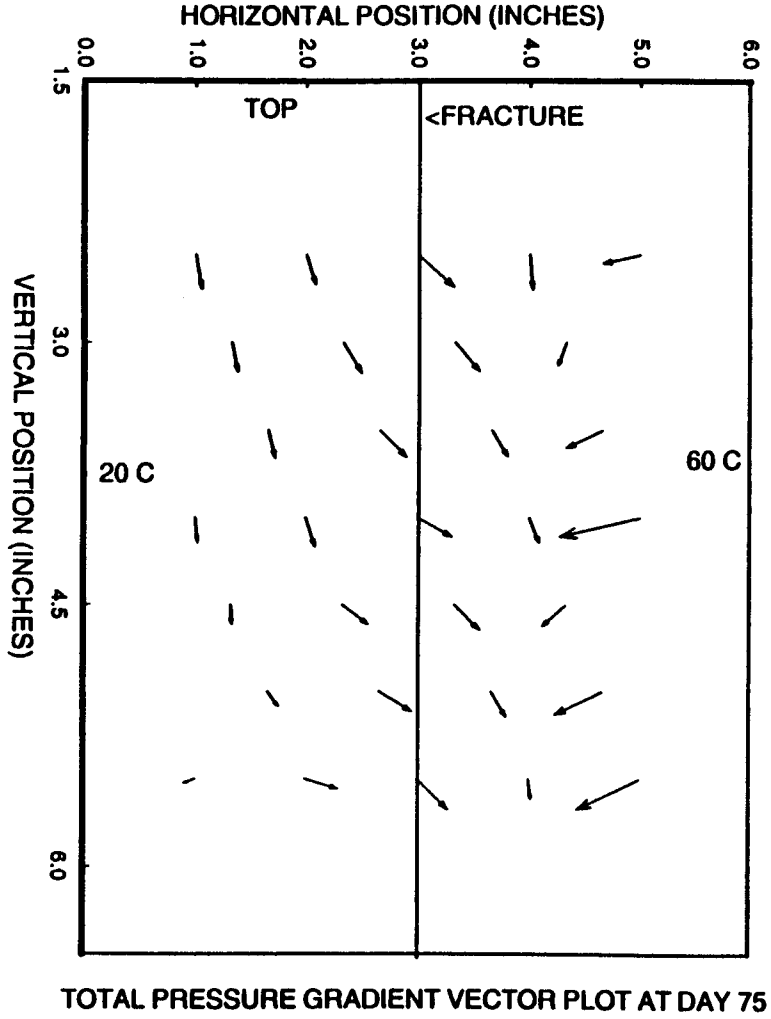

Figure 6-12. Total pressure gradient vector plot after 75 days during Test 6

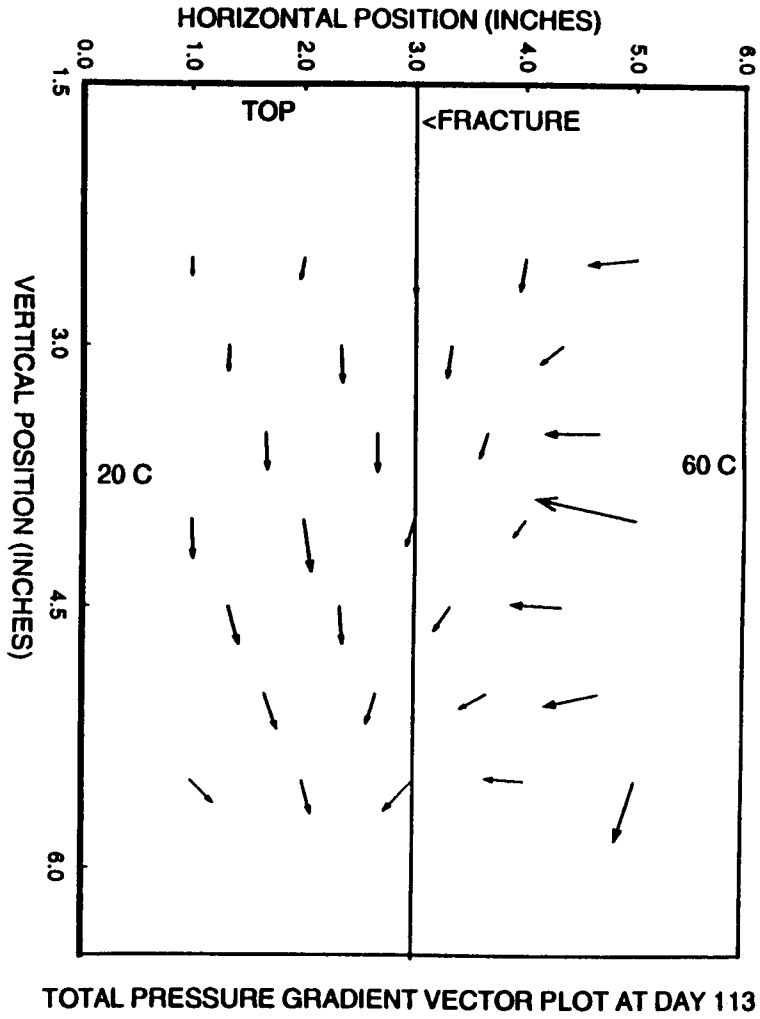

Figure 6-13. Suction gradient vector plot after 113 days during Test 6

7 THERMOHYDROLOGIC MECHANISMS OF WATER REDISTRIBUTION

The driving mechanisms which redistribute the water in a nonisothermal, fractured porous media, especially as observed in Test 6, are discussed here. Since both advection and diffusion of water in both liquid and gas phases are considered, four categories are discussed:

- Liquid phase advection (Section 7.1);
- Liquid phase molecular diffusion (Section 7.2);
- Gas phase advection (Section 7.3); and
- Gas phase molecular diffusion (Section 7.4).

The driving mechanism in each of the four categories is presented in a mathematical model and qualitatively discussed.

Summary of Mechanisms. The categorization scheme and the identified driving mechanisms to redistribute water in a nonisothermal, fractured porous media may not be comprehensive. However, these are all of the mechanisms that have been identified in the mathematical model and potentially observed in Test 6.

It should be noted that the mechanisms are not independent. They are coupled and interact, especially through dependencies on temperature and liquid saturation. To the extent possible, however, each mechanism will be discussed individually and related to the observed phenomena in Test 6.

7.1 LIQUID PHASE ADVECTION

Recall the equation for the advection of the mass of water in the liquid phase is restated from Eqn. (A-31) using Eqns. (A-49), (A-50), and (A-62):

$$q_{m,w,l} = - \frac{k_{sat}\, k_{rel,l}}{\mu_l} \left(- P_c \left(\frac{1}{J} \frac{dJ}{dS_l} \right) \nabla S_l - P_c \left(\frac{1}{\sigma} \frac{d\sigma}{dT} \right) \nabla T + P_c \frac{1}{d} \nabla d + \rho_l g \hat{k} \right) \tag{7-1}$$

It is noted that Eqn. (7-1) is based on the J-Leverett function [Eqn. (A-50)] which is considered a "working model" for rendering the capillary pressure dimensionless. Equation (7-1), therefore, is not considered a definitive mathematical model for liquid advection, but is considered a realistic model which can be used to investigate different driving mechanisms for liquid advection. In Eqn. (7-1), four advection mechanisms have been explicitly identified in separate terms:

- Liquid phase advection due to a liquid saturation gradient;
- Liquid phase advection due to a temperature gradient;
- Liquid phase advection due to a pore size gradient; and
- Liquid phase advection due to gravity.

Three additional mechanisms that may contribute to liquid phase advection are also discussed, however, they are considered difficult (if not impossible) to include in Eqn. (7-1):

- Liquid phase advection due to buoyancy;
- Liquid phase advection due to hysteresis; and
- Liquid phase advection due to thermochemical mechanisms.

7.1.1 Liquid Phase Advection due to a Liquid Saturation Gradient

The most commonly described and easily understood driving mechanism for liquid water redistribution in a partially saturated medium is a gradient in liquid saturation. When the liquid saturation is low, the remaining water is held tightly by adsorption forces and the capillary pressure is large. As the liquid saturation increases, the water is held by capillary forces and the capillary pressure is lower. The difference in capillary pressure (due to differences in liquid saturation) provides a drawing force for water movement through the medium.

It is common to express the capillary pressure as a function of liquid saturation. For simple calculations, the experimental data from Test 6 have been approximated with a linear function for liquid saturation from 0.4 to 0.8:

$$P_c \sim J(S_l) = \frac{(2.4 - S_l)}{0.14514} \qquad (7\text{-}2)$$

where J is the J-Leverett function. Equation (7-2) can be substituted for the liquid saturation gradient in Eqn. (7-1) to yield:

$$P_c \frac{1}{J} \frac{dJ}{dS_l} \sim \text{negative constant} \qquad (7\text{-}3)$$

It should be emphasized that the liquid will always flow from a region of high saturation to a region of low saturation as a result of this mechanism. (Later, liquid phase advection due to hysteresis, where liquid can be drawn from low to higher saturation, is discussed.)

In the next section of this discussion, the liquid saturation gradient driving force will be counteracted by the temperature gradient driving force to establish an equilibrium saturation profile in a nonisothermal porous medium.

7.1.2 Liquid Phase Advection due to a Temperature Gradient

For moderate levels of liquid saturation, the capillary pressure is proportional to the surface tension, a relationship which is frequently expressed using the J-Leverett function (recalled here for convenience):

$$P_c = \frac{\sigma(T)}{d} J(S_l) \qquad (7\text{-}4)$$

In Test 6, the medium had an average liquid saturation of 0.65, a level of liquid saturation considered moderate such that Eqn. (7-4) is assumed applicable.

The surface tension is a function of both liquid composition and temperature. In this work, liquid composition was noted to be potentially important, however it is not considered here. The influence of temperature is assumed in Test 6 to be an approximately linear temperature profile between the hot (60 C) and cold boundaries (20 C).

$$T(x) = 20 + (60-20)\frac{x}{L} \qquad (7\text{-}5)$$

The surface tension of water expressed as a function of temperature is (interpreted from Incropera and DeWitt, 1981):

$$\sigma = (72.8 - 0.16475\ (\ T - 20\ C\ ))\times 10^{-3}\ \ [N/m] \qquad (7\text{-}6)$$

or

$$\frac{\sigma}{\sigma_r} = 1 - \frac{0.16475}{72.8}(T-20) \qquad (7\text{-}7)$$

where σ_r = reference surface tension at 20 C.

Because a temperature gradient was established in Test 6, and surface tension is dependent on temperature, and capillary pressure is dependent on surface tension, and liquid saturation is dependent on capillary pressure, then the equilibrium liquid saturation was not expected to be horizontally uniform.

To demonstrate the potential importance of temperature-dependent surface tension during Test 6, a one-dimensional horizontal model between the cold and hot walls is considered. The model is based on the condition that at equilibrium the capillary pressure is constant throughout the medium and only temperature-gradient and saturation-gradient driven liquid advection are modelled. A simple linear approximation of capillary pressure as a function of saturation was determined from the experimental data valid for ($0.4 < S_l < 0.8$), so that the temperature and saturation effects can be combined, as follows:

$$P_c = \frac{\sigma}{\sigma_r}\left(\frac{2.4 - S_l}{0.14514}\right) = \left(1 - \frac{0.16475\ (T-20)}{72.8}\right)\left(\frac{2.4 - S_l}{0.14514}\right) \qquad (7\text{-}8)$$

where P_c is in kilopascals, and T is in C.

The one-dimensional model is idealized for a uniform porous medium of length L=14.6 cm. The media is initially saturated to a uniform level of 0.65. The system is sealed to eliminate any loss of water, and the temperatures of the walls are controlled to be 60 C for the hot side, and 20 C for the cold side. Liquid water will be transported from the hot side to the cold side because the surface tension decreases with temperature. At equilibrium, a new nonuniform liquid saturation will be established to balance the temperature driven suction, so that the capillary pressure will be constant throughout the medium.

$$P_{const} = P_c = \left(1 - \frac{0.16475}{72.8}(T - 20)\right)\left(\frac{2.4 - S_l}{0.14514}\right) \qquad (7\text{-}9)$$

Equation (7-9) can be solved for the liquid saturation:

$$S_l = 2.4 - 0.14514\ \frac{P_{const}}{\left(1 - \frac{0.16475}{72.8}(T - 20)\right)} \qquad (7\text{-}10)$$

The equilibrium saturation distribution must satisfy the mass conservation equation which can be stated as:

$$\frac{1}{L}\int_o^L S_l\,(T(x))\,dx = 0.65 \qquad (7\text{-}11)$$

Equation (7-11) can be solved for the new uniform capillary pressure, P_{const}. The result is P_{const} = 11.5 kPa. The new liquid saturation at the cold end is computed to be 0.73 and at the hot end is computed to be 0.56. Based on this simple model, the liquid saturation has a maximum difference of 0.17. Saturation differences of this magnitude and of the correct direction were observed in the test data. Although this simple model neglects the other transport mechanisms, one can conclude that a surface tension gradient has the potential of significantly redistributing the water in a heated, partially saturated porous medium.

7.1.3 Liquid Phase Advection due to a Pore Size Gradient.

A fracture was experimentally simulated in Test 6 by adding a layer of larger diameter glass beads. It was experimentally observed that the simulated fracture acted as a barrier to liquid transport, where no dye was observed to cross the fracture (this was especially evident in Test 5). This observed phenomena can be explained with the mathematical model,

especially the casting of the capillary pressure in term of surface tension, pore diameter and J-Leverett function of saturation [Eqn. (A-50) recalled here for convenience].

$$P_c = \frac{\sigma}{d} J(S_l) \tag{7-12}$$

To explain why the fracture remained dry and acted as a barrier, an analysis is begun by noting that near equilibrium conditions, the liquid pressure is uniform so that the gradient of liquid pressure is zero.

$$\nabla P_l = 0 \tag{7-13}$$

The liquid pressure is related to the gas and capillary pressure.

$$P_l = P_g - P_c \tag{7-14}$$

The gas pressure is assumed to be approximately uniform and constant, so that the gradient of liquid pressure is equal to the gradient of capillary pressure, both being equal to zero.

$$\nabla P_c = 0 \tag{7-15}$$

Substituting the expression for capillary pressure and carrying out the differentiation yields:

$$\frac{1}{P_c} \nabla P_c = \frac{1}{\sigma} \nabla \sigma + \frac{1}{J} \nabla J - \frac{1}{d} \nabla d \tag{7-16}$$

Because the influence of temperature in the immediate vicinity of the fracture is not of interest, the temperature is assumed constant so that:

$$\nabla T = 0 \tag{7-17}$$

so that

$$\nabla \sigma = 0 \tag{7-18}$$

The requirement of equilibrium reduces to a balance of liquid saturation gradient and pore size gradient.

$$\frac{1}{J} \nabla J = \frac{1}{d} \nabla d \tag{7-19}$$

Recall the J-Leverett function depends only on liquid saturation, so that:

$$\left(\frac{1}{J} \frac{dJ}{dS_l} \right) \nabla S_l = \frac{1}{d} \nabla d \qquad (7\text{-}20)$$

Note the dependencies and signs (either positive or negative) of each of the multiplying components:

- $J(S_l) > 0$ (i.e., always positive, only function of saturation);
- $\frac{dJ}{dS_l} < 0$ (i.e., always negative, only function of saturation); and
- $d > 0$ (i.e, always positive, only function of location)

In summary, it has been shown that the gradient in liquid saturation is roughly proportional to the negative of the gradient in pore size.

$$\nabla S \sim - \nabla d \qquad (7\text{-}21)$$

Equation (7-21) is considered a rough approximation which can be used to explain why the simulated fractures in both Test 5 and 6 were visually observed to be drier than the surrounding medium. Many assumptions are implicit in Eqn. (7-21), the most significant are that (i) expressing $P_c \sim J/d$ is acceptable for both matrix and simulated fracture; and (ii) J is only a function of S_l and is the same for both matrix and simulated fracture, hence the only difference between the matrix and fracture is a change in d.

Theoretically, fractures can be considered as thin regions of larger pore size in comparison with the surrounding medium, as illustrated in Figure 7-1(a). Similarly, the gradient of the pore size is illustrated in Figure 7-1(b). From this analysis, the gradient of liquid saturation is proportional to the negative of the gradient of pore size, as illustrated in Figure 7-1(c). The resulting liquid saturation is illustrated in Figure 7-1(d) which is interpreted directly from the gradient in saturation (Figure 7-1(c)).

From the theoretical discussion presented here, one can understand why a fracture is dryer than the surrounding medium, and why the surrounding medium is frequently described as "drawing" water from a fracture (if the fracture initially has a high liquid saturation).

Because the fracture is dry, the relative liquid permeability is much lower than for the surrounding medium. The relative liquid permeability can be assumed, for instance, to be a cubic function of saturation (Bear, 1972):

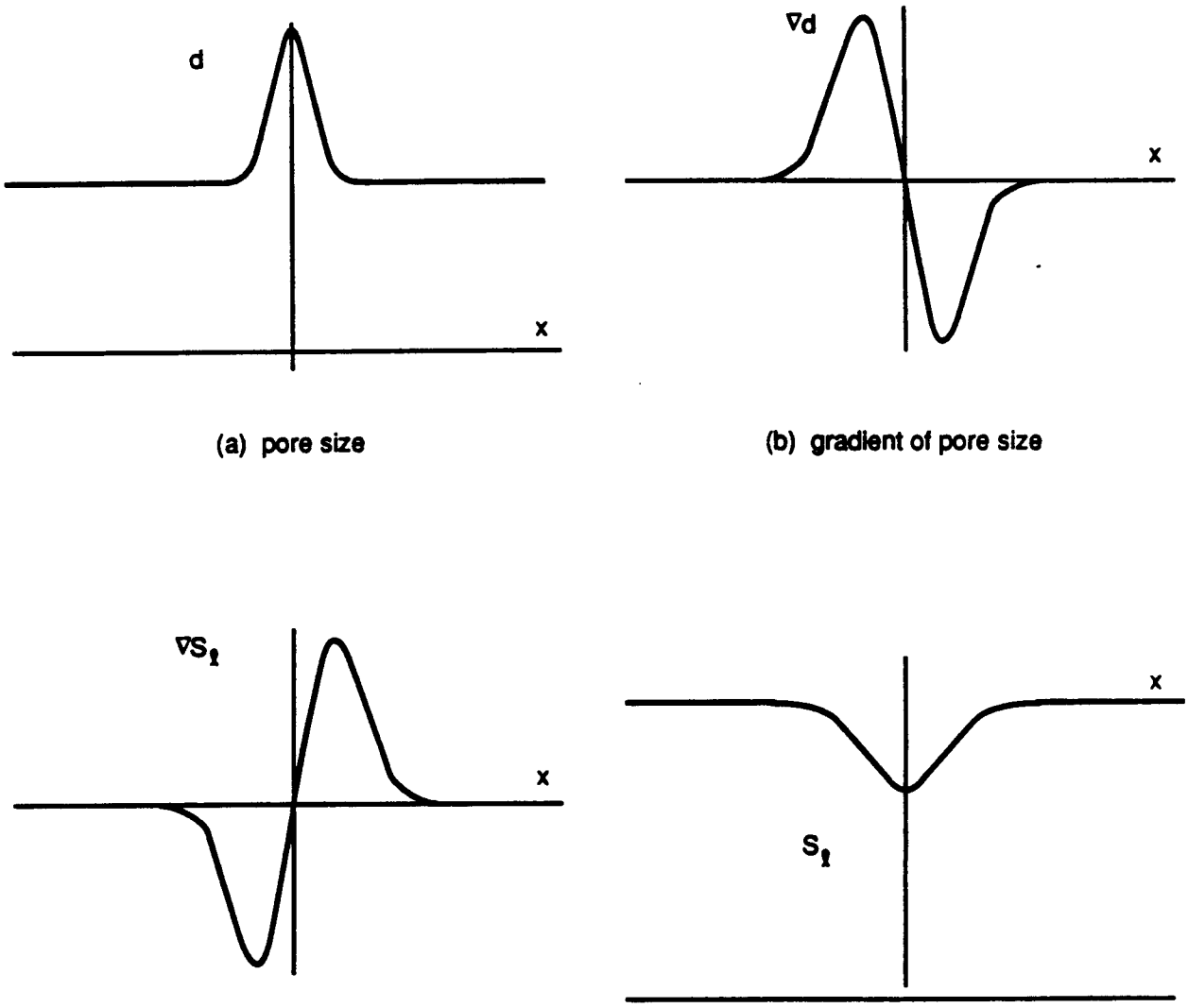

Figure 7-1. Illustration of the effect of a fracture, where (a) pore size, (b) gradient of pore size, (c) gradient of liquid saturation, and (d) liquid saturation

$$k_{rel,l} = (S_l)^3 \tag{7-22}$$

Therefore, even if the medium on one side of a fracture has a higher saturation that the other, the low relative permeability of the fracture will severely restrict flow from one side to the other. This phenomenon was observed in the experiments.

7.1.4 Liquid Phase Advection due to Gravity

The initial six day period with no heating allowed enough time to complete the expected water redistribution due to hydrostatic effects. The eventual isothermal saturation distribution is predicted to vary from 0.51 at the top of the container to 0.79 at the bottom, as contrasted to the initial uniform 0.65.

The capillary suction pressure P_c is a function of the saturation S_l in the medium. At steady state, the capillary pressure is related hydrostatically to the vertical distance z measured downward from the top of the container; that is $P_c = P_{c,top} - \rho gz$. The saturation must eventually obtain a distribution that makes these two alternative descriptions of the pressure equal:

$$P_c(S_l) = P_{c,top} - \rho g_l z \tag{7-23}$$

The saturation distribution must satisfy conservation of mass, or:

$$\frac{1}{L}\int_0^L S_l(z)\, dz = 0.65 \tag{7-24}$$

where L is the total depth of the container (L = 0.216m). To determine the equilibrium distribution, it is convenient to express the saturation explicitly in terms of capillary pressure. As previously determined, the relation between saturation and pressure is approximately linear over the saturation range from approximately 0.4 to approximately 0.8:

$$S_l = 2.4 - 0.14514\ P_c \tag{7-25}$$

where the capillary pressure is positive and in kilopascals. Hence, the equilibrium conservation of mass condition can be expressed as:

$$\frac{1}{L}\int_0^L \left[2.4 - 0.14514(P_{c,top} - \rho g z)\right] dz = 0.65 \tag{7-26}$$

which can be integrated and solved for the capillary pressure P_c at z = 0. The result is that $P_{c,top}$ = 13.06 kPa (1.89 psi) which yields a corresponding saturation S_{top} = 0.51. The

saturation at the bottom z = L, where the capillary pressure is computed to be 11.06 kPa (1.61 psi), and saturation is S_{bot} = 0.79. Thus, there is a saturation difference of 0.28 from top to bottom. The pressure at z = 9 cm was measured with a tensiometer during the tests and found to be about 8.3 kPa (1.2 psi) during day 5. The predicted equilibrium pressure is 12.4 kPa (1.8 psi). The discrepancy between the measured and the predicted isothermal, hydrostatic pressure is not considered significant and may be due to experimental measurement error.

A simple one-dimensional transient flow model was formulated and solved to determine the time required to obtain the equilibrium distribution. This calculation depends on both the saturated permeability, k_{sat}, of the medium and the relative liquid permeability, $k_{rel,l}$, that would allow the water to obtain near-equilibrium in six hours. The model is developed here.

Consider a one-dimensional column of porous medium, with the z-axis pointed downward. The conservation of liquid water (this is isothermal, hence no evaporation) can be expressed in differential form as:

$$\phi \rho_l \frac{\partial}{\partial t}(S_l) = \frac{\partial}{\partial z}\left(\rho_l \frac{k_{sat} k_{rel,l}}{\mu_l}\left(\frac{\partial P_l}{\partial z} + \rho_l g z\right)\right) \qquad (7\text{-}27)$$

where

ϕ	=	porosity [dimensionless],
ρ_l	=	liquid density [kg/m^3],
μ_l	=	liquid dynamic viscosity [N-s/m^2],
g	=	gravity [m/s^2],
S_l	=	liquid saturation [dimensionless],
P_l	=	liquid pressure [N/m^2], and
z	=	distance from top measured downward [m].

The liquid pressure is given by $P_l = P_g - P_c$ and the gas pressure is assumed uniform and constant. The capillary pressure P_c is expressed as $P_c = A - B S_l$, where A and B are constants determined from curve fitting experimental data. The saturation is expressed as the sum of the equilibrium saturation S_e and a deviation S′; that is $S_l = S_e + S'$. The liquid pressure gradient is thus:

$$\frac{dP_l}{dz} = -\frac{dP_c}{dz} = B\left(\frac{dS_e}{dz} + \frac{dS'}{dz}\right) \qquad (7\text{-}28)$$

and it is observed that the sum of the equilibrium suction pressure gradient and the hydrostatic gradient is ρg is zero (hydrostatic equilibrium). It is assumed that the range of S_l is small so that $k_{rel,l}$ is approximately constant and Eqn. (7-28) can be simplified to:

$$\phi \frac{\partial S'}{\partial t} = \frac{k_{sat} k_{rel,l} B}{\mu_l} \frac{\partial}{\partial z^2} (S') \tag{7-29}$$

The initial conditions on S′ can be calculated given the uniform initial saturation of S_l (z,t=0) = 0.65 and final equilibrium saturation of S_e (z,t= all time) = 0.51 + (0.79-0.51) z/L, so that:

$$S'(z,t=0) = 0.14 - 0.28(z/L) \tag{7-30}$$

The boundary conditions are no flux, so that

$$\left.\frac{\partial S'}{\partial z}\right|_{z=0} = 0 \tag{7-31}$$

$$\left.\frac{\partial S'}{\partial z}\right|_{z=L} = 0 \tag{7-32}$$

From symmetry, one can use a midpoint boundary condition and analyze only half of the domain (i.e., $0 < z < L/2$):

$$S'(z=L/2, t) = 0 \tag{7-33}$$

A solution to this problem can be found in Carslaw and Jaeger [1959, pg 98, Fig 10(b)]. The solution is interpreted into the present discussion as steady state being reached when the Fourier number is greater than or equal to 1.0. The Fourier number is a dimensionless time and defined for this problem to be:

$$Fo \equiv \frac{4 k_{sat} k_{rel,l} B t_{ss}}{\phi \mu_l L^2} \tag{7-34}$$

The steady state requirement is expressed as a requirement on k_{sat} as:

$$k_{sat} \geq \frac{\phi \mu_l L^2}{4 k_{rel,l} B t_{ss}} \tag{7-35}$$

where

ϕ	=	porosity [0.35, dimensionless],
μ_l	=	dynamic viscosity of water [700 x 10^{-6} N-s/m^2],
L	=	length [0.203 m],
$k_{rel,l}$	=	relative permeability [$\sim (0.51)^3 = 0.13$ dimensionless],
B	=	coefficient [6,890 N/m^2], and
t_{ss}	=	time to reach steady state [s].

Using this conservative one-dimensional model, an upper limit on k_{sat} was estimated so that the water would obtain near-equilibrium in six hours (t_{ss} = 518,400 s). It was found that $k_{sat} \geq 10^{-10}$ cm^2 was sufficient. Since a value of $k_{sat} = 10^{-6}$ - 10^{-10} cm^2 corresponds roughly to that of silty sand, the predicted value of k_{sat} thus seems reasonable (Freeze and Cherry, 1979).

From these calculations it is concluded that (i) there was an approximately linear vertical saturation gradient from top (S_{top} = 0.51) to bottom (S_{bot} = 0.79), and (ii) the time required to reach this linear gradient was less than six hours and much shorter than the waiting period of five days before the side temperatures were controlled in Test 6.

7.1.5 Liquid Phase Advection due to Buoyancy

Although not explicitly represented in Eqn. (7-1), the possibility of buoyancy-driven natural convection in the liquid phase does exist. As noted in the discussion on similitude (Appendix D.4.2), the possibility of natural convection in the liquid phase is mathematically restricted by the assumptions that a hydrostatic pressure gradient exists both in the liquid and gas phases, and that the liquid pressure is dictated by the local gas pressure and liquid saturation (through capillary pressure). These equations restrict the liquid pressure so that it is difficult to mathematically show the presence of buoyancy-driven, liquid-phase, natural convection. Physically, the two requirements of having a gravitational body force and temperature dependent liquid density are sufficient to support natural convection currents in the liquid. In Test 6, no experimental data indicated that natural convection existed in the liquid phase, so it was assumed to be negligible.

The relative importance of natural convection in the liquid and gas phases can be compared through changes in fluid density. For the liquid, one can compare the change in liquid density to the average liquid density for a 40 C increase in temperature.

$$\frac{\Delta \rho_l}{\bar{\rho}_l} = \frac{\rho_l(20\ C) - \rho_l(60\ C)}{\rho_l(40\ C)} = \frac{998.2 - 983.1}{992.3} = 1.5\,\% \qquad (7\text{-}36)$$

Here, the percent change in liquid density is found to be approximately 1.5 percent from 20 to 60 C. Similarly, the change in gas density compared to the average gas density is approximately 13.0 percent from 20 to 60 C.

$$\frac{\Delta \rho_g}{\bar{\rho}_g} = \frac{\rho_g(20\ C) - \rho_g(60\ C)}{\rho_g(40\ C)} = \frac{313\ (60 - 20)}{293\ 333} = 13\,\% \qquad (7\text{-}37)$$

The percent change in gas density is, therefore, an order of magnitude larger than that of liquid. This simple comparison suggests that natural convection in the gas phase will be more probable than in the liquid phase.

7.1.6 Liquid Phase Advection due to Hysteresis

In Test 6, liquid advection was experimentally observed in a direction of increasing saturation and increasing temperature. The observations were made with dye which was injected into the hot side port. The traces of the dye after injection into either of the two ports is illustrated in Figure 7-2 for ten different times. The dye was injected on approximately day 63 of the experiment so that the dry zone was established and visually distinguishable (zone to right of wet band in Figure 7-2). The dye on the cool side showed negligible bulk liquid motion, and appeared to diffuse into the surrounding liquid. The dye injected into the hot side port also exhibited molecular diffusion which tended to smear-out the location of the dye, but in addition it showed bulk liquid advection towards a band (or line) of higher liquid saturation. The band of increased saturation was visibly noticeable and detected with densitometer measurements (Figures 6-3 and 6-4). After reaching the saturation band, the dye moved downward in the saturation band. In summary, the dye injected into the hot side port moved towards the hot side and into the saturation band where it then moved downward continuing in the saturation band (Figure 7-2).

A one-dimensional, horizontal illustration of the saturation profile observed in Test 6 on the day 63 is shown in Figure 7-3. A region of high saturation was located between the dye injection port and the heated edge. The location of the injection port is also shown in Figure 7-3. The region near the dye injection port was sufficiently far from the simulated fracture such that the medium was uniform and no pore-size gradient existed. However, the injected dye was observed to move with the liquid in the direction of increasing liquid saturation and increasing temperature, which is opposite of that predicted by the previously discussed saturation gradient and temperature gradient mechanisms. In summary, none of these mechanisms explain the experimental observations.

A mechanism which can explain the observed liquid flow is hypothesized to be hysteresis in the capillary pressure versus liquid saturation curves (see Figure 7-4). Hysteresis occurs in the P_c versus S_l curves as a function of the medium decreasing and increasing in liquid saturation (i.e., drying or wetting) (Bear and Bachmat, 1991; Freeze and Cherry, 1979; Hillel, 1980a; de Marsily, 1986).

In Test 6, the region near the hot wall dried out. The dry region grew in size as the experiment continued. The mechanism for drying was evaporation associated with molecular diffusion in the gas phase of water towards regions of lower temperature. As the vaporous water reached the cooler regions, it condensed. The evaporation was a drying process and condensation a wetting process.

Two points are illustrated in Figure 7-4 where point 1 is in a wetting region and point 2 is in a drying region. It is hypothesized that the hysteresis effect created a higher capillary pressure at the drying front which "sucked" liquid from the cooler region. It is highlighted that point 1 has a lower liquid saturation than point 2; however, point 2 has a higher

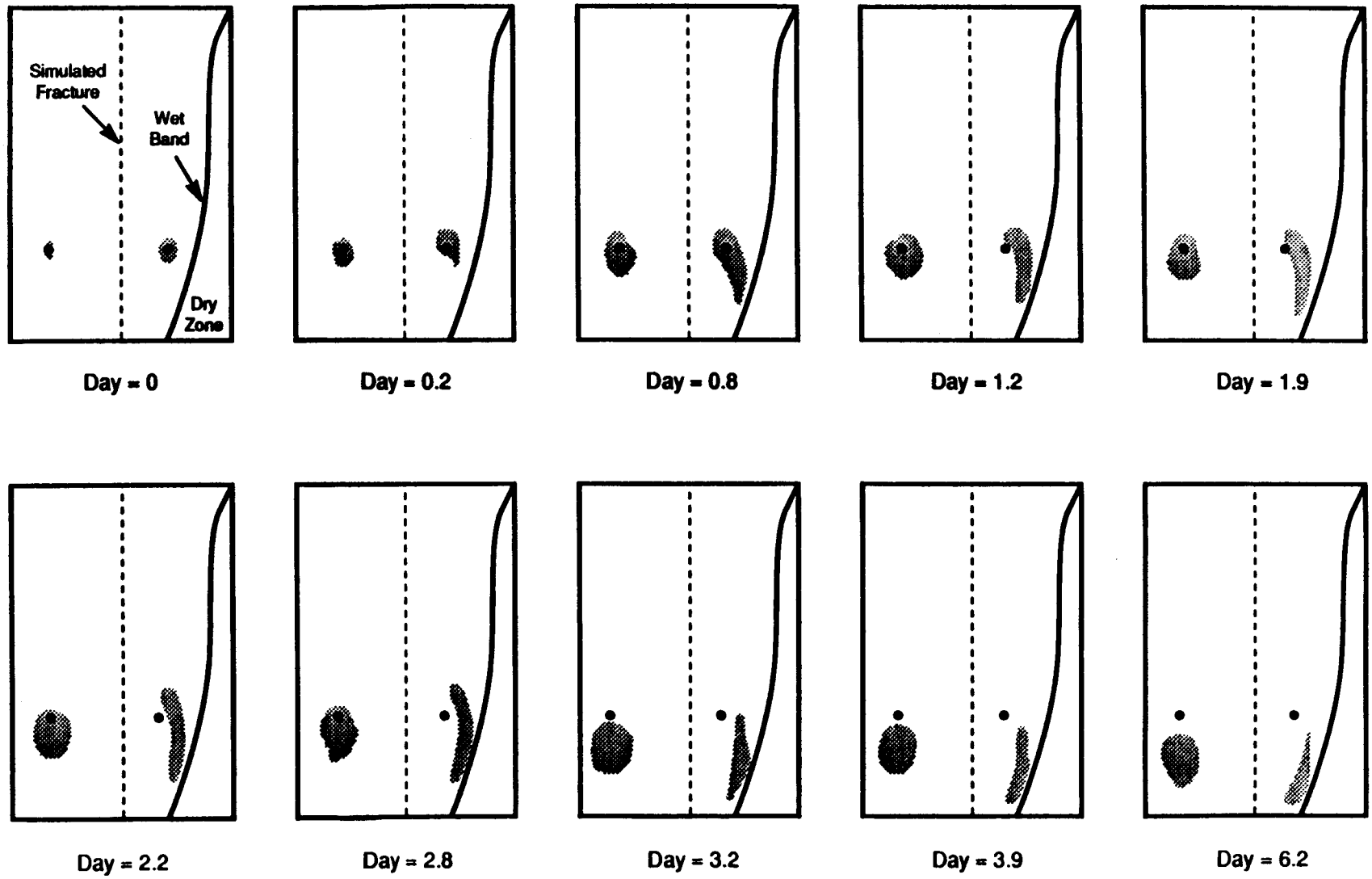

Figure 7-2. Observation of dye location after injection into either the hot side (right) or cold side (left) ports starting on day 63 of the experiment

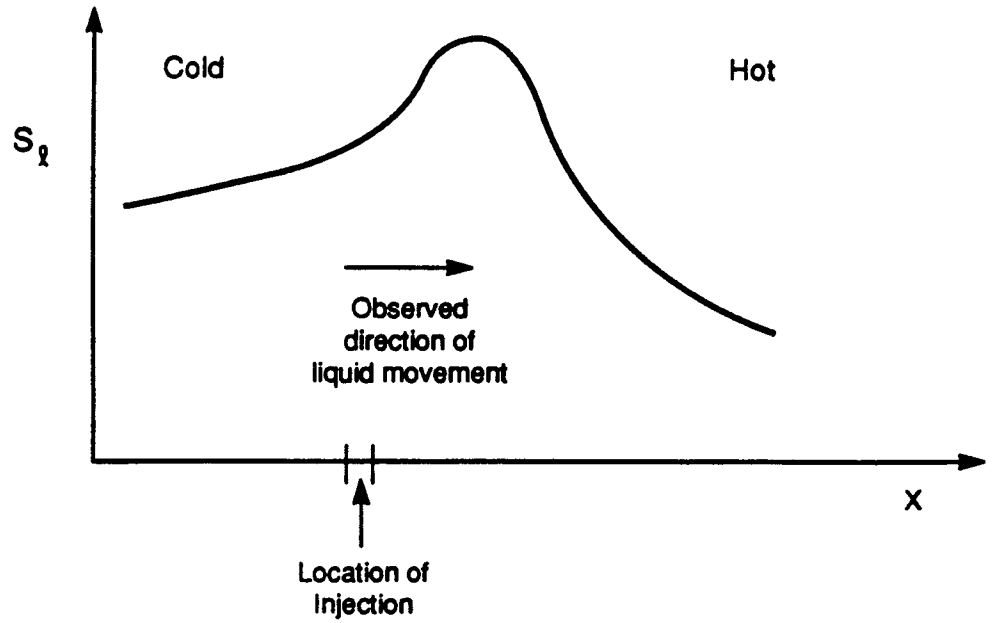

Figure 7-3. One-dimensional liquid saturation profile highlighting location of injection and observed direction of liquid movement

capillary pressure. Hence, the hysteresis in the P_c versus S_l curves is a plausible mechanism to explain the observed dye movements.

7.1.7 Liquid Phase Advection due to Thermochemical Mechanisms

Before finishing the discussion of liquid phase transport mechanisms, the possibility of coupled thermochemical interactions should be mentioned. In the mathematical model, thermochemical mechanisms are not modelled. One possible thermochemical mechanism may have been created by the dissolution of the gas beads. Using a scanning electron microscope (SEM) at SwRI, it was observed that the glass beads exhibited dissolution features, suggesting the mobilization of silica through the dissolution of the glass beads. In a pure water-silica system, the solubility of amorphous silica increases with increasing temperature. At the same time, the rate of dissolution also increases. Given the relatively high surface area of the glass beads and the SEM evidence of dissolutions, it is likely that the fluids on the hot side contained higher concentrations of dissolved silica than those on the cold side. Similarly, the water vaporized near the hot wall, and created higher concentrations of silica. Silica is a heavier molecule so the density of the liquid in the saturation band is expected to be higher than that of pure water. The denser liquid would tend to fall to the bottom, thereby displacing lighter liquid and creating a thermochemical natural convection in the liquid. This is mentioned because the dye in the liquid was observed to fall once it reached the saturation band.

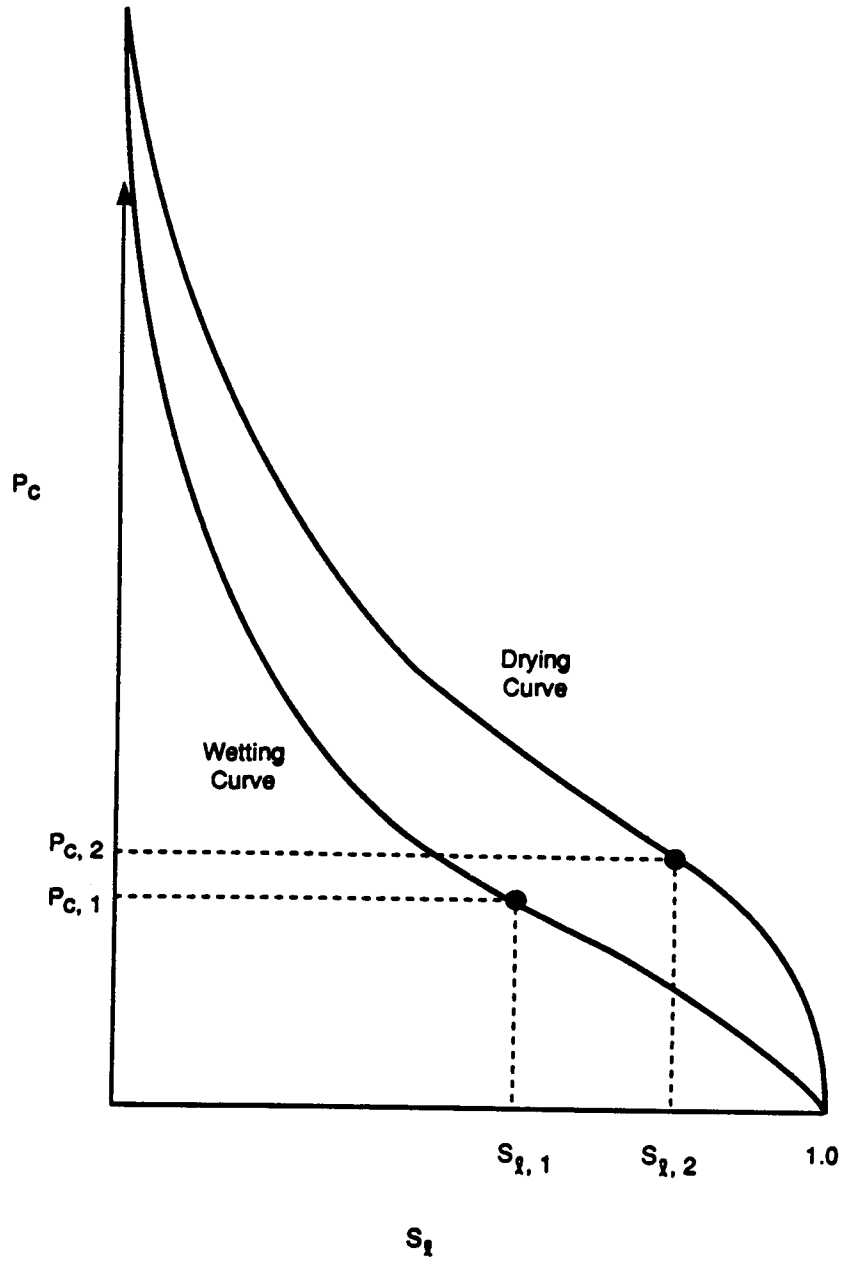

Figure 7-4. Typical capillary pressure versus liquid saturation curves exhibiting hysteresis

7.2 LIQUID PHASE MOLECULAR DIFFUSION

In theory, the liquid can consist of a number of components other that water. If so, then molecular diffusion of water in the liquid phase may exist and would need to be considered. For this work, however, the liquid phase is assumed to consist of water and the quantity of other components is considered negligible. Therefore, the molecular diffusion of water in the liquid phase is zero and explicitly stated for theoretical completeness (molecular diffusion of water in the gas phase is not necessarily negligible as it will be discussed):

$$j_{m,w,l} = 0 \tag{7-38}$$

7.3 GAS PHASE ADVECTION

Water may be transported in the gas phase due to either advection or molecular diffusion. The equation describing the advection of the mass of water in the gas phase is recalled here:

$$q_{m,w,g} = - \rho_g \, m_{w,g} \frac{k_{sat} \, k_{rel,g}}{\mu_g} \left(\nabla \tilde{P}_g - \rho_{g,o} g \beta_g \Delta T \hat{k} \right) \tag{7-39}$$

where two driving mechanisms have been identified:

- Gas phase advection due to nonhydrostatic gas pressure gradients; and
- Gas phase advection due to buoyancy.

7.3.1 Gas Phase Advection due to Nonhydrostatic Gas Pressure Gradients

In Eqn. (7-39), the first term describes gas phase advection due to a nonhydrostatic gas pressure gradient. This term may become important if an external gas flow term was introduced into the problem (probably in the form of a nonzero gas velocity boundary condition). In Test 6, there was no cause for this term to be considered an important transport mechanism, hence it is considered negligible.

7.3.2 Gas Phase Advection due to Buoyancy

In the mathematical model and in the related theoretical discussion presented in this report, the possibility exists for buoyancy-driven, gas-phase advection (or more commonly called natural convection). The requirements for natural convection are a gravitational body force, temperature-dependent gas density and a nonisothermal temperature field, all of which were present in Test 6. Based upon the experimental data from Test 6, it was assumed that gas phase natural convection was not an important transport mechanism for water.

7.4 GAS PHASE MOLECULAR DIFFUSION

Water may be transported in the gas phase due to molecular diffusion where the equation describing diffusion is recalled here:

$$j_{m,w,g} = - \tau \, \phi \, S_g \, D_{wa,g} \, \rho_g \, \nabla m_{w,g} \tag{7-40}$$

The two driving mechanisms for molecular diffusion of water in the gas phase are:

- Gas phase molecular diffusion due to a temperature gradient; and
- Gas phase molecular diffusion due to a liquid saturation gradient.

Although not explicitly stated in Eqn. (7-40), the mass fraction of water in the gas phase is related to the temperature [through the Claperyon-Clausius equation, Eqn. (A-81)], and liquid saturation [through Kelvin's equation, Eqn. (A-78)].

If the gas is assumed to behave as ideal, and that Kelvin's equation for vapor pressure reduction is negligible, and that the Claperyon-Clausius equation applies, then the binary diffusion is approximately:

$$j_{m,w,g} = -\tau \phi S_g D_{wa,g} \left(\frac{P_v h_{lg} (M_w)^2}{R^2 T^3} \right) \nabla T \qquad (7\text{-}41)$$

where the Claperyon-Clausius equation is used here to express the vapor pressure temperature relationship:

$$P_v = P_{v,o} \exp\left(\frac{h_{lg} M_w}{R} \left(\frac{1}{T_o} - \frac{1}{T} \right) \right) \qquad (7\text{-}42)$$

Here, the mass flux of water due to molecular diffusion in the gas phase is clearly proportional to the temperature gradient as previously suggested.

7.4.1 Gas Phase Molecular Diffusion due to a Temperature Gradient

One of the primary transport mechanisms in Test 6 was molecular diffusion of vaporous water. The high temperature for the hot side created a high partial pressure of water in the gas phase. The high partial pressure was an indication of a higher concentration of water molecules in the gas phase. Through random molecular movements, water molecules diffused from regions of high concentration to low concentration, thereby creating a net flux of water. Because the horizontal temperature profile was approximately linear in Test 6, the water was evaporated near the hot wall, moved by molecular diffusion towards the cool wall, and continually condensed as it entered cooler and cooler regions.

It should be emphasized that the evaporation and condensation did not occur in localized regions, but over extended regions of the porous media. At the start of Test 6, evaporation was restricted to the hot wall, but as the test progressed, evaporation occurred over larger areas as the dry-out region grew. Of the two processes, evaporation was the most localized. In comparison, condensation occurred over a much larger region which extended from the dry-out region to the cold wall. Because the vapor pressure of water increases rapidly with temperature (see Claperyon-Clausius equation), the majority of condensation occurred nearest the dry-out region, hence this encouraged the development of a region of higher saturation. Once the region near the hot wall dried-out, the evaporation process began to be more defined at the front of the high saturation band. The condensation process continued on the cool side of the saturation band, hence creating the drying-wetting hysteresis phenomena which was experimentally observed using dye and has been previously discussed in this chapter.

Both the rapid change of vapor pressure with temperature and the drying-wetting hysteresis encouraged the development of a region of high saturation (saturation band).

The presence of a "dry zone" and a "saturation band" (or region of high liquid saturation) clearly developed at late times in Test 6 (after approximately 50 days) [Figure 7-5(a)]. The saturation band extended from the upper right corner of the test section down towards the lower-middle right of the test section. A one-dimensional model of Test 6 is shown in Figure 7-5(b) where the dry region, saturation band, and liquid and gas flow directions are illustrated. By comparison, a one-dimensional model captures the major features of the experimental data.

One explanation for the skewed shape of the observed dry zone is that the horizontal temperature profiles across the top and bottom of the test container were different [Figure 7-5(c)]. It is hypothesized that the temperature profile along the top of the test container decreased more rapidly from the hot to the cold side. In comparison, the bottom of the test container retained a more linear temperature profile. Additionally, the upper hot side temperature may have been less than the lower hot side temperature (i.e., $T_{max,top} < T_{max,bot}$). Differences in the temperature profiles are plausible if one considers the enhanced heat transfer with the surrounding laboratory room (especially thermal radiation and natural convection) that the top of the test container potentially experienced. With these temperature profiles, the molecular diffusion mechanism was weaker at the top and stronger at the bottom of the test container (due to vapor pressure being an exponential function of temperature, through the Claperyon-Clausius equation), hence the dry zone grew quicker at the bottom.

7.4.2 Gas Phase Molecular Diffusion due to a Liquid Saturation Gradient

In the mathematical models, the partial pressure of water in the gas phase, $P_{w,g}$, can be calculated by using both the (i) Claperyon-Clausius equation (which is a function of temperature), and (ii) Kelvin's equation (which is a function of liquid saturation through capillary pressure). Temperature is the dominant variable which dictates $P_{w,g}$ and the effect of saturation is almost always negligible. For completeness of the theoretical development the influence of saturation is discussed here.

The effects of Kelvin's equation are only important at high capillary pressures. For example, at $P_c = 100$ atm and $T = 300$ K, the relative humidity is 93 percent (or $P_{w,g}$ is reduced by 0.93). Hence, it requires large changes in P_c to influence $P_{w,g}$ and provide a driving mechanism for binary diffusion. In Test 6, capillary pressures were recorded well below 0.5 atm so that the effects of gas phase binary diffusion due to a gradient in liquid saturation were considered negligible.

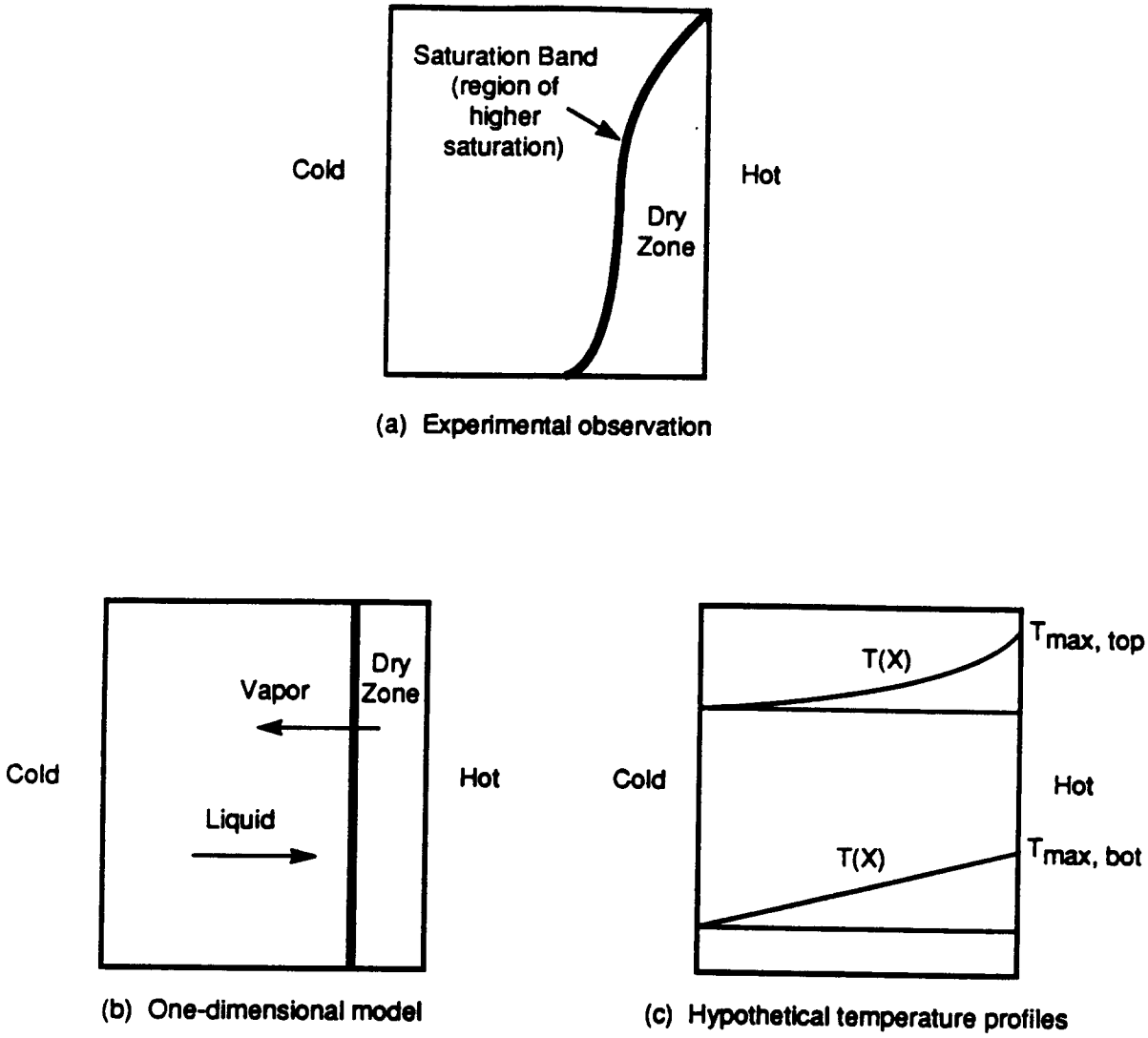

Figure 7-5. Comparison of (a) experimentally observed dry zone and saturation bands, with (b) one-dimensional model of vapor and liquid counterflow, and (c) comparison of horizontal temperature profile at the top and bottom of experiment

7.5 SUMMARY OF THERMOHYDROLOGIC MECHANISMS OF WATER REDISTRIBUTION OBSERVED IN TEST 6

In this section, the experimental data were qualitatively discussed as to hypothetical or plausible transport mechanisms for the water. The observed experimental data were interpreted to be horizontally one-dimensional (from the hot to the cold wall). A dry-out region and a saturation band were experimentally observed, and the fracture was experimentally observed to remain "dry" and restrict the flow of liquid water. The primary mechanisms which redistributed

the water were evaporation, gas phase binary diffusion, condensation, and liquid phase advection due to differences in capillary pressure. The mechanism which restricted liquid flow across the fracture was concluded to be the difference in pore size.

8 NUMERICAL SIMULATIONS OF THERMOHYDROLOGICAL PHENOMENA

8.1 BACKGROUND

Numerical simulations were conducted to gain insight into the coupled thermohydrological mechanisms observed in the laboratory experiments and were discussed and evaluated in Chapter 6. Another objective of these simulations was to assess the capability of a numerical code to simulate the mechanisms observed in the laboratory experiments.

The computer codes TOUGH (Pruess, 1987) and its enhanced, vectorized version, VTOUGH, are used at several DOE contracting agencies (e.g. LBL, LLNL, PNL) to model two-phase flow through fractured, porous media. Since it appears likely at this time that DOE will use a form of the TOUGH during the licensing process, the numerical code VTOUGH (Nitao, 1987) was selected to perform these simulations. A computer code other than TOUGH may be used in future simulations to provide an additional perspective of the capabilities to simulate the key thermohydrological mechanisms targeted with the laboratory-scale experiments. However, TOUGH (and VTOUGH) has been used in these analyses because it is a prominent numerical code in the literature.

The models were simulated for periods up to 116 days (10^7 seconds), durations similar to that of Test 6. The simulations included nonisothermal boundary conditions, exclusion and inclusion of a fracture within the matrix and examination of liquid and vapor saturations at various stages of water redistribution.

All simulations conducted as part of this exercise were two dimensional and vertically oriented, similar to the configurations of Tests 5 and 6. The simulated medium was a 20.7 cm by 14.6 cm grid with variably-sized elements that decrease in width proximal to a vertically-oriented 1-mm wide fracture located approximately equidistantly from the two vertical boundaries (Figure 8-1). The two vertical edges of the container were simulated as constant temperature (20 C or 60 C), no-flow boundaries and the two horizontal edges were treated as adiabatic, no-flow boundaries.

The physical properties assigned to the models were selected to be similar to those of Tests 5 and 6. These attributes have been measured when possible, otherwise the physical values have been taken from the literature. Additionally, the appropriateness of the selected values was assessed during modeling exercises in these simulations and in the simulations performed as part of the dimensionless analysis exercise of this project (Chapter 9).

8.2 NUMERICAL SIMULATION RESULTS

A series of numerical simulations was conducted to assess the redistribution of vapor and liquid in the presence of a fracture simulated in the medium. The simulations were conducted

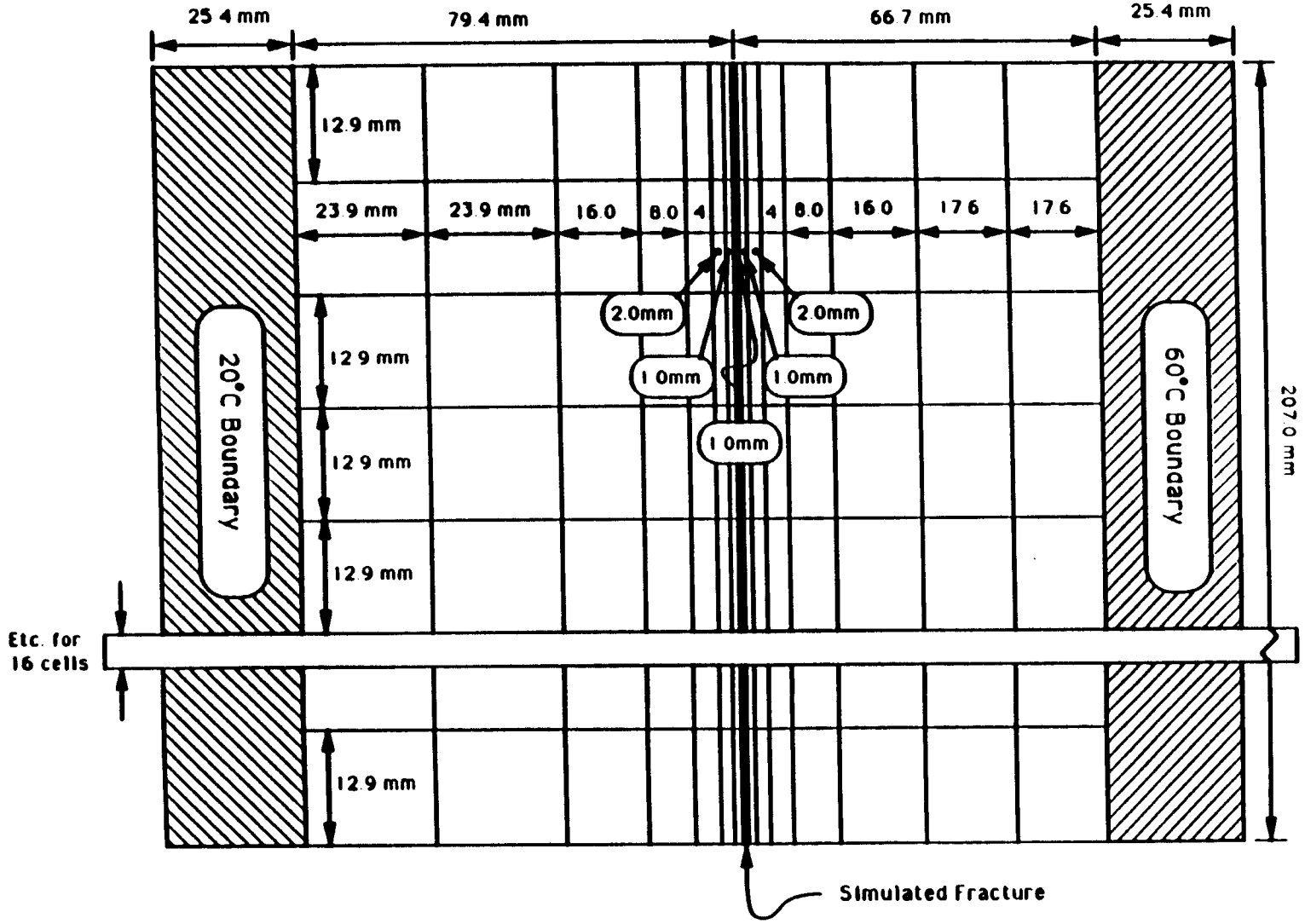

Figure 8-1. Schematic of finite difference grid used in numerical simulations

under nonisothermal conditions (20 C at the left vertical boundary and 60 C at the right vertical boundary). In order to provide a baseline standard against which the effect of a fracture could be assessed, movement of heat, water vapor, and water was simulated through a medium resembling Tests 5 and 6 but without a fracture imposed upon the matrix. This simulation was performed to assess the effect of nonisothermal boundary conditions upon heat and water flow through the medium but without flow disruption resulting from emplacement of a fracture.

Flow was simulated for 116 days (10^7 seconds), similar to the duration of Test 6. The temperature profile approached steady state early in the simulation. The temperature at the middle of the domain was within 2 C of the final temperature after 1.5 days and was essentially unchanged after 60 days. The distribution of liquid water saturation at the end of the simulation (116 days) for a medium under nonisothermal conditions with no fracture present is illustrated in Figure 8-2. The general effect of the heated (right) boundary in the simulation is to dry out the upper right portion of the test container and increase the liquid saturation in the lower (cooler) left side.

The effect of a vertically-emplaced fracture upon the movement of heat and water was simulated and compared to the baseline simulation with no fracture (Figure 8-2). The liquid and gas saturation of the nonisothermal simulation incorporating a fracture proved to be highly sensitive to the selection of the values assigned to the hydraulic properties of the fracture. This observation has been noted by others (Klavetter and Peters, 1986; Peters et al., 1984; Pruess et al., 1986; Nitao, 1988) with no consensus of what hydraulic properties to assign fractures. The hydraulic conductivity model proposed by van Genuchten (1978) was used in these simulations. The value for $\beta = 4.23$, was taken from Peters et al. (1984) but the air-entry value was calculated for a medium with a hydraulic radius of 80 microns (assumed to be essentially equal to the radius of the larger-sized beads used to simulate the fracture in Tests 5 and 6). Accordingly, the air-entry value (equal to the inverse of α, the van Genuchten parameter) was assigned a value of 1820 Pa.

The values for liquid saturation at 0.5, 1.5, 19.5, 57, and 116 days for the nonisothermal simulation with an imposed fracture are illustrated in Figures 8-3(a) to (e). As presented in this series of figures, the effect of the fracture has been to restrict the flow of liquid water from the cool left side of the container to the heated right side. However, the movement of water vapor does not appear to be impeded by the presence of the fracture. Vector plots of the direction of liquid and water vapor flow are shown in Figures 8-4(a)-(e) to illustrate the direction of flow predicted using VTOUGH as compared to the direction of liquid flow observed using the dye tracers in Tests 5 and 6.

8.3 COMPARISON OF LABORATORY AND SIMULATION RESULTS

A sequence of photographs of dye injected during Test 5 (Figures 5-3 through 5-5) and Test 6 (Figure 7-2) illustrate the direction of movement of the liquid in the test container. Although the duration of the numerical simulations is different from that represented in the photographs, the movement of the dye is helpful in illustrating the direction of flow in the test

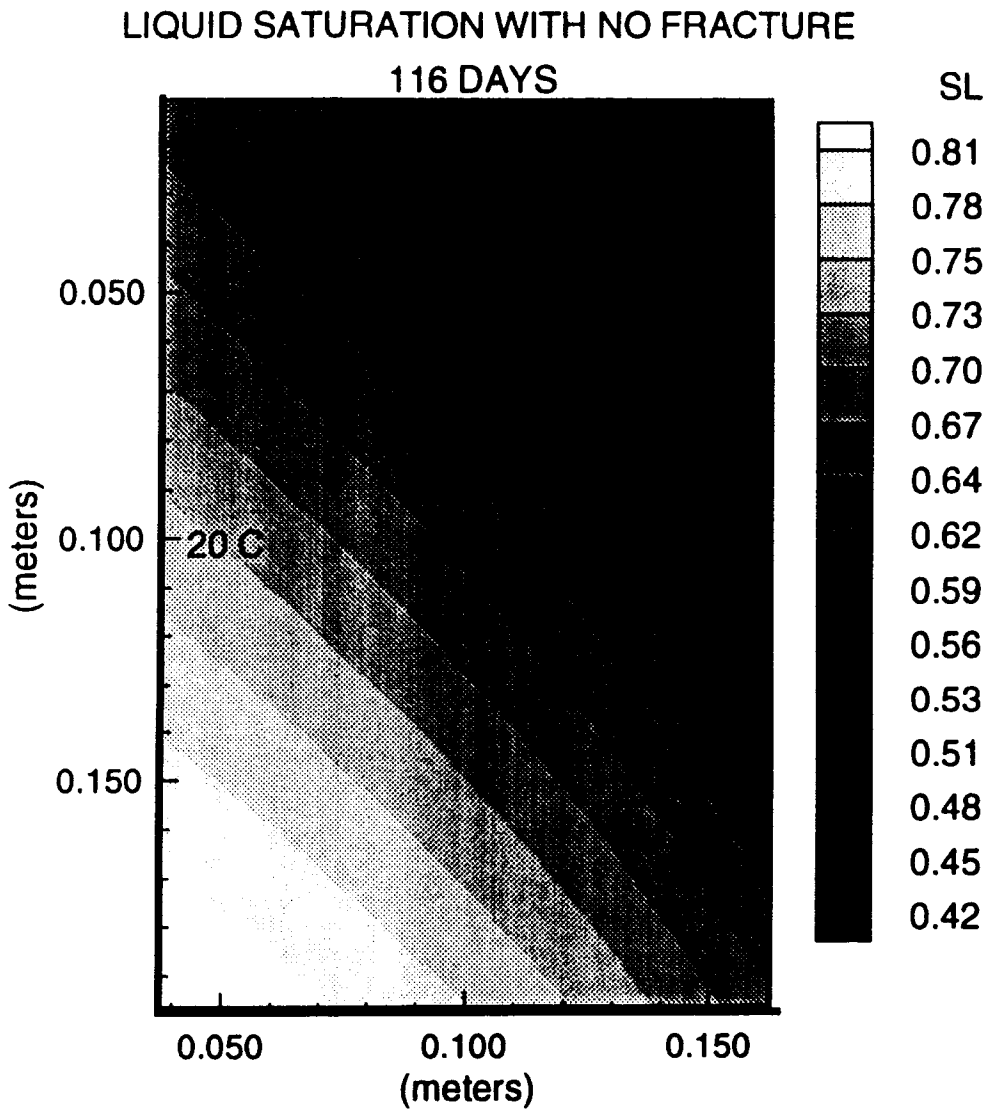

Figure 8-2. Liquid saturation at day 116 with nonisothermal boundary conditions, but no fracture

container at the time the photographs were taken (from 63 to 70 days after the start of Test 6) which is close to Figures 8-3(d) and 8-4(d) (57 days). As illustrated in the photographs, the direction of liquid water flow in the heated side of the test container was downward from the point of injection, in a direction sub-parallel to the heated boundary. The direction of flow shifted toward the center at the bottom of the test container. Although this basic flow regime was also observed in Test 5, it was not replicated in the numerical simulations.

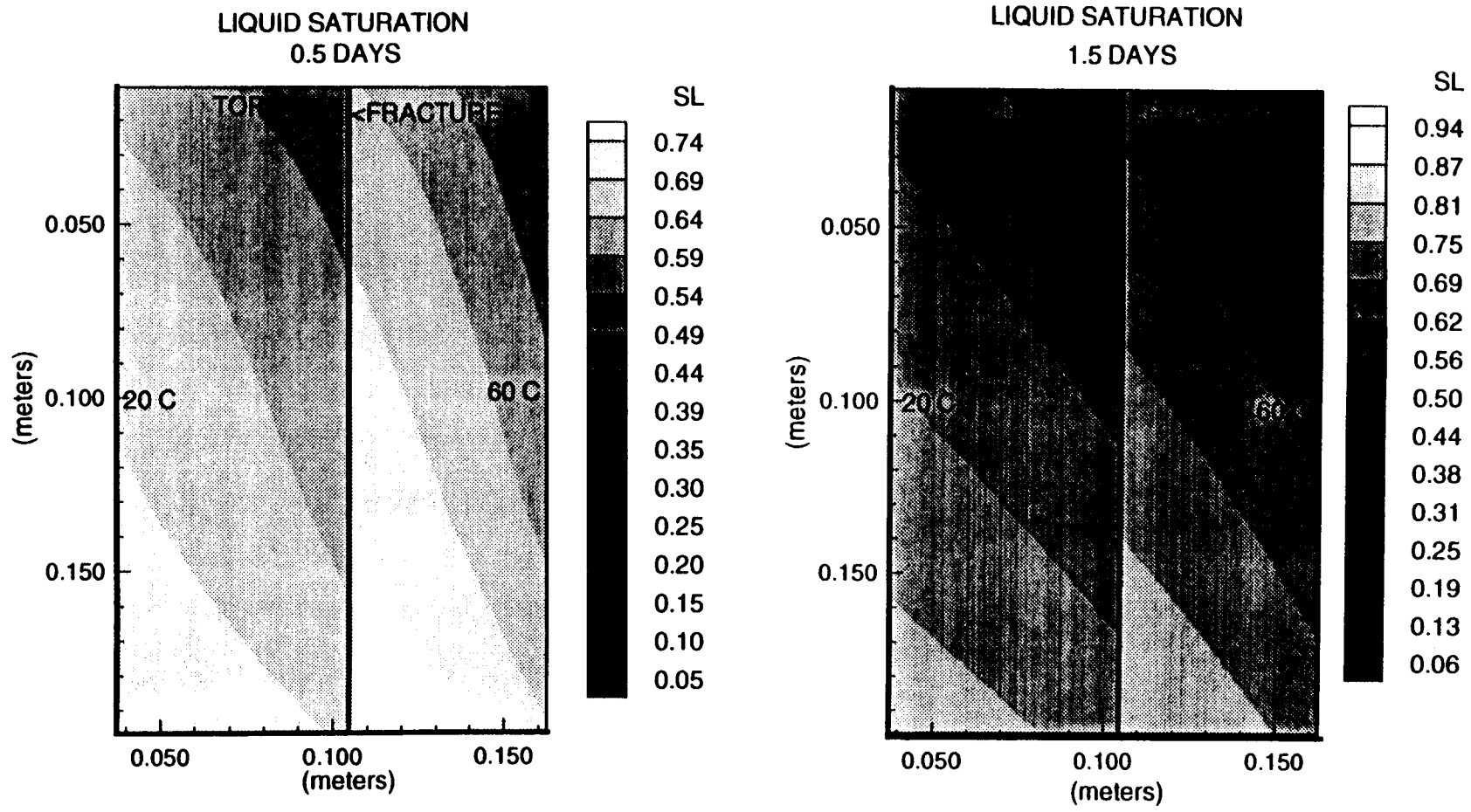

Figure 8-3. Liquid saturation at (a) day 0.5 and (b) day 1.5 with a fracture and with nonisothermal boundary conditions

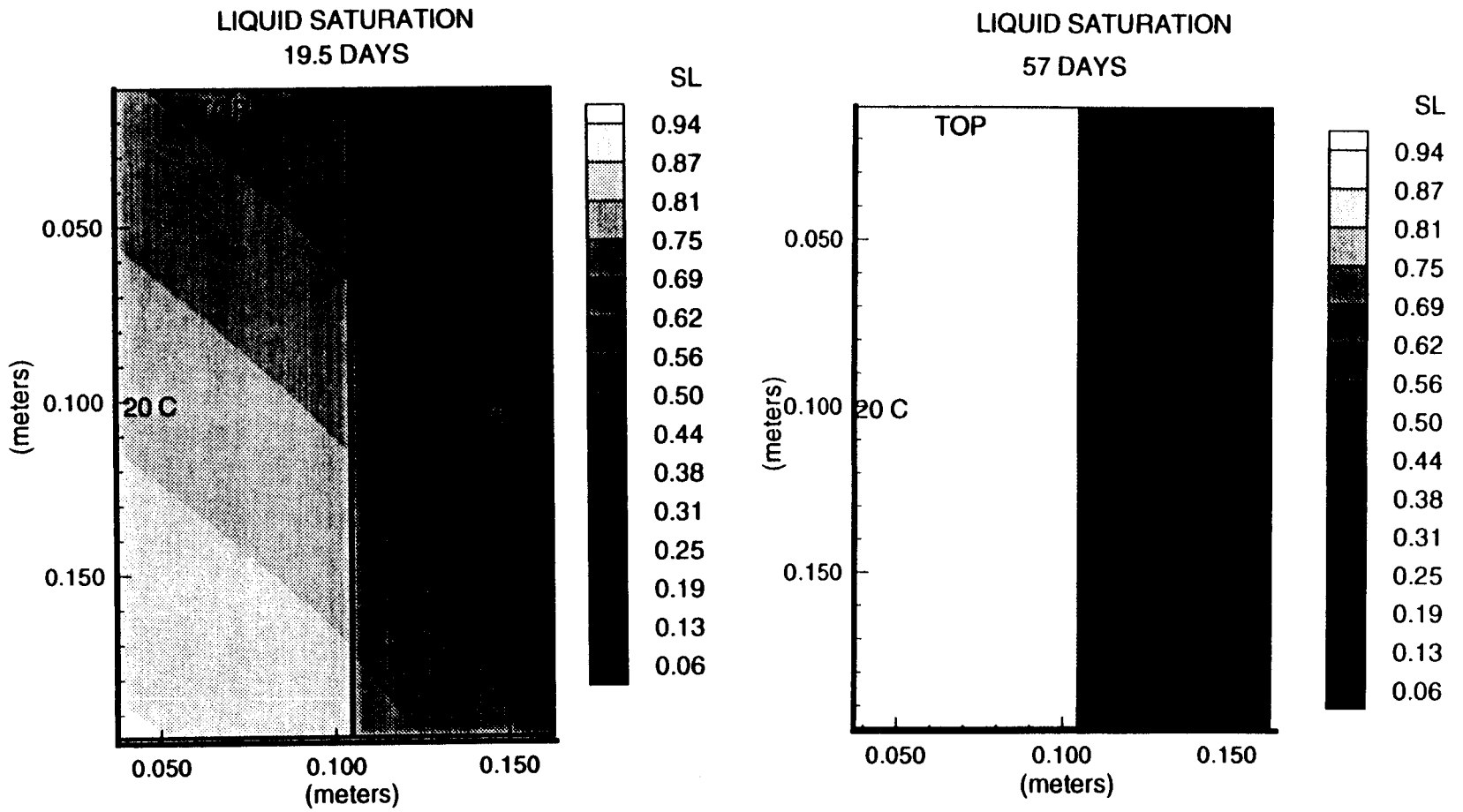

Figure 8-3 (cont'd). Liquid saturation at (c) day 19.5 and (d) day 57 with a fracture and with nonisothermal boundary conditions

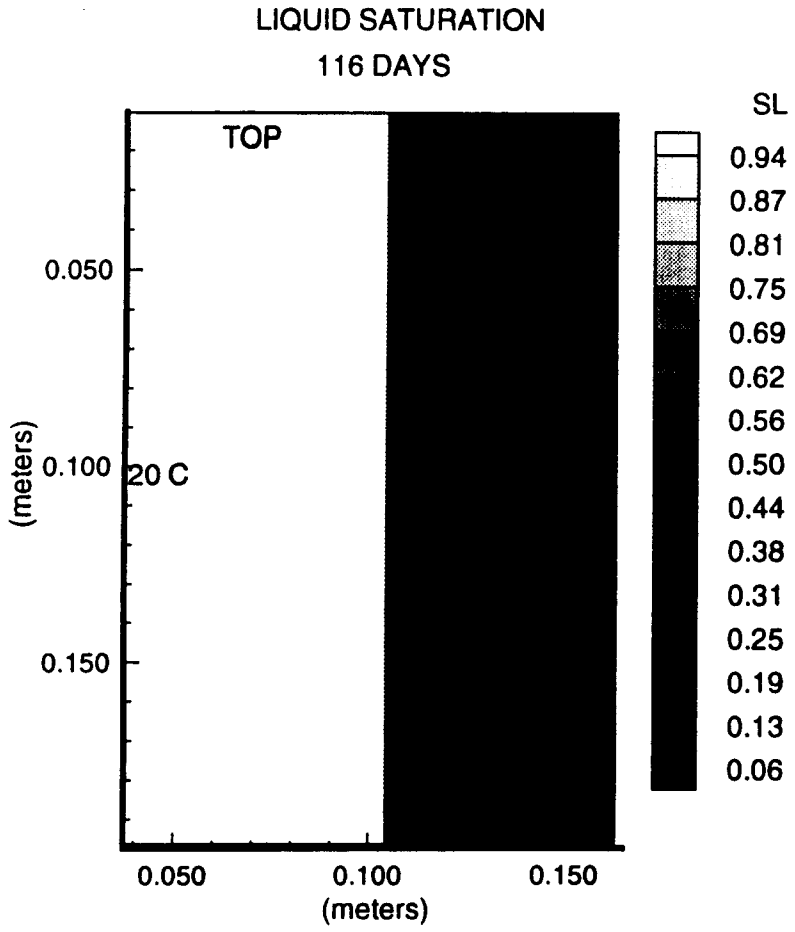

Figure 8-3 (cont'd). Liquid saturation at (e) day 116 with a fracture and with nonisothermal boundary conditions

A conclusive explanation for the discrepancy between the predicted and observed flow regimes has not been identified. One aspect of the laboratory experiment that has not been incorporated into the numerical model is the possible thermo-chemical consequences of: (i) the effect of the chemical (and possible hydraulic) nature of the dye tracer, and (ii) the effect that dissolution and precipitation of the glass beads had upon the hydraulic characteristics of the test medium.

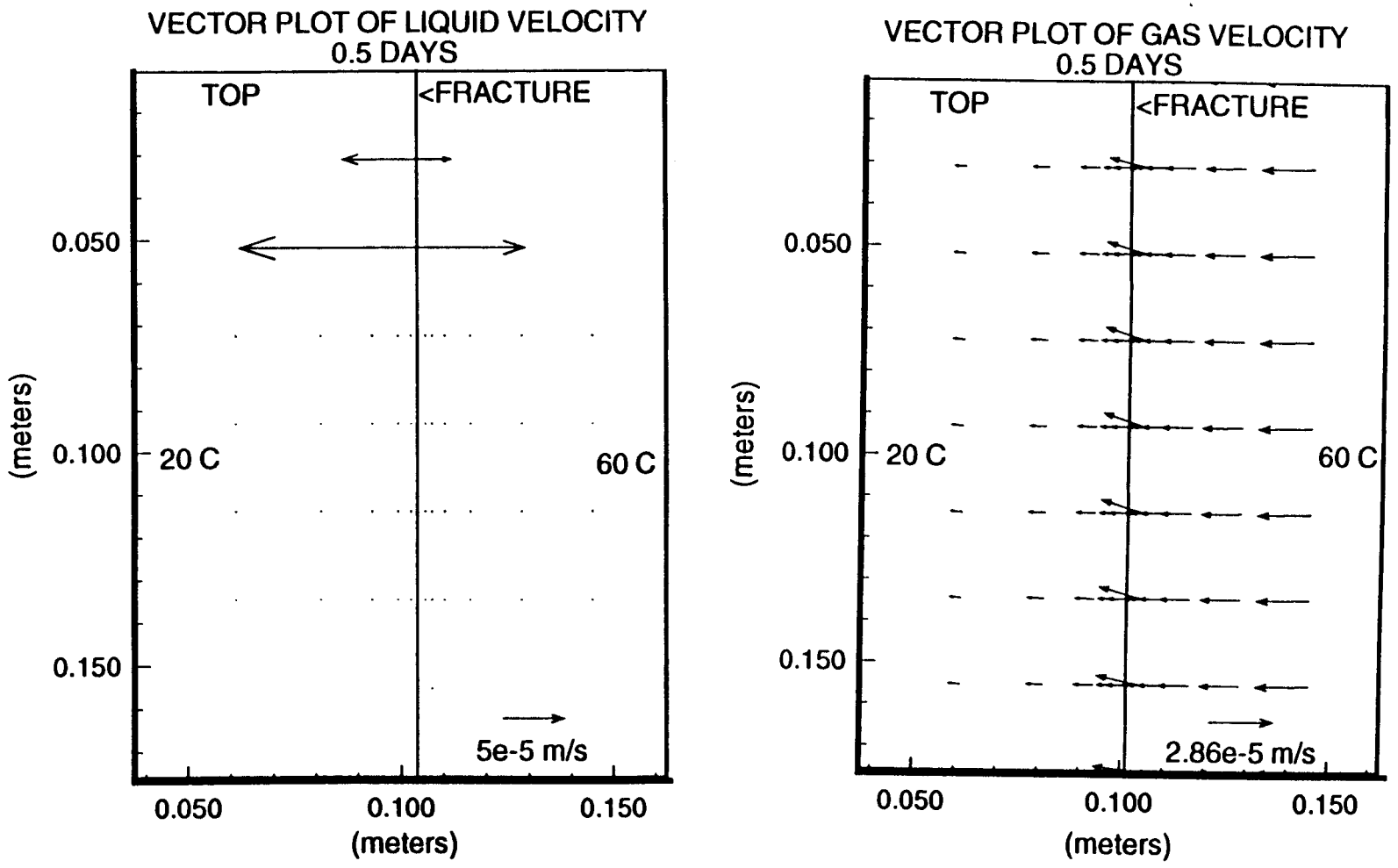

Figure 8-4(a). Vector plot of liquid and water vapor velocities at day 0.5 with a fracture and nonisothermal boundary conditions

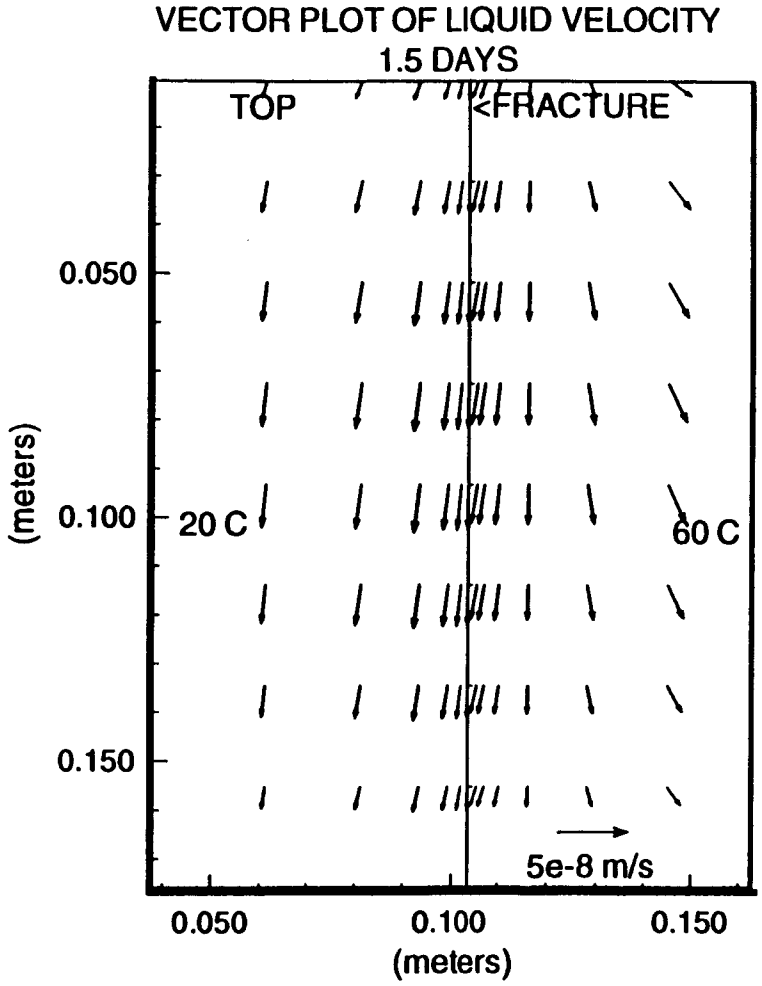

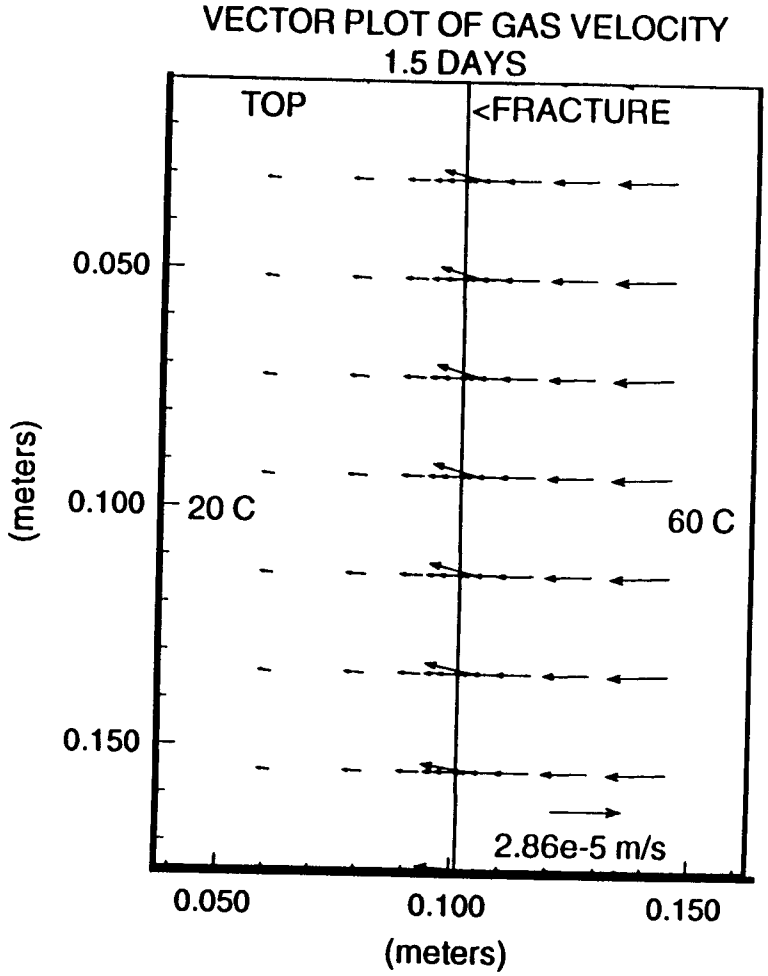

Figure 8-4(b). Vector plot of liquid and water vapor velocities at day 1.5 with a fracture and nonisothermal boundary conditions

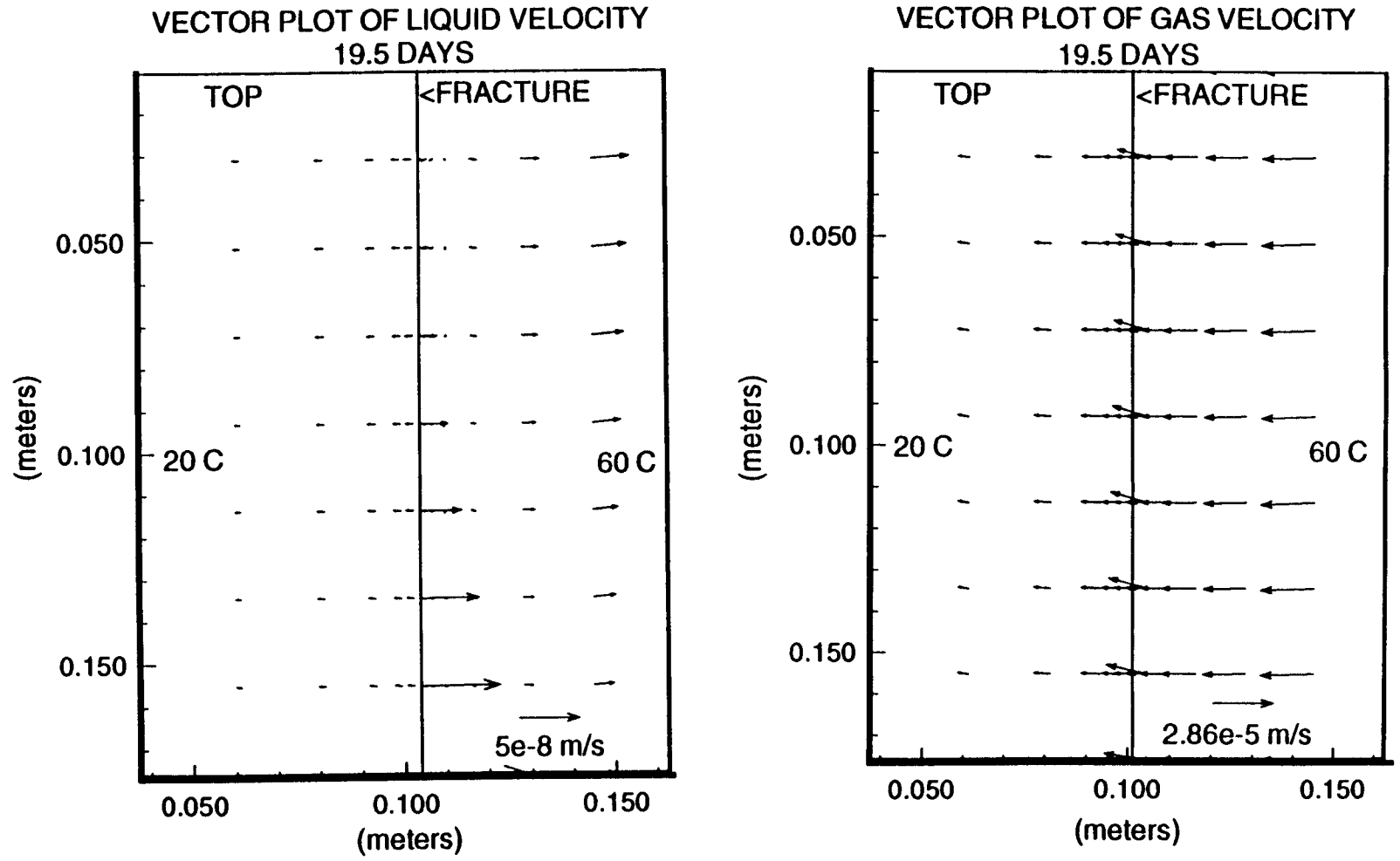

Figure 8-4(c). Vector plot of liquid and water vapor velocities at day 19.5 with a fracture and nonisothermal boundary conditions

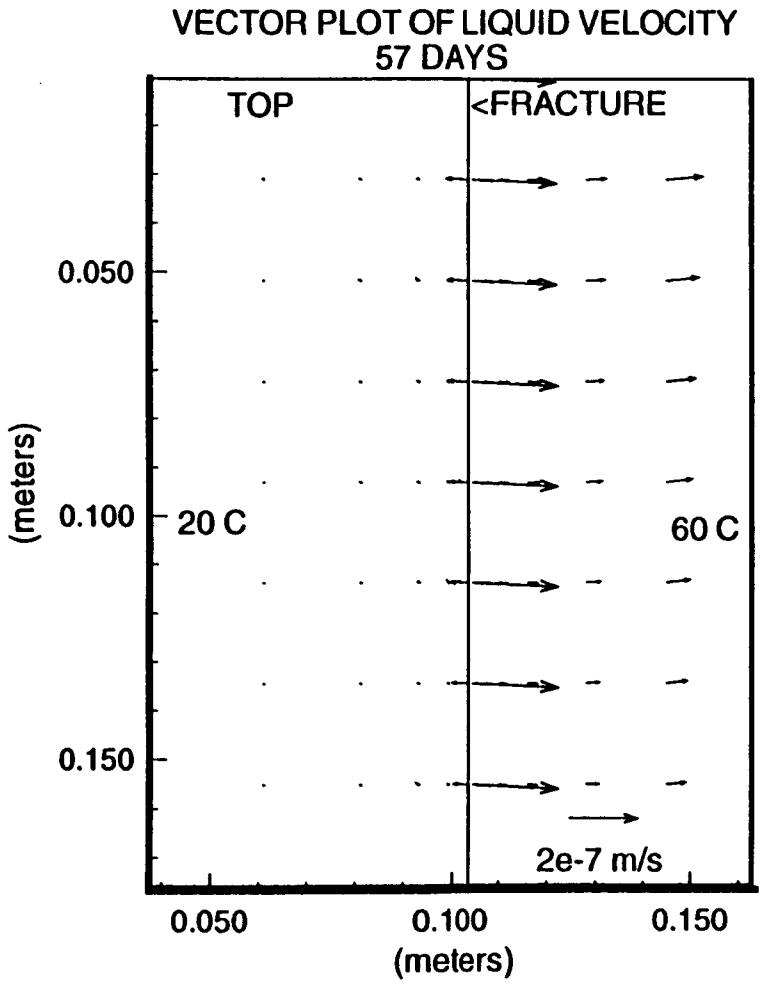

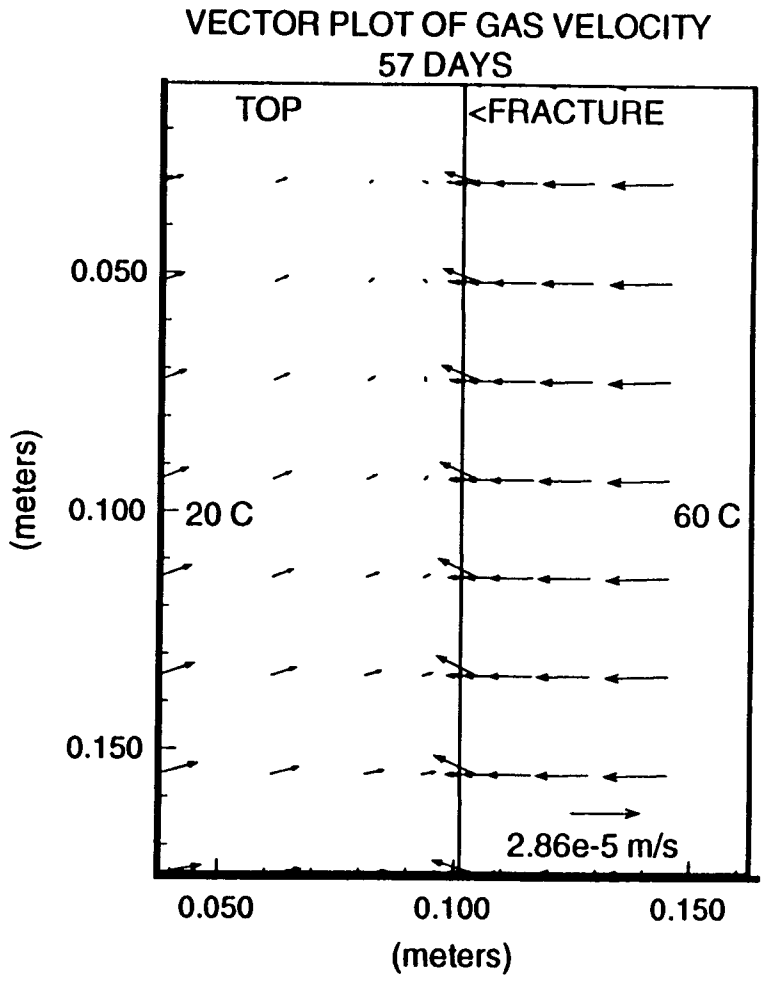

Figure 8-4(d). Vector plot of liquid and water vapor velocities at day 57 with a fracture and nonisothermal boundary conditions

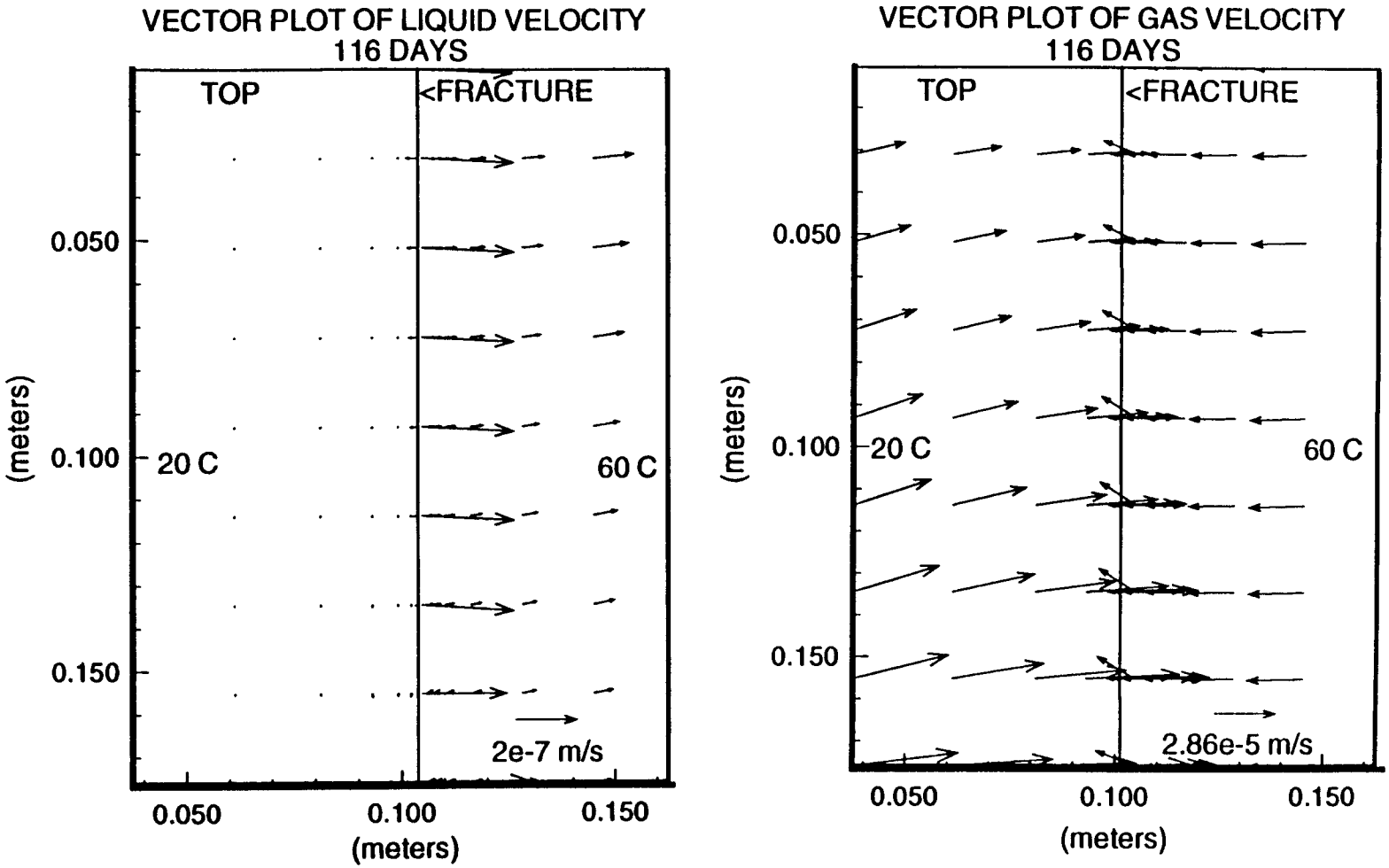

Figure 8-4(e). Vector plot of liquid and water vapor velocities at day 116 with a fracture and nonisothermal boundary conditions

Another possible cause for the observed flow is the quantity of injected liquid dye. The quantities of dye injected during Test 5 (approximately 2 ml per injection) were significantly reduced in Test 6. This was changed to reduce the impact on the local saturation caused by the introduction of a significant quantity of fluid. Consequently, smaller quantities of dye were injected during Test 6. Additionally, the interior end of the dye injection port was advanced to within 2 mm of the front wall of the test container to permit visual tracking of the smaller amount of injected dye. It is believed that injection of the smaller dye quantity, as in Test 6, did not affect the local liquid saturation with the result that the downward traced liquid movement could be attributed to gravity flow caused by the increased saturation.

The chemical attributes of the dye could have also affected the flow pathways taken by the tracer. Residual amounts of the dye were observed to precipitate in the varve-like features of the drying fronts. It is possible, although unsubstantiated, that either the precipitated dye, silica, other material, or a combination of the precipitates could have created preferential pathways followed by liquid water.

Significant degradation of the glass bead medium was experienced over the course of the experiments. Silica from the glass beads was observed to dissolve into the de-ionized water used to partially saturate the test medium. Precipitation of the silica within the medium was also observed. Typically, the silica dissolved from the body of the spheres and precipitated at the contact points between beads with the result that the glass beads were fused together resulting in a consolidated test medium. This observation was substantiated with scanning electron microscope photographs and an examination of the consolidated beads after the termination of the experiment.

In summary, flow through a nonisothermal, fractured porous medium has been numerically simulated and compared to flow observed during the conduct of laboratory-scale experiments. However, the predicted flow patterns were not in agreement with the observed flow patterns. The flow patterns and associated saturation distributions predicted numerically appear to be intuitively correct whereas the patterns and distributions observed in the laboratory were not. Key among the mechanisms observed in the laboratory was a drying zone that formed in the lower corner of the test container near a heated boundary. This drying zone and the associated ridge of increased liquid saturation are believed to be real and not apparent phenomena based on the following consistent observations: (i) densitometer measurements, (ii) tensiometer measurements, (iii) visual observations of dye movement and medium coloration, and (iv) the presence of the same phenomena in both Test 5 and 6. Mechanisms and conditions that could have contributed to the flow patterns observed in the laboratory-scale experiments include the following:

- The effect of the boundary conditions imposed by the side walls of the experimental test container;

- The effect of the chemical (and possible hydraulic) nature of the dye tracer;

- The effect that dissolution and precipitation of the glass beads had upon the hydraulic characteristics of the test medium;

- Mechanisms associated with the hysteretic nature of the test medium.

9 NUMERICAL SIMULATIONS BASED ON DIMENSIONAL ANALYSIS

9.1 BACKGROUND

Dimensional analysis has been proposed in this project as a method to apply the available experimental database and mathematical models to the long-term, full-scale geologic repository. In particular, dimensional analysis has been used to determine dimensionless formulations of the governing equations for the physical processes associated with nonisothermal flow through partially saturated, fractured porous media (see Section 2.1.5). A set of dimensionless terms has been determined from these equations. The parameters contained in the dimensionless terms were assigned values representative of the physical characteristics of a series of laboratory-scale separate-effect experiments conducted at CNWRA, especially Test 6 and of the parameter values used in the VTOUGH simulations described in Chapter 8. Dimensionless terms identified as important were selected for further numerical analyses. These dimensionless terms were numerically evaluated for different property and system values using a computer program, TOUGH (Pruess, 1987), to assess the sensitivity of the flow regime to changes in the values of the dimensionless terms. In other words, the importance of the dimensionless terms has been further assessed by way of sensitivity analysis.

9.2 EXPERIMENTAL DATABASE

The database from which the dimensional analysis was conducted was taken from Tests 5 and 6 of the separate-effect thermohydrological experiments. Although it was the intention of these laboratory-scale experiments to be analogous to a field-scale repository, inherent differences are encountered due to the temporal- and spatial-scale contrasts between the two systems.

Nominal values for the physical characteristics of the separate-effect experiments have been selected for use in the dimensional analysis. These values are listed in Table 9-1. For the purposes of this preliminary assessment, the effect of the fracture has not been incorporated into the evaluation. However, subsequent analyses will incorporate different geometries and features such as a fracture, if warranted.

The dimensionless equations have been derived in Appendix B, hence they are not reproduced here. Values of the dimensionless terms contained in the dimensionless equations have been calculated using the nominal values for the physical characteristics and are listed in Table 9-2.

As part of the initial assessment, the dimensionless terms were evaluated to identify those terms that, at least during this preliminary assessment, merit further evaluation. The parameters that comprise the dimensionless terms have been assigned values representative of the physical characteristics of the laboratory-scale, separate-effect experiments. The numerical magnitude

Table 9-1. NOMINAL VALUES FOR PHYSICAL AND SYSTEM PROPERTIES

Physical properties

Symbol	Description	Value	Units
$c_{p,w,g} \approx c_{v,w,g}$	specific heat for gaseous water	2000	J/kg-K
$c_{p,a} \approx c_{v,a}$	specific heat for air	1000	J/kg-K
c_l	specific heat for liquid	4200	J/kg-K
c_s	specific heat for solid (glass)	≈ 800	J/kg-K
$\rho_{g,o}$	reference gas density	1.0	kg/m^3
$\rho_{s,slg}$	average solid density ($= (1-\phi)\rho_s$)	≈ 2000	kg/m^3
ρ_l	density of liquid	1000	kg/m^3
k_t	saturated thermal conductivity	≈ 1	W/m-K
$k_{t,g}$	gas thermal conductivity	0.025	W/m-K
$k_{t,l}$	liquid thermal conductivity	0.6	W/m-K
u_{lg}	change in internal energy of water for vaporization	2.3×10^6	J/kg
h_{lg}	change in enthalpy of water for vaporization	2.4×10^6	J/kg
α_g	thermal diffusity of gas	20×10^{-6}	m^2/s
α_l	thermal diffusity of liquid	0.1×10^{-6}	m^2/s
α	thermal diffusity of matrix	$\approx 0.7\times10^{-6}$	m^2/s
ν_g	gas kinematic viscosity	20×10^{-6}	m^2/s
ν_l	liquid kinematic viscosity	0.7×10^{-6}	m^2/s
$D_{wa,g}$	binary diffusion coefficient of air and water in gas phase	20×10^{-6}	m^2/s
μ_g	gas dynamic viscosity	20×10^{-6}	$N\text{-}s/m^2$
μ_l	liquid dynamic viscosity	700×10^{-6}	$N\text{-}s/m^2$

Table 9-1. NOMINAL VALUES FOR PHYSICAL AND SYSTEM PROPERTIES (continued)

Physical properties

Symbol	Description	Value	Units
β_g	gas thermal expansion coefficient	0.0034	1/K
T_{ref}	reference temperature	293	K
k_{sat}	saturated hydraulic permeability	$\approx 1.0\times10^{-14}$	m^2
P_g	average gas pressure	1.0×10^5	N/m^2
σ_o	average surface tension	73	N/m
$\frac{d\sigma}{dT}$	rate of change of σ w.r.t. temperature	-0.17	N/m-K

System Properties

Symbol	Description	Value	Units
ΔT_{max}	maximum temperature difference	40	K
g	gravity	9.81	m/s^2
L	height of experiment	0.216	m
τ	tortuosity	$\approx 2/3$	—
ϕ	porosity	≈ 0.35	—

of the dimensionless terms was calculated using the assigned parameter values. Generally, a very large or very small dimensionless term indicates that one of the effects in the ratio that forms the term is unimportant relative to the other. Dimensionless terms were selected for further examination based on physical reasoning, on the observed experimental results of the preliminary separate-effect tests, and on the numerical magnitude of the terms.

Using these criteria, a total of five dimensionless terms were selected for sensitivity analyses. The physical meanings of these five terms are as follows: (i) Ca is the Capillary number, which is the ratio of capillary forces to viscous forces; (ii) Pr_g is the gas Prandtl

Table 9-2. NOMINAL VALUES FOR DIMENSIONLESS TERMS

Geometrical Terms

Term	Value or Range
ϕ	0.35
k_{sat} / L^2	$10^{-12} - 10^{-14}$
τ	2/3

Property Ratio Terms

Term	Value or Range
$\rho_{g,o} / \rho_{s,slg}$	0.0005
$\rho_l / \rho_{s,slg}$	0.5
μ_g / μ_l	0.03
$c_{w,g} / c_{s,slg}$	2.5
$c_a / c_{s,slg}$	1.0
$c_l / c_{s,slg}$	5.0
$Pr_g \equiv \nu_g / \alpha_g$	0.7
$Pr_l = \nu_l / \alpha_l$	5.0
$Le_g \equiv D_{wa,g} / \alpha_g$	1.0
α / α_g	0.035
α / α_l	7.0
$\rho_{g,o} / \rho_l$	0.001

Source Input Term

Term	Value or Range
$\hat{Q}_e \equiv \dfrac{Q_e}{\left(\dfrac{k_t \Delta T_{max}}{L^2}\right)}$	0

Table 9-2. NOMINAL VALUES FOR DIMENSIONLESS TERMS (continued)

Physical Effect Terms

Term	Value or Range
$Bo \equiv \frac{(\rho_l - \rho_{g,o}) g L \sqrt{k_{sat}/\phi}}{\sigma_o}$	1.0×10^{-5}
$Ca \equiv \frac{(\mu_l)^2}{\rho_l \sigma_o \sqrt{k_{sat}/\phi}}$	4.0×10^{-5}
$Gr \equiv \frac{g \beta_g \Delta T_{max} (k_{sat}/\phi) L}{(\nu_g)^2}$	5.0×10^{-5}
$Su \equiv \frac{\Delta T_{max}}{\sigma_o} \left.\frac{d\sigma}{dT}\right\|_o$	- 0.1
$U \equiv \frac{u_{lg}}{(c_l \Delta T_{max})}$	14
$H \equiv \frac{h_{lg}}{(c_l \Delta T_{max})}$	14

Constitutive Terms

Term	Value or Range
$k_{rel,l}$	function of S_l, (0,1)
$k_{rel,g}$	function of S_g, (0,1)
J	function of S_l
$\left(\frac{dJ}{dS_l}\right)$	function of S_l, $(-\infty,0)$

Table 9-2. NOMINAL VALUES FOR DIMENSIONLESS TERMS (continued)

Time Term

Term	Value or Range
$\hat{t} \equiv \frac{t}{\left(\frac{L^2}{\alpha}\right)}$	»1

Response Terms

Term	Value or Range
$m_{a,g}$	function of $T(\theta)$, $P_c(S_l)$
$m_{w,g}$	(= 1 - $m_{a,g}$)
$\hat{\rho}_g$	function of $T(\theta)$, P_g
S_l	(0,1)
S_g	(= 1 - S_l)
θ	(0,1)

number, which is the ratio of viscous diffusion to thermal diffusion; (iii) dJ/dS_l (also known as the inverse of the specific moisture capacity) is the ratio of the change of capillary pressure to the change in liquid saturation; (iv) Su is the surface tension number which is the change in capillary pressure with temperature; and (v) Le_g is the Lewis number, which is the ratio of mass diffusion to thermal diffusion.

Dimensionless time, $\hat{t}$, and relative hydraulic conductivity, k_{rel}, are recognized as difficult yet important dimensionless terms in the analysis. Although relative hydraulic conductivity is not explicitly addressed in the five dimensionless terms selected for analysis, it is implicitly contained in the dimensionless terms Ca and dJ_s/dS_l. Dimensionless time is included in the analysis as a dependent variable.

The influence of each dimensionless term was investigated separately by increasing and decreasing each term by 25 percent relative to its nominal value, while holding all the other

terms constant. The effect of variations in the input values of the five dimensionless terms was evaluated using a numerical model called TOUGH (Pruess, 1987) and a variation of the code, VTOUGH (Nitao, 1989). TOUGH calculates the flow of air and water through fractured porous media. In each simulation, the input parameters, except for the perturbed variable, were assigned values from a nominal case.

One parameter in each of the five dimensionless terms was varied by 25 percent to vary the value of the dimensionless term. For example, $Ca = (\mu_l)^2 / (\rho_l \sigma_o \sqrt{k_{sat}/\phi})$ was varied by changing the shape factor c that relates the saturated permeability k_{sat} to the pore size d_o, that is, $k_{sat} = c d_o^2$. By changing c, Ca could be varied, and none of the other dimensionless terms was altered. In similar fashion, Pr_g was varied by changing specific heat and Le_g was varied by changing tortuosity.

Unfortunately, some dimensionless terms cannot be easily varied without varying other dimensionless terms. Accordingly, not all of the dimensionless terms selected for this analysis could be treated in the straightforward manner of simply varying one parameter because of this and because the TOUGH code is written in such a way that many of the parameters in the dimensionless terms do not appear in the code. For that reason, neither Su nor dJ/dS_l could be varied simply by changing one parameter. Instead, a more complicated method was used. The empirical function used in this application of the code to relate the capillary pressure P_c to the liquid saturation S_l was:

$$P_c = P_o \left[S_l^{\frac{\beta}{1-\beta}} - 1 \right]^{1/\beta} \sim J(S_l) \qquad (9\text{-}1)$$

where P_o is the air-entry value (the inverse of α) and β is the van Genuchten parameter to be specified. The baseline values used in the study were: $S_l = 0.65$; $P_o = 1.344 \times 10^6$ [N/m^2]; and $\beta = 4.23$. By choosing other appropriate values for P_o and β, P_c can be varied while holding dJ/dS_l constant, or dJ/dS_l can be varied while holding P_c constant, for a saturation of 0.8; this allowed us to vary both of the capillary pressure terms, dJ/dS_l and Su, individually while holding all other dimensionless terms constant. Of course, if the saturation level at a point changed significantly from its initial value, many of the dimensionless terms appropriate to that location deviated from their nominal values; but this procedure still allowed investigation of the influence of the dimensionless terms separately.

It is recognized that some combinations of parameters, such as P_o and λ for instance, may not be realistic. This fact, however, should not detract from the preliminary nature of this analysis and the information base contributed by these results.

Numerical simulations were performed to determine the magnitude of change caused by variation of each dimensionless term while holding the input values of all other dimensionless terms constant. The computed values for gas saturation at a point in the model near the fracture

were plotted against time for each simulation. The selected point was near the imposed fracture so that gas saturation values at a location of thermohydrological interest would be observed.

The computed gas saturation values from the simulations for the five cases for each dimensionless term are illustrated in Figures 9-1 through 9-5. Also illustrated in each figure for comparison is a plot of gas saturation against time for the nominal case.

9.3 RESULTS OF DIMENSIONAL ANALYSIS

Evaluation of the flow regime by dimensional analysis has yielded a range in the sensitivity of gas (and liquid) saturation to changes in the values of the dimensionless terms. Changes in dimensionless terms that result in significant changes in the flow regime identify those parameters that require further evaluation when using results at one scale to imply behavior at another scale. Examination of the results reveals that the flow regime is relatively insensitive to variation in Ca (Figure 9-1) and Pr_g (Figure 9-2), moderately sensitive to Le_g (Figure 9-5), and highly sensitive to dJ/dS_l (Figure 9-3) and Su (Figure 9-4). These results indicate that Ca and Pr_g can be varied by moderate amounts (25 percent) without adversely affecting the flow field, a property not true for the other three dimensionless terms. Of notable importance is that although a 25-percent change in tortuosity is significant, a 25-percent change in permeability is not. Changes in saturated permeability, k_{sat}, of several orders of magnitude over small distances are commonly encountered in field situations.

Variation of the parameters in dJ/dS_l and Su, however, results in large changes to the flow regime. Both of these dimensionless terms are associated with liquid surface tension and capillary pressure which, in turn, are related to moisture content and the saturated permeability. The results of these two analyses further illustrates the difficulties associated with the nonlinearity of flow through partially saturated, fractured porous media.

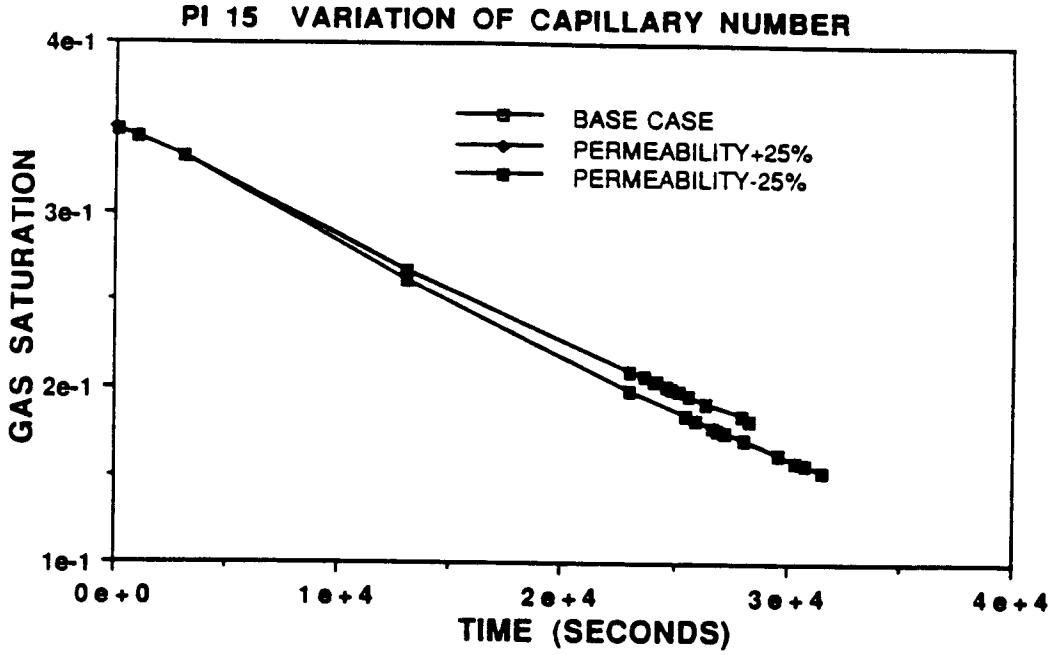

Figure 9-1. Plot of gas saturation numerically calculated vs time using the TOUGH code at a grid point near a simulated fracture. Capillary number, Ca, was varied by changing the input value of permeability by 25 percent while keeping all other input values the same. Gas saturation for simulations with nominal input values is included for comparison.

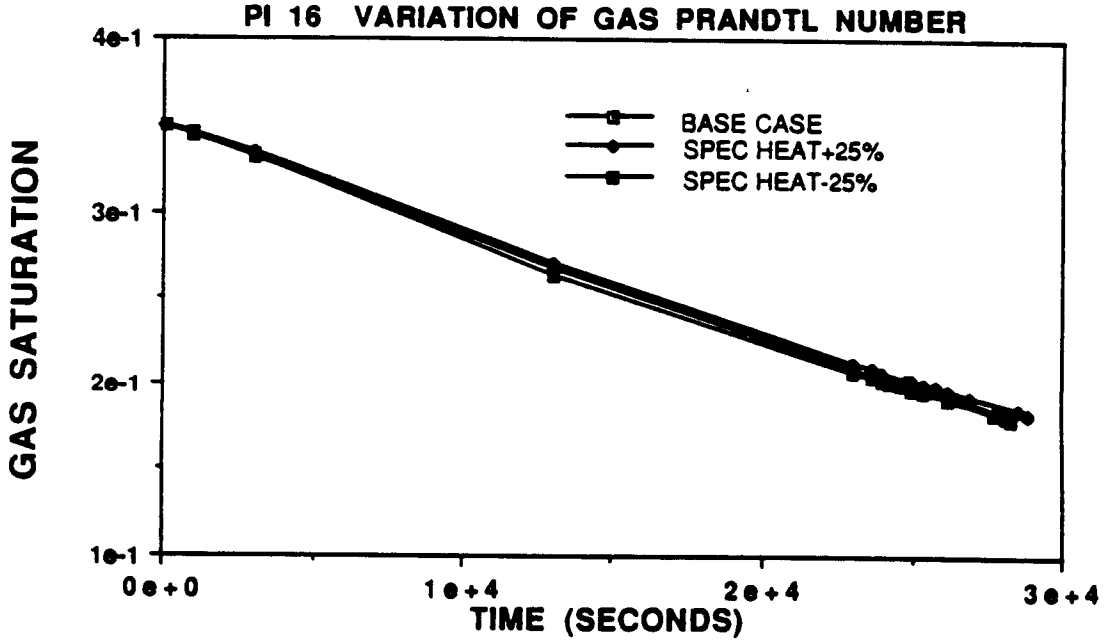

Figure 9-2. Plot of gas saturation numerically calculated vs time using the TOUGH code at a grid point near a simulated fracture. Gas Prandtl number, Pr_g, was varied by changing the input value of specific heat by 15 percent while keeping all other input values the same. Gas saturation for simulations with nominal input values is included for comparison.

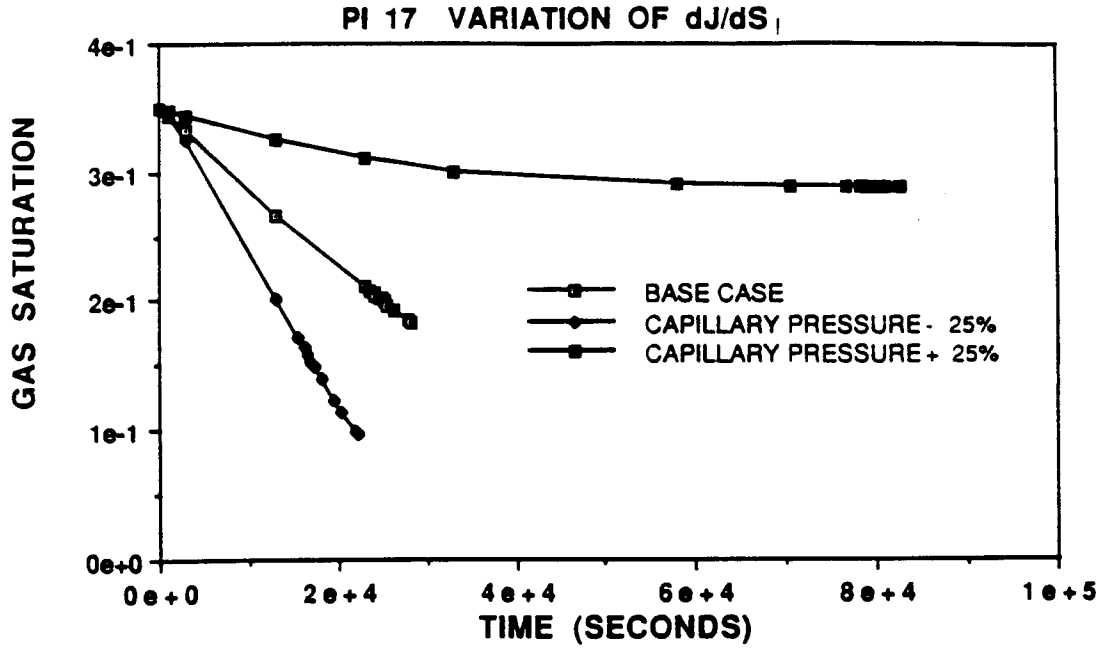

Figure 9-3. Plot of gas saturation numerically calculated vs time using the TOUGH code at a grid point near a simulated fracture. Inverse specific moisture capacity, dJ/dS_l, was varied by changing the input value of capillary pressure by 25 percent by varying P_o and β while keeping all other input values the same. Gas saturation for simulations with nominal input values is included for comparison.

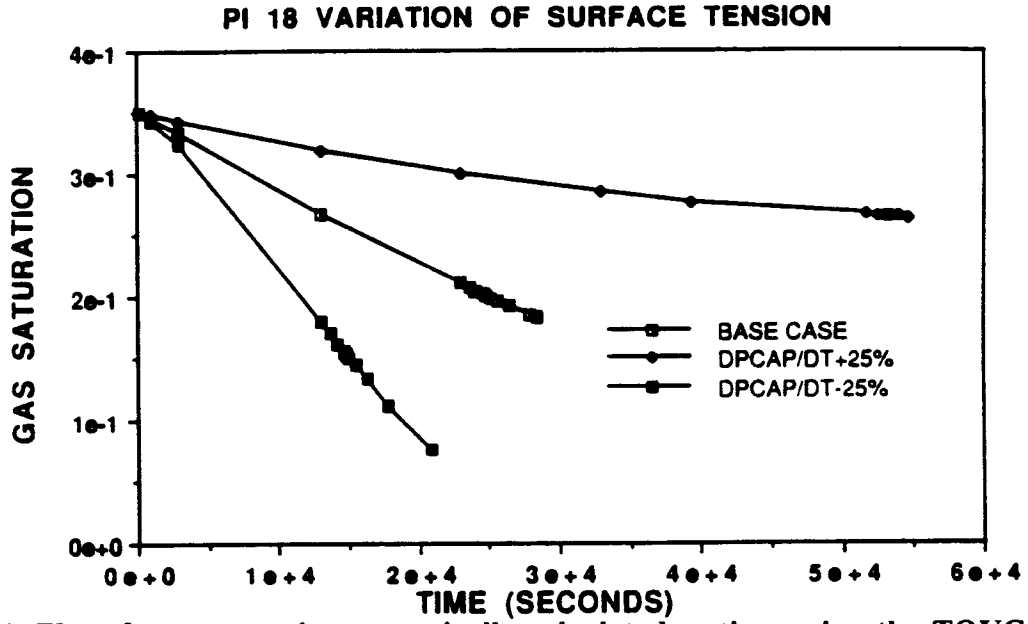

Figure 9-4. Plot of gas saturation numerically calculated vs time using the TOUGH code at a grid point near a simulated fracture. Surface tension ratio, Su, was varied by changing the input value of the matrix hydraulic characteristics, α and β, by 25 percent while keeping all other input values the same. Gas saturation for simulations with nominal input values is included for comparison.

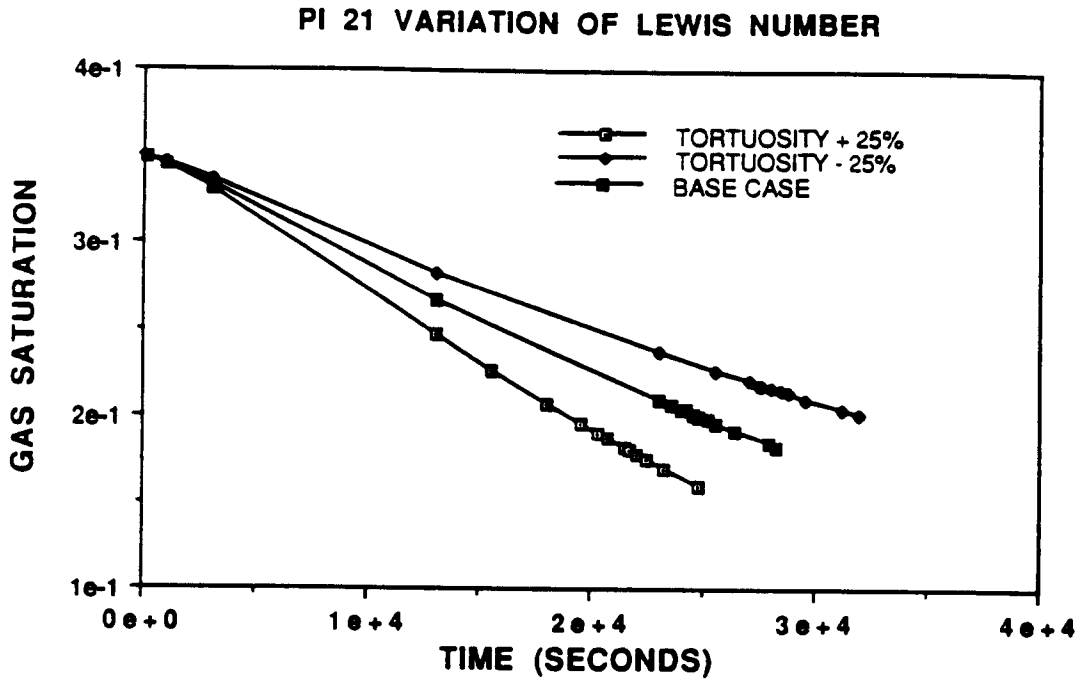

Figure 9-5. Plot of gas saturation numerically calculated versus time using the TOUGH code at a grid point near a simulated fracture. Gas Lewis number, Le_g, was varied by changing the input value of tortuosity by 25 percent while keeping all other input values the same. Gas saturation for simulations with nominal input values is included for comparison.

10 SUMMARY AND CONCLUSIONS

Thermohydrological phenomena (i.e., heat transfer, thermally driven flow in liquid and gas phase, coupled mass transfer) will play a key role in the performance of a high-level waste repository. The current lack of a definitive information base relevant to the proposed repository setting has led to questions of the adequacy of the present state of knowledge about these phenomena. For this reason, the Thermohydrology Research Project was initiated.

A detailed knowledge of thermohydrologic phenomena is needed to support a thorough assessment of:

- The effects of thermohydrologic phenomena on waste package corrosion, failure and release of contaminants;
- The extent of the thermally-disturbed zone;
- Fluid and contaminant transport from the repository to the accessible environment.

The knowledge gained from this experimental and analytical program will also directly benefit NRC's independent review of other elements of the repository program such as repository design, site geochemistry and scenario analysis. Specific objectives have been identified to support this assessment. These are summarized as the following:

- Perform a critical assessment of the state-of-knowledge of thermohydrology in partially saturated fractured media;
- Perform a detailed dynamic similarity or similitude analysis on the complete set of governing equations relevant to partially saturated flow and to determine the set of dimensionless parameters required to conduct appropriate laboratory simulations;
- Identify potential problems associated with the design and performance of laboratory simulations;
- Design and perform laboratory experiments to identify key dependent and independent parameters and their relationships in the context of thermohydrologic issues;
- Develop the laboratory facilities, experimental methods, measurement technqiues, and associated analytic skills to evaluate and validate other program results;
- Examine and correlate laboratory results with field data, to aid in the design of future field experiments;

- Perform numerical simulations of two-phase flow through partially saturated, fractured porous media under nonisothermal conditions as part of the dynamic similitude analysis and to evaluate the capability to numerically simulate thermohydrological processes.

The scope of this project encompasses three specific and related areas: (i) laboratory experiments, (ii) mathematical models, and (iii) dimensional (or similitude) analysis. The technical objectives and accomplishments of each of the research areas are described below.

10.1 LABORATORY EXPERIMENTS

Laboratory experiments of nonisothermal flow and transport phenomena is the primary focus of the research project. The basic objectives of these experiments are:

- Determine how to accurately measure fluid state parameters (suction heads, temperatures, water content, etc.) in a variably-saturated, fractured porous medium;
- Develop experimental designs that will permit the careful and systematic study of individual thermohydrologic processes;
- Compile experimental data that can be used in testing mathematical models.

The accomplishments to date in the area of laboratory experiments include:

- A survey and evaluation of experimental measurement techniques;
- A series of scoping experiments to study the capabilities and limitations of experimental instruments;
- A series of separate-effect experiments to study various aspects of thermohydrologic processes in a porous medium with a simulated fracture.

Instrumentation and measurement techniques that proved to be useful in experiments conducted as part of this project include (i) a densitometer used to provide data for moisture content measurements; (ii) tensiometers for suction pressure measurements; (iii) thermistors for temperature measurements; and (iv) dye tracers to indicate the direction of liquid flow.

Experiments were conducted on a test container of (initially) unconsolidated porous media with a simulated fracture. The test containers were configured in two dimensions and subjected to nonisothermal boundary conditions. Accomplishments in this area include the following.

- Laboratory instrument and measurement techniques have been developed to provide meaningful quantitative results of two-phase experiments in a porous medium.

Gamma-ray densitometers for moisture content and tensiometers for suction pressure have been selected to support two-dimensional laboratory-scale experiments.

- Two-phase flow mechanisms that could potentially be present in a HLW repository have been designed, conducted, and observed at the laboratory scale.

- Key nonisothermal mechanisms in the laboratory experiments have been identified and observed. Intriguing results including moisture content distributions, liquid flow patterns, and the establishment of a drying front were observed but are not yet fully explained.

10.2 MATHEMATICAL MODELS

Data collected from laboratory experiments are interpreted using various mathematical models. These interpretations enhance the general knowledge regarding such technical issues as:

- What degree of predictive error is introduced when Darcy's law is applied to situations of very low saturation?

- Does the local equilibrium assumption in two-phase flow introduce large or small predictive error?

- What is the significance of the various empirical coefficients in vapor and liquid phase transport theories?

- How well can we mathematically describe fluid flow through discrete fractures and interactions with the porous matrix?

The knowledge gained from this effort will allow us to assess the relative importance of different phenomena and improve the design of laboratory and field experiments. To date, the accomplishments in this area include the following.

- A comprehensive review of the literature on the theory of heat and mass transfer in partially saturated porous medium.

- A detailed development of the governing conservation and constitutive equations.

- Mathematical models of key nonisothermal mechanisms observed in the laboratory have been proposed.

- Numerical models containing specified mathematical models were used to simulate processes observed in the laboratory experiments. Neither the mathematical models

nor the numerical models have successfully simulated the nonisothermal liquid flow observed in Tests 5 and 6 in the laboratory.

10.3 DIMENSIONAL ANALYSIS

Based on a mathematical model, dimensional (or similarity) analysis is proposed to extrapolate laboratory experimental data to predict the thermohydrologic response at field experiments and at the proposed HLW repository. Relevant questions that were addressed during the analyses included the following:

- What is the list of dimensionless terms for thermohydrologic processes?
- What are the important dimensionless terms at the laboratory scale that need to be matched to the field or repository scale?

To date, the accomplishments in this area include the following.

- A detailed development of the dimensionless equations was completed and documented, and a total of twenty-seven dimensionless terms in the governing equations were identified.
- The significance of the dimensionless terms for conditions resembling the laboratory experiments was evaluated. Five dimensionless terms were selected for additional evaluation.
- A numerical study was performed to investigate the deterministic sensitivity of heat and mass transfer processes incorporated in the dimensionless terms. Processes associated with the moisture-content/suction-pressure relationships were identified as being the most sensitive.

10.4 OVERALL SUMMARY

Overall, significant progress has been made in the areas of laboratory experiments, mathematical models, and dimensional analysis for the Thermohydrology Research Project. However, this project is continuing as resolution on many topics has not been achieved. In the area of laboratory experiments, experimental techniques have been extensively reviewed and the most promising techniques have been tested. In the area of mathematical models, the governing conservation and constitutive equations have been developed, and areas for continuing investigation have been highlighted. In the area of dimensional analysis, the governing equations have been expressed in terms of dimensionless groups, and a preliminary assessment to identify the dimensionless groups important to fluid flow and heat transport through partially saturated fractured porous media has been completed. Although significant progress has been made in these three technical areas, efforts will be continued to build on results based on the foundational work completed to date.

11 REFERENCES

Ababou, R. 1991. *Approaches to Large Scale Unsaturated Flow in Heterogeneous, Stratified, and Fractured Geologic Media.* NUREG/CR-5743. Washington, DC: Nuclear Regulatory Commission.

Adamson, A.W. 1967. *Physical Chemistry of Surfaces.* New York, NY: Intersciences Press.

Allen, N.F., F.E. Richart, and R.D. Woods. 1980. Fluid Wave Propagation in Saturated and Nearly Saturated Sands. *ASCE Journal of the Geotechnical Engineering Division* 106(6T3): 235-254.

Archie, G.E. 1942. The electrical resistivity log as an aid in determining some reservoir characterisitcs. *Trans. A.I.M.E.* 146: 54-62.

Baker, W.E., P.S. Westine and F.T. Dodge. 1973. *Similarity Methods in Engineering Dynamics.* Rochelle Park, NJ: Hayden Book Co.

Basel, M.D. and K.S. Udell. 1989. Two-dimensional study of steam injection into porous media. *Multiphase Transport in Porous Media-1989.* R.R. Eaton, K.S. Udell, M. Kaviany, and K. Vafai, eds. FED-82, HTD-127. New York: American Society of Mechanical Engineers: 39-46.

Batchelor, G.K. 1967. *An Introduction to Fluid Dynamics.* London: Cambridge University Press.

Bear, J. 1972. *Dynamics of Fluids in Porous Media.* New York: Dover Publications.

Bear, J. and Y. Bachmat. 1991. *Introduction to Modeling of Transport Phenomena in Porous Media.* Norwell, MA: Kluwer Academic Publishers Group.

Bejan, A. 1984. *Convection Heat Transfer.* New York: John Wiley.

Bian, S.H., M.J. Budden and S.C. Yung. 1987. *Application of GEOTHER/VT4 to Assess Groundwater Transients in a High Level Radioactive Waste Repository.* PNL-SA-14502. Richland WA: Pacific Northwest Laboratory.

Bian, S.H., M.J. Budden, C.L. Bartley, and S.C. Yung. 1988a. *GEOTHER Evaluation and Improvement: A Progress Report Including Test Cases for Two-Dimensional BWIP Analysis.* PNL-6245. Richland WA: Pacific Northwest Laboratory.

Bian, S.H., M.J. Budden, C.L. Bartley, and S.C. Yung. 1988b. *GEOTHER/VT4: A Two-Phase Groundwater Fluid Flow and Heat Transport Code for High-Level Radioactive Waste Applications*. PNL-6517. Richland WA: Pacific Northwest Laboratory.

Bird, R.B., W.E. Stewart, and E.N. Lightfoot. 1960. *Transport Phenomena*. New York: John Wiley.

Bixler, N.E. 1985. *NORIA - A Finite Element Computer Program for Analyzing Water, Vapor, Air, and Energy Transport in Porous Media*. SAND84-2057. Albuquerque, NM: Sandia National Laboratories.

Briscoe, R.D. 1984. *Thermocouple Psychrometers for Water Potential Measurements*. Ciocco, Italy: NATO Advanced Study Institute on Advanced Agricultural Instrumentation II.

Brooks, R.H. and A.T. Corey. 1966. Properties of porous media affecting fluid flow. *J. Irrig. and Drain. Div., Proc. ASCE, IR2*. 92: 61-88.

Bruce, R.R. 1972. Hydraulic conductivity evaluation of the soil profile from soil water retention relations. *Soil Sci. Soc. Am. Proc.* 36: 555-561.

Brutsaert, W. 1967. Some methods of calculating unsaturated permeability. *Trans. ASAE*. 10: 400-404.

Buckingham, E. 1914. Model experiments and the forms of empirical equations. *Physical Review*. 4: 345.

Burdine, N.T. 1953. Relative permeability calculation from size distribution data. *Trans. AIME*. 198: 71-78.

Buscheck, T.A. and J.J. Nitao. 1988. *Preliminary Scoping Calculations of Hydrothermal Flow in Variably Saturated, Fractured, Welded Tuff during the Engineered Barrier Design Test at the Yucca Mountain Exploratory Shaft Test Site*. UCID-21571. Livermore, CA: Lawrence Livermore National Laboratory.

Carman, P.C. 1937. Fluid flow through a granular bed. *Trans. Instn Chem Engrs (London)*. 15: 150-156.

Carslaw, H.S. and J.C. Jaeger. 1959. *Conduction of Heat in Solids*. Oxford, Great Britain: Oxford University Press.

Chen, S. and S. Chung. 1990. Capillary effect on superheated vapor condensation in porous media. *Journal of the Chinese Society of Mechanical Engineers*. 11(5): 423-431.

Chuang, Y., W.R. Haldeman, T.C. Rasmussen, and D.D. Evans. 1989. *Laboratory Analysis of Fluid Flow and Solute Transport Through a Variably Saturated Fracture Embedded in Porous Tuff.* FIN D1662. Draft Report. Washington, DC: Nuclear Regulatory Commission.

Clemo, T.M., J.D. Miller, L.C. Hull, and S.O. Magnuson. 1990. *FRAC-UNIX Theory and User's Manual.* EGG-EP-9029. Idaho Falls, ID: EG&G Idaho.

Corey, A.T. 1986. *Mechanics of Immiscible Fluids in Porous Media.* Littleton, CO: Water Resources Publications.

Cravalho, E.G. and J.L. Smith. 1981. *Engineering Thermodynamics.* Cambridge, MA: by authors.

CRC Handbook of Chemistry and Physics. 1982. R.C. Weast, ed., Cleveland, OH: CRC Press.

Dagan, G. 1986. Statistical theory of groundwater flow and transport: pore to laboratory, laboratory to formation, and formation to regional scale. *Water Resources Research.* 22(9): 120S-134S.

Daily, W. and W. Lin. 1989. *Laboratory Determined Suction Potential of Topapah Spring Tuff.* UCRL-102127. Livermore, CA: Lawrence Livermore National Laboratory.

Daily, W. and A. Ramirez. 1989. Evaluation of electromagnetic tomography to map in situ water in heated welded tuff. *Water Resources Research.* 25(6): 1083-1096.

Daniel, D.E., J.M. Hamilton, and R.E. Olson. 1981. Suitability of thermocouple psychrometers for studying moisture movement in unsaturated soils. *Permeability and Groundwater Contaminant Transport.* T.F. Zimmie and C.O. Riggs, eds. American Society for Testing and Materials ASTM STP 746: 84-100.

Davies, B.E. 1987. *Water Movement in Nonisothermal Tuff.* M.S. Thesis. Tucson: University of Arizona.

Davis, J.L. and W.J. Chudobiak. 1975. In-situ meter for measuring relative permeability of soils. *Geol. Surv. Can.* Paper 75-1, Part A.

Defay, R., I. Prigogine, and A. Bellemans. 1966. *Surface Tension and Adsorption.* New York: John Wiley.

de Marsily, G. 1986. *Quantitative Hydrogeology, Groundwater Hydrology for Engineers.* New York: Academic Press.

de Vries, D.A. 1963. Thermal properties of soils. Chapter 7. *Physics of Plant Environment.* W.R. Van Wijk, ed. Amsterdam: North-Holland Publishing Company.

de Vries, D.A. 1975. Heat transfer in soils. *Heat and Mass Transfer in the Biosphere.* D.A. de Vries and N.N. Afgan, eds. Washington, DC: Scripta Book Co.: 5-28.

Domenico, P.A. and F.W. Schwartz. 1990. *Physical and Chemical Hydrogeology.* New York: John Wiley.

Doughty, C. and K. Pruess. 1988. A semianalytical solution for heat-pipe effects near high-level nuclear waste packages buried in partially saturated geological media. *International Journal of Heat and Mass Transfer.* 31(1): 79-90.

Doughty, C. and K. Pruess. 1990. A similarity solution for two-phase fluid and heat flow near high-level nuclear waste packages emplaced in porous media. *International Journal of Heat and Mass Transfer.* 33(6): 1205-1222.

Doughty, C. and K. Pruess. 1991. *A Mathematical Model for Two-Phase Water, Air, and Heat Flow around a Linear Heat Source Emplaced in a Permeable Medium.* LBL-30050. Berkeley, CA: Lawrence Berkeley Laboratory.

Doughty, C. and K. Pruess. 1992. A similarity solution for two-phase water, air, and heat flow near a linear heat source in a porous medium. *Journal of Geophysical Research.* 97(B2): 1821-1838.

Dunn, P.D. and D.A. Reay. 1982. *Heat Pipes.* New York, NY: Pergamon Press.

Dykhuizen, R.C. 1990. A new coupling term for dual-porosity models. *Water Resources Research.* 26(2): 351-356.

Eaton, R.R., N.E. Bixler, and D.C. Reda. 1985. Coupled hydrothermal flows of liquid and vapor in welded tuff; numerical modeling of proposed experiment. *Proceedings, International Symposium of Coupled Processes Affecting the Performance of a Nuclear Waste Repository.* Lawrence Berkeley Laboratories.

Eckert, E.R.G. and R.M. Drake. 1987. *Analysis of Heat and Mass Transfer.* New York: Hemisphere.

Edlefsen, N.E. and A.B.C. Anderson. 1943. Thermodynamics of soil moisture. *Hilgardia.* 15(2): 31-298.

Encyclopedia Britannica. 1974. *Lord Kelvin, Whilliam Thomson.* Chicago, IL: Encyclopedia Britannica: 414-415.

Evans, D.D. 1983. *Unsaturated Flow and Transport Through Fractured Rock — Related to High-Level Waste Repositories.* Final Report - Phase 1. NUREG/CR-3206. Washington, DC: Nuclear Regulatory Commission.

Evans, D.D. and T.J. Nicholson. 1987. Flow and Transport Through Unsaturated Fractured Rock. *Geoph. Monograph 42. AGU.*

Fewell, M.E. and B.S. Langkopf. 1990. *Review of Models in Available Nonisothermal 2-Phase Flow Codes.* SAND-90-2193C. Albuquerque, NM: Sandia National Laboratories.

Flint, L.E. and A.L. Flint. 1991. Use of a submersible pressure outflow cell for determination of moisture characteristic curves on rock core. *Proc. 5th Workshop on Flow and Transport through Unsaturated Fractured Rock.* Tucson, AZ. in press.

Forsyth, P.A. 1990. Radioactive waste disposal heating effects in unsaturated fractured rock. *Numerical Heat Transfer.* A17: 29-51.

Forsyth, P.A. and R.B. Simpson. 1989. *A Two Phase, Two Component Model for Natural Convection in a Porous Medium.* CS-89-55. Waterloo, Ontario, Canada: Department of Computer Science, University of Waterloo.

Forsyth, P.A. and R.B. Simpson. 1991. A two-phase, two-component model for natural convection in a porous medium. *International Journal for Numerical Methods in Fluids.* 12: 655-682.

Fox, R.W. and A.T. McDonald. 1978. *Introduction to Fluid Mechanics.* New York, NY: McGraw-Hill Publishing Co.

Fredlund, D.D. and D.K.H. Wong. 1989. Calibration of thermal conductivity sensors for measuring soil suction. *ASTM Geotechnical Testing Journal.* GTJODJ, 12(3): 188-194.

Freeze, R.A. and J.A. Cherry. 1979. *Groundwater.* Englewood Cliffs, New Jersey: Prentice-Hall.

Glass, R.J., J.Y. Parlange, and T.S. Steenhuis. 1989a. Wetting front instability 1. theoretical discussion and dimensional analysis. *Water Resources Research.* 25(6): 1187-1194.

Glass, R.J., J.Y. Parlange, and T.S. Steenhuis. 1989b. Wetting front instability 2. experimental determination of relationships between system parameters and two-dimensional unstable flow field behavior in initially dry porous media. *Water Resources Research.* 25(6): 1195-1207.

Gray, W.G. and S.M. Hassanizadeh. 1991a. Paradoxes and realities in unsaturated flow theory. *Water Resources Research.* 27(8): 1847-1854.

Gray, W.G. and S.M. Hassanizadeh. 1991b. Unsaturated flow theory including interfacial phenomena. *Water Resources Research*. 27(8): 1855-1863.

Green, R.E. and J.C. Corey. 1971. Calculation of hydraulic conductivity: a further evaluation of some predictive methods. *Soil Sci. Soc. Am. Proc.* 35: 3-8.

Green, R.T. and F.T. Dodge. 1991. Thermohydrology. *Report on Research Activities for Calendar Year 1991*. W.C. Patrick, ed. CNWRA 90-01A. San Antonio, TX: Center for Nuclear Waste Regulatory Analyses.

Green, R.T. and S. Svedeman. 1991. Thermohydrology. *Report on Research Activities for the Quarter April 1 Through June 30, 1991*. W.C. Patrick, ed. CNWRA 91-02Q. San Antonio, TX: Center for Nuclear Waste Regulatory Analyses.

Gureghian, A.B., D.S. Ward, and R.W. Cleary. 1977. *Calculation of Unsaturated Hydraulic Conductivity*. Research Report Number 77-WR-13. Princeton, NJ: Princeton University, Department of Civil Engineering.

Gureghian, A.B., B.R. Stitt, and L.P. Sanathanan. 1982. *Calculation of Unsaturated Hydraulic Conductivity*. ANL/EIS-14. Argonne, IL: Argonne National Laboratory.

Gureghian, A.B. and B. Sagar. 1991. Evaluation of DCM3D - A dual continuum, 3-D groundwater flow code for unsaturated, fractured, porous media. *Report on Research Activities for Calendar Year 1990*. NUREG/CR-5817. CNWRA 90-01A. Washington, DC: Nuclear Regulatory Commission.

Hadley, G.R. 1985. *PETROS - A Program for Calculating Transport of Heat, Water, Vapor and Air Through a Porous Material*. SAND-0878. Albuquerque, NM: Sandia National Laboratories.

Hillel, D. 1971. *Soil and Water, Physical Principles and Processes*. New York, NY: Academic Press.

Hillel, D. 1980a. *Fundamentals of Soil Physics*. New York, NY: Academic Press.

Hillel, D. 1980b. *Applications of Soil Physics*. New York, NY: Academic Press.

Hindmarsh, A.C. 1974. *GEAR: Ordinary Differential Equation System Solver*. UCID-30001. Livermore, CA: Lawrence Livermore National Laboratory.

Hindmarsh, A.C. 1983. ODEPACK: A systematized collection of ODE solvers. *Scientific Computing*. R.S. Stepleman et al., eds. Amsterdam: North-Holland Publishing Co.: 55-64.

Incropera, F.P. and D.P. DeWitt. 1981. *Fundamentals of Heat Transfer.* New York: John Wiley.

Jackson, R.D., R.J. Reginato, and C.H.M. van Bavel. 1965. Comparison of measured and calculated hydraulic conductivites of unsaturated soils. *Water Resources Research* 1: 375-380.

Jackson, R.D. 1972. On the calculation of hydraulic conductivity. *Soil Sci. Soc. Am. Proc.* 36: 380-382.

Kaviany, M. 1991. *Principles of Heat Transfer in Porous Media.* New York, NY: Springer-Verlag.

Kays, W.M. and M.E. Crawford. 1980. *Convective Heat and Mass Transfer.* New York: McGraw-Hill.

Keller, G.V. and F.C. Frischknecht. 1966. *Electrical Methods in Geophysical Prospecting.* Oxford, England: Pergamon Press: 135.

Keyhani, M., F.A. Kulacki, and R.N. Christensen. 1981. *Convective Heat Transfer within Spent Fuel Canisters: An Experimental Laboratory Study.* BMI/ONWI-229. Columbus, OH: Battelle Memorial Institute.

Keyhani, M., F.A. Kulacki, and R.N. Christensen. 1987. *Heat Transfer Within Spent Fuel Canisters: Phase Two of an Experimental Laboratory Study.* BMI/ONWI-530. Columbus, OH: Battelle Memorial Institute.

Klavetter, E.A. and R.R. Peters. 1985. *Development of Flow Models for Fractured, Porous Media Based on Two Different Conceptual Models.* SAND85-0855C. Albuquerque, NM: Sandia National Laboratories.

Klavetter, E.A. and R.R. Peters. 1986. *Estimation of Hydrologic Properties of an Unsaturated, Fractured Rock Mass.* SAND84-2642. Albuquerque, NM: Sandia National Laboratories.

Klavetter, E.A. and R.R. Peters. 1987. *An evaluation of the use of mercury porsimitry in calculating hydrologic properites of tuffs from Yucca Mountain, Nevada.* SAND86-0286. Albuquerque, NM: Sandia National Laboratories.

Klinkenberg, L. 1941. The permeability of porous media to liquids and gases. *Amer. Petrol. Inst. Drilling Prod. Pract.* 200-213.

Koorevaar, P., G. Menelik and C. Dirksen. 1983. *Elements of Soil Physics.* New York, NY: Elsevier.

Kozeny, J. 1927. Uber kapillare leitun des wassers im i boden, sitzungsber akab. wiss, wien 136, 271-396. (Citation is from a translation by W.F. Striedieck and C. M. Davis, Published by the Petroleum Branch of the *AIME).*

Kulacki, F.A. and A.A. Emara. 1975. *High Rayleigh Number Convection in Enclosed Fluid Layers with Internal Heat Sources.* NUREG-75/065. Washington, DC: Nuclear Regulatory Commission.

Kulacki, F.A. and A.A. Emara. 1976. *Transient Natural Convection in an Internally Heated Fluid Layer.* NUREG-0078. Washington, DC: Nuclear Regulatory Commission.

Kulacki, F.A. and M. Keyhani. 1987. Heat transfer aspects of nuclear waste disposal. *Heat Transfer Problems in Nuclear Waste Management.* E.V. McAssey, Jr. and V.E. Schrock, eds. HTD-67. New York: American Society of Mechanical Engineers: 1-17.

Land, N.S. 1972. *A Compilation of Nondimensional Numbers.* NASA SP-274. Washington, DC: National Aeronautics and Space Administration.

Latorre, V.R. 1989. *Microwave Measurements of Water Vapor Partial Pressure at Temperatures Up to 350 C.* Livermore, California: Lawrence Livermore National Laboratory, UCRL-101866.

Latorre, V.R. and H.D. Glenn. 1991. *Microwave Measurements of the Water Content of Bentonite.* Livermore, California: Lawrence Livermore National Laboratory, UCRL-JC-104768.

Leverett, M.C., W.B. Lewis, and M.E. True. 1941. *Dimensional-Model Studies of Oil-Field Behavior.* Technical Publication No. 1413. New York: American Institute of Mining and Metallurgical Engineers.

Lienhard, J.H. 1987. *A Heat Transfer Textbook.* Englewood Cliffs, New Jersey: Prentice-Hall.

Mao, N. and H.F. Wang. 1991. *Thermocouple Psychometer Measurements of in situ Water Potential Changes in Heated Welded Tuff.* UCRL-ID-104729. Livermore, CA: Lawrence Livermore National Laboratory.

Martinez, M.J. 1988. *Capillary-Driven Flow in a Fracture Located in a Porous Medium.* SAND84-1697. Albuquerque, NM: Sandia National Laboratories.

Matthews, D.W. 1986. *Thermally Induced Countercurrent Flow in Unsaturated Rock.* M.S. Thesis. Tucson, AZ: University of Arizona.

Mualem, Y. 1976. A new model for predicting the hydraulic conductivity of unsaturated porous media. *Water Resources Research* 12(3): 513-522.

Miller, E.E. and R.D. Miller. 1956. Physical theory for capillary flow phenomena. *Journal of Applied Physics*. 27(4): 324-332.

Miller, E.E. 1980. Similitude and scaling of soil-water phenomena. *Applications of Soil Physics*. D. Hillel, ed. New York, NY: Academic Press: 300-318.

Miller, D.E. and W.H. Gardner. 1962. Water infiltration into stratified soil. *Soil Sci. Soc. Am. Proc.* 26: 115-119.

Millington, R.J. and J.P. Quirk. 1961. Permeability of porous solids. *Trans. Faraday Soc.* 57: 1200-1206.

Moore, W.J. 1963. *Physical Chemistry*. Englewood Cliffs, NJ: Prentice-Hall.

Morrison, R.D. 1983. *Ground Water Monitoring Technology - Procedures, Equipment and Applications*. Prairie Du Sac, Wisconsin: Timco Mfg., Inc.: 1-34.

Mulay, S.P. 1988. *Diffusion of Heat and Mass Transfer in Partially Saturated Porous Media*. Ph.D. Thesis. Chicago, IL: Illinois Institute of Technology.

Mulay, S.P. and Z. Lavan. 1989. Transient heat and mass transfer in a partially saturated porous media -a scale analysis. *Multiphase Transport in Porous Media - 1989*. R.R. Eaton, K.S. Udell, M. Kaviany and K. Vafai, eds. FED-82, HTD-127. New York: American Society of Mechanical Engineers: 63-69.

Narasimhan, T.N. 1982. Physics of saturated-unsaturated subsurface flow. *Geological Society of America*. Special Paper 189.

Nicholls, C.I. and J. Heaviside. 1988. Gamma-ray-absorption techniques improve analysis of core displacement tests. *SPE Formation Evaluation. SPE Paper 14421*. 69-75.

Nield, D.A. and A. Bejan. 1992. *Convection in Porous Media*. New York, NY: Springer-Verlag.

Nitao, J.J. 1988. *Numerical Modeling of the Thermal and Hydrological Environment Around a Nuclear Waste Package Using the Equivalent Continuum Approximation: Horizontal Emplacement*. UCID-21444. Livermore, CA: Lawrence Livermore National Laboratory.

Nitao, J. 1989. *V-TOUGH - An Enhanced Version of the TOUGH Code for the Thermal and Hydrologic Simulation of Large-Scale Problems in Nuclear Waste Isolation*. Draft 1.1, Livermore, CA: Lawrence Livermore National Laboratory.

Osiensky, J.L. and L. Davis. 1988. *A Summary of Groundwater Testing Methodologies Applicable to Unsaturated Fractured Rock at Yucca Mountain.* Final Report on NRC Contract No. NRC-02-85-008. Washington, DC: Nuclear Regulatory Commission.

O'Sullivan, M.J. 1981. A similarity method for geothermal well test analysis. *Water Resources Research.* 17(2): 390-398.

Parlar, M., M. Zeybek, and Y.C. Yortsos. 1990. *Steady-State, Vapor-Liquid Concurrent Flow: Relative Permeabilities and End Effects.* DOE/BC/14126-24. Washington, DC: U.S. Department of Energy.

Perkins, R.A. and M.C. Jones. 1989. Fiber-optic fluorescence array to study free convection in porous media. *Rev. Sci. Instrum.* 60(11): 3492-3497.

Persoff, P., C.J. Radke, K. Pruess, S.M. Benson, and P.A. Witherspoon. 1989. *A Laboratory Investigation of Foam Flow in Sandstone at Elevated Pressure.* Society of Petroleum Engineers Regional Meeting. Bakersfield, California: SPE 18781.

Peters, R.R., E.A. Klavetter, I.J. Hall, S.C. Blair, P.R. Heller and G.W. Gee. 1984. *Fracture and Matrix Hydrologic Characteristics of Tuffaceous Materials from Yucca Mountain, Nye County, Nevada.* SAND84-1471. Albuquerque, NM: Sandia National Laboratories.

Phene, C.J., G.J. Hoffman, and S.L. Rawlins. 1971a. Measuring soil matric potential in situ by sensing heat dissipation within a porous body: I. Theory and sensor construction. *Soil Science Society of America Proceeding.* 35: 27-33.

Phene, C.J., G.J. Hoffman, and S.L. Rawlins. 1971b. Measuring soil matric potential in situ by sensing heat dissipation within a porous body: II. Experimental results. *Soil Science Society of America Proceeding.* 35: 225-229.

Philip, J.R. and D.A. de Vries. 1957. Moisture movement in porous materials under temperature gradients. *Transactions, American Geophysical Union.* 38(2): 222-232.

Philip, J.R. 1960. General method of exact solution of the concentration-dependent diffusion equation. *Australian Journal of Physics.* 13: 1-12.

Philip, J.R. 1960. A very general class of exact solutions in concentration dependent diffusion. *Nature.* 185: 233.

Philip, J.R. 1970. Flow in porous media. *Annual Reviews of Fluid Mechanics.* Palo Alto, CA: Annual Reviews, Inc.: 2: 177-204.

Phillips, O.M. 1991. *Flow and Reactions in Permeable Rocks.* New York, NY: Cambridge University Press.

Pollock, D.W. 1982. *Fluid Flow and Energy Transport in a High-Level Radioactive Waste Repository in Unsaturated Alluvium*. Ph.D. Thesis. Urbana, IL: University of Illinois at Urbana-Champaign.

Pollock, D.W. 1986. Simulation of fluid flow and energy transport processes associated with high-level radioactive waste disposal in unsaturated alluvium. *Water Resources Research*. 22(5): 765-775.

Prazák, J., J. Tywoniak, F. Peterka, and T. Slonc. 1990. Description of transport of liquid in porous media — a study based on neutron radiography data. *Int. J. Heat Mass Transfer*. 33(6): 1105-1120.

Pruess, K., R.C. Schroeder, P.A. Witherspoon, and J.M. Zerzan. 1979. *SHAFT 78-A Two-Phase Multidimensional Computer Program for Geothermal Reservoir Simulation*. LBL-8264. Berkeley California: Lawrence Berkeley Laboratory.

Pruess, K., Y.W. Tsang, and J.S.Y. Wang. 1984. *Numerical Studies of Fluid and Heat Flow Near High-Level Nuclear Waste Packages Emplaced in Partially Saturated Fractured Tuff*. LBL-18552. Berkeley, CA: Lawrence Berkeley Laboratory.

Pruess, K. 1985. *A Quantitative Model of Vapor Dominated Geothermal Reservoirs as Heat Pipes in Fractured Porous Rock*. LBL-19366. Berkeley, CA: Lawrence Berkeley Laboratory.

Pruess, K., Y.W. Tsang, and J.S.Y. Wang. 1985. Modeling of strongly heat driven flow in partially saturated fractured porous media. *Mem. International Association of Hydrogeologists* 17: 486-497.

Pruess, K., C. Calore, R. Celati, and Y.S. Wu. 1987. An analytical solution for heat transfer at a boiling front moving through a porous medium. *International Journal of Heat and Mass Transfer*. 30(12): 2592-2602.

Pruess, K. 1987. *TOUGH User's Guide*. NUREG/CR-4645. Berkeley, California: Lawrence Berkeley Laboratory.

Pruess, K., J.S.Y. Wang, and Y.W. Tsang. 1990a. On thermohydrologic conditions near high-level nuclear wastes emplaced in partially saturated fractured tuff 1. simulation studies with explicit consideration of fracture effects. *Water Resources Research*. 26(6): 1235-1248.

Pruess, K., J.S.Y. Wang, and Y.W. Tsang. 1990b. On thermohydrologic conditions near high-level nuclear wastes emplaced in partially saturated fractured tuff 2. effective continuum approximation. *Water Resources Research*. 26(6): 1249-1261.

Rasmussen, T.C. and D.D. Evans. 1987. *Unsaturated Flow and Transport Through Fractured Rock Related to High-Level Waste Repositories*. NUREG/CR-4655. Washington, DC: Nuclear Regulatory Commission.

Rasmussen, T.C. and D.D. Evans. 1989. *Fluid Flow and Solute Transport Modeling Through Three-Dimensional Networks of Variably Saturated Discrete Fractures*. NUREG/CR-5239. Washington, DC: Nuclear Regulatory Commission.

Reda, D.C. 1987. Slip-flow experiments in welded tuff: the Knudsen diffusion problem. *Coupled Processes Associated with Nuclear-Waste Repositories*. C.F. Tsang, ed. New York, NY: Academic Press.

Richards, L.A. and W. Gardner. 1936. Tensiometers for measuring the capillary tension of soil water. *J. Amer. Soc. Argron.* 28:352-358.

Rohsenow, W.M. and H.Y. Choi. 1961. *Heat, Mass, and Momentum Transfer*. Englewood Cliffs, New Jersey: Prentice-Hall.

Rousseau, J., M. Kurzmack, C. Loskot, and D. Stanley. 1989. *USGS Thermocouple Psychrometer Experience - Results of Laboratory Calibration and GTUF Field Applications*. Presentation to Nuclear Waste Technical Review Board (NWTRB). April 11.

Runchal, A.K. and B. Sagar. 1992. *PORFLOW: A Multifluid Multiphase Model for Simulating Flow, Heat Transfer and Mass Transport in Fractured Porous Media, User's Manual - Version 2.40*. CNWRA 92-003. San Antonio, TX: Center for Nuclear Waste Regulatory Analyses.

Russo, A.J. and D.C. Reda. 1989. Drying of an initially saturated fractured volcanic tuff. *Journal of Fluids Engineering*. 111: 191-196.

Sagar, B. and A.K. Runchal. 1990. *PORFLO-3: A Mathematical Model for Fluid Flow, Heat, and Mass Transport in Variably Saturated Geologic Media, Theory and Numerical Methods, Version 1.0*. WHC-EP-0042. Richland, WA: Westinghouse Hanford Company.

Sagar, B. and A.B. Gureghian. 1991. Performance Assessment Research. *Report on Research Activities for Calendar Year 1991*. W.C. Patrick. CNWRA 90-01A. San Antonio, TX: Center for Nuclear Waste Regulatory Analyses.

Schaaf, S.A. and P.L. Chambre. 1958. Flow of rarefied gases. *Fundamentals of Gas Physics*. H.E. Emmons, ed. Princeton, NJ: Princeton University Press.

Scott, R.B., R.W. Spengler, S. Diehl, A.R. Lappin, and M.P. Chornack. 1982. Geologic character of tuffs in the unsaturated zone at Yucca Mountain, Southern Nevada. *Role of the Unsaturated Zone in Radionuclide and Hazardous Waste Disposal.* J. Mercer, P.S. Rao, and I.W. Marine, eds. Ann Arbor, MI: Ann Arbor Science: 289-335.

Shaw, B. and L.D. Baver. 1939a. An electrothermal method for following moisture changes of the soil in situ. *Soil Science Society of America Proceeding.* 4: 78-83.

Shaw, B. and L.D. Baver. 1939b. Heat conductivity as an index of soil moisture. *Journal of the American Society of Agronomy.* 31: 886-891.

Silling, S.A. 1983. *Technical Position on Documentation of Models.* NUREG-0856. Washington, DC: Nuclear Regulatory Commission.

Stallman, R. W. 1964. *Multiphase Fluids in Porous Media - A Review of Theories Pertinent to Hydrologic Studies.* Geological Survey Professional Paper 411-E. Washington, DC: U.S. Government Printing Office.

Stillwater, R. and A. Klute. 1988. Improved methodology for a collinear dual-energy gamma radiation system. *Water Resources Research.* 24(8): 1411-1422.

Telford, W.M., L.P. Geldart, R.E. Sheriff and D.A. Keys. 1976. *Applied Geophysics.* New York, NY: Cambridge University Press.

Thamir, F. and C.M. McBride. 1985. Measurements of matric and water potentials in unsaturated tuff at Yucca Mountain, Nevada. *NWAA Proceedings of Conference on Characterization and Monitoring of the Vadose Zone.* Denver, CO: U.S. Geological Survey.

Thomson, W. 1871. On the equilibrium of vapor at a curved surface of liquid. *Philisophical Magazine.* 42: 448-452.

Thunvik, R. and C. Braester. 1988. *GWHRT - A Flow Model for Coupled Groundwater and Heat Flow.* SKB-88-10. Stockholm, Sweden: Swedish Nuclear Fuel and Waste Management.

Todreas, N.E. and M.S. Kazimi. 1990. *Nuclear Systems I, Thermal Hydraulic Fundamentals.* New York: Hemisphere.

Topp, G.C., J.L. Davis, and A.P. Annan. 1980. Electromagnetic determination of soil water content: measurement in coaxial transmission lines. *Water Resources Reserch.* 16(3): 574-582.

Topp, G.C., J.L. Davis, and J.H. Chinnick. 1983. Using TDR water content measurements for infiltration studies. *Proceedings of International Conference Advances in Infiltration*, Dec. 12-13.

Updegraff, C.D. 1989. *Comparison of Strongly Heat-Driven Flow Codes for Unsaturated Media.* NUREG/CR-5367. Washington, DC: U.S. Nuclear Regulatory Commission.

Updegraff, C.D., C.E. Lee, and D.P. Gallegos. 1991. *DCM3D: A Dual-Continuum, Three-Dimensional, Ground-Water Flow Code for Unsaturated, Fractured, Porous Media.* NUREG/CR-5536. Washington, DC: Nuclear Regulatory Commission.

Van Wijk, W.R. and D.A. de Vries. 1963. The atmosphere and the soil. Chapter 2. *Physics of Plant Environment.* W.R. Van Wijk, ed. Amsterdam: North-Holland Publishing Company.

Van Wylen, G.J. and R.E. Sonntag. 1978. *Fundamentals of Classical Thermodynamics.* New York: John Wiley.

van Genuchten, R. 1978. *Calculating the Unsaturated Hydraulic Conductivity with a New, Closed-Form Analytical Model.* Research Report 78-WR-08. Princeton, NJ: Department of Civil Engineering, Princeton University.

van Genuchten, M.T. 1980. A closed-form equation for predicting the hydraulic conductivity of unsaturated soils. *Soil Sci. Soc. Am. J.* 44: 892-898.

Verma, A.K., K. Pruess, G.S. Bodvarsson, C.F. Tsang, and P.A. Witherspoon. 1983. *Design and Development of a Test Facility to Study Two-phase Steam/Water Flow in Porous Media.* Berkeley, California: Lawrence Berkeley Laboratory, LBL-17172.

Verma, A.K., K. Preuss, C.F. Tsang, and P.A. Witherspoon. 1985. *A Study of Two-Phase Concurrent Flow of Steam and Water in an Unconsolidated Porous Medium.* Berkeley, California: Lawrence Berkeley Laboratory, LBL-19804.

Verma, A. and K. Pruess. 1986. *Enhancement of Steam Phase Relative Permeability Due to Phase Transformation Effects in Porous Media.* Berkeley, California: Lawrence Berkeley Laboratory Report, LBL-21027.

Vincenti, W.G. and C.H. Kruger. 1965. *Introduction to Physical Gas Dynamics.* Malabar, FL: Krieger Publishing.

Wang, J.S.Y. and T.N. Narasimhan. 1985. Hydrologic mechanisms governing fluid flow in a partially saturated, fractured, porous medium. *Water Resources Research.* 21(12): 1861-1874.

Wang, J.S.Y. and T.N. Narasimhan. 1986. *Hydrologic Mechanisms Governing Partially Saturated Fluid Flow in Fractured Welded Units and Porous Nonwelded Units at Yucca Mountain*. LBL-21022. Berkeley, CA: Lawrence Berkeley Laboratory.

Wark, K. 1983. *Thermodynamics*. New York: McGraw-Hill.

Warren, J.E. and P.J. Root. 1963. The behavior of naturally fractured reservoirs. *Society of Petroleum Engineers Journal*. 3: 245-255.

Warrick, A.W. and D.R. Nielsen. 1980. Spatial variability of soil physical properties in the field. *Applications of Soil Physics*. D. Hillel, ed., New York, NY: Academic Press.

Whitaker, S. 1977. Simultaneous heat, mass, and momentum transfer in porous media: a theory of drying. *Advances in Heat Transfer*. J.P. Hartnett and T.F. Irvine, eds. New York: Academic Press.

Wiebe, H.H., R.W. Brown, and J. Barker. 1977. Temperature gradient effects on in situ hygrometer measurements of water potential. *Agronomy Journal*. 69: 933-939.

Wong, D.K.H. and A. Ho. 1987. *An Evaluation of a Thermal Conductivity Sensor for the Measurement of Soil Matric Suction*. Internal Report, Geotechnical Engineering Group, Saskatchewan, Canada: Department of Civil Engineeing: University of Saskatchewan, Saskatoon: 150.

Wylie, M.R.J and G.H.F. Gardner. 1958. The generalized Kozeny-Carman equation. *World Oil*. 146: 210-22

Yeh, G.T. and R.J. Luxmoore. 1983a. *MATTUM: A Multidimensional Model for Simulating Moisture and Thermal Transport in Unsaturated Porous Media*. ORNL-5888. Oak Ridge, TN: Oak Ridge National Laboratory.

Yeh, G.T. and R.J. Luxmoore. 1983b. Modeling moisture and thermal transport in unsaturated porous media. *Journal of Hydrology*. 64: 299-309.

Yow, J.L. Jr., A.M. Wijesinghe, R.K. Thorpe, and R.B. Knapp. 1989. *Repository Technology Program Activities*. Lawrence Livermore National Laboratory, UCID-21600.

Zegelin, S.J., I. White, and D.R. Jenkins. 1989. Improved field probes for soil water content and electrical conductivity measurement using time domain reflectometry. *Water Resources Research*. 25(11): 2367-2376.

Zimmerman, R.W. and G.S. Bodvarsson. 1989. Semi-analytical solutions for flow problems in unsaturated porous media. *Multiphase Transport in Porous Media-1989*. R.R. Eaton et al., eds., FED-82 HTD-127. New York, NY: American Society of Mechanical Engineers: 23-28.

Zyvoloski, G., Z. Dash, and S. Kelkar. 1988. *FEHM: Finite Element Heat and Mass Transfer Code*. LA-11224-MS. Los Alamos, NM: Los Alamos National Laboratory.

Zyvoloski, G., Z. Dash, and S. Kelkar. 1991. *FEHMN 1.0: Finite Element Heat and Mass Transfer Code*. LA-12062-MS. Los Alamos, NM: Los Alamos National Laboratory.

ASTM D 2325. 1977. Capillary Moisture Relationships for Coarse- and Medium-Textured Soils by Porous-Plate Apparatus.

APPENDIX A: DEVELOPMENT OF CONSERVATION AND CONSTITUTIVE EQUATIONS

In this appendix, a mathematical model for nonisothermal flow in a partially saturated porous medium is developed.

A.1 A GENERAL FRAMEWORK

The physics of heat transfer and fluid flow through a partially saturated fractured porous medium is succinctly described in the format of (i) conservation equations, (ii) constitutive equations, (iii) material properties, and (iv) associated definitions. In some cases, the conservation equations can more properly be called balance equations. The conservation/ constitutive equation formulation should be familiar to the reader. The most important points of this section are: (i) the nomenclature, and (ii) the assumptions and approximations. Some of the nomenclature and the assumptions vary from model to model used by different researchers (Whitaker, 1977; Pollock, 1982, 1986; Pruess, 1987, 1990a,b; Forsyth, 1990; Forsyth and Simpson, 1991; Runchal and Sagar, 1992).

The coupled thermohydrologic transport of heat and fluid in a partially saturated porous medium can be formulated in either of the following (but not limited to the following) sets of conservation equations:

- Conservation of mass of water (H_2O);
- Conservation of mass of air (N_2, O_2, Ar, ...);
- Conservation of energy;

- Conservation of mass of water in the liquid phase;
- Conservation of mass of water in the gaseous phase;
- Conservation of mass of air;
- Conservation of energy;

- Conservation of mass of water in the liquid phase;
- Conservation of mass of air in the liquid phase;
- Conservation of mass of water in the gaseous phase;
- Conservation of mass of air in the gaseous phase; and
- Conservation of energy.

Most of these conservation equations are expected to be familiar to the reader. For clarity, the energy equation is considered very general at this time. Approximations will be introduced to (i) subtract the mechanical energy, (ii) neglect changes in kinetic energy, (iii) neglect viscous dissipation of mechanical energy, and (iv) neglect the pressure work term (which is approximately equivalent to neglecting the difference between internal energy and enthalpy) (Todreas and Kazimi, 1990). These approximations yield a conservation of thermodynamic

energy equation. For clarity, air is assumed to dissolve in the liquid as described by Henry's Law (Pruess, 1987). These equations will be discussed in more detail. The important point is that no unique set of conservation equations exists. Ultimately, these sets of conservation equations must be equivalent by the introduction of appropriate assumptions and/or approximations.

The first set of conservation equations has been used by many researchers (Pollock, 1986; Pruess, 1987; Forsyth, 1990) and is essentially the format adopted in this work. The liquid and its vapor are assumed in local equilibrium so that only one conservation of water equation is necessary. The single conservation of water equation then accounts for water in both the liquid and gas phase, and the conservation of energy equation accounts for the heat of phase change. Similarly, either the air in the liquid phase is neglected or assumed to be maximally dissolved in the water.

The second set of equations has been used by a few researchers (Bixler, 1985; Runchal and Sagar, 1992) and is equivalent with the first set, except that the liquid water and gaseous water are accounted separately. By distinguishing between the liquid and gaseous phases, the phases are not required to be in equilibrium; however, the rate of transfer between the phases must be specified (this introduces a new unknown, or an additional constitutive relation).

The third set of equations, which is the most general, is only proposed in this discussion, and, to our knowledge, no one has explicitly applied them to the coupled thermohydrologic problems associated with the proposed HLW repository. For discussion purposes, this third formulation concentrates on the conservation of species in each phase. In the literature, Gray and Hassanizadeh (1991b) have proposed a generic model for partially saturated flow which concentrates on the conservation of each phase.

The first, second, and third sets of equations represent a transition from species only, to species and phase representations of the conservation laws. The concept of species conservation is loosely applied to water (H_2O) and air (N_2, O_2, Ar, ...). The phases currently considered include liquid and gas where, if the need arises, the solid phase can be included.

It is by introducing assumptions that the first and/or second set of equations can be derived as a subset of the third. Conceptually, each conservation equation introduces a new unknown or an additional primary variable. Fewer conservation equations imply that there are fewer primary variables. In the most general formulation, one must consider the conservation of species in each phase at each spatial location. By assumptions and approximations, the number of conservation equations can be reduced and replaced by additional constitutive equations.

Two assumptions are introduced to reduce the five initial equations of third set to the three equations of the first set. Both assumptions are discussed here.

The first assumption is that either there is a negligible amount of air in the liquid phase, or air is maximally dissolved in the liquid water, with the amount being governed by Henry's Law (Freeze and Cherry, 1979, pg 95; Domenico and Schwartz, 1990, pg 427). Hence, the need for an equation governing the conservation of air in the liquid phase is eliminated. Henry's Law is introduced as a new constitutive equation. This assumption derives the second set from the third set of conservation equations.

The second assumption is that the gas is locally saturated with water, so that the partial pressure of water equals the vapor pressure of water. When the liquid-gas interface (meniscus) is not planar, the partial pressure of the water in the gas equals the reduced vapor pressure. Kelvin's equation is frequently applied to estimate the reduced vapor pressure (Bear, 1972, pg 516). Knowing the local gas pressure, temperature and liquid saturation (or capillary pressure), the mass fraction of water vapor can be calculated using Kelvin's equation. Hence, the need for an equation governing the conservation of water in the gaseous phase is eliminated, and Kelvin's equation is introduced as a new constitutive equation. This assumption derives the first set from the second set of conservation equations.

The present formulation is based on a mass description, yet equally valid would be a mole description. For mass and momentum considerations, a mass description appears more appropriate than a mole description. For species considerations with the possibility of chemical reactions, a mole description appears more appropriate. Since mass and momentum are of interest and chemical reactions are not addressed in the study, a mass description will be used in the following development.

A.2 CONSERVATION EQUATIONS

The conservation of water (H_2O) includes both liquid and vapor phases and can be written in either integral

$$\frac{d}{dt}\iiint \rho_{w,slg}\, dV = -\iint (\mathbf{q}_{m,w} + \mathbf{j}_{m,w}) \cdot \mathbf{n}\, dA + \iiint Q_{w,s} dV \qquad \text{(A-1)}$$

or differential equation form

$$\frac{\partial \rho_{w,slg}}{\partial t} = -\nabla \cdot (\mathbf{q}_{m,w} + \mathbf{j}_{m,w}) + Q_{s,w} \qquad \text{(A-2)}$$

where

$\rho_{w,slg}$	=	water density averaged over the porous medium [kg/m^3],
$\mathbf{q}_{m,w}$	=	advective mass flux of water [kg/m^2-s],
$\mathbf{j}_{m,w}$	=	diffusive mass flux of water [kg/m^2-s],
$\mathbf{n}$	=	outward-directed unit normal surface vector, and
$Q_{w,s}$	=	source/sink term for water [kg/m^3-s].

The density is based on the volumetric average over the solid, liquid, and gas phases (see Todreas and Kazimi, 1990, pg 131, for a discussion of volume-averaged properties). The advective and diffusive fluxes are area averaged properties and are typed in bold lettering to indicate vector quantities. For partially saturated porous media, a "representative elementary volume" (Bear, 1972) is occupied by solid, liquid and gaseous phases, which are indicated by "s", "l", and "g" subscripts, respectively. The subscript "w" is used to indicate water (H_2O), and "a" is used to indicate air. Air is a mixture of many components (N_2, O_2, Ar, CO_2, etc.), however it is considered a single gas here.

The differential form of the conservation equation can be derived from the integral equation using Gauss's Divergence theorem and arguments concerning the arbitrariness of the control volume. This derivation is presented in many textbooks (e.g. Todreas and Kazimi, 1990, pg 96).

For discussion purposes, the differential formulation of the conservation equations has been adopted for this work, however it is important to note that an integral formulation is equally valid. Many researchers have pursued integral formulations presumably because these are easier to discretize (Pruess, 1987).

Similarly, the differential form of the equation governing the conservation of air is

$$\frac{\partial \rho_{a,slg}}{\partial t} = - \nabla \cdot \left(\mathbf{q}_{m,a} + \mathbf{j}_{m,a} \right) + Q_{a,s} \qquad \text{(A-3)}$$

where

$\rho_{a,slg}$	=	air density averaged over the porous medium which includes solid, liquid and gas phases [kg/m^3],
$\mathbf{q}_{m,a}$	=	advective mass flux of air [kg/m^2-s],
$\mathbf{j}_{m,a}$	=	diffusive mass flux of air [kg/m^2-s], and
$Q_{a,s}$	=	source/sink term for air [kg/m^3-s].

The equation governing the conservation of thermodynamic energy is

$$\frac{\partial e_{slg}}{\partial t} = - \nabla \cdot \left(\mathbf{q}_e + \mathbf{j}_e \right) + Q_e \qquad \text{(A-4)}$$

where

e_{slg}	=	internal energy averaged over the solid, liquid and gas phase [J/m^3],
$\mathbf{q}_e$	=	advective flux of energy [J/m^2-s],
$\mathbf{j}_e$	=	diffusive flux of energy [J/m^2-s], and
Q_e	=	volumetric generation of energy [J/m^3-s].

In Eqn. (A-4) the changes in the kinetic and gravitational-potential energy are assumed small in comparison with changes in the internal energy, so that the total volumetric energy is

assumed equal to the volumetric internal energy. Similarly, the mechanical energy, compressible work, and viscous dissipation terms are neglected so that the resulting equation is known in the literature as the thermodynamic energy equation (Todreas and Kazimi, 1990). The thermodynamic energy equation is frequently known as the heat equation for a stationary medium.

The reader is cautioned to distinguish between volumetric energy and specific energy, where volumetric is per cubic volume and specific is per unit mass. The symbol "u" will be used to indicate specific internal energy, so that $e=\rho u$.

Purposefully, each conservation statement has been structured to reveal their commonality. Each equation relates the change of the stored property (first term) to the divergence of transport fluxes (second terms) and to the volumetric creation/destruction (optional third term). An example of a volumetric source of thermal energy generation may be the radioactive waste modelled as being uniformly distributed throughout a fixed volume.

A.3 ACCUMULATION TERMS

A.3.1 Average Water Density

The volumetric-average water density, $\rho_{w,slg}$ [kg/m^3], is defined as the weighted sum of the water density in solid, liquid, and gaseous phases

$$\rho_{w,slg} = f_s \rho_{w,s} + f_l \rho_{w,l} + f_g \rho_{w,g} \qquad \text{(A-5)}$$

where f_s, f_l, and f_g are the volume fractions occupied by the solid, liquid, and gas phases, respectively, and $\rho_{w,s}$, $\rho_{w,l}$, and $\rho_{w,g}$ are the densities of water [kg/m^3] in the solid, liquid, and gas phases, respectively.

The solid liquid and gas phase volume fractions are related to the porosity and phase saturations as:

$$\begin{aligned} f_s &= (1-\phi) + \phi S_s \\ f_l &= \phi S_l \\ f_g &= \phi S_g \end{aligned} \qquad \text{(A-6)}$$

where

f_s, f_l, f_g	=	volume fraction of solid, liquid, and gas phases, respectively, (m^3 phase / m^3 medium) [dimensionless],
ϕ	=	porosity (m^3 void / m^3 medium) [dimensionless], and
S_s, S_l, S_g	=	saturation of solid, liquid, and gas phases (m^3 phase / m^3 void) [dimensionless], respectively.

It is noted that the solid phase consists of both rock and any fluid that solidifies, such as frozen water (ice). It is noted that the volume fractions sum to unity

$$1 = f_s + f_l + f_g \tag{A-7}$$

The saturations also sum to unity.

$$1 = S_l + S_g + S_s \tag{A-8}$$

In all cases of present interest, the temperature is sufficiently high ($T > 0$ C at $P = 1$ atm) such that water in the solid phase (ice) is not considered further in this development. Additionally, any water that is trapped in the solid rock material and acts as a solid is also neglected. The density of water in the solid phase (i.e., mass of water per unit volume of solid) is assumed equal to zero:

$$\rho_{w,s} = 0 \tag{A-9}$$

Also, the solid phase saturation is assumed equal to zero:

$$S_s = 0 \tag{A-10}$$

The liquid phase is constituted predominantly of water (H_2O). There is also a small mass contribution from dissolved gases. For the current discussion, it is assumed that dissolved gases make a negligible contribution to the density of the liquid so that the liquid density is equal to the liquid density of water.

$$\rho_{w,l} = \rho_l \tag{A-11}$$

Water in the gas phase is assumed to behave as an ideal gas, hence its density is given by the ideal gas law,

$$\rho_{w,g} = \frac{M_w P_{w,g}}{R T} \tag{A-12}$$

where

M_w	=	molecular weight of water (M_w = 18.02 kg/kgmole),
$P_{w,g}$	=	partial pressure of water in the gas phase [N/m^2],
R	=	ideal gas law constant (R = 8314.0 J/kgmole-K), and
T	=	temperature [K].

A.3.2 Average Air Density

The volumetric-average air density, $\rho_{a,sig}$ [kg/m^3], is the sum over solid, liquid, and gas phases,

$$\rho_{a,slg} = f_s \rho_{a,s} + f_l \rho_{a,l} + f_g \rho_{a,g} \quad \text{(A-13)}$$

where $\rho_{a,s}$, $\rho_{a,l}$, and $\rho_{a,g}$ is the air density in the solid, liquid, and gas phases, respectively.

The volumetric-average air densities in the solid and liquid phases are assumed to be negligible in comparison with the mass of air in the gas phase.

$$\rho_{a,s} = 0 \quad \text{(A-14)}$$

$$\rho_{a,l} = 0 \quad \text{(A-15)}$$

The air in the gas phase is assumed to behave as an ideal gas, hence

$$\rho_{a,g} = \frac{M_a P_{a,g}}{R T} \quad \text{(A-16)}$$

where

M_a = molecular weight of air (M_a = 28.97 kg/kgmole), and
$P_{a,g}$ = partial pressure of air in the gas [N/m^2].

A.3.3 Average Energy Density

Typically, the volumetric-average energy density, e_{slg}, is reported as a constant value regardless of saturation because of the low rock porosity and high rock specific energy (density times specific heat). However, the energy density of the medium is more generally given by the weighted sum of the volumetric-averages for the solid, liquid, and gas phases,

$$e_{slg} = f_s \rho_s u_s + f_l \rho_l u_l + f_g \rho_g u_g \quad \text{(A-17)}$$

where the solid, liquid, and gas internal energies are primarily functions of temperature:

$$u_s = c_{v,s} (T - T_{ref}) + u_{ref,s} \quad \text{(A-18)}$$

$$u_l = u_{w,l} = c_{v,w,l} (T - T_{ref}) + u_{ref,w,l} \quad \text{(A-19)}$$

$$u_g = m_{w,g} u_{w,g} + m_{a,g} u_{a,g} \quad \text{(A-20)}$$

In these expressions:

$$u_{w,g} = c_{v,w,g}\left(T - T_{ref}\right) + u_{ref,w,g} \tag{A-21}$$

$$u_{a,g} = c_{v,a,g}\left(T - T_{ref}\right) + u_{ref,a,g} \tag{A-22}$$

and the remaining quantities are defined as:

$c_{v,s}$, $c_{v,l}$, $c_{v,w,g}$, $c_{v,a,g}$	=	specific heat at constant volume for the solid (rock), liquid (water), water in the gas phase, and air in the gas phase [J/kg-K],
$m_{w,g}$, $m_{a,g}$	=	mass fraction of water or air in gas phase [dimensionless],
T_{ref}	=	reference temperature [K], and
$u_{ref,s}$, $u_{ref,w,l}$, $u_{ref,w,g}$, $u_{ref,a,g}$	=	reference specific internal energies [J/kg].

The phase volume fractions (f_s, f_l, and f_g) are defined in Eqn. (A-6).

A.3.4 Internal Energy of Water

The internal energies for the water need to be consistent in the choice of reference temperatures (or datum values). It is important to recognize that the liquid water may be evaporated and become gaseous water. Therefore, the liquid and gas phases of the water must use the same datum values. Because the rock is always in the solid phase and because the air is always in the gas phase, they can have different choices for a reference temperature (or datum point). It is when a component can exist in two or more phases that a consistent datum point must be chosen for the component. For our current discussion, the reference states for water in either the liquid or gas phase can be related using a datum temperature of $T_{ref} = T_{sat} = 100$ C, so that:

$$u_{ref,w,g} = u_{ref,w,l} + u_{lg} \tag{A-23}$$

where

u_{lg}	=	change in specific internal energy of water from the liquid to the gas phase ($u_{lg} = u_g - u_l$) [J/kg].

As an aside, u_{lg} is related to the "latent heat of vaporization" as (Van Wylen and Sonntag, 1978; Wark, 1983; Todreas and Kazimi, 1990):

$$h_{lg} = u_{lg} + P\left(\frac{1}{\rho_g} - \frac{1}{\rho_l}\right) \tag{A-24}$$

where

h_{lg}	=	change in enthalpy (or latent heat of vaporization) of water from liquid to gas phase ($h_{lg} = h_g - h_l$) [J/kg],

P	=	pressure [N/m^2],
ρ_g	=	gas density [kg/m^3], and
ρ_l	=	liquid density [kg/m^3].

Hence, the enthalpy includes the energy required to (i) change the internal energy, and (ii) expand the volume occupied by the water. In many cases, the expansion energy is considered a compressible work (e.g. Pollock, 1982) or a thermal expansion work (e.g. Todreas and Kazimi, 1990). In almost all cases, the compressible work is negligible in comparison with the change in internal energy. The difference between internal energy and enthalpy is considered negligible in most cases and enthalpy is used instead of internal energy (Pollock, 1982). In this work, the distinction between u and h is maintained with the understanding that they are close in value.

It has been assumed here that the internal energies are only a function of temperature, and the functional relationship is linear. This is considered a good approximation for the air and the solid. For the gas phase water, the internal energies can be considered as functions of both pressure and temperature, especially when the system pressure can experience large changes.

The dependence of specific internal energy of water on temperature and pressure is illustrated in Figure A-1. In Figure A-1(a), three distinct regions are shown: subcooled liquid, two-phase mixture, and superheated gas. The three regions are separated by the saturated liquid and saturated gas lines of the typical two-phase "dome" (which is typically indicated on a pressure-volume or temperature-entropy diagram in thermodynamic text books, see Cravahol and Smith, 1981). For completeness, the critical point for water (T_c=374 C, P_c=20 MPa) is indicated. For temperatures and pressures above T_c and P_c, there is no distinction between a liquid and a gas phase. For illustration purposes, three isobars (lines of constant pressure) are drawn for a range of temperature. It is noted that in the two-phase region, the pressure and temperature are not independent, hence each distinct isobar has a unique temperature, that is, it is vertical in the two-phase region [see Figure A-1(a)].

In Figure A-1(b), the region of interest is indicated, where the gas pressure is close to one atmosphere and the temperature ranges from approximately 20 C to 200 C. For applications, it is possible to approximate the internal energy as functions of temperature (primary) and pressure (secondary). For example, in Figure A-1(c), the range of interest is approximated using linear relationships for du/dT in both the gas and liquid phases, and for du_{sat}/dP for both saturated liquid and saturated gas. The net result is that the internal energy of liquid water can be expressed as:

$$u_{w,l} = u_{ref,w} + \left.\frac{du_{sat,w,l}}{dP}\right|_{P_{ref}} \left(P_g - P_{ref} \right) + c_{v,w,l} \left(T - T_{sat} \right) \quad \text{(A-25)}$$

and the internal energy for the gaseous water is:

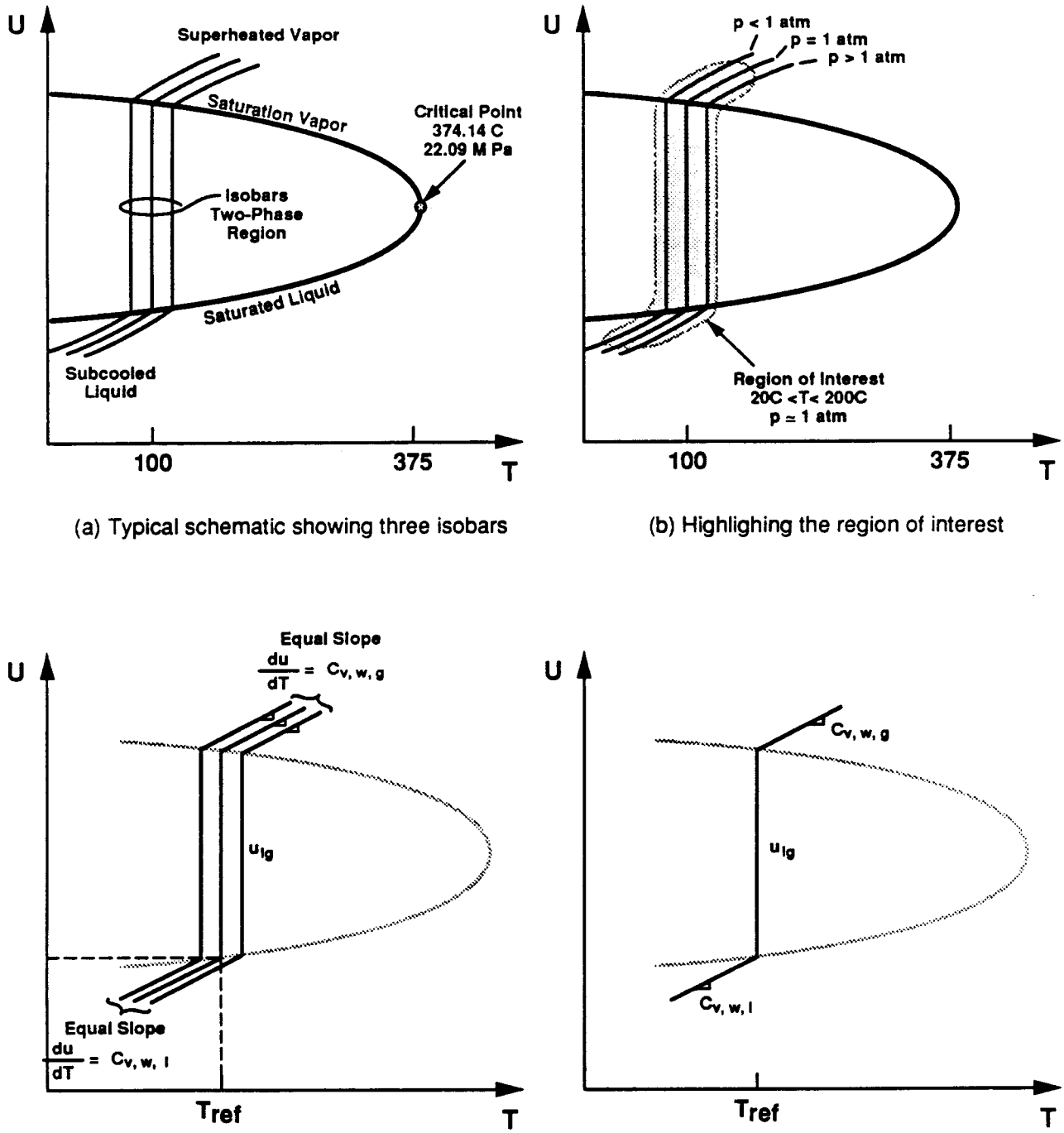

(a) Typical schematic showing three isobars

(b) Highlighing the region of interest

(c) Linear approximation of U as a function of P and T

(d) Linear approximation of U as a function of T

Figure A-1. Schematic representation of internal energy (u) as a function of temperature (T) and pressure (P) for water including saturated liquid, two-phase mixture, and superheated vapor.

$$u_{w,g} = u_{ref,w} + \left.\frac{du_{sat,w,l}}{dP}\right|_{P_{ref}} (P_g - P_{ref}) + u_{lg} + c_{v,w,g} (T - T_{sat}) \qquad \text{(A-26)}$$

where the saturation temperature is a function of pressure

$$T_{sat} = T_{ref} + \left.\frac{dT_{sat}}{dP}\right|_{P_{ref}} (P_g - P_{ref}) \qquad \text{(A-27)}$$

and the specific internal energy of vaporization is a function of pressure.

$$u_{lg} = u_{lg,ref} + \left.\frac{du_{lg}}{dP}\right|_{P_{ref}} (P_g - P_{ref}) \qquad \text{(A-28)}$$

One choice for the reference temperature, T_{ref}, is the saturation temperature for a specified local gas pressure (T_{ref} = 100 C at P_g = 1 atm). As stated earlier, the effect of pressure on the internal energy is considered secondary and is frequently neglected. For illustration purposes, Figure A-1(d), shows the most frequently used functionality with respect to temperature, where the functionality with respect to pressure is neglected.

A.3.5 Dalton's Law

The gas consists of both air and water. As it has been introduced, both the air and water have associated partial pressures. The sum of the partial pressures is equal to the total gas pressure, and this is known as Dalton's Law.

$$P_g = P_{w,g} + P_{a,g} \qquad \text{(A-29)}$$

At this point, all of the volumetrically stored properties (accumulation terms) have been defined. The advective fluxes will be discussed next.

A.4 ADVECTIVE FLUXES

The property being conserved within a control volume (mass of water, mass of air, and energy) may be transported across the enclosing control volume area by advection, diffusion, and mechanical dispersion. In this discussion, advection is distinguished from molecular diffusion and mechanical dispersion: advection is due to bulk fluid motion, diffusion is due to molecular mixing and mechanical dispersion is another mixing process due to advection in tortuous porous media (Bear, 1972, pg 646). To distinguish between these transport mechanisms, $\mathbf{q}$ is used to indicate advection, $\mathbf{j}$ is used to indicate molecular diffusion, and $\mathbf{j}_d$ is used to indicate mechanical dispersion. Bold characters are used to highlight that these are

vector quantities. In this section, advective fluxes are discussed, and in the next sections, molecular diffusive and mechanical dispersive fluxes are discussed.

A.4.1 Advective Flux of Water

The advective mass flux of water, $q_{m,w}$ [kg/m^2-s], is the sum of contributions from both liquid, $q_{m,w,l}$, and gas, $q_{m,w,g}$, mass fluxes,

$$\mathbf{q}_{m,w} = \mathbf{q}_{m,w,l} + \mathbf{q}_{m,w,g} \tag{A-30}$$

The advective mass flux of water in the liquid or gas phase is equal to the density of water in the liquid or gas phase, ($\rho_{w,l}$ or $\rho_{w,g}$), times the area-average liquid or gas velocity, ($\mathbf{v}_l$, $\mathbf{v}_g$). The area-average velocities are also known as the specific discharge or Darcy's velocity (Bear, 1972; Freeze and Cherry, 1979; Domenico and Schwartz, 1990),

$$\mathbf{q}_{m,w,l} = \rho_{w,l}\, \mathbf{v}_l \tag{A-31}$$

$$\mathbf{q}_{m,w,g} = \rho_{w,g}\, \mathbf{v}_g \tag{A-32}$$

It was assumed that the fraction of dissolved air in the liquid is negligible, so that

$$\rho_{a,l} = 0 \tag{A-33}$$

The liquid is primarily composed of water, so that the liquid density is assumed equal to the density of liquid water.

$$\rho_{w,l} = \rho_l$$

A.4.2 Advective Flux of Air

The advective mass flux of air, $q_{m,a}$ [kg/m^2-s], is the sum of liquid, $q_{m,a,l}$, and gas, $q_{m,a,g}$, phase contributions.

$$\mathbf{q}_{m,a} = \mathbf{q}_{m,a,l} + \mathbf{q}_{m,a,g} \tag{A-35}$$

The advective liquid and gas phase mass fluxes of air are defined as follows:

$$\mathbf{q}_{m,a,l} = \rho_{a,l}\, \mathbf{v}_l \cong 0 \tag{A-36}$$

$$\mathbf{q}_{m,a,g} = \rho_{a,g}\, \mathbf{v}_g \tag{A-37}$$

A.4.3 Advective Flux of Energy

The advective flux of energy (neglecting kinetic energy), q_e [J/m^2-s], is the sum of liquid and gas phase transport contributions.

$$q_e = q_{e,l} + q_{e,g} \tag{A-38}$$

Being consistent with the conservation of mass formulations, both water (H_2O) and air may advect energy in the liquid and gas phases. The energy associated with air in the liquid phase is negligible compared to the energy associated with the liquid water.

$$q_{e,l} = q_{e,w,l} \tag{A-39}$$

Energy advected in the liquid water is equal to the enthalpy of water in the liquid phase, $h_{w,l}$ [J/kg] times the advective mass flux in the liquid phase, $q_{m,l}$.

$$q_{e,w,l} = h_{w,l}\, q_{m,w,l} \tag{A-40}$$

The enthalpy of liquid water can be a function of temperature and pressure, however it is frequently defined as the specific heat of water at constant pressure, $c_{p,w,l}$ [J/kg-K], times the temperature difference measured from a reference temperature.

$$h_{w,l} = c_{p,w,l}\,(T - T_{ref}) + h_{ref,w} \tag{A-41}$$

Similarly, the advective flux of energy in the gas phase, $q_{e,g}$, consists of contributions due to both water, $q_{e,w,g}$, and air, $q_{e,a,g}$.

$$q_{e,g} = q_{e,w,g} + q_{e,a,g} \tag{A-42}$$

The advective energy flux due to water in the gas phase, $q_{e,w,g}$, is equal to the enthalpy of water in the gas phase, $h_{w,g}$ [J/kg], times the advective mass flux of water in the gas phase, $q_{m,w,g}$.

$$q_{e,w,g} = h_{w,g}\, q_{m,w,g} \tag{A-43}$$

The enthalpy of gaseous water can be expressed as the specific heat at constant pressure, $c_{p,w,g}$, times temperature. To be consistent with the enthalpy in the liquid phase, the enthalpy of liquid-to-gas transformation, h_{lg}, is added:

$$h_{w,g} = c_{p,w,g}\,(T - T_{ref}) + h_{lg} + h_{ref,w} \tag{A-44}$$

Similarly, the advective energy flux due to air movement in the gas phase, $q_{e,a,g}$, is equal to the enthalpy of air in the gas phase, $h_{a,g}$, times the advective mass flux of air in the gas phase, $q_{m,a,g}$.

$$q_{e,a,g} = h_{a,g}\, q_{m,a,g} \tag{A-45}$$

where

$$h_{a,g} = c_{p,a,g}\,(T - T_{ref}) \tag{A-46}$$

The advective mass fluxes of water, air, and energy depend upon the liquid and gas area-averaged velocities, (v_l, v_g). The liquid and gas velocities, in turn, are dependent upon the geometry through which the fluids flow, fluid pressures, gravity and the degree of saturation. Prior to introducing an expression with which to determine the liquid and gas velocities (Darcy's law); liquid and gas pressures, and geometries of flow are discussed.

A.4.4 Potential of Water in Partially Saturated Media

The presence of liquid water in porous media under less than fully saturated conditions is affected by several different forces. Some of these forces differ from those found in free, pure water existing under fully saturated conditions. The total potential energy of liquid water (analogous to total-soil water potential in soil science) can be expressed as follows (Hillel, 1971; Koorevaar et al., 1983):

$$\psi_t = \psi_g + \psi_p + \psi_o + \psi_{other} \tag{A-47}$$

where ψ denotes potential energy and the subscripts t, g, p, and o denote total, gravity, pressure, and osmotic, respectively. Potential energy is typically expressed in terms of energy per unit mass, volume, or weight. Energy per unit weight is commonly referred to as hydraulic head in terms of height (e.g. meters) of standing water.

Gravitational potential, ψ_g, equals ρgz where g is the acceleration of gravity and z is the elevation about a datum when expressed in terms of energy per unit volume. The presence of a semipermeable membrane is required to sustain an osmotic potential that could induce liquid flow. The subscript "other" allows for additional potential forces, should they exist. For most cases of interest, these two categories of potential forces, ψ_o and ψ_{other} are not significant to this research project and will not be further considered. Therefore, Eqn. (A-47) reduces to:

$$\psi_t = \psi_g + \psi_p \tag{A-48}$$

The pressure potential, ψ_p, for less than fully saturated media is a subpressure condition that results from the combined effects of: (i) direct adhesion of water molecules to a solid surface; (ii) capillarity; and (iii) osmotic binding of water in double layers (Koorevaar et al., 1983). The pressure potential under partially saturated conditions is commonly referred

to as suction or tension and denoted by the symbol ψ (with no subscript). Pressure, P, is equal to ψ when expressed in terms of potential energy per unit volume.

Additional terms commonly used for pressure potential include matric potential, matric suction, and soil-water suction. In strict terms, matric potential includes osmotic potential, however, as stated above, osmotic potential is assumed to be negligible for this application and will not be further considered. Pressure, in turn, can be determined using the formula $P = \rho g z$, where z is the submergence depth below the free-water surface, when expressed in terms of energy per unit volume.

A.4.5 Capillary Pressure

By definition, the liquid pressure, P_l, is related to the gas pressure, P_g, by the capillary pressure, P_c.

$$P_c \equiv P_g - P_l \qquad \text{(A-49)}$$

By convention in this work, the capillary pressure has a positive value and is increasingly positive as the liquid saturation decreases. In other works, the capillary pressure is assumed negative, hence this is considered an important convention to be brought to the reader's attention.

As discussed by many investigators (Hillel, 1980a; de Marsily, 1986; Pruess et al., 1990a,b; Gray and Hassanizadeh, 1991a) the capillary pressure is primarily a result of water-gas interfacial surface tension effects and water adsorption to the solid material. At extremely low values of liquid saturation, water remains in the porous medium due to adsorptive forces. The fundamental mechanism of adsorptive forces is not discussed here, however it is noted that water is a bipolar molecule and solid surfaces are frequently surface charged. The term "pressure", although commonly used, is misleading if understood in its normal usage.

At higher values of liquid saturation, water is held in the porous media primarily by capillary forces. Physically, the capillary forces cannot exert a capillary pressure greater than 1 atmosphere. (This is considered correct and obvious, yet has recently been discussed by Gray and Hassanizadeh, 1991a.) For this reason, the terminology suction pressure is frequently used instead of capillary pressure. In this report, the terminology of capillary pressure is used with the understanding that it includes the combination of both surface tension effects (which dominate at $P_c < 1$ atm) and water adsorption in solids (which dominate at $P_c > 1$ atm).

A.4.6 J-Leverett Function

From dimensional analysis, the capillary pressure can be normalized by a combination of surface tension, pore size, and saturation (Leverett et al., 1941):

$$P_c = \frac{\sigma}{d} J(S_l) = \frac{\sigma}{\sqrt{k_{sat}/\phi}} J(S_l) \qquad \text{(A-50)}$$

where

S_l	=	liquid saturation (m^3 liquid / m^3 void) [dimensionless],
$J(S_l)$	=	J-Leverett function [dimensionless],
d	=	mean pore diameter [m],
σ	=	surface tension, which is temperature dependant [N/m], and
ϕ	=	porosity (m^3 void / m^3 medium) [dimensionless].

The J-Leverett function (Leverett et al., 1941; Bear, 1972, pg 446) may be a hysteretic function of liquid saturation. The mean pore diameter, d, may be roughly related to the permeability and porosity as (Leverett et al., 1941):

$$d = \sqrt{k_{sat}/\phi} \qquad \text{(A-51)}$$

It is recognized that Eqn. (A-51) is a crude approximation which does not account for the specific area of grains and other topological features of the medium (Kozeny, 1927). When the capillary pressure is less than 1 atm (0 atm $< P_c <$ 1 atm), then the capillary forces are primarily responsible for holding the water in the medium, and Eqn. (A-51) is considered appropriate. Conversely, when $P_c >$ 1 atm, adsorptive forces dominate and Eqn. (A-51) is not appropriate.

For the experiments conducted at CNWRA, saturation levels always remained above 50 percent (Green and Svedeman, 1991), and the capillary pressure was always measured to be above 0.2 atm or 20 kPa (Green and Dodge, 1991). In this range of saturations (hence capillary pressures), Eqn. (A-50) is expected to be a good approximation.

By assuming Eqn. (A-50) applies, the temperature, geometric, and saturation dependencies have been separated. The surface tension is a function of temperature, the mean pore diameter is a length scale, and the J-Leverett function is saturation dependent. Equation (A-50) will be used in at least the early dimensional analysis of the governing equations performed as part of the project.

Surface tension is a function of the temperature and chemical composition of both phases. Chemical composition of water is not currently addressed in this research project, and is therefore not considered to affect surface tension. This decision may be reconsidered in the future if the surface tension of rock waters of interest is found to vary significantly from that of pure water. The dependency of surface tension (hence capillary pressure) on temperature, however, is a relationship that will be included (σ = 72.7 dynes/cm at 20 C and 58.9 dynes/cm at 100 C for pure water).

A.4.7 Partially Saturated Hydraulic Conductivity

Fluid flow through partially saturated media can be predicted provided the hydraulic properties of the media are sufficiently characterized. Characterization of the hydraulic properties of partially saturated media can be defined with three media properties: moisture content, suction pressure, and hydraulic conductivity.

Saturated hydraulic conductivity, K_{sat} [m/s], is related to intrinsic permeability, k_{sat} [m^2], (also referred to as saturated hydraulic permeability or simply permeability) by the expression

$$K_{sat} = \frac{\rho g}{\mu} k_{sat} \qquad \text{(A-52)}$$

where

g	=	acceleration of gravity [m/s^2], and
μ	=	dynamic viscosity of liquid water [N s/m^2].

Permeability of partially saturated media is occasionally expressed in terms of relative permeability, k_{rel} [dimensionless], multiplied by saturated permeability, k_{sat},

$$k = k_{rel}\, k_{sat} \qquad \text{(A-53)}$$

likewise with hydraulic conductivity

$$K = K_{rel}\, K_{sat} \qquad \text{(A-54)}$$

Because of the difficulty associated with direct measurement, partially saturated hydraulic conductivity is frequently calculated using a theoretical model incorporating physical data such as moisture content, suction pressure, and pore-size distribution. Historically, several different approaches have been used to determine partially saturated hydraulic conductivity. One common approach was to determine partially saturated hydraulic conductivity using the relationship between suction pressure and saturation.

The relationship between the degree of saturation and suction pressure can be determined experimentally through a variety of methods. This relationship can be graphically represented with a moisture characteristic curve. A medium with a well-graded pore-size distribution will exhibit a gently sloping moisture characteristic curve. Whereas, the moisture characteristic curve of a medium with a poorly-graded pore-size distribution will be more nonlinear in nature and have a steeper slope. This latter condition is a source of computational difficulty when attempting to analytically or numerically represent the suction pressure/saturation relationship.

Further complicating the suction-pressure/saturation relationship is the difference between characteristic curves representing sorption (wetting or imbibition) and desorption (nonwetting or draining). This physical phenomenon, which is referred to as hysteresis, is attributed to the geometric configuration of the pores and to the consequences of entrapment of the nonwetting fluid (air) in the pores. Although the sorption and desorption curves bound the extreme values of the suction-pressure/saturation relationship, innumerable intermediate (scanning) curves can be observed depending upon the wetting/nonwetting history of the medium. The difference between the sorption and desorption curves is generally overlooked when characterizing the hydraulic properties of a medium mainly because of computational difficulties that arise when attempting to accommodate both curves. For example, the imbibition portion of the curve will be used when investigating infiltration events.

Previously, a computational method by Millington and Quirk (1961) and modified by others (Jackson, 1965; Jackson et al., 1965; Green and Corey, 1971; Bruce, 1972) was commonly used to calculate hydraulic conductivity values from the moisture characteristic curve. A major disadvantage resulting from using this method is realized when applying the method to anisotropic, inhomogeneous media because the suction-pressure/saturation values are presented in tabular form.

Gureghian et al. (1977) presents a series of computer programs to determine the partially saturated hydraulic conductivity as a function of moisture content based on field experiments for at least the Brooks-Corey and Mualem analytical models. The analytical models for relative hydraulic conductivity will now be discussed.

A.4.8 Analytical Model for Relative Hydraulic Conductivity

A different group of models is available that provides an analytical solution to the determination of saturated hydraulic conductivity based on values of the suction-pressure/saturation relationship. An early review of this group of analytic models was prepared by Brutsaert (1967). These analytical models have been categorized by Mualem (1976) into two groups: (i) those in which the relative hydraulic conductivity is a power function of the effective saturation, and (ii) those based upon the functional relationship between either pore-size distribution or suction pressure and moisture content. Although a variety of models are available, the models commonly used are those by Brooks and Corey (1966), from the first group, and Burdine (1953) and Mualem (1976), from the second group. Models similar to that described in Brooks and Corey may be thought of as generalized Kozeny-Carman equations (Kozeny, 1927; Carman, 1937). These models are semi-empirical and not valid for anisotropic media because there is no allowance for preferred pore space. The Burdine model and the Mualem model from the second group were obtained by analyzing simplified porous media models, in this case capillary bundles, to arrive at analytical expressions for partially saturated hydraulic conductivity in terms of saturation and suction pressure.

The Brooks and Corey (1966) model can be written in terms of relative hydraulic conductivity as

$$K_{rel} = K(S)/K_{sat} = (S_{eff})^{\epsilon} = \left(\frac{S - S_r}{1 - S_r}\right)^{\epsilon} \qquad \text{(A-55)}$$

where S_{eff} is the effective or dimensionless saturation ($S_{eff} = \{S - S_r\}/\{1 - S_r\}$), S_r is the residual saturation, and ϵ is the Brooks and Corey constant. The Brooks and Corey constant is defined to equal $(2 + 3\lambda)/\lambda$ where λ is an empirical exponent used as an index of pore-size distribution. λ was found by Brooks and Corey (1966) to have a value of less than two for soils with well-developed structures, two for typical porous media, and up to five for sands. For material such as volcanic tuff with a narrow pore-size distribution, ϵ may have a much larger value (Klavetter and Peters, 1986).

However, predictions of partially saturated hydraulic conductivity using an analytical method such as that by Brooks and Corey (1964) exhibit a discontinuity in the slope of the predicted moisture characteristic curve and appear to give less accurate results than do (modified) Millington and Quirk methods (van Genuchten, 1978).

The Burdine (1953) model is written as follows:

$$K_{rel} = S_{eff}^2 \frac{\int_0^{S_{eff}} dS/\psi^2}{\int_0^1 dS/\psi^2} \qquad \text{(A-56)}$$

where ψ is the capillary pressure head.

And finally the Mualem (1976) model,

$$K_{rel} = S_{eff}^{0.5} \left[\frac{\int_0^S \frac{dS}{\psi}}{\int_0^1 \frac{dS}{\psi}}\right]^2 \qquad \text{(A-57)}$$

Because of the functional dependence of partially saturated hydraulic conductivity on both saturation and suction pressure, Burdine's and Mualem's predictive models, as presented in Eqns. (A-56) and (A-57), respectively, cannot be directly applied. To address this difficulty, van Genuchten (1978) developed a closed-form analytical solution to determine saturation relative to the suction pressure as follows:

$$S_{eff} = \left[\frac{1}{1 + | \alpha \psi |^{\beta}} \right]^{\lambda} \qquad \text{(A-58)}$$

where α, β and λ are three independent parameters determined by matching the proposed curve with experimental moisture content/matric pressure data. For the particular relationship where $\lambda = 1 - 1/\beta$, Eqn. (A-58) assumes a common form

$$S_{eff} = \left[\frac{1}{1 + | \alpha \psi |^{\beta}} \right]^{1 - \frac{1}{\beta}} \qquad \text{(A-59)}$$

Substitution of Eqn. (A-59) into Burdine's model [Eqn. (A-56)] or Mualem's model [Eqn. (A-57)] permits determination of a closed-form solution to partially saturated hydraulic conductivity. The closed-form solution using Burdine's model is

$$K_{rel} = S_{eff}^{2} \left[1 - \left(1 - S_{eff}^{\frac{1}{\lambda}} \right)^{\lambda} \right] \qquad \text{(A-60)}$$

and the closed-form solution using Mualem's model is

$$K_{rel} = S_{eff}^{\frac{1}{2}} \left[1 - \left(1 - S_{eff}^{\frac{1}{\lambda}} \right)^{\lambda} \right]^{2} \qquad \text{(A-61)}$$

The substitution of van Genuchten's analytical solution of saturation in terms of suction pressure into Burdine's predictive model has become a popular method for calculation of partially saturated hydraulic conductivity (Klavetter and Peters, 1986; Pruess, 1987). Additional models for capillary pressure and partially saturated hydraulic conductivity are available. A document by Pruess (1987) contains appendices for each of these functions which list several other models that are commonly used.

Complications are also encountered when characterizing flow of water through partially saturated, fractured porous media in assigning hydraulic property values to the fractures (Peters et al., 1984; Klavetter and Peters, 1986; Pruess et al., 1986, Nitao, 1988).

A.4.9 Darcy's Law for Partially Saturated Media

The gas and liquid velocities can be calculated assuming that Darcy's Law is valid for partially saturated medium (Bear, 1979; Hillel, 1980; de Marsily, 1986) using the following expressions:

$$\mathbf{v}_l = - \frac{k_{sat}\, k_{rel,l}}{\mu_l} \left[\nabla P_l - \rho_l \mathbf{g} \right] \qquad \text{(A-62)}$$

$$\mathbf{v}_g = - \frac{k_{sat}\, k_{rel,g}}{\mu_g} \left[\nabla P_g - \rho_g \mathbf{g} \right] \qquad \text{(A-63)}$$

where

k_{sat}	=	hydraulic permeability at saturation [m^2],
$k_{rel,g}$ $k_{rel,l}$	=	gas and liquid phase relative permeability [dimensionless],
P_g, P_l	=	gas and liquid phase pressure [N/m^2],
ρ_g, ρ_l	=	gas and liquid phase density, respectively, [kg/m^3],
μ_g, μ_l	=	gas and liquid phase dynamic viscosity [$N\ s/m^2$], and
$\mathbf{g}$	=	gravitational vector, magnitude = 9.81 [m/s^2] in direction of decreasing elevation.

The applicability of Darcy's Law for the liquid in a partially saturated medium has been questioned by Gray and Hassanizadeh (1991a,b). The crux of Gray and Hassanizadeh's discussion is that the liquid phase may not be sufficiently connected so that the pressure gradient would not be transmitted in a partially saturated medium.

Given the low density of a gas (air and H_2O mixture), it is commonly assumed that the gas is at a uniform and constant pressure of one atmosphere. This appears reasonable except at low gas saturations (high liquid saturations) where small amounts of air exist in the medium and are "trapped" by the liquid. Also, in the immediate vicinity of a heat-generating source, high gas pressures may be due to rapid evaporation (i.e. boiling) of water, however this did not occur in experiments reported here.

More important is the assumption relating to the liquid pressure. At complete liquid saturation, it is straightforward to rationalize how the liquid transmits a pressure. However, it is likely that at low liquid saturations, the liquid is not well-connected and that the pressure is not transmitted continuously through the medium.

Since the degree of connectivity would decrease with decreased levels of saturation, the hydrostatic pressure component to total pressure would be less in a medium at low levels of saturation that for similar media at full or near-full saturation. Discussions by Gray and Hassanizadeh (1991a,b) provide a possible explanation of this mechanism. The velocity of the liquid phase of water which is typically expressed as in Eqn. (A-62) is modified for partially saturated conditions to the following:

$$\mathbf{v}_l = - \frac{k_{sat}\, k_{rel,l}}{\mu_l} \left[\nabla P_l - \rho_l \mathbf{g} + \left(\Omega_l - \Omega_g \right) \frac{\nabla S_l}{S_l} \right] \qquad \text{(A-64)}$$

where

Ω_l, Ω_g = wettability potential for the liquid and gas phase [N/m^3].

The capillary pressure, using Eqn. (A-64), is then not only a function of saturation but also interfacial area. The effect of interfacial area between the wetting (water) and nonwetting (air) phases is included to macroscopically account for the attraction forces between the solid and fluid phases which become increasingly important at lower saturations. Basically, the pressure gradient component, as stated in Eqn. (A-64), is less because an attraction to the solid phase by the wetting phase exerts force on the water and the degree of attraction is a function of the water/air and water/solid interfacial areas.

A.4.10 Klinkenberg Effect (Knudsen Flow)

It has been noted in the literature that Darcy's Law may underestimate the gas flow, especially at low pressures (Bear, 1972; Hillel, 1980a). At low gas pressures, the gas flow was found to be higher than predicted. This effect is caused by the gas not behaving as a continuum in the porous medium. This phenomena was reported by Klinkenberg (1941) and is known either as the Klinkenberg effect or as Knudsen flow.

Knudsen flow occurs when the mean free path of the gas molecules is large in comparison with the mean pore length scale. This situation results in the gas molecules having a higher probability of colliding with the pore walls than with other gas molecules. The presence of slip flow along the pore walls is referred to as the Klinkenberg effect and the resulting increased flow is called Knudsen flow.

The mean pore length scale is difficult to characterize for a porous medium, and in this work the mean pore diameter is used as that length scale. The Knudsen number is the ratio of the molecular mean free path to the length scale (Schaaf and Chambre, 1958; Vincenti and Kruger, 1965; Rohsenow and Choi, 1960):

$$\mathbf{Kn} = \frac{\lambda}{d} \qquad \text{(A-65)}$$

where

Kn	=	Knudsen number [dimensionless],
λ	=	mean free path of a gas molecule [m], and
d	=	mean pore diameter of the porous medium [m].

The mean free path is based on an infinite gas medium and can be characterized by the gas temperature and pressure (Schaaf and Chambre, 1958; Vincenti and Kruger, 1965; Rohsenow and Choi, 1960). For air the mean free path is (Rohsenow and Choi, 1960):

$$\lambda = 2.14 \times 10^{-10} \frac{T}{P} \quad [m\text{-}atm/K] \qquad (A\text{-}66)$$

The mean free path for a mixture of air and water vapor is expected to be close to that for air. For comparison purposes, the mean free path for air at atmospheric pressure and 15 C is approximately 6.2×10^{-8} m.

For a small pore diameter, the Knudsen number will be large and the gas will not exhibit continuum behavior but exhibit free-molecular flow behavior. The cause for the transition is that the gas molecules near the solid surface will not strike the surface a sufficient number of times to attain a bulk molecular velocity of zero. In the continuum case, the molecules near the solid surface repeatedly bounce against the solid surface and surrounding gas molecules so that the molecules close to the solid surface attain a bulk molecular velocity of zero. In the free-molecular flow case, the molecules near the solid surface bounce from the solid surface and continue until they strike a different surface. The net effect is that the gas does not have a "no-slip" velocity at the solid surface. In this case, it is customary to model the fluid as having a reduced effective dynamic viscosity (Vincenti and Kruger, 1965), or an increased gas phase relative permeability (Bear, 1972).

The transition from continuum to free-molecular flow regimes has been characterized by a Knudsen number, Kn, in the range from 0.01 to 1.0. At Kn = 0.01, the continuum regime begins to exhibit some "slip" behavior. At Kn = 1.0, the free-molecular flow regime is dominant. To calculate the Kn, however, the mean pore diameter length scale must be chosen. For comparison purposes, if $d < 6.2 \times 10^{-6}$ m (6 microns), then Kn > 0.01 and the Klinkenberg effect should be expected.

In the experiments reported here, the mean pore diameter was greater than 25 microns. Based on this value for d, the Klinkenberg effect is considered negligible. However, experiments performed on densely welded tuffaceous material indicated that an order of magnitude increase in flow velocity could be expected for the mechanism (Reda, 1987). Therefore, Knudsen flow and the Klinkenberg effect may be considered significant when investigating geologic materials.

A.5 MECHANICAL DISPERSIVE FLUXES

In the literature, when advection is discussed, mechanical dispersion is frequently discussed. Because a reader may be looking for a discussion of mechanical dispersion, this section has been included. However, it has been concluded that mechanical dispersion is not important in this work and will be neglected.

When fluid flows through a porous media, the fluid is effectively mixed by alternatively splitting, joining and mixing of the fluid through the tortuous path on the pore level (Bear, 1972; Freeze and Cherry, 1979; Hillel, 1980a; Domenico and Schwartz, 1990). This splitting, joining,

and mixing of the fluid roughly has the macroscopic effect of enhancing molecular diffusion so that concentrations of species traveling in the fluid are spread out. This phenomenon is known as mechanical dispersion (or hydrodynamic dispersion or hydraulic dispersion) because it depends on fluid advection and tortuous paths in the porous media. The mechanical dispersive flux can be written as:

$$j_d = - D_d \nabla C \qquad \text{(A-67)}$$

where

D_d = mechanical dispersion tensor, and
C = concentration of species or quantity of interest.

The mechanical dispersion tensor is a function of media properties and fluid flow rates. The dispersion tensor will not be discussed further here. The concentration of species is a quantity which is being advected with the fluid. In many studies the concentration of interest is a chemical pollutant or a radioisotope. For the current discussion, it could be interpreted to be either concentrations of water (or air) in the gas phase or internal energy (thermodynamic energy or heat).

The macroscopic effect of mechanical dispersion is very similar to molecular diffusion. Mechanical dispersion, however, differs from molecular diffusion in that it requires fluid advection. Mechanical dispersion can significantly spread the location of a species which has been introduced at an isolated location into a flowing liquid. Hence, it may need to be taken into account.

Because the current interest is in the transfer of water and air, and in the transfer of heat, mechanical dispersion is not considered important. It is not considered important because there is a lack of sharp "concentration" gradients in air, water, or heat profiles, due to the presence of other efficient distribution mechanisms (such as heat conduction). The main reason for the distribution of water vapor and internal energy is that they are primarily dependent on temperature which is distributed by conduction in the porous media. In review, mechanical dispersion is not considered an important transport mechanisms for heat and mass transfer as currently being studied in this project.

A.6 DIFFUSIVE FLUXES

The diffusive fluxes include both species and energy diffusion. In the solid and liquid phases, diffusion of mass is negligible, however, the mass molecular diffusion of water in the air (or air in the water) in the gas phase is modelled. In the gas phase, water and air are assumed to diffuse according to Fick's law (Bird et al., 1960; Incropera and Dewitt, 1981, pg 718; Lienhard, 1987), accounting for open cross-sectional area (ϕS_g) and tortuosity or irregular void connectivity (τ) (Hillel, 1980a; Pruess et al., 1990a).

$$j_{m,w,g} = - \eta \tau \phi S_g \rho_g D_{wa,g} \nabla m_{w,g} \qquad \text{(A-68)}$$

$$j_{m,a,g} = - \tau \phi S_g \rho_g D_{wa,g} \nabla m_{a,g} \quad \text{(A-69)}$$

where

$j_{m,w,g}$ and $j_{m,a,g}$	=	diffusive mass fluxes of water and air in the gas phase [kg/m^2-s],
η	=	gas diffusion enhancement factor for water [dimensionless],
τ	=	tortuosity [dimensionless],
ϕ	=	porosity [dimensionless],
S_g	=	gas phase saturation [dimensionless],
ρ_g	=	gas density (Note: $\rho_g = \rho_{a,g} + \rho_{w,g}$) [kg/m^3],
$D_{wa,g}$	=	gaseous molecular diffusion coefficient of water in air [m^2/s], and
$m_{a,g}$, $m_{w,g}$	=	mass fraction of air and water in the gas [dimensionless].

It is noted that diffusive mass fluxes are calculated relative to the bulk gas velocity (Bird et al., 1960). As such, the net mass flux is required to be zero:

$$j_{m,a,g} + j_{m,w,g} = 0 \quad \text{(A-70)}$$

Relatedly, the molecular diffusion coefficient is equal for water molecules through air, $D_{wa,g}$, and air molecules through water vapor, $D_{aw,g}$. It is emphasized that air is considered as a single component in this work.

A.6.1 Gas Diffusion Enhancement Factor

The gas phase mass diffusion enhancement factor, η, has been included for water in a nonisothermal partially saturated porous media. It has been noted (Phillip and de Vries, 1957; Pollock, 1982; Mulay, 1988) that a straightforward application of Fick's law underestimates the nonisothermal gas phase diffusion of water. Phillip and de Vries (1957) proposed two explanations for this phenomena: (i) coupled gas-liquid transfer and (ii) increased temperature gradients in the gas phase. The explanations are not discussed here, however, one should note that the diffusion enhancement factor has been estimated to be between two and eight, depending on the degree of saturation (Phillip and de Vries, 1957). Not all researchers, however, acknowledge the need for η. For comparison, different approaches reported in the literature are discussed further.

Pollock (1982) and Mulay (1988) discuss the importance and necessity of the diffusion enhancement factor. Stallman (1964) acknowledges that large discrepancies have been reported between measurements and calculated rates of vapor flow. Stallman (1964) notes that Phillip and de Vries (1957) have hypothesized some interaction between the liquid and vapor phases and have developed a theoretical model for estimating the nonisothermal vapor flow, however, Stallman notes that the model still needs to be experimentally substantiated. Stallman

describes the existing experimental data as frequently incomplete such that it is impossible to perform comparative analyses of experimental data.

Pruess (1987) is brief in his discussion of the nonisothermal vapor flow and appears to have adopted a straightforward application of Fick's law. In recent work, Pruess et al. (1990a) neglect diffusion of vapor in air, the result of which is not clear at this time. Similarly, Forsyth (1990) and Forsyth and Simpson (1991) simply reference the work of Pruess (1987) and have no discussion of nonisothermal diffusion enhancement. Bixler (1985) similarly does not discuss vapor diffusion enhancement.

Because of the lack of a solid theoretical basis (although it has been reported experimentally), the diffusion enhancement factor for water vapor is neglected in this work. A review of the literature continues in an effort to determine if additional experimental work has been completed in this area. However, the inclusion of η appears lacking sound justification so that it may be assumed:

$$\eta = 1 \tag{A-71}$$

realizing that in future work this assumption may be revisited.

A.6.2 Thermal Energy

Thermal energy is assumed to be transported by three diffusion mechanisms: conduction in the porous medium, diffusion of air in the gas phase, and diffusion of water in the gas phase

$$\mathbf{j}_e = \mathbf{j}_{e,cond} + \mathbf{j}_{e,a,g} + \mathbf{j}_{e,w,g} \tag{A-72}$$

The heat transfer due to the enthalpy of air diffused in the gas phase is

$$\mathbf{j}_{e,a,g} = h_{a,g}\, \mathbf{j}_{m,a,g} \tag{A-73}$$

and due to the enthalpy of water diffused in the gas phase is:

$$\mathbf{j}_{e,w,g} = h_{w,g}\, \mathbf{j}_{m,w,g} \tag{A-74}$$

Thermal energy (heat) is assumed to conduct through the porous medium according to Fourier's Law (Bird et al., 1960; Lienhard, 1987).

$$\mathbf{j}_{e,cond} = - k_t \nabla T \tag{A-75}$$

where

$\mathbf{j}_{e,cond}$ = conductive heat flux [W/m^2], and
k_t = thermal conductivity of the porous medium [W/m-C].

It is emphasized that the saturated hydraulic permeability, k_{sat}, has units m^2, while the thermal conductivity, k_t, has units W/m-C. It is noted that $j_{e,cond}$ includes conduction through solid, liquid, and gas phases. Conduction through the solid is dominant with the influence of liquid saturation frequently being modelled and the influence of gas composition being neglected. Models for k_t will be discussed in the next section. Following is a discussion of mass fraction, partial pressure of water in the gas phase (needed in the determination of mass fraction), the diffusion coefficient, and thermal conductivity.

A.6.3 Mass Fractions of Water and Air in the Gas Phase

The mass fractions of water and air in the gas need to be calculated in order to determine the diffusive fluxes. Because the fluids travel relatively slowly through the porous medium, there is sufficient time to reach local thermodynamic equilibrium. Hence, it is assumed that the gas is locally saturated with water vapor at all times. Using this assumption, the mass fraction of water in the gas, $m_{w,g}$, can be calculated as a function of only temperature and pressure. By definition, the mass fraction can be related to the densities as:

$$m_{w,g} \equiv \frac{\rho_{w,g}}{\rho_g} = \frac{\rho_{w,g}}{\rho_{a,g} + \rho_{w,g}} \qquad \text{(A-76)}$$

so that the mass fraction of water in the gas is directly related to the gas pressure and temperature by the perfect gas law [by combination of Eqns. (A-76), (A-11) and (A-15)]:

$$m_{w,g} = \frac{P_{w,g}\, M_w}{P_{w,g}\, M_w + (P_g - P_{w,g})\, M_a} \qquad \text{(A-77)}$$

where

$P_{w,g}$ = partial pressure of water in the gas [N/m^2], and
M_w = molecular weight of water (M_w = 18.02 kg/kgmole).

A.6.4 Kelvin's Equation

As the porous medium dries, the amount of water in both the liquid and gas phases decreases. In this work and in most other works, only one equation is used to express the conservation of water in both the liquid and gas phases. The single conservation equation requires a constitutive equation predicting the amount of water in the gas phase based on the temperature and amount of water in the liquid phase. The amount of water in the gas phase is conveniently expressed as the partial pressure of water in the gas phase. A relation known as Kelvin's equation (Thomson, 1871) has been cited and used in the literature to predict the decrease in gaseous water partial pressure.

$$P_{w,g} = P_v \exp\left(\frac{-M_w P_c}{\rho_l R T}\right) \qquad \text{(A-78)}$$

where

P_v	=	equilibrium vapor pressure of water over a planar free surface [N/m^2],
ρ_l	=	liquid water density [kg/m^3],
M_w	=	molecular weight of water [18.02 kg/kgmole],
T	=	temperature [K],
P_c	=	capillary pressure [N/m^2], and
R	=	ideal gas law constant [R = 8314 J/kgmole-K].

It should be noted that William Thomson was knighted by Queen Victoria in 1866 and became Lord Kelvin (Encyclopedia Britannica); hence, the attribution to Kelvin.

Kelvin's equation indicates that the vapor pressure above a curved air-water interface is different from that above a planar interface. When the interface is concave with respect to the liquid, then the liquid pressure is less than the gas pressure. This is the case for partially saturated porous media because water is a wetting fluid for rock. For comparison purposes, a liquid drop in a gas has a convex interface (with respect to the liquid); hence, the liquid drop is at a higher pressure than the gas. When the air-water interface is planar, the pressure difference across the interface is zero and the partial pressure of water in the gas phase is equal to the vapor pressure. Kelvin's equation predicts the reduced vapor pressure for a partially saturated porous media.

The origins and development of Kelvin's equation were unclear, so they were investigated in the literature. From this review, it was found that Kelvin's equation was originally derived for convex air-water interfaces in capillary tubes (Thompson, 1871) and has been applied to partially saturated porous media (Edlefsen and Anderson, 1943). The sources cited for Kelvin's equation are compared in Table A-1. Kelvin's equation only becomes important for dry soils with a capillary pressure greater than tens of atmospheres. As it has been discussed in this report, the liquid phase behaves quite differently when it is held by capillary forces (P_c < 1 atm) or adsorption forces (P_c > 1 atm). It is important to review Kelvin's equation and concur with its applicability when the capillary pressure is greater than one atmosphere. Of the investigators listed in Table A-1, a few present derivations of Kelvin's equation (Thompson, 1871; Edlefsen and Anderson, 1943; van Wijk and de Vries, 1963; Bear and Bachmat, 1991). Most of the derivations are based on the original capillary tube model presented by Thompson (1871) with the exception of Bear and Bachmat (1991) who present a brief derivation using Gibb's free energy. At this time, the literature investigation continues. These concerns are summarized by Edlefsen and Anderson (1943, pg 198) who write:

> [Kelvin's] relation was developed by using an assumption that seems unjustifiable at low soil moisture contents. In developing [Kelvin's equation] it was assumed

Table A-1. SUMMARY OF INVESTIGATORS WHO DEVELOPED OR CITED KELVIN'S EQUATION

Investigator(s)	Use Name "Kelvin"	Reference Cited
Thomson (1871)	No	None, developed
Edlefsen and Anderson (1943)	No	None, developed
Philip and de Vries (1957)	No	Edlefsen and Anderson (1943)
van Wijk and de Vries (1963)	No	None, developed
Stallman (1964)	No	Edlefsen and Anderson (1943)
Defay et al. (1966)	Yes	Thomson (1871)
Bear (1972)	Yes	Thomson (1871) Stallman (1964)
Whitaker (1977)	Yes	Defay et al. (1966)
Hillel (1980a)	No	de Vries (1975)
Pollock (1986)	No	Edlefsen and Anderson (1943)
Mulay and Lavan (1989)	No	Edlefsen and Anderson (1943)
Pruess et al. (1990a)	Yes	Edlefsen and Anderson (1943)
Bear and Bachmat (1991)	Yes	Adamson (1967) Edlefsen and Anderson (1943) developed

that the soil particles do not attract the water molecules lying in the vapor-liquid interface and therefore do not affect their vapor pressure outside the interface. Curiously enough, we apparently cannot get interfaces concave towards the vapor phase without assuming that water adheres to the surface of the solid. Necessarily, therefore, the soil must have an adsorptive force field that attracts the water molecules. At low moisture contents this adsorptive field surrounding the soil particle must affect the vapor pressure and cause a derivation from [Kelvin's equation]. The vapor pressure of water in small capillaries has been found to be much small than [Kelvin's equation] would predict.

A.6.5 Clapeyron-Clausius Equation

The equilibrium vapor pressure is a function of temperature and can be calculated using either the thermodynamic steam tables or an approximate formula frequently called the Clapeyron-Clausius equation. The Clapeyron-Clausius equation is sufficiently accurate for water over the temperature range of interest (20 C < T < 100 C). In every thermohydrologic study reviewed from the literature, the effect of liquid composition is neglected and pure water was assumed to constitute the liquid for the calculation of the vapor pressure. The assumption of pure water is frequently not true, especially in a porous media, so that the perceived increase in accuracy gained by referencing thermodynamic steam table is frequently misleading. The single, approximate Clapeyron-Clausius equation is considered sufficiently accurate for use in this development.

The Clapeyron-Clausius equation is derived from the Clapeyron equation which relates the vapor pressure, heat of vaporization, vapor density, and temperature (Van Wylen and Sonntag, 1978, pg 371; Cravalho and Smith, 1981, pg 284; Wark, 1983, pg 484):

$$\frac{dP_v}{dT} = \frac{h_{lg}\,\rho_v}{T} \qquad \text{(A-79)}$$

The water vapor density can be approximated using the ideal gas law, and the Clapeyron equation can be integrated from a reference vapor pressure and a reference temperature ($P_{v,o}$, T_o) to an unknown vapor pressure and temperature (P_v, T). The resulting algebraic equation is frequently called the Clapeyron-Clausius equation (Wark, 1983, pg 487):

$$\ln\left(\frac{P_v}{P_{v,o}}\right) = \frac{h_{lg}\,M_w}{R}\left(\frac{1}{T_o} - \frac{1}{T}\right) \qquad \text{(A-80)}$$

where

$P_{v,o}$ = vapor pressure at temperature T_o [N/m^2], and
T_o = reference temperature [K].

The equation can be manipulated to yield

$$P_v = P_{v,o}\exp\left(\frac{h_{lg}\,M_w}{R}\left(\frac{1}{T_o} - \frac{1}{T}\right)\right) \qquad \text{(A-81)}$$

Kelvin's equation and the Clapeyron-Clausius equation are frequently combined to yield the partial pressure of water in the gas phase as a function of temperature and capillary pressure (Whitaker, 1977; Chen and Chung, 1990; Parlar et al., 1990).

$$P_{w,g} = P_{v,o} \exp\left(\frac{-M_w P_c}{\rho_l R T} + \frac{h_{lg} M_w}{R}\left(\frac{1}{T_o} - \frac{1}{T}\right)\right) \qquad \text{(A-82)}$$

where

M_w	=	molecular weight of water (M_w = 18.02 kg/kgmole),
R	=	ideal gas law constant (R = 8314 J/kgmole-K),
ρ_l	=	density of liquid water ($\rho_l \simeq$ 1000 kg/m^3),
h_{lg}	=	heat of vaporization for water ($h_{lg} \simeq$ 2400 kJ/kg at $\approx$40 C),
T_o	=	reference temperature (T_o = 313 K), and
$P_{v,o}$	=	reference vapor pressure ($P_{v,o} = 7.4 \times 10^3$ N/m^2 at $\approx$40 C).

A.6.6 Gaseous Air-Water Diffusion Coefficient

The gaseous bimolecular diffusion coefficient for water and air, $D_{wa,g}$, has been used in this work, hence it needs to be calculated. Based on a billiard-ball concept of diffusion in an ideal gas, the bimolecular diffusion coefficient is proportional to the inverse of pressure, and temperature to the three-halves (3/2) power (Bird et al., 1960, pg 510; Rohsenow and Choi, 1961, pg 382; Lienhard, 1987, pg 531).

$$D_{wa,g} = D_{wa,g,o}\left[\frac{P_o}{P_g}\right]\left[\frac{T}{T_o}\right]^{3/2} \qquad \text{(A-83)}$$

$D_{wa,g,o}$	=	reference molecular diffusion coefficient (2.2×10^{-5} m^2/s),
T_o	=	reference temperature (273 K), and
P_o	=	reference pressure (1 atm).

There is good agreement between theory and experimental data on scaling of the diffusion coefficient, $D_{wa,g}$, with pressure. However, scaling the diffusion coefficient with temperature is frequently reported in the range from 3/2 to 2 (Eckert and Drake, 1987, pg 787; Lienhard, 1987, pg 534). The different scaling factors are attempts to accurately scale the power of temperature with experimental data. Because the reported scaling with temperature varies throughout the literature and because the differences are similar to viscosity and conductivity differences, a brief overview of the temperature scaling is presented here.

The difference between simple theory based on the billiard-ball model and experimental data for thermal conductivity, k_t, and dynamic viscosity, μ, are the same for the binary diffusion coefficient. Theoretically, from a billiard-ball model of molecular interactions in an ideal gas, it can be shown (Bird et al., 1960; Rohsenow and Choi, 1961; Vincenti and Kruger, 1965) that thermal conductivity scales as temperature to the 1/2 power, (half-power) where thermal conductivity describes the diffusion of thermal energy. Similarly, dynamic viscosity scales as temperature to the 1/2 power, where dynamic viscosity describes the diffusion of momentum. Using experimental data, however, the scaling of both k_t and μ is more closely

related to the 0.75 power or 1.0 power of temperature. Similarly, the simple theory predicts that the bimolecular diffusion coefficient scales temperature to the 3/2 power, however experimental data scale more closely with temperature to the 7/8 power. For discussion purposes, it is assumed that either the 3/2 or 7/8 power is adequate over the temperature range of interest.

A.6.7 Porous Media Thermal Conductivity

Thermal conductivity, k_t, needs to be calculated. Thermal conductivity for a partially saturated porous medium is primarily a function of liquid saturation. Only a limited discussion of the dependency of thermal conductivity on saturation has been located in the literature, with the most common assumption being that it is either a linear function of saturation from zero liquid saturation ($S_l = 0$) to full liquid saturation ($S_l = 1.0$) (e.g. Pruess, 1987 among others),

$$k_t = k_t(S_l=0) + S_l \left[k_t(S_l=1) - k_t(S_l=0) \right] \qquad \text{(A-84)}$$

or, alternatively, a square-root function of saturation.

$$k_t = k_t(S_l=0) + \sqrt{S_l} \left[k_t(S_l=1) - k_t(S_l=0) \right] \qquad \text{(A-85)}$$

Kaviany (1991, pg 514) reports that the "square-root" function has been used by other researchers while the "linear" function is not as widely used. In this work either functionality is considered adequate for the rock in the proposed HLW repository. The main reason that either equation is adequate is that rock has a low porosity, hence the majority of the conducted heat will be through the rock matrix and saturation is expected to be of reduced consequence. The fundamental work of de Vries (1963) is continuing to be investigated and may provide a more rigorous expression of effective thermal conductivity.

A.7 SUMMARY OF EQUATIONS

The preceding equations complete the mathematical model for coupled thermohydrologic transport in a porous media. The equations were presented in a form which loosely followed the common conservation and constitutive equation outline. In themselves, each equation should appear simple. However, many auxiliary definitions were introduced to simplify the equations, as a result, the continuity from equation to equation may be lost. For the sake of conciseness, the equations are combined into fewer, yet more complex equations. The conservation of water equation can be written as:

$$\frac{\partial}{\partial t}\left(\rho_{w,l} S_l \phi + \rho_{w,g} S_g \phi\right) =$$

$$\nabla \cdot \left(\rho_{w,l} \frac{k_{sat}\, k_{rel,l}}{\mu_l} \left[\nabla P_l + \rho_l g \hat{k} \right] \right.$$

$$\left. + \rho_{w,g} \frac{k_{sat}\, k_{rel,g}}{\mu_g} \left[\nabla P_g + \rho_g g \hat{k} \right] \right) \qquad \text{(A-86)}$$

$$+ \nabla \cdot \left(\tau \phi S_g \rho_g D_{wa,g} \nabla m_{w,g} \right)$$

The conservation of air equation is

$$\frac{\partial}{\partial t}\left(\rho_{a,g} S_g \phi\right) =$$

$$\nabla \cdot \left(\rho_{a,g} \frac{k_{sat}\, k_{rel,g}}{\mu_g} \left[\nabla P_g + \rho_g g \hat{k} \right] \right) \qquad \text{(A-87)}$$

$$+ \nabla \cdot \left(\tau \phi S_g \rho_g D_{wa,g} \nabla m_{a,g} \right)$$

The conservation of energy equation is

$$\frac{\partial}{\partial t}\left(\phi \rho_{s,slg} h_s + \phi S_l \rho_l h_l + \phi S_g \rho_g \left[m_{w,g} h_{w,g} + m_{a,g} h_{a,g} \right]\right) =$$

$$\nabla \cdot \left(h_{w,l} \rho_l \frac{k_{sat}\, k_{rel,l}}{\mu_l} \left[\nabla P_l + \rho_l g \hat{k} \right] \right)$$

$$+ \nabla \cdot \left(\left(h_{w,g} m_{w,g} + h_{a,g} m_{a,g} \right) \rho_g \frac{k_{sat} k_{rel,g}}{\mu_g} \left[\nabla P_g + \rho_g g \hat{k} \right] \right) \qquad \text{(A-88)}$$

$$+ \nabla \cdot \left(\left(h_{w,g} - h_{a,g} \right) \tau \phi S_g \rho_g D_{wa,g} \nabla m_{w,g} \right)$$

$$+ \nabla \cdot \left(k_t \nabla T \right) + Q_e$$

In these expanded conservation equations, the relative permeability is a function of liquid saturation, the water-air bimolecular diffusion coefficient is a function of temperature and pressure, the mass fraction of water in the gas is a function of temperature and pressure, the internal energies and enthalpies are functions of temperature (and possibly pressure), and the gas

density is a function of temperature and pressure. Although the expanded conservation equations are more concise, they still require additional relationships.

A.8 CONSIDERATION OF FRACTURES

Throughout this section, fractures have not been explicitly referenced. It is believed that the rock of the proposed HLW repository in Yucca Mountain has a well-connected fracture network (Scott et al., 1982). The fractures have been characterized to have a width of 10 to 100 microns, and an individual permeability of 10^{-16} to 10^{-11} m^2. In comparison, the rock matrix has a much lower permeability of approximately 10^{-18} (Pruess et al., 1990). Ultimately, one needs to develop a sufficient understanding of the thermohydrology as encountered in the fractured repository environment.

Fracture modelling techniques have been summarized by Sagar and Gureghian (1991). In addition, Ababou (1991) has discussed the effective permeability of a fracture network. The scope of fracture models is very large and currently under extensive investigation. Within the scope of this research project, however, fracture modeling is afforded limited investigation. For more extensive developments, the reader is referred to Gureghian and Sagar (1991) and Ababou (1991) among others. Three of the techniques, known as the effective-continuum, the dual-continuum, and explicit representation are briefly discussed here.

The effective-continuum is the least complicated model and is closely related to the volume and area averaging process inherent in the porous medium formulations. In review, Darcy's law is a simple statement describing the average behavior of a very complicated flow phenomenon. This is precisely the motivation in the effective-continuum model of fractured porous medium as it is described in textbooks (e.g. Domenico and Schwartz, 1990). In applications, the most important properties of the effective-continuum model are the relative permeabilities of the matrix and the fractures, and capillary pressure as functions of saturation. The relative permeability of the medium plotted against saturation is assumed to have a characteristic double-hump shape which represents the combined effect of the relative permeability of the fractures and the matrix (Domenico and Schwartz, 1990). Pruess et al. (1990) have applied the effective-continuum model to the problem of HLW in a geologic repository and report good agreement with more explicit simulations using simplified fracture networks.

The dual-continuum (also known as double porosity) approach doubles the sets of conservation equations. Two sets of equations, one for the matrix and the second for the fractures, are superimposed over the entire volume of interest and at each point in space. The matrix and fracture equations are coupled with a matrix-to-fracture transfer term. Warren and Root (1963) applied the dual-continuum approach to problems in the petroleum industry, and lately, Updegraff et al. (1991) has applied the dual-continuum method to partially saturated, fractured rock, analogous to the setting at the proposed HLW geologic repository. For a more in-depth discussion of the dual-continuum approach, see Ababou (1991).

The explicit fracture approach has the most geometrically and computationally complex features. The geometry and extent of individual fractures are modelled explicitly with specified width and permeability. This formulation requires an overwhelming amount of information which typically does not exist except in a statistical format. A primary advantage of this method is that the fracture and matrix are not assumed to be in thermal and/or hydraulic equilibrium. This quality is not important since the assumption of equilibrium is generally considered valid in the far-field for the proposed HLW repository because of the long time scales under consideration. The proposed HLW repository has large length scales of the order of 10 to 500 meters, so that for far-field studies, the explicit fracture model would be overwhelmingly complicated. However, the explicit fracture model does offer the best spatial resolution on small length scales where only a few fractures exist.

The flow equations for partially saturated media can formally be applied to either the effective-continuum, dual-continuum, or explicit fracture models without significant modification. The most important change for the effective-continuum method is that the relative permeabilities are more complicated (double-hump) functions of saturation. For the explicit fracture model, one needs to specify fracture location, size and relative permeability. The most involved adaptation to the equations presented in this section would be for the dual-continuum model which requires a matrix-to-fracture transfer term which would need to be added as sink/source terms to the conservation equations.

APPENDIX B: INITIAL AND BOUNDARY CONDITIONS

In this appendix, the thermohydrologic initial and boundary conditions that need to be determined before a mathematical model can be used to predict fluid flow and heat transfer for either a laboratory experiment or the full-scale repository are discussed. The initial and boundary conditions are exceedingly important. For discussion purposes, the initial and boundary conditions for a laboratory experiment are described, followed by a discussion for the full-scale repository.

For discussion purposes, the focus is on determining the initial and boundary conditions for three primary variables: temperature, liquid saturation, and gas pressure. However, alternative initial and boundary condition descriptions exist. In many cases, the boundary conditions are statements about fluxes of mass or energy. For the laboratory experiment, the confining walls are impermeable so that no fluid penetrates the walls. Similarly in the geologic repository, a mean geothermal flux of thermal energy has been used as a boundary heat flux.

Strong differences exist between the initial and boundary conditions for a laboratory experiment and a full-scale repository. Probably the most important difference is the geometrical extent. A laboratory experiment is comparatively well confined and the boundaries of the domain are well known (e.g. sides of an enclosure). For the laboratory experiment, it is a trade-off of a smaller, manageable size which is large enough to best reproduce the flow processes without impeding them. In the full-scale repository, however, there is no clear choice for the geometrical extent for analysis purposes. The analyst must decide, however, the size of domain. Typically, the size of a domain is decided by considering computational efficiency, natural boundaries, and the assumed boundary condition influence on the desired calculations. In theory, a large full-scale repository domain can be selected. However, it may not have well-characterized boundary conditions and it may include a large region where the results of the analysis are neither important nor desired. Hence, the size of the domain is clear for a laboratory experiment and both unclear and exceedingly important for the full-scale repository. The choice of geometrical domains is considered to be one of the most important choices that must be made in order to perform an analysis of the full-scale repository.

B.1 LABORATORY EXPERIMENT

The typical initial conditions and boundary conditions for a laboratory experiment are summarized in Table B-1 for the temperature, liquid saturation and gas pressure. The initial conditions for temperature are normally isothermal (before a heat or constant temperature source is turned on). The liquid saturation is normally close to a gravity drainage profile, depending of the rate at which liquid redistributes due to gravity drainage. The gas pressure is typically in a hydrostatic state where the hydrostatic gas pressure gradient is negligible. These values for initial conditions are based on a sealed experimental domain (such as conducted at CNWRA), and would change if initial nonzero mass or heat flux boundary conditions existed.

Table B-1. INITIAL AND BOUNDARY CONDITIONS FOR TEMPERATURE, LIQUID SATURATION AND GAS PRESSURE IN A LABORATORY EXPERIMENT CONDUCTED AT CNWRA

	Initial Conditions	Boundary Conditions
T	isothermal	constant temperature or insulated
S_l	gravity drainage profile	impermeable walls, no liquid penetration
P_g	uniform	impermeable walls, no gas penetration

The typical laboratory boundary conditions for temperature are either (i) constant temperature, (ii) constant heat flux (with insulated boundaries being a zero heat flux condition), or (iii) convective heat flux. These three boundary conditions are frequently expressed using mathematical terminology as either Dirichlet, Neumann, or mixed. For the experiments conducted at CNWRA, the boundary conditions were approximately either constant temperature:

$$T(\mathbf{x}_b) = T_{const} \tag{B-1}$$

or insulated:

$$\mathbf{q}_{e,cond} \cdot \mathbf{A} \sim \frac{\partial T}{\partial x} \cdot \mathbf{A} \sim \frac{\partial T}{\partial x_b} = 0 \tag{B-2}$$

where

A = normal boundary surface area vector, and
x_b = location of boundary, measured normal to the boundary surface area.

The no heat flux boundary condition is clearly a constraint on the temperature gradient normal (i.e. perpendicular) to the boundary surface.

The typical laboratory boundary condition for liquid is more exactly expressed as a constraint on the mass flux of water across the solid boundary. The confining walls in the experiment are considered impermeable to water:

$$\mathbf{q}_{m,l} \cdot \mathbf{A} = 0 \tag{B-3}$$

For convenience, the zero mass flux boundary condition may approximately be expressed as a constraint on the gradient of the liquid saturation at the wall (just as the zero heat flux boundary

condition fixed the temperature gradient). To be more specific, this is true only if the hydraulic properties of the medium are constant.

The typical laboratory boundary condition for gas pressure is very similar to that for liquid saturation. The boundary walls are considered impermeable to gas flow:

$$q_{m,g} \sim \frac{\partial P_g}{\partial x_b} = 0 \qquad \text{(B-4)}$$

The zero gas phase mass flux boundary condition is shown to constrain the gas pressure gradient normal (i.e. perpendicular) to the boundary surface.

This concludes a discussion of the initial and boundary conditions for a typical laboratory experiment conducted at CNWRA. The case of the full-scale repository is discussed next.

B.2 FULL-SCALE REPOSITORY

In comparison, the initial and boundary conditions for the full-scale repository are difficult (if not impossible) to state with confidence. Of the three primary variables, initial condition for liquid saturation are considered the most uncertain. The uncertainties in the initial liquid saturation distribution originates from (i) the relatively long times required for the liquid saturation to reach steady state (assuming that steady boundary conditions existed), (ii) relatively short times over which the infiltration boundary conditions change, (iii) strong media heterogeneities, and (iv) changes in water table recharge which may result from changes at great distances from the repository. Bagtzoglou, Ababou, and Sagar (1992) discuss a successive approximation method to obtain consistent initial boundary conditions for variably saturated flow in a layered and faulted domain similar to Yucca Mountain. The mathematical formulation of the coupled thermohydrologic problem is nonlinear so that multiple mathematical solutions may exist where only one physical solution exists. The nonlinearity adds an additional complication so that the choice of initial conditions may lead to very different mathematical predictions which may be inconsistent with the physics. Similarly, the initial temperature and gas pressure distributions have uncertainties. For comparison, the expected full-scale repository initial and boundary conditions are tentatively given in Table B-2.

As discussed earlier, the spatial extent is probably the most important and difficult aspect of the problem to address. The repository can be considered to have a lateral and a vertical extent. The vertical extent has a logical choice: from the ground surface to the water table. The lateral extent is considered very difficult to determine. Frequently, the analyst will select a lateral extent such that it does not influence the results of the analysis. This is good, however, the size should not be so large that significant effort is devoted to regions where the results are not of interest or that the boundary conditions are uncertain. Liquid water is expected to be nonzero at the lateral boundaries, but the magnitude and the temporal occurrence of liquid inflow is considered uncertain. Although boundary conditions at the proposed HLW repository are speculative and uncertain, they are compared in Table B-2 because in a dimensional analysis,

Table B-2. INITIAL AND BOUNDARY CONDITIONS FOR TEMPERATURE, LIQUID SATURATION AND GAS PRESSURE IN A MODEL OF THE PROPOSED REPOSITORY

	Initial Conditions	Boundary Conditions
T	primarily linear geothermal (yet fluctuations exist)	at ground surface, approximately constant at water table, approximately constant at sides, approximately geothermal gradient
S_l	largely uncertain (may have perched water and other anomalies)	at ground surface, time-varying infiltration at water table, $S_l = 1$ (location of water table probably uncertain) at sides, S_l (or $q_{m,l}$) highly uncertain
P_g	primarily hydrostatic (or approximately uniform)	at ground surface, approximately constant at water table, approximately constant at sides, approximately constant

they will need to be consistent between a laboratory experiment and the proposed repository in order to predict repository performance.

APPENDIX C: SOLUTION TECHNIQUES

In this section, techniques for solving the governing equations and computer programs that implement those techniques are briefly described. It is important that the reader be made aware of five important points: (i) the development of analytic methods, numerical methods and computer programs is outside the scope of this research project, (ii) the development of new analytical methods, numerical methods or computer programs is not anticipated, (iii) other projects at CNWRA have and are continuing to develop thermohydrologic (or closely related) numerical techniques and computer programs (Runchal and Sagar, 1992), (iv) other projects funded by the NRC have developed hydrologic computer programs (e.g. Updegraff et al., 1991) and have documented existing thermohydrologic computer programs (e.g. Pruess, 1987), and (v) analytical methods, numerical methods, and computer programs are being used in this research project to make predictions and comparisons with the experimental data. In this project, no specific analytical method, numerical method, or computer program is recommended. Rather, the scope of this project includes mathematical models, dimensional analysis, experimental techniques, and laboratory experiments. However, a literature review has been conducted in the areas of analytical techniques, numerical techniques, and computer programs because these are expected to be used as tools. This review of solution techniques is documented here by presenting a brief overview of the characteristics in each area (i.e., analytical techniques frequently are based on a Boltzmann transformation, numerical techniques frequently must devote considerable attention to choice of primary variables and transient integration schemes, and computer programs frequently have spatial restrictions and/or phenomenological restrictions). Each source is cited by author and is followed by a brief description of capabilities, restrictions, and peculiarities.

C.1 ANALYTICAL TECHNIQUES

As a general rule, analytical solutions are only possible in cases with simple geometries and simple thermohydrologic couplings. An example of a simple geometry is an infinite cylindrical source of thermal energy in an infinite homogeneous medium. A simple thermohydrologic coupling is a nonhysteretic capillary pressure versus liquid saturation curve (this is also a common assumption adopted in computational techniques).

Many proposed semi-analytical solutions for parabolic partial differential equations are based on the Boltzmann transformation which is described in the heat transfer and thermohydrologic textbooks (Carslaw and Jaeger, 1959, pg 89), soil physics textbooks (Hillel, 1980a, pg 207), geothermal applications (O'Sullivan, 1981), and nuclear waste applications (Doughty and Pruess, 1988, 1990). In the Boltzmann transformation, the spatial and temporal independent variables are combined into a single independent variable as follows

$$\eta \equiv \frac{x}{\sqrt{t}}$$

The partial differential equation (PDE) then becomes a ordinary differential equation (ODE) which is simpler to solve because it has only one independent variable. It should be noted that simplifying assumptions are frequently necessary for the Boltzmann transformation to be useful.

There have been many analytical solutions published for purely hydrologic problems without the effects of heat (Philip, 1960; Hillel, 1980b). However, the present discussion primarily considers analytical techniques for thermohydrologic problems of which there has been fewer publications.

Doughty and Pruess (1988, 1990) have reported a semi-analytical method for two-phase fluid and heat flow near a cylindrical nuclear waste package. The semi-analytical method is based on three zones around the waste package: inner conduction zone, heat pipe zone, and outer conduction zone. In the inner and outer conduction zones, heat transfer is primarily by conduction with no heat transfer by advection. The heat pipe zone is an isothermal region (100 C for P=1 atm) where vapor flows away from and liquid towards the heat-generating waste package. By assumption, the heat pipe is assumed to be purged of air, hence it is a two-phase single-component region (e.g., only liquid water and water vapor). Because the heat-pipe zone is nearly isothermal and has fluid flow, the heat transfer is by advection only, with no heat transfer by conduction. Analytical solutions can be derived under these simplifying assumptions. In the solution process, the analytical expressions were numerically integrated to obtain quantitative predictions.

C.2 NUMERICAL SOLUTION TECHNIQUES

There has been a great amount of discussion on numerical solution techniques for coupled thermohydrologic equations. The main difficulty stems from the choice of primary variables and the choice of time integration schemes.

The choice of primary variables has been discussed earlier in this report where it is noted that each conservation equation has a transient term equal to the net flux due to diffusion and advection. The choice of primary variables should facilitate (instead of hinder) the computation of the net flux.

Forsyth (1990) and Forsyth and Simpson (1989, 1991) devote considerable attention to describing a primary variable substitution algorithm which is used to change the primary variables from gas pressure, liquid saturation, and temperature $\{P_g, S_l, T\}$; to gas pressure, temperature, and gas phase air mole fraction $\{P_g, T, Y_a\}$; then to gas pressure, temperature, and liquid phase air mole fraction $\{P_g, T, X_a\}$, as a local control volume in the domain changes from a two-phase system, to a dry single-phase system (e.g., no liquid phase), to a saturated single-phase system (e.g., no gas phase), respectively. Much of the difficulty stems from the

elimination of a conservation equation, such as the conservation of air for liquid saturated conditions. Similarly, the conservation of liquid water equation does not apply as the medium dries. However, Forsyth continues to solve for each equation and never eliminates an equation from the set. One interpretation of Forsyth's work is that the change in primary variables is a method for handling the change in the number of applicable conservation equations.

Pollock (1982, 1986) describes a complete Newton-Raphson expansion of the governing conservation equations and constitutive equations in terms of only three unknowns: gas pressure, temperature, and liquid saturation $\{ P_g, T, S_l \}$. Pollock (1982) notes that the conservation equations are conveniently expressed in terms of eight unknowns: densities of air, liquid water, and gaseous water; liquid saturation; temperature; gas pressure; mass fractions of water in the gaseous phase; and "capillary pressure": $\{ \rho_{a,slg}, \rho_{w,l,slg}, \rho_{w,g,slg}, S_l, T, P_g, m_{w,g}, P_c \}$. By introducing the constitutive equations, the conservation equations can be expressed in only three unknowns. Pollock (1982) utilizes Kelvin's equation for vapor pressure lowering. Although its applicability is questionable at capillary pressures greater than one atmosphere, Kelvin's equation yields the correct trend of reducing the amount of water vapor as the porous medium dries. Numerically, Kelvin's equation acts to gradually eliminate the gaseous water as the liquid saturation goes to zero, if for example, the medium dries.

The numerical algorithm employed to temporally integrate the conservation equation is also important. The governing equations are coupled PDEs with spatial and temporal dimensions being the independent variables. By discretizing the spatial dimensions (using either finite element, control volume, or finite difference techniques) the PDEs are transformed into first-order ODEs with time as the independent variable.

The ODEs can be solved using a number of time integration techniques such as forward difference (explicit), backward difference (implicit), Crank-Nicholson (weighted explicit-implicit), Runge-Kutta, Adams-Bashforth, Adams-Molton, etc. The main difficulty is that many of the time integration schemes perform poorly because the equations are nonlinear and stiff. The term "stiff" is used to indicate that there is a combination of fast and slow transient components which make up the true solution (e.g., there exists a large difference between magnitude of the largest and smallest eigenvalues). Since the problem is stiff, many of the time integration schemes have numerical difficulty or simply fail. Special numerical techniques need to be used.

A widely available solver of coupled, stiff ODEs is LSODES in the ODEPACK package (Hindmarsh, 1983) which supersedes the older GEARS code (Hindmarsh, 1974). Clemo et al. (1990) use the older GEARS code, Updegraff et al. (1991) uses LSODES while Bixler (1985), Pruess (1987), and Forsyth (1990), among others, develop their own solvers.

C.3 COMPUTER PROGRAMS

Much effort has been devoted to the development and enhancement of computer programs to model the coupled thermohydrologic problems associated with the proposed HLW repository. Especially since 1985, there has been a dramatic increase in the level of effort.

Pollock (1982, 1986) gives one of the clearest descriptions of the balance equations, constitutive equations, thermodynamic relationships, and a numerical solution strategy for the present problem. The nomenclature and modelling approach adopted in this work is closely aligned with Pollock's work. Pollock wrote a computer program to solve the coupled fluid flow and energy transport problems applied to a HLW repository in partially saturated conditions, however, a name for the code was not referenced. The balance equations are for masses of air and water, and energy. The water equation is for both liquid and gas phase, assuming the gas phase is in thermodynamic equilibrium with the partial pressure governed by Kelvin's equations. Water vapor and air are assumed to behave as ideal gases, and the specific enthalpies of the solid, liquid water, gaseous water, and air are noted to all be related to a common datum point (reference temperature). Darcy's, Fourier's, and Fick's laws are assumed for mass advection, heat diffusion and mass diffusion. The primary variables are selected to be temperature, liquid saturation and gas pressure $\{T, S_l, P_g\}$. The differential equations are approximated in both space and time using finite differences. The resulting nonlinear algebraic equations are solved using an iterative Newton-Raphson technique.

Pruess (1987) developed TOUGH, a widely cited and used computer program for this class of problems. TOUGH is a member of the MULKOM family of multi-phase, multi-component codes that were initially developed at Lawrence Berkeley Laboratory (LBL) for geothermal reservoir applications. TOUGH was developed for application to the proposed geologic HLW repository located in partially saturated fractured rock. TOUGH is described to solve three-dimensional, two-phase (liquid and gas), two-component (water and air) fluid and heat transfer in porous and fractured media. The equations in TOUGH include gaseous diffusion, Darcy flow, capillary pressure, vaporization and condensation. TOUGH is specifically designed for strongly heat-driven partially saturated flow, so that the heat of vaporization/ condensation, conduction, and convection are included in the energy equation. The conservation equations include air, water (including liquid and gas phase), and energy. The water in the gas phase is assumed to be in local thermodynamic equilibrium so that the partial pressure of water in the gas equals the reduced vapor pressure as per Kelvin's equation. TOUGH has been used at CNWRA to simulate portions of the thermohydrological experiments. Currently, several numerical difficulties are limiting the range of problems which can be simulated. A new version called VTOUGH (Nitao, 1989) was developed at Lawrence Livermore National Laboratory for the U.S. Department of Energy with better numerical convergence/stability properties, and will hopefully remedy the numerical problems.

Sagar and Runchal (1990) developed PORFLO-3 to model fluid flow, heat transfer, and mass transport in variably saturated geologic media. PORFLO-3 was developed in support of environmental remediation activities being conducted at the Hanford Site, for the U.S. DOE.

A main feature is its ability to model three-dimensional geometries in both Cartesian and cylindrical coordinate systems. The primary variables are hydraulic head (or pressure), temperature and chemical species concentration. The gas phase is assumed stagnant and molecular diffusion is neglected. Runchal and Sagar (1992) have recently updated PORFLO-3.

Zyvoloski et al. (1991) developed FEHMN to model heat and mass transfer using the finite element method. FEHMN was developed at Los Alamos National Laboratory and was designed for the partially saturated zone around the proposed Yucca Mountain Repository. The code can solve non-isothermal, multiphase, multicomponent flows in a porous medium in cartesian two- and three-dimensional space, and in cylindrical coordinate systems.

Bixler (1985) developed NORIA, and Hadley (1985) developed PETROS which are similar finite element codes for solving two-phase, two-component heat and mass transfer in porous media. Both codes were developed at Sandia National Laboratories in support of the Nevada Nuclear Waste Storage Investigations (NNWSI). The major distinction is that NORIA is only applicable for two-dimensional geometries, and PETROS is a one-dimensional code. Updegraff (1989) reports that NORIA was not able to simulate many of the test problems, including the radial boiling front, the heat pipe, two-dimensional infiltration, convection cell, and the two-phase flow problems. Updegraff (1989) also reports that NORIA requires significantly greater CPU times than TOUGH for a number of test problems.

Clemo et al. (1990) developed FRAC-UNIX at EG&G Idaho for the U.S. Department of Energy. FRAC-UNIX is a two-dimensional, saturated fluid and heat transport code for fractured porous media. FRAC-UNIX was originally designed to analyze fractured geothermal reservoirs, however it has been updated using NRC guidelines (Silling, 1983) to be used in support of license applications for high-level waste disposal. FRAC-UNIX uses a dual-permeability model for the matrix and fracture hydrology, and uses a random-walk (marker particle transport) model for heat transfer. It is claimed that the random-walk model drastically reduces computer CPU time, however the authors do not discuss the requirements in terms of the number of marker particles. This issue can be related to the slow rate of convergence associated with Monte-Carlo (or stochastic) algorithms (standard deviation proportional to the square-root of the number of samples).

Updegraff et al. (1991) developed, at Sandia National Laboratories for the NRC, DCM3D, a dual-continuum, three-dimensional code for partially saturated fractured porous media. The dual-continuum formulation is based on a fracture continuum and a matrix continuum which overlap the entire domain of interest and co-exist at each point in space. The dual-continuum model is one formulation which can be used to account for both fractures and matrix in a continuum manner. DCM3D currently does not have heat transfer capabilities. As such, the media are assumed isothermal which eliminates the need to model gas phase binary diffusion of water and air. Similarly, the gas phase pressure is assumed uniform so that there is no gas phase advection of water. These restrictions limit DCM3D's ability to model coupled thermohydrologic phenomena.

Yeh and Luxmoore (1983a,b) developed MATTUM, a code to model multidimensional moisture and thermal transport in partially saturated porous media. MATTUM was developed at ORNL for the EPA for modelling hazardous waste contamination of groundwater. MATTUM makes the common assumption that the gas phase is at a constant pressure of one atmosphere and is stagnant. This *a priori* assumption eliminates the code's ability to model pressure driven vapor (gas) flow. It is interesting that the basic equations are fundamentally the same as other codes explicitly developed for HLW applications, however, MATTUM does not appear to have been updated or applied to HLW applications. It is possible that MATTUM is a predecessor for a later code, however, this was not searched in the literature.

Thunvik and Braester (1988) developed GWHRT, a code to model coupled groundwater and heat flow specifically around a hard rock repository for disposal of nuclear fuel waste. GWHRT was developed by the Swedish Nuclear Fuel and Waste Management Company (SKB) so that it is tailored for the Swedish HLW program. GWHRT offers either a dual-continuum or a single-continuum approach. The code is based on the finite element method in one-, two-, or three-dimensions. Because the proposed Swedish HLW repository is in the saturated zone, only saturated liquid flow is modeled. As such, GWHRT does not model gas flow which can be important in water transport in a repository located in partially saturated media. Similarly, GWHRT does not model the latent heat of vaporization which can be important in the energy equation.

Bian et al. (1987, 1988a,b) developed GEOTHER (or GEO2), to model two-phase groundwater fluid flow and heat transport for high-level radioactive waste applications. GEOTHER evolved from a code developed by the U.S. Geological Survey. GEOTHER simulates multi-component (water, non-condensable gases, rock/solid), porous and non-porous media (rock, waste container), two-phase (liquid, vapor) fluid and heat transfer using the finite volume method. The current status and availability of the code has not been researched.

C.4 SUMMARY

In this section, the application of analytical and numerical techniques for simulating nonisothermal partially saturated flow of heat and fluid in a porous fractured media was reviewed. Analytical techniques typically require simple geometrical and thermohydrological models, and are usually based on a Boltzmann transformation. Numerical techniques are required for more complicated problems where considerable effort is devoted to the choice of primary variables, choice of a time integration scheme, nonlinear system solvers, and algorithms to handle extreme cases where the number of applicable conservation equations changes (dry out, complete liquid saturation). The available computer programs were summarized and their limitations and unique features were noted.

APPENDIX D: SIMILITUDE

In this appendix, the governing equations are re-expressed using dimensionless groups. Similitude and the resulting dimensionless groups are proposed to enhance the range of applicability of laboratory experiments so that mathematical models can be used to predict the flow of heat and mass in (i) other laboratory experiments which have different shapes, sizes, and conditions; (ii) field experiments; and (iii) the proposed HLW repository. Through scaling analysis, it is anticipated that the laboratory experimental data can be effectively used (Baker et al., 1973; Bejan, 1984; Miller, 1980).

D.1 MOTIVATION FOR SIMILITUDE ANALYSIS

Any physical laboratory model that is used to investigate the thermohydrological phenomena that might occur in the Yucca Mountain repository must adequately represent those phenomena and the relationships among them. Since the model can duplicate neither the large physical extent of the repository nor the long time periods of interest, many of the other physical parameters of the model must be changed relative to those of the repository to represent the desired phenomena and the relationships among them. That is, the model must be designed, constructed, and operated in accordance with the principles of *similitude*, through the use of *dimensionless parameters*. (Dimensionless parameters are formed by various combinations of the dimensional, physical parameters.) The motivation of the similitude study described here is the formulation and analysis of the relevant dimensionless thermohydrological parameters for the Yucca Mountain repository.

As an introduction to the methods described here, it is well established theoretically and experimentally (Baker et al., 1973; Bejan, 1984; and many others), that when (i) all the relevant parameters of a physical system are identified, (ii) an independent set of dimensionless parameters is formed from the physical parameters, and (iii) the dimensionless parameters of the laboratory model are maintained identically to those of the prototype (i.e. repository), then the dimensionless phenomena, called "responses," measured in the model are the same as the dimensionless responses of the prototype. The relevant dimensionless parameters can be determined by any of several equivalent methods, such as nondimensionalizing the governing differential equations (when they are known), or by use of the Buckingham Pi Theorem. After the model responses are measured in the laboratory, the prototype responses can be predicted by transforming the dimensionless responses measured in the model back to the physical responses of the prototype by using the relevant physical parameters of the prototype.

Unfortunately, for large, complicated systems such as thermohydrologic phenomena that occurs in the Yucca Mountain repository, it is unlikely that all the prototypical dimensionless parameters can be maintained identically in the scale model. Consequently, a crucial part of designing a model or models of the repository is to identify those phenomena and parameters which are the most important and to limit the model to an adequate representation of them. This identification process depends on a combination of preliminary experiments, mathematical

modeling, physical insight, and analysis of the influence of the various dimensionless parameters in simpler but similar circumstances.

The following sections of the report discuss in detail the similitude study conducted for the Thermohydrology Research Project.

D.2 TYPES OF SIMILARITY

The nature of the relationships of models that are similar to prototypes define the nature of the similarity between the model and prototype. These relationships determine if the similarity is of a geometric, kinematic, dynamic, or constitutive nature, or some other type of similarity. If all relationships between the prototype and model are similar, the systems are described to have complete similarity (Baker et al., 1973). Each type of similarity is briefly described here.

Geometric similarity is the condition in which the model and prototype have the same shape and constant proportions between all linear dimensions.

Kinematic similarity is the condition in which the flow net of the model, comprised of the streamlines and equipotentials, is geometrically similar to the flow net of the prototype. This condition specifies that velocities at corresponding points in the two systems are in the same direction and are related in magnitude by a constant scale factor.

Dynamic similarity is the condition in which forces and accelerations at homologous points and homologous times acting on homologous elements of fluid mass must be in the same ratio throughout all parts of both systems (Bear, 1972). The term homologous as used here means at corresponding, but not necessarily equal values of a variable (Baker et al., 1973). Of the conditions that must be met, dynamic similarity is the most restrictive since the conditions for both geometric and kinematic similarity must be attained in order to be dynamically similar (Fox and McDonald, 1978).

Constitutive similarity is the condition in which the constitutive properties of materials of both systems have the same functional dependencies and relationships (Baker et al., 1973). An example of constitutive similarity is either the relationship between capillary pressure and saturation, or the relationship between hydraulic conductivity and saturation. The model and the prototype can have constitutive similarity if a scale factor relating the capillary pressure/ saturation relationship of the prototype to the model can be identified. The establishment of similarity of the capillary pressure/saturation relationship between the prototype and the model is an important, yet difficult technical issue.

D.3 METHODS TO PERFORM SCALING ANALYSIS

Scaling according to the concepts of similarity as described above can be accomplished using either dimensional analysis or similitude. The dimensionless parameters needed to equate

the model to the prototype can be deduced by either analysis methodology, and each are briefly described here.

Dimensional analysis is the procedure by which the variables are grouped together to form dimensionless terms by dimensional considerations alone. An implicit knowledge of all pertinent variables and constant parameters is required in dimensional analysis (Buckingham, 1914; Fox and McDonald, 1978; Corey, 1986).

Similitude analysis is the procedure by which dimensionless parameters are developed by starting with the representative mathematical equations, then transforming these equations into dimensionless form through the use of a simple set of transformations or a change of variables. All aspects of the actual physical system and all the macroscopic phenomena need to be expressed in terms of mathematical equations for similitude analysis to be used. Typically, each of the governing equations is divided by some value of the same dimensions as those terms appearing in the governing equations (Bear, 1972; Baker et al., 1973; Fox and McDonald, 1978; Miller, 1980; Corey, 1986).

In this work, the similitude analysis method is adopted where the constitutive equations, the differential equations, and boundary conditions are transformed into dimensionless forms.

D.4 ADVECTIVE FLUXES: DARCY'S LAW

Similitude analysis begins with the constitutive equation for advective fluxes. In the similitude analysis the natural scaling for pressure and advective mass fluxes will become apparent. In dimensional analysis, a large number of equally valid groupings are possible. Hence, through similitude the details of the dimensionless groupings more naturally fall out of the analysis.

D.4.1 Gas Phase Darcy's Law

One of the fundamental equations for fluid flow in porous media is Darcy's Law for the area-average gas phase velocity (which is recalled for convenience):

$$\mathbf{v}_g = - \frac{k_{sat}\, k_{rel,g}}{\mu_g} \left(\nabla P_g - \rho_g \mathbf{g} \right) \qquad \text{(D-1)}$$

It is assumed that the gas phase is well-connected vertically so that the possibility for thermally driven natural convection exists. The driving mechanism for natural convection is thermal buoyancy which requires the combination of gravity and temperature-dependent fluid density. The Boussinesq approximation, which assumes that the gas density is only a function of temperature, is introduced (Bejan, 1984; Lienhard, 1987).

$$\rho_g = \rho_{g,o} \left(1 - \beta_g \Delta T \right) \tag{D-2}$$

where

$$\beta_g \equiv - \frac{1}{\rho_{g,o}} \left. \frac{\partial \rho_g}{\partial T} \right|_o \tag{D-3}$$

and where

ΔT	=	temperature difference from the reference temperature ($\Delta T = T - T_{ref}$) [C],
β_g	=	thermal expansion coefficient (for ideal gas, $\beta_g = 1/T$) [1/K],
T_{ref}	=	reference temperature [C], and
$\rho_{g,o}$	=	reference gas density [kg/m^3].

The gas pressure is idealized to be composed of hydrostatic and nonhydrostatic [also known as reduced pressure (Phillips, 1991, pg 26)] components

$$P_g = \tilde{P}_g - \rho_{g,o} \, g \, (z - z_o) \tag{D-4}$$

where

P_g	=	total gas pressure [N/m^2],
$\tilde{P}_g$	=	nonhydrostatic component of the gas pressure [N/m^2],
$\rho_{g,o} \, g \, (z-z_o)$	=	hydrostatic component of the pressure [N/m^2],
g	=	magnitude of gravity ($g = 9.81 m/s^2$) [m/s^2],
z	=	the elevation (or height) [m], and
z_o	=	a reference elevation (or height) [m].

The z-axis is taken vertically upward so that gravity is in the negative z-direction:

$$\mathbf{g} = - g \, \hat{\mathbf{k}} \tag{D-5}$$

where

$\hat{\mathbf{k}}$	=	unit vector in direction of increasing elevation (opposite gravity) [dimensionless].

The hat symbol over k indicates a unit size vector in the direction of increasing elevation. Later in this section, an over-hat will be used to indicate a dimensionless quantity (which is consistent here because it represents a dimensionless vector).

Therefore, the gravitational portion of Darcy's law for the gas phase can be approximated as:

$$\rho_g \, \mathbf{g} = -\rho_{g,o} \, g \, \hat{k} + \rho_{g,o} \, g \, \beta_g \, \Delta T \, \hat{k} \qquad \text{(D-6)}$$

so that the driving potential in the gas phase Darcy's Law becomes

$$\nabla P_g - \rho_g \, \mathbf{g} = \nabla \tilde{P}_g - \rho_{g,o} \, g \, \beta_g \, \Delta T \, \hat{k} \qquad \text{(D-7)}$$

At this point, the terms can be grouped to form dimensionless parameters which are common in the literature. Because natural convection is expected in the gas phase, a form of the gas phase Grashof number, Gr, or equivalently the Rayleigh number, Ra, where the Rayleigh is equal to the Grashof times Prandtl, Ra = Gr · Pr, is sought.

There are a number of different options for scaling the temperature. A single temperature, a temperature difference, or a heat flux with heat transfer coefficient are all valid choices. For this work the temperature is scaled by the maximum temperature difference. Dimensionless temperature is defined:

$$\theta \equiv \frac{T - T_{ref}}{T_{max} - T_{ref}} = \frac{\Delta T}{\Delta T_{max}} \qquad \text{(D-8)}$$

where

T_{ref}	=	reference temperature [C],
T_{max}	=	maximum temperature [C],
ΔT	=	temperature difference ($\Delta T = T - T_{ref}$) [C], and
ΔT_{max}	=	maximum temperature difference ($\Delta T_{max} = T_{max} - T_{ref}$) [C].

Logically, T_{ref} is a reference temperature which represents the "ambient temperature," which is expected to be the lowest temperature assuming a heat source is added to the system. The maximum temperature may not be known *a priori*; however, that does not preclude its use here. If T_{max} is unknown, then it must be calculated, perhaps iteratively.

The Grashof number for porous media (Bejan, 1984; Nield and Bejan, 1992) is defined as:

$$Gr \equiv \frac{g \, \beta_g \, \Delta T_{max} \, (k_{sat}/\phi) \, L}{(\nu_g)^2} \qquad \text{(D-9)}$$

where

k_{sat}	=	saturated permeability [m^2],
L	=	macroscopic length scale, should be in the direction of gravity [m], and
ν_g	=	kinematic viscosity of the gas ($\nu = \mu/\rho$) [m^2/s].

The porous medium Grashof number is equal to the traditional Grashof number times the Darcy number (Nield and Bejan, 1992).

$$Gr_{porous} = Gr_{traditional}\ Da \tag{D-10}$$

where

Gr_{porous}	=	porous media Grashof number [dimensionless],
$Gr_{traditional}$	=	traditional Grashof number [dimensionless], and
Da	=	Darcy number [dimensionless].

The Darcy number is the ratio of saturated permeability to the macroscopic length scale squared.

$$Da = \frac{k_{sat}}{L^2} \tag{D-11}$$

For convenience, the porous medium Grashof number is denoted by Gr without a subscript and the traditional Grashof number is not used in this development.

The Grashof number is discussed in the heat transfer literature as the ratio of buoyancy to viscous forces. The buoyancy forces tend to move the fluid by natural convection and, hence, increase the heat transfer. The viscous forces tend to resist fluid motion and, hence, decrease natural convection heat transfer. As the Grashof number increases, the heat transfer by natural convection increases.

The porous medium Grashof number is for a medium "saturated" with gas. The effect of a partially saturated porous medium will be seen shortly through the relative permeability.

By establishing the Grashof number in Darcy's law, the nonhydrostatic pressure is naturally scaled by:

$$\hat{P}_g \equiv \frac{\tilde{P}_g}{\left(\frac{(\mu_g)^2}{\rho_{g,o}\ k_{sat}/\phi}\right)} \tag{D-12}$$

In addition, the macroscopic length is scaled as

$$\hat{x} \equiv \frac{x}{L} \tag{D-13}$$

so that the divergence and gradient operators are scaled as:

$$\hat{\nabla} \equiv L \nabla = L \left(\frac{\partial}{\partial x} \hat{i} + \frac{\partial}{\partial y} \hat{j} + \frac{\partial}{\partial z} \hat{k} \right) \tag{D-14}$$

$$\hat{\nabla} \cdot \equiv L \nabla \cdot \tag{D-15}$$

Substitution of these expressions into the gas phase Darcy's Law gives:

$$v_g = - \frac{\mu_g}{\rho_{g,o} L} \phi k_{rel,g} \left(\hat{\nabla} \hat{P}_g - Gr \theta \hat{k} \right) \tag{D-16}$$

This suggests a scaling for the gas phase velocity:

$$v_g \sim \frac{\mu_g \phi}{\rho_{g,o} L} \tag{D-17}$$

so that the dimensionless gas phase velocity is:

$$\hat{v}_g \equiv \frac{v_g}{\left(\frac{\mu_g \phi}{\rho_{g,o} L} \right)} \tag{D-18}$$

The final form of the dimensionless Darcy's law for the gas phase is:

$$\hat{v}_g = - k_{rel,g} \left(\hat{\nabla} \hat{P}_g - Gr \theta \hat{k} \right) \tag{D-19}$$

Different Scaling Choices. The process of nondimensionalizing the gas phase Darcy's Law started with a desire to generate a Grashof number, which is a traditional number characterizing the strength of natural convection. By generating the Grashof number, the scaling for the nonhydrostatic component of pressure was naturally produced in the analysis. Similarly, a choice for the scaling for the gas velocity became apparent in the analysis. These are not, however, the only valid choices for the scalings. For example, an equally valid scaling for the gas velocity is:

$$v_g \sim \frac{k_{sat} \rho_{g,o} g}{\mu_g} \tag{D-20}$$

The rationale for this gas velocity scaling is suggested by a similar liquid velocity scaling:

$$v_l \sim \frac{k_{sat}\ \rho_l\ g}{\mu_l} \tag{D-21}$$

which can be derived by considering the "free-falling" liquid phase velocity through saturated porous media where there is negligible liquid pressure gradient.

Similarly, a different scaling for the nonhydrostatic gas pressure is suggested by the stagnation pressure of the gas.

$$\tilde{P}_g \sim \rho_{g,o} (v_g)^2 \sim \rho_{g,o} \left(\frac{k_{sat}\ \rho_{g,o}\ g}{\mu_g} \right)^2 \tag{D-22}$$

Although these scalings for the gas velocity and pressure are valid, they are not adopted in this work. They are mentioned to emphasize that other scalings exist, and may be used for similar analyses.

D.4.2 Liquid Phase Darcy's Law

The liquid phase Darcy's law is cast in dimensionless format following a similar outline as used for the gas phase. Darcy's Law for the liquid phase is recalled here for the convenience of the reader.

$$v_l = - \frac{k_{sat}\ k_{rel,l}}{\mu_l} \left(\nabla P_l - \rho_l g \right) \tag{D-23}$$

At this point, two distinct options are available to be pursued in the nondimensionalization strategy. The first option is to assume the pressure in the liquid consists of both a hydrostatic and a nonhydrostatic pressure component (this follows the outline used for the gas phase Darcy's law):

$$P_l = \tilde{P}_l - \rho_{l,o}\ g(z - z_o) \tag{D-24}$$

and the liquid density is only a function of temperature.

$$\rho_l = \rho_{l,o} \left(1 - \beta_l\ \Delta T \right) \tag{D-25}$$

where

$$\beta_l \equiv - \frac{1}{\rho_{l,o}} \left. \frac{\partial \rho_l}{\partial T} \right|_o \qquad \text{(D-26)}$$

and where

β_l	=	thermal expansion coefficient for the liquid [1/K], and
ΔT	=	temperature difference from a reference value [C].

As can be imagined, this choice of pressure definition indicates the possibility of natural convection in the liquid phase and leads to the introduction of a liquid phase Grashof number.

The second option is to view the liquid pressure as being dictated by the average local gas pressure and the local capillary pressure, according to:

$$P_l = P_g - P_c \qquad \text{(D-27)}$$

It follows that the gradient of the liquid pressure is

$$\nabla P_l = \nabla P_g - \nabla P_c \qquad \text{(D-28)}$$

the gradient of the gas pressure is assumed to be primarily due to hydrostatics. The nonhydrostatic component of the gas pressure is neglected, therefore:

$$\nabla P_g = - \rho_{g,o} \, g \, \hat{k} \qquad \text{(D-29)}$$

As discussed earlier in this work, the capillary pressure is assumed to be a function of surface tension, permeability, porosity, and liquid saturation (through the J-Leverett function):

$$P_c = \frac{\sigma}{\sqrt{k_{sat}/\phi}} J(S_l) \qquad \text{(D-30)}$$

The surface tension is assumed to be temperature dependent as:

$$\sigma = \sigma_o + \left. \frac{d\sigma}{dT} \right|_o \Delta T \qquad \text{(D-31)}$$

With some algebra, the dimensionless liquid phase Darcy's law can be shown to be

$$\hat{v}_l = - \left(\frac{1}{Ca}\right) k_{rel,l} \left(- J\, Su \hat{\nabla}\theta - \frac{dJ}{dS_l} \hat{\nabla} S_l + Bo\, \hat{k} \right) \tag{D-32}$$

where the dimensionless liquid phase velocity is

$$\hat{v}_l \equiv \frac{v_l}{\left(\frac{\mu_l\, \phi}{\rho_l\, L}\right)} \tag{D-33}$$

the Capillary number is

$$Ca \equiv \frac{(\mu_l)^2}{\rho_l\, \sigma \sqrt{k_{sat}/\phi}} \tag{D-34}$$

the Surface tension number is

$$Su \equiv \frac{\Delta T_{max}}{\sigma_o} \left.\frac{d\sigma}{dT}\right|_o \tag{D-35}$$

and the Bond number is

$$Bo \equiv \frac{(\rho_l - \rho_{g,o})\, g\, L \sqrt{k_{sat}/\phi}}{\sigma_o} \tag{D-36}$$

The capillary number, Ca, is described in the literature as the ratio of viscous forces to capillary (or surface tension) forces (Land, 1972). Most frequently, the capillary number is defined using a liquid velocity:

$$Ca \equiv \frac{\mu_l\, v_l}{\sigma} \tag{D-37}$$

Frequently, the liquid velocity is a known input from a boundary condition (Basel and Udell, 1989); however, in this work the liquid velocity is typically not specified. The scaling for liquid velocity adopted in this work can be substituted to yield:

$$Ca = \frac{\mu_l \left(\frac{\mu_l \phi}{\rho_l L} \right)}{\sigma} \qquad \text{(D-38)}$$

If the additional change in length scale is substituted

$$L \sim \sqrt{k_{sat} \phi} \qquad \text{(D-39)}$$

then the traditional capillary number in the literature is shown to be the same as the definition adopted just above, that is:

$$Ca = \frac{(\mu_l)^2}{\rho_l \sigma \sqrt{k_{sat}/\phi}} \qquad \text{(D-40)}$$

The Surface tension number, Su, is introduced in this work, however it is not based on a definition described in the literature. It is simply a convenient grouping of terms which are a measure of the importance of temperature on the surface tension.

The Bond number, Bo, is described in the literature as the ratio of gravitational forces to capillary forces (Land, 1972). The definition used in this work is consistent with the literature (Basel and Udell, 1989).

Both options for modelling P_l appear equally valid (i.e., either hydrostatic plus nonhydrostatic components, or gas minus capillary pressures). Both options were considered in this work. In final review, the second option ($P_l = P_g - P_c$) is adopted. The choice between either option is not trivial.

The first choice is considered more appropriate if the liquid saturation is high because the liquid phase is well-connected in the direction of gravity, and this would allow a transmission of liquid-phase hydrostatic head. Hydrostatic head (or gravity) coupled with a temperature-dependent density is necessary for natural convection.

The second choice is more appropriate if the gas saturation is high because the gas phase would be well-connected, and the liquid phase would not be well-connected. Similarly, the gas phase would transmit, and the liquid phase would not transmit a hydrostatic head. In summary, the first option is considered valid for saturated porous media and the second option is valid for partially saturated porous media. In this work, the primary interest is in partially saturated conditions; hence, the second option is used.

D.4.3 Advective Mass Fluxes

Building on the dimensionless results of Darcy's Law, the advective mass fluxes can be cast in dimensionless form. The advective mass flux of air is

$$\hat{q}_{m,a} = m_{a,g}\ \hat{\rho}_g\ \hat{v}_g \tag{D-41}$$

where the dimensionless advective mass flux of air is

$$\hat{q}_{m,a} \equiv \frac{q_{m,a}}{\left(\frac{\mu_g\ \phi}{L}\right)} \tag{D-42}$$

and the dimensionless gas density is

$$\hat{\rho}_g \equiv \frac{\rho_g}{\rho_{g,o}} \tag{D-43}$$

The mass fraction of air in the gas phase is recalled for the convenience of the reader.

$$m_{w,g} \equiv \frac{\rho_{w,g}}{\rho_g} \tag{D-44}$$

Similar definitions can be introduced to nondimensionalize the advective mass flux of water in the liquid phase.

$$\hat{q}_{m,w,l} = \hat{v}_l \tag{D-45}$$

where

$$\hat{q}_{m,w,l} \equiv \frac{q_{m,w,l}}{\left(\frac{\mu_l\ \phi}{L}\right)} \tag{D-46}$$

The dimensionless advective mass flux of water in the gas phase is

$$\hat{q}_{m,w,g} = m_{w,g}\ \hat{\rho}_g\ \hat{v}_g \tag{D-47}$$

where the dimensionless advective mass flux of water in the gas phase is

$$\hat{q}_{m,w,g} \equiv \frac{q_{m,w,g}}{\left(\frac{\mu_g \phi}{L}\right)} \tag{D-48}$$

D.4.4 Advective Energy Fluxes

The advective fluxes of energy can also be cast in dimensionless form.

$$\hat{q}_e = \hat{q}_{e,w,l} + \hat{q}_{e,w,g} + \hat{q}_{e,a,g} \tag{D-49}$$

The dimensionless energy advected by the water in the liquid phase is

$$\hat{q}_{e,l} = \theta \, \hat{q}_{m,w,l} \tag{D-50}$$

where

$$\hat{q}_{e,l} \equiv \frac{q_{e,l}}{\left(\frac{\mu_l \phi c_l \Delta T_{max}}{L}\right)} \tag{D-51}$$

It is noted that liquid water is approximately incompressible. Therefore, the specific heat at constant pressure, $c_{p,w,l}$, and specific heat at constant volume, $c_{v,w,l}$, are approximately equal. In this work they are considered equal, and the specific heat of the liquid, c_l, is denoted (assuming that the liquid is water)

$$c_l = c_{p,w,l} = c_{v,w,l} \tag{D-52}$$

The dimensionless energy advected by water in the gas phase is

$$\hat{q}_{e,w,g} = \left(\left(\frac{c_{p,w,g}}{c_l}\right)\theta + H\right)\left(\frac{\mu_g}{\mu_l}\right)\hat{q}_{m,w,g} \tag{D-53}$$

where

$$\hat{q}_{e,w,g} \equiv \frac{q_{e,w,g}}{\left(\frac{\mu_l \phi c_l \Delta T_{max}}{L}\right)} \tag{D-54}$$

The enthalpy number, H, is introduced as:

$$H \equiv \frac{h_{lg}}{c_l \, \Delta T_{max}} \tag{D-55}$$

The enthalpy number is the same as the Jacob number defined by Land (1972). For comparison purposes, Land (1972) distinguished between the Jacob and Jakob numbers which are similar yet different numbers. Basel and Udell (1989) and Lienhard (1987) describe the Jakob number equal to the reciprocal of the enthalpy number we have introduced here. Because of different definitions in the literature, and because an internal energy number is introduced, the name "enthalpy number" is adopted here instead of the Jacob or Jakob number.

The dimensionless energy advected by the air is

$$\hat{q}_{e,a,g} = \left(\frac{c_{p,a,g}}{c_l}\right) \theta \left(\frac{\mu_g}{\mu_l}\right) \hat{q}_{m,a,g} \tag{D-56}$$

where

$$\hat{q}_{e,a,g} \equiv \frac{q_{e,a,g}}{\left(\frac{\mu_l \, \phi \, c_l \, \Delta T_{max}}{L}\right)} \tag{D-57}$$

This completes the nondimensionalization of the advective fluxes.

D.5 DIFFUSIVE FLUXES: FICK'S LAW AND FOURIER'S LAW

D.5.1 Diffusive Mass Fluxes

Fick's law for the mass diffusion of water in the gas phase can be cast in dimensionless form:

$$\hat{j}_{m,w,g} = - S_g \, \hat{\rho}_g \, \hat{\nabla} m_{w,g} \tag{D-58}$$

where

$$\hat{j}_{m,w,g} \equiv \frac{j_{m,w,g}}{\left(\frac{\tau \, \phi \, \rho_{g,o} \, D_{wa,g}}{L}\right)} \tag{D-59}$$

Similarly, the mass diffusion of air in the gas phase becomes

$$\hat{j}_{m,a,g} = - S_g \hat{\rho}_g \hat{\nabla} m_{a,g} \tag{D-60}$$

where

$$\hat{j}_{m,a,g} \equiv \frac{j_{m,a,g}}{\left(\frac{\tau \phi \rho_{g,o} D_{wa,g}}{L}\right)} \tag{D-61}$$

It is noted that the dimensionless mass diffusion fluxes of air and water are equal in magnitude and opposite in sign due to an inherent assumption that the diffusion mass fluxes are measured relative to the bulk fluid velocity (Bird et al., 1960).

$$\hat{j}_{m,a,g} = -\hat{j}_{m,w,g} \tag{D-62}$$

D.5.2 Diffusive Energy Fluxes

The diffusive flux of thermal energy can be cast in nondimensional form as:

$$\hat{j}_e = \hat{j}_{e,cond} + \hat{j}_{e,w,g} + \hat{j}_{e,a,g} \tag{D-63}$$

The dimensionless equation for heat transfer due to conduction in the porous medium is:

$$\hat{j}_{e,cond} = -\hat{\nabla}\theta \tag{D-64}$$

where

$$\hat{j}_{e,cond} \equiv \frac{j_{e,cond}}{\left(\frac{k_t \Delta T_{max}}{L}\right)} \tag{D-65}$$

Here, we have neglected the dependence of k_t on liquid saturation. For the current analysis this is not considered a significant approximation; however, it may need to be revisited in the future. At this point, k_t is assumed to be the saturated porous medium thermal conductivity.

The dimensionless equation for heat transfer due to diffusion of water in the gas phase is:

$$\hat{j}_{e,w,g} = \left[\left(\frac{c_{p,w,g}}{c_l}\right)\theta + H\right]\left(\frac{\rho_{g,o}}{\rho_{s,slg}}\right)\left(\frac{c_l}{c_s}\right)\left(\frac{\alpha_g}{\alpha}\right) Le_g \tau \phi \hat{j}_{m,w,g} \tag{D-66}$$

$$\hat{j}_{e,w,g} \equiv \frac{j_{e,w,g}}{\left(\frac{k_t \Delta T_{max}}{L}\right)} \tag{D-67}$$

The dimensionless equation for heat transfer due to diffusion of air in the gas phase is:

$$\hat{j}_{e,a,g} = \left(\frac{c_{p,a,g}}{c_s}\right)\left(\frac{\rho_{g,o}}{\rho_{s,seg}}\right)\theta\left(\frac{\alpha_g}{\alpha}\right) Le_g\ \tau\ \phi\ \hat{j}_{m,a,g} \tag{D-68}$$

$$\hat{j}_{e,a,g} \equiv \frac{j_{e,a,g}}{\left(\frac{k_t \Delta T_{max}}{L}\right)} \tag{D-69}$$

D.6 CONSERVATION OF AIR EQUATION

Using the previous results, the equation for the conservation of air can be cast in dimensionless form:

$$\left(\frac{\alpha}{\alpha_g}\right)\frac{\partial\ \hat{\rho}_{a,slg}}{\partial\ \hat{t}} = -\ Pr_g\ \hat{\nabla}\cdot\hat{q}_{m,a,g} - \tau\ Le_g\ \hat{\nabla}\cdot\hat{j}_{m,a,g} \tag{D-70}$$

where the dimensionless mass density of air in the porous medium is defined as:

$$\hat{\rho}_{a,slg} \equiv \frac{\rho_{a,slg}}{\phi\ \rho_{g,o}} \tag{D-71}$$

and is equal to:

$$\hat{\rho}_{a,slg} = m_{a,g}\ \hat{\rho}_g\ S_g \tag{D-72}$$

The gas phase Prandtl number and Lewis number are:

$$Pr_g \equiv \frac{\nu_g}{\alpha_g} \tag{D-73}$$

$$Le_g \equiv \frac{D_{wa,g}}{\alpha_g} \tag{D-74}$$

The Prandtl number, Pr_g, is described in the literature as the ratio of momentum diffusion to thermal diffusion. The Lewis number, Le, is described in the literature as being the ratio of molecular diffusion to thermal diffusion. However, it should be noted that many researchers define the Lewis number to be the reciprocal of that defined here (i.e., Le = α/D instead of D/α). In comparison, the Prandtl number is consistently defined as (Pr = ν/α). For comparison purposes, Land (1972), Lienhard (1987), Eckert and Drake (1987), and Kays and Crawford (1980) define Le = D/α, while Incropera and DeWitt (1981), Rohsenow and Choi (1961), Todreas and Kazimi (1990) and Bejan (1984) define Le = α/D. The reader should check the definition of the Lewis number when comparing this work with that of other researchers.

D.7 CONSERVATION OF WATER EQUATION

The dimensionless conservation of water equation will first be presented for the gas and liquid phases separately, then for the combined gas and liquid phases.

D.7.1 Gas Phase Water Equation

Using the previous result, the dimensionless conservation equation for water in the gaseous phase is:

$$\left(\frac{\alpha}{\alpha_g}\right)\frac{\partial\,\hat{\rho}_{w,g,slg}}{\partial\,\hat{t}} = -\,Pr_g\,\hat{\nabla}\cdot\hat{q}_{m,w,g} - \tau\,Le_g\,\hat{\nabla}\cdot\hat{j}_{m,w,g} + \left(\frac{\rho_l}{\rho_{g,o}}\right)\left(\frac{\alpha_l}{\alpha_g}\right)\hat{Q}_{m,w,l\to g} \tag{D-75}$$

where the dimensionless mass density of water in the gas phase is defined as:

$$\hat{\rho}_{w,g,slg} \equiv \frac{\rho_{w,g,slg}}{\phi\ \rho_{g,o}} \tag{D-76}$$

and is equal to:

$$\hat{\rho}_{w,g,slg} = m_{w,g}\ \hat{\rho}_g\ S_g \tag{D-77}$$

The dimensionless time is introduced as:

$$\hat{t} \equiv \frac{t}{\left(\frac{L^2}{\alpha}\right)} \tag{D-78}$$

where the thermal diffusivity for a porous medium is expected to be dominated by the saturated medium thermal diffusivity (where it is assumed that the liquid and gas have smaller contributions to the heat capacity of the porous medium):

$$\alpha \equiv \frac{k_t}{\rho_{s,slg}\ c_s} \tag{D-79}$$

The dimensionless liquid-to-gas phase water transfer term is introduced as:

$$\hat{Q}_{m,w,l\text{-}g} \equiv \frac{Q_{m,w,l\text{-}g}}{\left(\frac{\phi\ \rho_{w,l}\ \alpha_l}{L}\right)} \tag{D-80}$$

In this work and in most other works, the liquid and gas are assumed to be in local thermodynamic equilibrium so that the partial pressure of water in the gas phase is equal to the reduced vapor pressure for the liquid phase. When this assumption is made, the liquid-to-gas transfer term is eliminated from the equations. For the sake of simplicity and generality, it has been included here but will be eliminated in the combined liquid and gas water equation.

D.7.2 Liquid Phase Water Equation

The dimensionless liquid phase water equation is

$$\left(\frac{\alpha}{\alpha_l}\right) \frac{\partial\ \hat{\rho}_{w,l,slg}}{\partial\ \hat{t}} = -\ Pr_l\ \hat{\nabla}\cdot\ \hat{q}_{m,w,l} - \hat{Q}_{m,w,l\text{-}g} \tag{D-81}$$

where the dimensionless mass density of liquid water is defined as:

$$\hat{\rho}_{w,l,slg} \equiv \frac{\rho_{w,l,slg}}{\phi\ \rho_{w,l}} \tag{D-82}$$

and is equal to:

$$\hat{\rho}_{w,l,slg} = S_l \tag{D-83}$$

The liquid phase Prandtl number is also introduced as

$$Pr_l \equiv \frac{\nu_l}{\alpha_l} \tag{D-84}$$

D.7.3 Combined Gas and Liquid Phase Water Equation

The liquid-to-gas transfer term can be eliminated as an unknown by adding the gas phase and liquid phase water equations. This yields:

$$\left(\frac{\alpha}{\alpha_l}\right)\left(\frac{\partial\,\hat{\rho}_{w,l,slg}}{\partial\,\hat{t}} + \left(\frac{\rho_{g,o}}{\rho_l}\right)\frac{\partial\,\hat{\rho}_{w,g,slg}}{\partial\,\hat{t}}\right) =$$

$$- Pr_l\,\hat{\nabla}\cdot\hat{q}_{m,w,l}$$

$$- Pr_g\left(\frac{\alpha_g}{\alpha_l}\right)\left(\frac{\rho_{g,o}}{\rho_l}\right)\hat{\nabla}\cdot\hat{q}_{m,w,g} \tag{D-85}$$

$$- \tau\,Le_g\left(\frac{\alpha_g}{\alpha_l}\right)\left(\frac{\rho_{g,o}}{\rho_l}\right)\hat{\nabla}\cdot\hat{j}_{m,w,g}$$

D.8 CONSERVATION OF ENERGY EQUATION

The dimensionless conservation of energy equation is

$$\frac{\partial\,\hat{e}_{slg}}{\partial\,\hat{t}} = -\,\phi\,Pr_l\left(\frac{\alpha_l}{\alpha}\right)\left(\frac{\rho_l}{\rho_{s,slg}}\right)\left(\frac{c_l}{c_s}\right)\hat{\nabla}\cdot\hat{q}_e - \hat{\nabla}\cdot\hat{j}_e + \hat{Q}_e \tag{D-86}$$

The dimensionless energy consists of contributions from the solid, liquid water, gaseous water, and air:

$$\hat{e}_{slg} = \hat{e}_s + \hat{e}_{w,l} + \hat{e}_{w,g} + \hat{e}_a \tag{D-87}$$

The dimensionless solid-phase energy is defined as:

$$\hat{e}_s \equiv \frac{e_s}{\rho_{s,slg}\, c_s\, \Delta T_{max}} \tag{D-88}$$

and is equal to the dimensionless temperature:

$$\hat{e}_s = \theta \tag{D-89}$$

All of the energy accumulation terms are nondimensionalized by dividing by the solid-phase energy accumulation term. It should be noted that the solid density is averaged over the porous medium (solid, liquid, and gas) as indicated by the additional "slg" in the subscript. This is considered the most appropriate density because it is the density most easily experimentally measured.

For convergence, all of the energy accumulation terms are normalized by the solid phase term. The dimensionless liquid water energy is defined as:

$$\hat{e}_{w,l} \equiv \frac{e_{w,l}}{\rho_{s,slg}\, c_s\, \Delta T_{max}} \tag{D-90}$$

and is equal to:

$$\hat{e}_{w,l} = \phi\, S_l \left(\frac{\rho_l}{\rho_{s,slg}}\right)\left(\frac{c_l}{c_s}\right)\theta \tag{D-91}$$

The dimensionless gaseous water energy is defined as:

$$\hat{e}_{w,g} \equiv \frac{e_{w,g}}{\rho_{s,slg}\, c_s\, \Delta T_{max}} \tag{D-92}$$

and is equal to:

$$\hat{e}_{w,g} = \phi\, S_g\, m_{w,g}\, \hat{\rho}_g \left(\frac{\rho_{g,o}}{\rho_{s,slg}}\right)\left(\frac{c_l}{c_s}\right)\left(\left(\frac{c_{v,w,g}}{c_l}\right)\theta + U\right) \tag{D-93}$$

The dimensionless air energy is defined as:

$$\hat{e}_a \equiv \frac{e_a}{\rho_{s,slg}\, c_s\, \Delta T_{max}} \tag{D-94}$$

and is equal to:

$$\hat{e}_a = \phi\, S_g\, m_{a,g}\, \hat{\rho}_g \left(\frac{\rho_{g,o}}{\rho_{s,slg}}\right)\left(\frac{c_{v,a,g}}{c_s}\right)\theta \qquad \text{(D-95)}$$

In these equations, the internal energy number, U, is defined as:

$$U \equiv \frac{u_{lg}}{c_l\, \Delta T_{max}} \qquad \text{(D-96)}$$

The internal energy number is a measure that is used to determine the ratio of the energy needed to change phase of water, to the energy required to elevate the temperature of water. As noted in the literature, water has a large latent heat of phase change, which is typically much larger than the energy required to raise the temperature without phase change.

And finally, the dimensionless energy generation term is

$$\hat{Q}_e \equiv \frac{Q_e}{\left(\frac{k_t\, \Delta T_{max}}{L^2}\right)} \qquad \text{(D-97)}$$

D.9 SUMMARY OF DIMENSIONLESS EQUATIONS

D.9.1 Air Equation

All of the components can be substituted into the air equation to generate a rather long final equation which has the benefit of identifying a minimum of unknowns and the important dimensionless parameters.

$$\left(\frac{\alpha}{\alpha_g}\right)\frac{\partial}{\partial \hat{t}}\left(m_{a,g}\, \hat{\rho}_g\, S_g\right) =$$

$$Pr_g\, \hat{\nabla}\cdot\left(m_{a,g}\, \hat{\rho}_g\, k_{rel,g}\left(\hat{\nabla}\hat{P}_g - Gr\, \theta\, \hat{k}\right)\right) \qquad \text{(D-98)}$$

$$+\, \tau\, Le_g\, \hat{\nabla}\cdot\left(\hat{\rho}_g\, S_g\, \hat{\nabla} m_{a,g}\right)$$

D.9.2 Water Equation

The previous equations relating to water can be substituted into the conservation of water equation to generate a single dimensionless water equation:

$$\left(\frac{\alpha}{\alpha_l}\right)\frac{\partial}{\partial \hat{t}}\left(S_l + \left(\frac{\rho_{g,o}}{\rho_l}\right) m_{w,g}\,\hat{\rho}_g\,S_g\right) =$$

$$Pr_l\,\hat{\nabla}\cdot\left(\left(\frac{1}{Ca}\right)k_{rel,l}\left(-J\,Su\,\hat{\nabla}\theta - \frac{dJ}{dS_l}\,\hat{\nabla}S_l + Bo\,\hat{k}\right)\right)$$

$$+ Pr_g\left(\frac{\alpha_g}{\alpha_l}\right)\left(\frac{\rho_{g,o}}{\rho_l}\right)\hat{\nabla}\cdot\left(m_{w,g}\,\hat{\rho}_g\,k_{rel,g}\left(\hat{\nabla}\hat{P}_g - Gr\,\theta\,\hat{k}\right)\right) \qquad \text{(D-99)}$$

$$+ \tau\,Le_g\left(\frac{\alpha_g}{\alpha_l}\right)\left(\frac{\rho_{g,o}}{\rho_l}\right)\hat{\nabla}\cdot\left(\hat{\rho}_g\,S_g\,\hat{\nabla}m_{w,g}\right)$$

D.9.3 Energy Equation

The previous equations relating to energy can be substituted into the conservation of energy equation to generate a single dimensionless energy equation:

$$\frac{\partial}{\partial \hat{t}}\left(\theta + \phi\,S_l\left(\frac{\rho_l}{\rho_{s,slg}}\right)\left(\frac{c_l}{c_s}\right)\theta\right.$$

$$+ \phi\,S_g\,m_{w,g}\,\hat{\rho}_g\left(\frac{\rho_{g,o}}{\rho_{s,slg}}\right)\left(\frac{c_l}{c_s}\right)\left(\left(\frac{c_{v,w,g}}{c_l}\right)\theta + U\right)$$

$$\left. + \phi\,S_g\,m_{a,g}\,\hat{\rho}_g\left(\frac{\rho_{g,o}}{\rho_{s,slg}}\right)\left(\frac{c_{v,a,g}}{c_s}\right)\theta\right) = \qquad \text{(D-100)}$$

$$\phi\,Pr_l\left(\frac{\alpha_l}{\alpha}\right)\left(\frac{\rho_l}{\rho_{s,slg}}\right)\left(\frac{c_l}{c_s}\right)\hat{\nabla}\cdot\left\{\theta\left(\frac{1}{Ca}\right)k_{rel,l}\left(-J\,Su\,\hat{\nabla}\theta - \frac{dJ}{dS_l}\,\hat{\nabla}S_l + Bo\,\hat{k}\right)\right.$$

$$\left. + \left(\left(\left(\frac{c_{p,w,g}}{c_l}\right)\theta + H\right)m_{w,g} + \left(\frac{c_{p,a,g}}{c_l}\right)\theta\,m_{a,g}\right)\left(\frac{\mu_g}{\mu_l}\right)\hat{\rho}_g\,k_{rel,g}\left(\hat{\nabla}\hat{P}_g - Gr\,\theta\,\hat{k}\right)\right\}$$

$$+ \phi\,Le_g\,\tau\left(\frac{\alpha_g}{\alpha}\right)\left(\frac{\rho_{g,o}}{\rho_{s,slg}}\right)\left(\frac{c_l}{c_s}\right)\hat{\nabla}\cdot\left(\left(\left(\frac{c_{p,w,g}}{c_l}\right) - \left(\frac{c_{p,a,g}}{c_l}\right)\right)\theta + H\right)S_g\,\hat{\rho}_g\,\hat{\nabla}m_{w,g}$$

D.10 SUMMARY OF DIMENSIONLESS GROUPS AND VARIABLES

The dimensionless terms are divided into seven categories: geometrical, property ratios, physical effects, source input, constitutive, time, and response. In Table D-1, the dimensionless terms are listed and described. Some terms are simple ratios of properties and do not have names. Of the seven categories of terms, the geometrical, property ratios, source input, constitutive, and time groups are self-explanatory. The rationale for the physical effects and response groups may not be obvious, and are discussed here.

The physical effects terms represent combinations of fluid properties (ρ, σ, $d\sigma/dT$, μ, c, u, h), geometrical data (L, k_{sat}, ϕ), and either input or boundary condition data (ΔT_{max}). The combination of fluid, geometrical, and input data dictate the importance of specific phenomenological behavior. For example, the natural convection is expected to increase in importance as the Grashof number increases. By increasing either ΔT_{max}, k_{sat}, or L, the Grashof number, Gr, which represents the ratio of buoyancy to viscous forces, will increase and the importance of natural convection will increase. Likewise, the importance of temperature-gradient driven capillary suction (due to the temperature dependence of surface tension) is measured in the surface tension number, Su. If either $d\sigma/dT$ or ΔT_{max} increases, then Su will increase. Thus, Su indicates the importance of temperature-gradient driven capillary suction. Additionally, the Bond number, Bo, represents the ratio of gravitational to capillary forces; the Capillary number, Ca, represents the ratio of viscous to capillary forces; the internal energy, U, and enthalpy, H, numbers represent ratio of energy in vaporization to energy in changing the temperature.

The response terms represent the unknowns or values to be calculated to solve the problem. As discussed earlier in this report, the mathematical description of two-phase mass and energy transport in a porous media is conveniently formulated in three conservation equations with numerous constitutive equations. The conservation equations are differential equations and the constitutive equations are mostly algebraic equations. In Table D-1, the response terms are those which are readily identified in the expanded summary of the conservation equations. By reviewing the constitutive equations, many of the response terms can be eliminated as unknowns, because they can be expressed as functions of a smaller subset of unknown response terms. For example, the mass fraction of air in the gas phase, $m_{a,g}$, can be expressed as a function of temperature and capillary pressure. In turn, temperature can be expressed as a function of dimensionless temperature, θ, and capillary pressure can be expressed as a function of liquid saturation, S_l.

D.11 SIMILARITY REQUIREMENTS

For dynamic similarity between a scale model and prototype, the geometrical, fluid, and physical dimensionless groups need to be the same. For most cases, this means that two finite numerical values are equal. An example is that the Grashof numbers be equal. This is the most common type of similarity discussed in the literature; however, another important type of similarity is "constitutive" similarity where the dimensionless group is not a finite numerical

Table D-1. SUMMARY OF DIMENSIONLESS TERMS

Property Ratio Terms

Term	Description
$\rho_{g,o} / \rho_{s,sig}$	reference gas to solid density ratio
$\rho_l / \rho_{s,sig}$	liquid to solid density ratio
μ_g / μ_l	gas to liquid viscosity ratio
$c_{w,g} / c_{s,sig}$	vapor to solid specific heat ratio
$c_a / c_{s,sig}$	air to solid specific heat ratio
$c_l / c_{s,sig}$	liquid to solid specific heat ratio
$Pr_g \equiv \nu_g / \alpha_g$	Prandtl number of gas phase
$Pr_l = \nu_l / \alpha_l$	Prandtl number of liquid phase
$Le_g \equiv D_{wa,g} / \alpha_g$	Lewis number of gas phase

Geometrical Terms

Term	Description
ϕ	porosity
$Da \equiv \left(\frac{k_{sat}}{L^2}\right)$	Darcy number

Constitutive Terms

Term	Description
$k_{rel,l}$	relative liquid phase permeability
$k_{rel,g}$	relative gas phase permeability
J	J-Leverett function
$\left(\frac{dJ}{dS_l}\right)$	derivative of J-Leverett function

Table D-1. SUMMARY OF DIMENSIONLESS TERMS (continued)

Physical Effect Terms

Term	Description
$Bo \equiv \frac{(\rho_l - \rho_{g,o}) g L \sqrt{k_{sat}/\phi}}{\sigma_o}$	Bond number
$Ca \equiv \frac{(\mu_l)^2}{\rho_l \sigma_o \sqrt{k_{sat}/\phi}}$	Capillary number
$Gr \equiv \frac{g \beta_g \Delta T_{max} (k_{sat}/\phi) L}{(\nu_g)^2}$	Grashof number for porous media
$Su \equiv \frac{\Delta T_{max}}{\sigma_o} \left.\frac{d\sigma}{dT}\right\|_o$	surface tension number
$U \equiv \frac{u_{lg}}{(c_l \Delta T_{max})}$	internal energy number
$H \equiv \frac{h_{lg}}{(c_l \Delta T_{max})}$	enthalpy number (also called Jacob or Jakob number)

Source Input Term

Term	Description
$\hat{Q}_e \equiv \frac{Q_e}{\left(\frac{k_t \Delta T_{max}}{L^2}\right)}$	dimensionless heat source

Time Term

Term	Description
$\hat{t} \equiv \frac{t}{\left(\frac{L^2}{\alpha}\right)}$	dimensionless time

Table D-1. SUMMARY OF DIMENSIONLESS TERMS (continued)

Response Terms

Term	Description
$m_{a,g}$	mass fraction of air in gas phase
$m_{w,g}$	mass fraction of water in gas phase
$\hat{\rho}_g$	dimensionless gas density
S_l	liquid phase saturation
S_g	gas phase saturation
θ	dimensionless temperature

value but is a function. An example of constitutive similarity is that the relative conductivities are functions of saturation:

$$k_{rel,l} = k_{rel,l}(S_l) \qquad \text{(D-101)}$$

and that these functions be the same for the scale model and prototype. In the present problem, constitutive similarity is required for:

$$k_{rel,l},\ k_{rel,g},\ J,\ \frac{dJ}{dS_l}$$

Although not explicitly discussed here, it is straightforward to argue that the geometrical shape and dimensionless boundary conditions need to be similar for two experiments to be geometrically and dynamically similar. An example is a boundary condition for the infiltration of liquid water, $q_{m,w,l,b}$ [kg/m^2-s]. An appropriate dimensionless quantity is

$$\hat{q}_{m,w,l,b} \equiv \frac{q_{m,w,l,b}}{\left(\frac{\mu_l \phi}{L}\right)} \qquad \text{(D-102)}$$

For complete similarity, the geometrical shapes, governing equations, and boundary conditions all need to be similar. Hence, complete similarity between a scale model (laboratory experiment) and prototype (i.e., the proposed HLW repository) is unlikely. Instead a more limited kind of similarity will be attempted in this project.

Property of
CNWRA Library